Inkjet-Printed Multisensor Platform on Flexible Substrates for Environmental Monitoring

THÈSE N^{O} 6191 (2014)

PRÉSENTÉE LE 20 JUIN 2014

À LA FACULTÉ DES SCIENCES ET TECHNIQUES DE L'INGÉNIEUR
LABORATOIRE DE CAPTEURS, ACTUATEURS ET MICROSYSTÈMES
PROGRAMME DOCTORAL EN MICROSYSTÈMES ET MICROÉLECTRONIQUE

ÉCOLE POLYTECHNIQUE FÉDÉRALE DE LAUSANNE

POUR L'OBTENTION DU GRADE DE DOCTEUR ÈS SCIENCES

PAR

Francisco MOLINA LOPEZ

acceptée sur proposition du jury:

Prof. H. Shea, président du jury
Prof. N. de Rooij, Dr D. Briand, directeurs de thèse
Prof. J. Brugger, rapporteur
Dr A. Oprea, rapporteur
Prof. K. Persaud, rapporteur

ÉCOLE POLYTECHNIQUE
FÉDÉRALE DE LAUSANNE
Suisse
2014

To everybody who made possible
this small contribution to science.

Acknowledgements

Research is definitely not an easy path to follow. Since the very first moment when I decided to dedicate the most part of my time to study sciences, and specially during the last 4 years and 3 months of my Ph.D., I had to face innumerable challenges and cope with complex concepts, tight deadlines, endless writing and reading, stubborn machines and disconcerting results. All the struggling becomes worth it when the expected result arrives, but until that precious moment, it is crucial to be constant and keep motivated. In my case, this positive state of mind would not have been possible without the permanent support of many people to whom I feel the need to show now my most sincere gratitude.

First of all I would like to express my gratitude to the members of my Ph.D. jury: Prof. H. Shea, Prof. K. Persaud, Dr. A. Oprea and Prof. J. Brugger for accepting to be part of it and for their valuable feedback to improve this document. I would like to thank Prof. Nico de Rooij for granting me the opportunity of working in SAMLAB, in an environment that brings together the highest research level with a great friendly atmosphere; Dr. Danick Briand for his constant supervision, professionalism, availability and for all the knowledge that he transferred to me in the last years, which will be extremely useful in my future career; and to all my previous colleagues from SAMLAB, LMTS and CSEM like J. Courbat who introduced me to the world of plastic electronics, helped me settling down at the very beginning of my Ph.D. and guided me through the equipment and work dynamics of the laboratory, but also to W. Noell, A. Homsy, P. Wägli, B. Guélat, J. Masson, S. Lani, D. Bayat, Y. Petremand, R. Bitterli, F. Jutzi, C. Ataman, R. Dauksevicius, R. Strässle, L. Ribetto, R. Gueye, Y. Wu and the division C from CSEM for their willingness to help whenever a doubt came up in the laboratory and for contributing to a wonderful work atmosphere. I would like to acknowledge M. Dadras for his fruitful discussions about microscopy and C. Novelli for doing his magic on my computer. Many special thanks go to David de Koninck, Franz Friedrich, Jason Ruan, Robert Lockhart, Nahtalie Frolet and Frédéric Loizeau for all the great technical and scientific interactions, the fun at every social event and their warm friendship. On top of that, I would like to thank my excellent current colleagues at SAMLAB and LMTS for helping me every time that I needed it till the very end of my Ph.D. journey: P. van der Wal, T. Akiyama, S. Gautsch, S. Talaei, M. Fighera, J. Bitterli, C. Borsa, P. Janphuang, Prof. J. L. Ramírez Falo, E. Lemaire, M. Camara, Prof. H. Shea, L. Maffli, S. Dandavino, A. Poulin, S. Araromi, N. Besse, D. Courtney, J. Zarate, etc. A very big "thanks" goes to Karine Frossard for her immense patience and quick support with all the administrative issues of living and working in Switzerland, and to Sandrine Piffaretti for her useful help in all the human resources-related issues.

A very special mention must go to the *FlexSmell* team in SAMLAB, my colleagues and very good friends Dr. Giorgio Mattana and Andrés Vásquez Quintero. I had the great fortune to work closely with them in Neuchâtel and around the world for the last few years. Work becomes a daily pleasure (and a lot of fun) with such good team around. Thank you also to the rest of the *FlexSmell* team in many countries in Europe for the exchange of knowledge and the big fun during the project meetings. Among them, I had the chance to collaborate and complete joint publications with C. Dehollain, A. Oprea, Prof. K. Persaud, E. Smits, K. Kapucu, S. Wang, S. Pandule, E. Danesh and G. Arutinov. All my gratitude goes to Maria Smolander for all the support that I received from her during my seven months stay in Finland and all the help that she is still providing to me in the present. Thanks to all the research staff at VTT (Finland) from whom I learned a lot, and specially to Nissanka Wickremassinghe and Cristina Gaspar who took very good care of my life inside and outside the lab during the tough Finnish winter. During my Ph.D., I had the great pleasure to collaborate with many people of great scientific and human potential. José Fernández Salmerón (Pepe) and Almudena Rivadeneyra from my home town University in Granada (Spain), are two excellent examples of it. Thank you guys for all the time spent together. My acknowledgement also goes to Thomas Kinkeldei for our smooth and fruitful collaboration.

My life out of the lab and the office in Switzerland would not have been so fun and pleasant without my good friends in Lausanne, as well as my excellent flatmate Gabriele Grosso (Lele). They are all responsible for my decision of taking the train from Lausanne to Neuchâtel every day to go to work! A special thought goes also to my friends from Granada for their timeless and "distanceless" friendship.

No less important than the people who supported me through my Ph.D. are those who motivated me to pursuit a research career when I was just an undergrad student. This is the case of Prof. Peter Asbeck from UCSD (USA), a great professional and personal reference for me since then; and Dr. Dennis Wang, a huge positive influence.

Finally, I would like to show my infinite gratitude to my mother, Caridad, who knew how to transmit to me, when I was only a child, the set of values that still today steer my life. She taught me with her example the rewarding feeling of thriving through endeavor and honesty, and never spared any effort to offer me the best for my education and for my life. I am also extremely grateful to my sister, Pepa, who has always looked for me and who still supports me, regardless of the distance, with this special connection between us that nobody else can understand. She is the best example of a great sister. I thank also those who are not with us anymore, but contributed to form and shape the person who I am today. I take the opportunity to thank also to the rest of my large Mediterranean family, who is always there for me and make every trip back to Spain the most enjoyable experience; and last but not least, I owe a big "thank you" to my beloved girlfriend, Yijie, for her unconditional support and generous patience during these last years. She knows how to cheer me up at every moment, brings harmony to my life and constantly challenges me with her curiosity and interest for science. Beside her, every next step becomes a new exciting and stimulating adventure to live.

Lausanne, 26 May 2014 F. Molina López

Abstract

The development of low-cost smart labels with sensing capabilities is raising a high interest among the scientific community due to the increasing need for monitoring ambient conditions in the fields of wearable electronics and logistics. Printed electronics gathers all the requirements to enable the development of cost-effective smart systems, the reason why the framework of this thesis, the EU project *FlexSmell*, targets the development of a printed radio frequency identification (RFID) smart label with sensing capabilities for perishable goods monitoring. In that respect, I present in this thesis the design, fabrication and characterization of different chemical gas, humidity and temperature microsensors fabricated on plastic foil by means of additive methods compatible with large-area and large-scale production. The high potential of integrating these microsensors together was demonstrated by inkjet printing a multisensing platform able to detect relevant parameters for perishable goods monitoring, such as temperature, relative humidity (R.H.) and presence of diverse chemical gases. On one hand the use of cost-effective polymeric substrates brings novel functionalities to the system, namely flexibility and light weight. On the other hand, owing to their simplicity and additive character, printed techniques can potentially lead to a reduction of the fabrication cost of smart labels by minimizing the number of processing steps, the usage of raw material and the need of expensive clean-room infrastructure. Inkjet printing is especially appealing for research among other printing techniques because it permits quick prototyping due to its digital character (no need of a mask) and enables local functionalization of the different sensors in the platform. The issue of the typical low resolution of inkjet printing was addressed in this work by proposing suitable sensors architecture and optimizing the fabrication processes of inkjet printing silver nanoparticles, plating on plastic foil and inkjet-printed polymers. The combination of the optimal process and materials with the investigation of different sensor architectures permitted the development, for the first time, of fully printed capacitive R.H. sensors with high performance and reduced footprint.

The sensors developed in this thesis were based on the absorption of the analyte in the sensing layer, which modified its relative permittivity and thickness. Cellulose acetate butyrate (CAB) has been inkjet-printed to perform as R.H. sensing layer in this work. Several theoretical models have been proposed and employed to understand the working principle of the different developed transducers and sensing layers, facilitating their optimization. Since the employed polymeric foils provided the system with mechanical flexibility, a new theoretical model to predict the effect of bending in sensors based on interdigitated electrodes (IDE) has been thoroughly described. The first developed sensor was based on IDE to facilitate the interaction

between analyte and sensing layer. The performance of the device was optimized through the electrodeposition of nickel on the silver electrodes, which contributed to sensor stability, and the use of differential methods to eliminate the undesired influence of the polymeric substrate. The reliable reduction of the IDE pitch and the passivation of the substrate against moisture were simultaneously achieved by introducing a thin dielectric interlayer between electrodes. The second capacitive device was based on a standard parallel-plate (PP) structure where the dielectric between electrodes acted as a sensing layer. It was demonstrated that once the issue of chemical incompatibility between printed stack layers was solved, the standard PP structure outperformed the others investigated in terms of capacitance per surface area (3.8 pF / mm^2), sensitivity towards R.H. (0.33% / 1% R.H.) and response time (50 seconds). The high porosity of the printed top electrode facilitated the humidity diffusion through the sensor, permitting the realization of devices as small as 1 mm^2, and opening a new door to further miniaturization of printed capacitive gas sensors. The third capacitive device developed consisted of a novel array of fully printed MEMS microbridges utilizing the substrate as sensing layer through a swelling-based sensing principle never reported before. The sensor is independent of the analyte permittivity complementing the others described above.

Last but not least, in order to broaden the functionality of our multisensing platform for temperature detection, inkjet-printed resistive thermodetectors (RTD) were developed on foil. Temperature plays a main role in gas sensing so its control resulted crucial for thermal compensation as well. To surmount the low sensitivity encountered for bare-printed RTD while keeping the additive character of their fabrication, electrodeposition of nickel on the printed lines was demonstrated. Plated RTD presented a three-fold sensitivity improvement, up to 1820 ppm / °C. The same meander structure used for the RTD has been adapted to form an integrated microhotplate for those sensing layers requiring relatively high temperature (100°C) of operation. The inkjet-printed microhotplate has been validated for sensitive and reversible chemiresistive detection of ammonia at 90°C, corresponding to a power consumption of 35 mW. Finally, all the described sensing elements (except the PP-MEMS sensors) were integrated for first time on a common substrate to form a multisensing platform compatible with a flexible and printed RFID smart label. Within the *FlexSmell* project framework, this smart label was applied to smart packaging for the reduction of perishable goods waste during their distribution. Nevertheless, the outcome of this work presents a high interest in general, for the development of very low-cost ubiquitous and wireless gas and temperature sensing systems conceived to fulfill the increasing demand in ambient monitoring in the fields of wearable electronics, distributed smart sensing objects or logistics.

Keywords: Gas sensor, Thermometer, Plastic foil, Inkjet printing, Capacitor, Microhotplate, MEMS, Smart sensing system, RFID.

Résumé

Le développement d'objets intelligents à bas coût possédant des capacités de détection soulève un grand intérêt dans la communauté scientifique en raison de la nécessité croissante de connaître les conditions ambiantes dans les domaines de l'électronique à porter et de la logistique. L'électronique imprimée rassemble toutes les conditions pour permettre le développement de tels dispositifs à faible coût, raison pour laquelle le cadre de cette thèse, le projet européen *FlexSmell*, visait le développement d'un Tag d'identification par radiofréquence (RFID) hybride (avec des composants en silicium et imprimés) et intelligent incluant des capacités de détection pour le suivi des biens périssables. À cet égard, je présente dans cette thèse la conception, la fabrication et la caractérisation de différents micro-capteurs de gaz, d'humidité et de température fabriqués sur des feuilles de plastique souples par des méthodes additives compatibles avec une production sur grande surface et à grande échelle. Le grand potentiel d'intégration de ces micro-capteurs a été démontré par la réalisation par impression jet d'encre d'une plateforme multi-capteurs permettant de mesurer les paramètres pertinents pour le suivi de produits périssables, tels que la température, l'humidité relative (H.R.) et la présence de gaz divers. D'une part, l'utilisation de substrats polymères peu coûteux apporte de nouvelles fonctionnalités à ces systèmes de capteurs, notamment souplesse et légèreté. D'autre part, en raison de leur simplicité et de leur caractère additif, les techniques d'impression peuvent conduire à une réduction significative du coût de production d'objets intelligents en réduisant au minimum le nombre d'étapes de fabrication ainsi que la quantité de matières premières utilisée, tout en s'affranchissant du besoin d'une infrastructure salle blanche lourde et coûteuse. L'impression par jet d'encre utilisée pour ces recherches est particulièrement attrayante car elle permet, grâce à son caractère digital, le prototypage rapide, en plus d'être appropriée pour une fonctionnalisation localisée des capteurs. Le problème de la faible résolution typique de l'impression à jet d'encre a été adressé en proposant des architectures de capteurs adaptées et en optimisant les procédés d'impression d'encres de nanoparticules d'argent et d'électrodéposition de métaux sur feuille de plastique. La combinaison optimale des procédés et des matériaux avec les différentes architectures de capteurs a permis un développement original de capteurs H.R. capacitifs totalement imprimés performants et de taille réduite. Les capteurs développés dans cette thèse sont basés sur l'absorption de l'analyte dans la couche active qui résulte en une modification de sa permittivité relative et de son épaisseur. Lors de ces travaux, l'impression jet d'encre d'une couche de détection en acétate butyrate de cellulose (CAB) a été mise en œuvre pour la détection H.R. Plusieurs modèles théoriques ont été décrits et ont servi à une meilleure compréhension du principe de fonctionnement des

différentes architectures de capteurs capacitifs développés et à leur optimisation. Notamment, un nouveau modèle théorique pour prédire l'effet de la flexion pour le capteur à électrodes interdigitées (IDE) a été proposé. Le premier capteur développé est basé sur des IDE afin de faciliter l'interaction entre l'analyte gazeux et la couche active. Les performances du dispositif ont été optimisées par l'électrodéposition de nickel sur les électrodes d'argent, pour une meilleure stabilité du capteur, et par l'utilisation de méthodes différentielles pour éliminer l'influence indésirable du substrat en polymère. La réduction de façon fiable du pas des IDE et la passivation du substrat contre l'humidité ont été obtenues par l'introduction d'une couche mince diélectrique intermédiaire entre les électrodes. Le second dispositif capacitif est basé sur une structure standard à plaques parallèles (PP), où le diélectrique entre les électrodes agit comme une couche sensible. Il a été démontré qu'une fois le problème de l'incompatibilité chimique entre les différentes couches imprimées a été résolu, la structure PP standard était plus performante que les autres étudiées en termes de capacité par unité de surface (3,8 pF / mm^2), de sensibilité à HR (0,33 % / 1 % H.R.) et de temps de réponse (50 secondes). Grâce à la porosité de l'électrode supérieure imprimée qui permet une bonne diffusion de l'humidité, une forte miniaturisation des capteurs de gaz capacitifs imprimés a été réalisée (1 mm^2). Le troisième dispositif capacitif développé est composé d'un réseau de micro-ponts entièrement imprimés qui utilise le substrat comme couche active avec un principe de détection original basé sur son expansion en présence de l'analyte. Le principe de fonctionnement du capteur est indépendant de la permittivité de l'analyte et donc complémentaire à ceux décrits auparavant. Finalement, afin d'étendre les fonctions de notre plateforme multi-capteurs à la détection de la température, des thermodétecteurs résistifs (RDT) imprimés par jet d'encre ont été développés sur feuille plastique, pour son suivi et/ou sa compensation. Pour remédier à la faible sensibilité des RDT imprimés tout en gardant le caractère additif de leur fabrication, l'électrodéposition de nickel sur les lignes d'argent imprimées a été implémentée. Les RDT avec électrodéposition présentaient une amélioration de la sensibilité de 300%, jusqu'à 1820 ppm / °C. La même structure en méandre utilisée pour le RDT a été adaptée pour former une micro-plaque chauffante nécessaire au bon fonctionnement de couches sensibles aux gaz nécessitant une température d'opération relativement élevée (100°C). Cette micro-plaque chauffante imprimée par jet d'encre a été appliquée à une détection résistive de l'ammoniac de façon réversible à 90°C, correspondant à une puissance de consommation de 35 mW. Enfin, tous les éléments de détection décrits (à l'exception des capteurs PP- MEMS) ont été intégrés pour une première fois sur un même substrat pour former une plateforme multi-capteurs compatible avec un Tag RFID intelligent imprimé sur support souple. Dans le cadre du projet *FlexSmell*, ce Tag a été appliqué au domaine du packaging intelligent visant la réduction des pertes lors de la distribution des produits périssables. Toutefois, les résultats de cette thèse présentent aussi un fort intérêt général pour le développement de systèmes intelligents distribués de détection de gaz et de température, sans fil et à faible coût, conçus pour répondre à la demande croissante en matière de contrôle, surveillance et suivi des conditions ambiantes dans les domaines de l'électronique à porter, des objets intelligents et de la logistique.

Mots-clés : Capteur de gaz, Thermomètre, Feuille plastique, Impression à jet d'encre, Condensateur, Microélément chauffant, MEMS, Système de détection intelligent, RFID.

Contents

List of Figures

List of Tables

1 Introduction

1.1 Introduction

Conventional electronics are based on rigid and brittle inorganic materials, such as Silicon or Gallium Arsenide, which are fabricated in clean-room environments at wafer-size level. This type of electronics starts to find severe limitations to satisfy the demands imposed by new applications, especially those requiring large area, mechanical flexibility or compatibility with biological systems. Thank to their particular properties, printed and organic electronics could fill this existing gap in technology, reason why they are recently gaining a lot of interest in the field of circuits, sensors, bioelectronics, photovoltaics, displays and lighting.

On one hand organic electronics, polymer electronics or plastic electronics consist of using organic materials as the substrate or active material in electronic circuits and systems. Some organic electronic devices have reached a level of technological maturity high enough to find a place in the market for large-area applications. This is the case of well established devices such as organic thin film transistors (OTFTs) or especially organic LEDs (OLEDs), already used on modern displays and TVs. As a natural expansion of the field, the development of low-cost ubiquitous flexible sensors, biomedical stretchable and implantable devices or intelligent surfaces are currently gaining a lot of interest. These devices require all the use of polymers as supportive substrate. Using polymers substrates as substrates for electronic systems is then opening new opportunities in the field of microengineering. Polymers have the potential of making electronics very low-cost, environmental friendly, disposable, biocompatible or biodegradable. Moreover, they can bring added value to electronic systems especially in those applications where optical opacity, weight or mechanical rigidity are limiting factors. Some polymers are also able to stretch or deform into arbitrary shapes without loosing their properties. The fact that they are inexpensive and compatible with large-scale production though roll-to-roll or sheet-to-sheet process make them the perfect complement to be used with printing technologies, rather than with standard clean-room techniques such as photolithography, lift-off or etching; to the point that the term printing electronics often implies the use of a plastic or paper substrate.

Printed electronics refer to a set of printing methods used to pattern electronic circuits on different substrates. Printed electronics are associated to low cost owing not only to their additive nature, which reduce the fabrication process complexity and optimize the material usage [1,2], but also to its compatibility with inexpensive substrate materials, such as plastic or paper. Printing techniques do not involve aggressive chemicals, high demanding conditions like ultra clean environments, or high temperatures. They are also suitable for large-scale production through sheet-to-sheet or roll-to-roll processes, which reduce further their production cost [3,4]. Traditional graphic printing is optimized for patterns size adapted to the human eye, which is able to resolve ~ 100 um [5]. Unlike in the case of graphic printing, in printing electronics the resolution is a key aspect to be optimized. Among the different printing technologies, screen printing, inkjet printing, gravure or flexography are the most common ones. Table 1.1 and Figure 1.1 summarizes the main features of these different printing technologies [6,7].

Table 1.1: Comparison of layer thickness, thickness variation and ink viscosity for different printing electronics techniques. Adapted from [6] [7].

Technique	Layer thickness (µm)	Thickness variation	Viscosity (cP)
Screen	5-20	huge	500-50000
Flexography	0.8-2.5	-	50-500
Gravure	0.1-3	medium	50-500
Inkjet	0.1-2	small	1-30

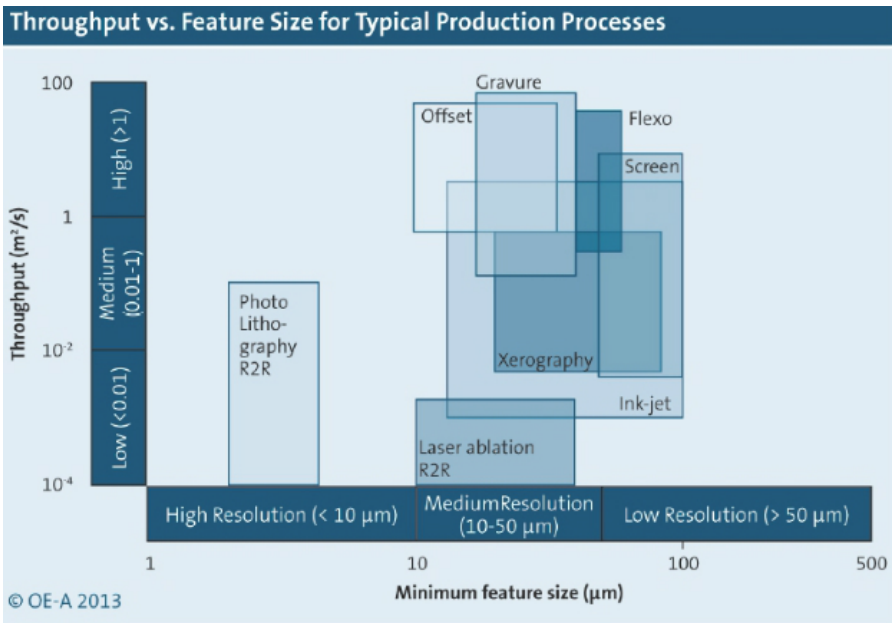

Figure 1.1: Comparison of resolution and throughput for different printing electronics techniques.

Among the different printing technique exposed above, inkjet printing has been selected as

the main technology during this thesis work because of its good resolution and also due to its non-contact and digital character, which makes unnecessary the use of a mask. This last aspect is key for quick prototyping, which lead to a significant saving of research time and cost. Concretely, drop-on-demand inkjet printing has been used, in which the drops are ejected only on the necessary location, by opposition to continuous jet printing. There are two main ways to generate the pressure pulse necessary to form and eject the ink drops out of their small reservoir through a micrometer sized nozzle (see Figure 1.2). The first way consists of the generation of a bubble by using a heater (thermal inkjet). The second way is to use a MEMS piezoelectric actuator that squishes the ink out (piezoelectric inkjet) [8]. The commercial availability of modern, yet economical, inkjet-printers based on piezoelectric actuation contributed to our selection of this method. Among the parameters that can influence the quality of inkjet-printed lines, the most significant ones for a defined combination of ink/substrate and a fixed drop volume are: substrate surface treatment, surface and ink temperature, jetting frequency and speed, and the drop-to-drop distance as it is depicted in Figure 1.3.

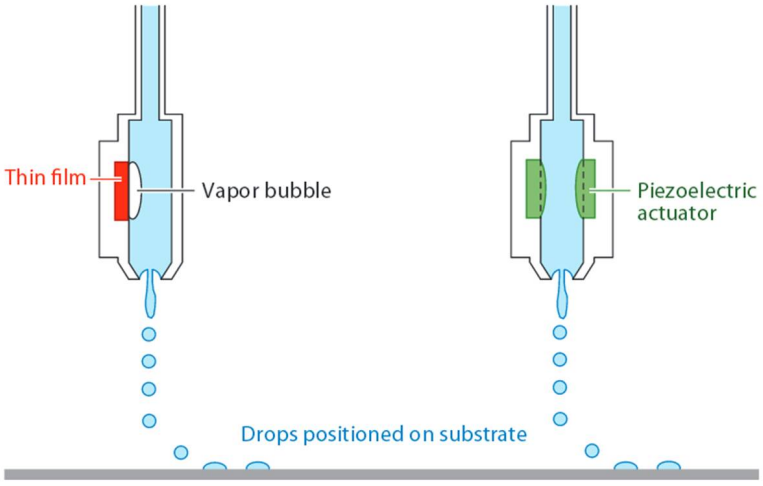

Figure 1.2: Schematic diagram showing the operation of drop-on-demand inkjet printing, where drops are formed and ejected in two ways: Thermal inkjet (on the left) and piezoelectric inkjet (on the right) [8].

Summarizing, the utilization of flexible low-cost polymeric substrates in combination with additive methods compatible with large-area and large-scale fabrication such as printing, is paving the way towards a new generation of thin and light-weight electronic systems able adapt to arbitrary shapes. On to top of that, owing to their ultra low fabrication cost, these systems can be ubiquitous and disposable. This set of characteristics enables new applications such as large-area displays, large-area photovoltaics or smart packaging.

1.2 Project background and motivation

Shortage of resources is one of the biggest issues of the world nowadays. The increasing world population demands every time more and more goods and the countries need to struggle to

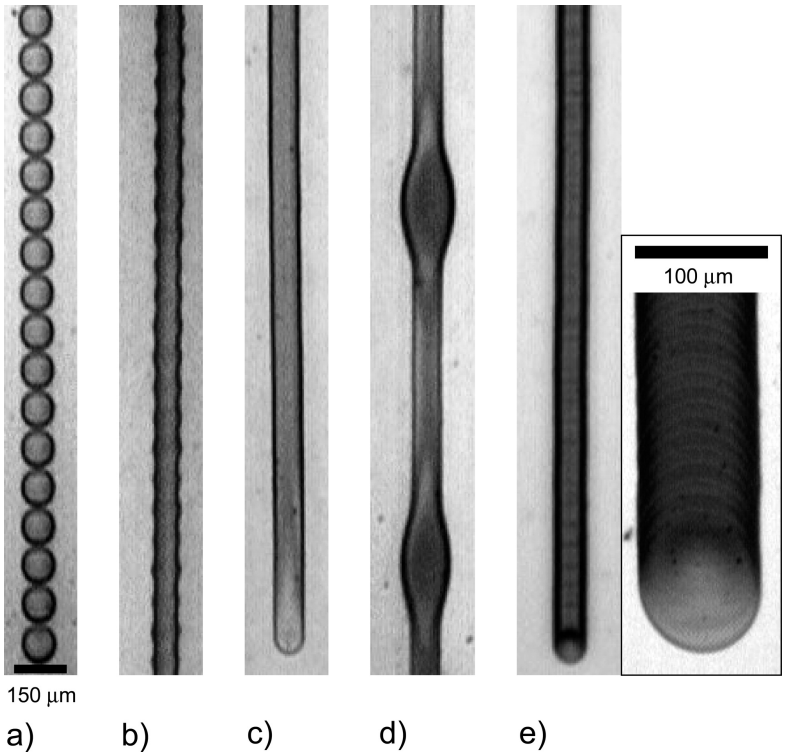

Figure 1.3: Examples of principal printed line behaviours: (a) individual drops, (b) scalloped, (c) uniform (ideal case), (d) bulging, and (e) stacked coins (formed when one drop lands onto another drop already dry). Drop spacing decreases from left to right [9].

fulfill these demands. Global market aggravates even more the situation since goods need to be transported across the world, complicating their distribution and generating a huge waste of perishable goods in the process. Recent studies about goods waste have thrown really worrisome numbers: for instance, 40% of the total perishable food in USA is wasted along the whole process "from the field to the the dish" [10]. Moreover, food waste contributes to excess consumption of freshwater and fossil fuels which, along with methane and CO_2 emissions from decomposing food, impacts global climate change [11]. A big part of that waste occurred during transportation [12]. Extracting information of the real ambient conditions that goods undergo during transportation could prevent a large part of this waste. However, obtaining this information requires gathering a large amount of data of temperature, relative humidity and presence of certain gases or volatile organic compounds (VOC) at many different points around the goods, and over certain time. Turning this concept into reality requires the development of extremely cheap sensing systems readily integrable in food packages. Inspired by this need, the Marie Curie Actions European project *FlexSmell* has targeted at producing a hybrid (organic-inorganic) very low-cost and ultra low-power olfaction RFID tag for freshness & quality traceability control of perishable goods through smart packaging. This system is based on transducers functionalized with different gas bio-receptors or specific sensing layers, and implemented on a flexible substrate on foil using printing techniques. Because logistics for medicines and food requires relatively slow sampling times of 10 to 15 minutes during no

more than few weeks, there is not special need for very fast or very long-lasting devices for this targeted application. Nonetheless, the sensors must be able to distinguish among different analytes, including humidity, ammonia, alcohols and other VOC. The resulting printed foil-like sensors needed to be also integrated with the rest of a RFID system. Two different approaches have been investigated by other partners in the project to include the flexible sensors on the RFID tag: either the sensors were patterned in a monolithical way on the tag, which was advantageous to minimize process steps, or they were realized on a different foil and then assembled into the main tag using low-cost foil-to-foil integration techniques. Although the last option is more complex from a processing point of view, it was preferred because it allowed more flexibility to fabricate the sensors and to test them before final integration into the tag. A hybrid approach has been also studied to assemble on the main flexible foil the silicon chips serving for sensors reading-out and RFID communication.

Different transduction principles such as field-effect, capacitance and resistance have been implemented on the tag to achieve low-power consumption, good selectivity and high sensitivity to different analytes relevant in food spoilage. Among them, I focused during my project on the development of resistive and especially on capacitive sensors by means of low-cost technologies such as inkjet printing and other additive methods on polymeric foil. The investigation of different methods for the functionalization and encapsulation of these devices have been addressed to form multisensing platforms at very low cost able to sense simultaneously ammonia vapour, relative humidity and temperature. The ability of a gas sensor to distinguish between different present analytes is one of the main challenges to solve in the field, and the concept of a many sensors integrated and operating together in a same platform presents itself as one of the best candidate to solve this issue. Other analytes of interest in food spoilage are detailed in Section 5.4.3 of Chapter 5. The detection of such analytes were the field of research of other partners of the *FlexSmell* project. At the end, the developed smart system was able to store data from the sensors and transmit them wirelessly, setting the ground for the future development of smart sensing RFID tags.

1.3 State of the art

Since the topic of this thesis is the development of resistive and capacitive gas sensors on flexible polymeric substrates for food monitoring through RFID labels, the sensors development required low-cost non-standard fabrication techniques such as inkjet printing or electrodeposition. With that consideration in mind, I developed three different kind of capacitive sensors, namely interdigitated electrode (IDE) with a sensing layer on top, parallel-plate sensors where the sensing layer is placed between plates, and parallel plates-like suspended beams utilizing the polymeric substrate as sensing layer. Thermoresistors and microhotplates have been also developed to deal with the influence of temperature on gas sensing: whereas the thermoresistors were used to account for the variations in capacitive detection of humidity at different temperatures, the microhotplates were used to heat up the sensing layer of an ammonia resistive sensor. Thus, in this section I review previously reported work dealing

with resistive, capacitive and beam-based gas sensors on foil as well as thermoresistors and heaters on foil, putting special emphasis on printed devices. Owing to their similarities with these devices, other capacitive structures realized by means of printing technologies are also described in this section despite their application in fields other than gas sensing. Finally, I mention previous existing work where some of the non-standard processes that I also optimized and used in this thesis were studied, namely inkjet printing, electrodeposition and diverse techniques to deposit sensing layers.

1.3.1 Resistive gas sensors on foil

There exists a relatively mature technology of microfabricated resistive gas sensors, some of them even commercially available. Those mature devices are based on metal oxide (MOX) sensing layers, which conductivity changes in presence of a gas as a result of a red-ox reaction occurring at high temperatures [13] (so they usually require the use of an integrated heater); or on conductive polymers which conductivity changes in presence of a target molecule for different reasons such as red-ox reactions, doping or dedoping [14, 15], swelling of the polymer [16], etc. In any case, these devices have traditionally been developed mostly on silicon and other rigid ceramic substrates and by means of standard expensive microfabrication techniques. Only recently (over the last 8 years) there has been some published work related with the development of flexible/polymeric resistive gas and vapour (humidity included) sensors fabricated by mostly using clean room technology. The sensors were mostly based either on conductive polymers or on MOX with integrated hotplate for detection of a high variety of vapours and gases. Among them, few examples can be found where printing technology was employed, and to the best of our knowledge there is only one example of printed resistive sensor on foil with integrated heater in the archival literature. In 2006, mechanically compliant humidity sensors were fabricated in nanoporous membranes such as polycarbonate, cellulose acetate, and nylon membranes [17]. The same year, resistive sensing for vapour (hexane, toluene, acetone, chloroform, acetonitrile, methanol, water, etc.) was demonstrated with films of single-walled carbon nanotube bundles (SWNT) on flexible PET substrates. These sensors were extremely easy to fabricate using the line patterning method, which could be considered as a hybrid printing method consisting on printing with a normal printer the negative of the pattern on a PET foil, where the SWNT attached directly after dipping the substrate in the SWNT dispersion. [18]. Another example of on-foil resistive sensor is found in [19], where gold electrodes were fabricated on a polyethylene terephthalate (PET) film using low temperature sputtering technique for a flexible resistive-type relative humidity (R.H.) sensor which used in situ co-polymerization of methyl methacrylate (MMA) and [3-(methacrylamino)propyl] trimethyl ammonium chloride (MAPTAC) copolymer as sensing layer. The logarithm of the sensor signal was linear in the range of 10–90% R.H., presented low hysteresis (within 6.1% R.H.), good response (45 s) and recovery time (150 s) and long-term stability (120 days at least). In 2008, resisitive sensors based on a drop-coated MOX (SnO_2) sensing layer with microheater integrated were fabricated by means of evaporation and lift-off on polyimide for CO, NO_x and CH_4 [20]. One year later, in 2009, a

chemoresistive gas sensor array for the volatile organic compounds based on electrospun nanofibrous was presented in [21]. The sensor included read-out electronics, both of them fabricated by means of standard clean room technologies on plastic substrate. Regarding devices fabricated using conventional printing techniques, silkscreen printed gold electrodes on alumina substrate covered with photocurable electrolyte inks for resistive measurements of humidity were reported in 2008 [22]. The same year Crowley *et al.* presented screen printing of silver electrodes using inkjet-printed polyaniline nanoparticle films as sensing layer for conductimetric detection of ammonia [23]. They used a commercially available external foil heater to improve the sensing performances. The same group has also reported on a fully printable polyaniline-copper (II) chloride chemoresistor for the detection of hydrogen sulfide gas. On exposure to hydrogen sulfide, 2.5 ppmv (parts per million by volume) is clearly detectable with a linear relationship between measured current and concentration over the 10–100 ppmv region [24]. Finally, Claramunt and colleagues have recently reported an ammonia sensor consisting of a polyimide flexible substrate, onto which an array of silver interdigitated electrodes were inkjet-printed on one side, and a common silver heater on the backside. The interdigitated electrodes were coated with carbon nanofibers decorated with metal nanoparticles (see Figure 1.4). The heater was used to chemically reset the nanofibers and make the sensor operation reversible. The sensor showed 3% change in resistance upon exposure to rather high concentrations of ammonia (500 ppm). A relatively high power consumption of around 150 mW was needed to achieve the optimal sensing temperature of 110 to 120 °C [25].

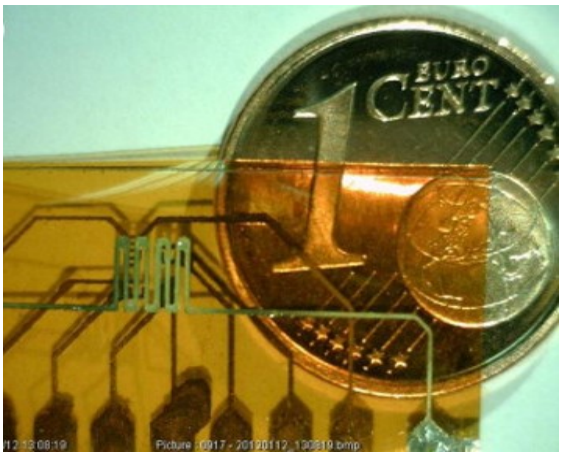

Figure 1.4: Optical picture of the sensor developed in [25]. A silver heater was printed on the bottom part of a polyimide foil and four comb electrodes on the other side of the foil to be functionalized for ammonia sensing.

As it has been described above, only few resistive gas sensors printed on foil appear in the literature, among them only one developed by Claramunt $etal$. includes a printed integrated heater to improve the sensor performances. In this thesis we present a microhotplate for ammonia sensing similar to the one developed by Claramunt $etal$. However, apart from using a different and more performing sensing layer (developed by our partners at the University of

Manchester), we utilized another sensor configuration to decrease the power consumption of the device. Basically, we decreased the size of the devices from few mm^2 to 1 mm^2 and used a thin dielectric layer instead of the 50 um-thick substrate to separate the heater from the sensing layer. We also replaced the expensive polyimide foil substrate for more cost effective polyethylene naphthalate (PEN), and demonstrated the possibility of electroplating noble materials like nickel or gold on the silver seed for better chemical compatibility and long-term stability.

1.3.2 Capacitive gas sensors on foil

Even though the previous examples of gas resistive sensors are significant in terms of the used technology, the requirements for low-power consumption of the *FlexSmell* project favored capacitive-based devices over resistive-based ones. An important part of these sensors utilizes the ability of certain polymers to absorb humidity and other vapours and gases, modifying their dielectric properties and/or swelling, inducing in that way changes in the capacitive structure in which they are placed. As in the case of resistive gas sensors, we can find companies like *Sensirion* in Stäfa (Switzerland) producing commercial humidity capacitive microsensors made on silicon by means of standard clean room technology. Within the *CATRENE* project *Pasteur*, CO_2 sensors have been developed through a fabrication process compatible with CMOS that included also post-processing coating of the transducers by means of inkjet-printing [26]. Also some examples of capacitive vapour (propan-1-ol, toluene, trichloromethane, n-octane, ethanol, etc.) sensors made on Si with CMOS integrated read-out circuitry can be found in the literature [27–30]. Since some years ago, the field is undergoing a transition towards foil technology while keeping traditional expensive patterning methods. Only very recently, very few capacitive gas sensors have been fabricated using only printing technologies for humidity detection. Two main geometries (shown in Figure 1.5) are commonly utilized for the fabrication of capacitive sensors: interdigitated electrode (IDE) and parallel plates (PP). Although some beam-based gas sensors use capacitive detection principle as well, they will be described in the Section 1.3.3 along with other microbeams-based systems. On the other hand, other capacitive microstructures fabricated by means of printing technologies for applications different from gas sensing will be reviewed at the end of this section.

Even though the number of capacitive gas sensors fabricated on foil by means of printing technology is swiftly increasing, the low resolution and poor reproducibility allowed by printing technologies along with the undesired gas absorption into the polymeric materials utilized as substrate, remain important unsolved issues that prevent printed gas sensors on foil to be as performing as their silicon counterparts.

Interdigitated (IDE) gas sensors on foil

We can find in archival literature few previous works highlighting the fabrication of IDE gas and vapour sensors on foil using standard microfabrication methods for relative humidity

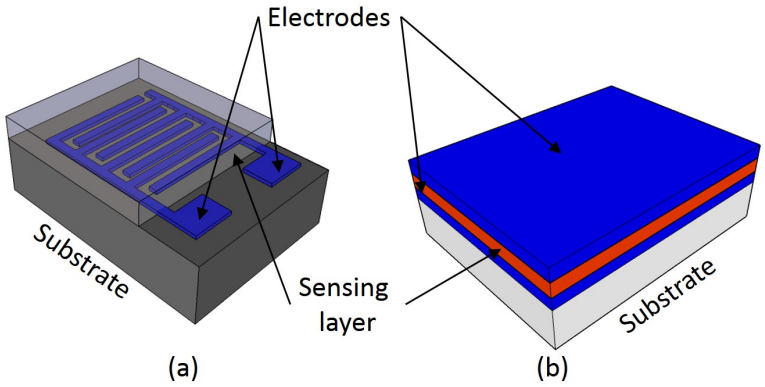

Figure 1.5: Sketch displaying the most typical capacitor configurations: (a) interdigitated electrode (IDE) and (b) parallel plates (PP).

(R.H.) and volatile organic compounds (VOC) detection. Some of these works come from our own group in collaboration with Institute of Physical Chemistry of the University of Tübingen (IPC-EKUT, Germany) (see Figure 1.6). Other groups have also reported on similar devices, but in both previous cases the emphasis was almost always on the sensing layer composition and the substrate contribution to the sensing behaviour rather than on the transducers themselves. That scenario is expected if one considers the low limitations in size offered by standard microfabrication methods. Only very recently, in the last 3 - 4 years, some authors have reported on partially or fully printed IDE-based gas sensors. Due to the new challenges introduced by the printing process, such as low patterning resolution, much more focus was put now on the fabrication of the IDE rather than on the sensing layer. The devices were usually tested only for R.H. which is the most straight forward analyte to detect due to its high permittivity and easiness to generate compared to other substances in gas state such as VOC.

In 2008, temperature and humidity sensors were developed by patterning gold (e-beam evaporated) on parylene and using polyimide as sensing layer. The sensitivity was 0.03 pF / % R.H. [32]. One year later, IDE capacitive humidity sensors based on multi-walled carbon nanotubes MWCNTs/polyelectrolyte interfaces on flexible substrates were reported [33]. Humidity sensing was demonstrated by a reversible change of capacitance, from few tens pF to hundreds pF, as the relative humidity level changed from 35% to 60%. The average response and recovery time of the devices was of few min. That same year Oprea *et al.*, in collaboration with EPFL-SAMLAB fabricated low-power temperature and VOC (ammonia, toluene, n-hexane, n-propanol and ethanol) sensors evaporated on flexible substrates and functionalized by spray coating of customized sensing layers [31]. They measured the capacitance using a differential method to subtract the parasitic effect of the substrate. The utilized sensing materials were common polymers, like PEUT or PDMS, and the sensitivity was good enough to detect gas well below time weighted average (TWA) levels. More recently, a humidity sensor based on evaporated gold on a substrate of cellulose-polypyrrole nanocomposite was reported. The response (continuous humidification from 27.8 to 94.2%) and recovery

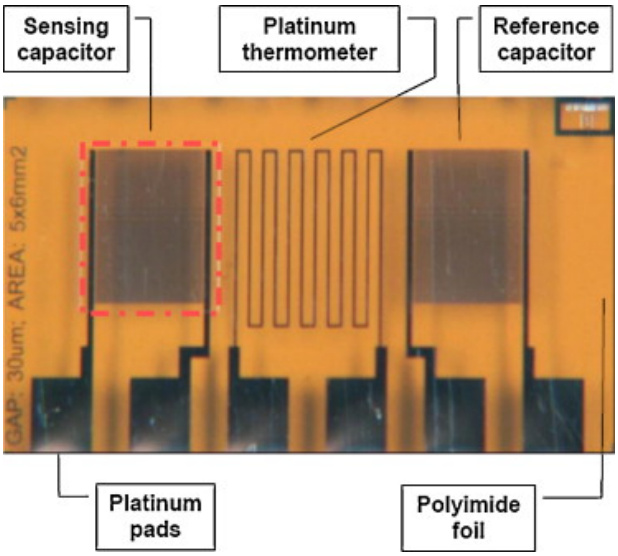

Figure 1.6: Sensor platform on polyimide substrate with Pt thermometer, IDE and connection pads. The IDE are capacitive transducers, a sensing one (left) and a reference one (right). The area reserved for the polymer sensing layer is surrounded by a dot line frame [31].

(continuous dehumidification from 91.7 to 28.9%) time was ~ 418 s (~ 7 s per 1 %R.H.) [34].

Only very recently we can find printed capacitive humidity sensors on foil where the capacitor is formed by a planar IDE strucutre: In 2011 and 2012, Starke *et al.* developed a silver-based inkjet-printed relative humidity sensor on polyimide and PET substrate respectively. The devices size was rather large, with a minimum line width and inter-lines gap of 119 and 90 µm respectively in the best cases. Their response behaved linearly up to ~ 70% R.H. and faster-than-linear above that level. The devices also presented certain hysteresis and the dependence with temperature was investigated [35, 36]. Our group also presented in 2011 IDE humidity sensors on paper. In spite of fact that the paper was passivated with a moisture barrier layer of parylene-C and that differential measurements were carried out to minimize the influence of the substrate [37], the capacitive sensors exhibited an exponential response with humidity level and an unstable output signal. One year later, another paper described inkjet printing of capacitive humidity sensors also based on nanoparticles of silver. The silver electrodes were inkjet-printed on polyimide, and the authors used Nafion® as humidity sensing layer during impedance measurements [38]. The minimum line width and gap achieved on the substrate was of ~ 49 µm and ~ 34 µm respectively. The sensors were tested in a broad humidity range of 5 – 95% R.H. For each humidity value, both impedance components have been measured in the frequency range of 20 Hz – 1 MHz. The signal did not show a linear behaviour neither. Other than inkjet, gravure-printed silver electrodes on PET foil covered with polymer poly (2-hydroxyethyl methacrylate) (pHEMA) for capacitive humidity sensing was presented in [39]. The sensor response was measured in the range of 30% R.H. to 80% R.H.; the maximum percentage change in capacitance was 172% at 80% R.H. when compared to base capacitance at 30% R.H. However, the signal was supralinear. The

humidity response of the printed sensor revealed a very high stability with a maximum error of 0.6% and 0.8% from the average value at 40% R.H. and 60% R.H., respectively. Another work from 2014 presented printed IDE using the polyimide substrate as sensing layer and achieving a sensitivity of 4.5 fF / % R.H. The dependence of the sensor with temperature was analyzed at different operation frequencies [40].

The performance of the previous printed sensors was limited and no special care was taken to study and remove the parasitic effect of the substrate [31] in the majority of the cases. This usually resulted in no stabilization of the sensor signal or in very long response time. This last point is however difficult to confirm because in the most part of the work presented above the authors did not study the transient response of the sensors.

Printed capacitors on foil for diverse applications As it can be drawn from the previous sections, not a lot of work has been found describing fully printed capacitive gas sensors. However, some work has been reported in the fabrication of printed capacitors for other sensing applications, describing interesting fabrication processes. For instance, in 2003 PEDOT:PSS (conductive polymer) inkjet-printed parallel-plate capacitors for RC filters were published [41, 42]. In 2009, an IDE capacitive and resistive strain sensor using inkjet printed PEDOT:PSS [43] was also reported. The reported geometries could be readily applicable to gas sensing although the possible interaction of of PEDOT:PSS in capacitive structures with humidity have not been studied.

In this thesis, different fully inkjet-printed IDE capacitive R.H. sensors will be developed while pushing forward the maximum resolution permitted by inkjet printing. Moreover, several strategies will be utilized to reduce the detrimental influence of the substrate in the sensor signal: Differential measurements, decrease of the IDE pitch or passivation of the substrate with a parylene-C dielectric barrier will be investigated through the study of both the dynamic and static response of the sensor to R.H.

Analytical models for IDE sensors The analytical calculation of the capacitance of IDE structures is not straight forward. Some groups have tried to calculate it using different approaches. One approach opts for figuring out the electric field in the devices from an electrostatic point of view, solving the Laplace's equation for the concrete geometry [44]. The other approach makes use of the conformal mapping method in which a space transformation is used to convert coplanar geometries in parallel plates geometries, which are much easier to dealt with. Such approach, combined with the partial capacitance concept has been developed in few previous works to analytically calculate the capacitance of IDE capacitors in a multi-layered structure [45–47], as well as the role of the thickness of a sensitive layer deposited on the IDE structure for gas sensing applications [48] respectively). In all the previous examples, only flat and regular IDE structures were addressed. Since I deal in this thesis with devices fabricated on flexible substrates, it is of high interest for the field to expand such models for

IDE structures subjected to bending conditions.

Parallel plates gas sensors on foil

IDE-based sensors present the advantage of requiring only one metalization layer and of maximizing the exposure of the sensing layer to its environment, since it is the last material to be deposited on top of the IDE structure. However, their patterning by printing technology is challenging if one targets small pitch. Also, since the electric field lines existing between IDE are also present in the substrate, the substrate becomes an undesirable sensing part of the device. This aspect will be described in detail in Section 2.2 of Chapter 2. On the other hand, the other most common capacitive structure, the parallel plates structure, can be also used for gas sensing. For this configuration, the sensing layer is placed between the two parallel electrodes so that the electric field is totally confined in it. Hence, sensors using this configuration are potentially more sensitive and whatever change undergoes in the substrate does not affect their behaviour. Furthermore, this geometry can provide higher values of nominal capacitance than IDE, since a very small distance between parallel plates is achievable by controlling the thickness of the dielectric layer in between. However, these devices require two metalization layers and complex patterning of the top electrode to permit the analyte reach the sensing layer underneath. Only two parallel plates-based gas sensors have been reported on polymeric foil so far, and to the best of our knowledge, none of them were fabricated by means of printing technologies, probably due to the challenges associated with the chemical compatibility between the solvent of the ink used to pattern the top electrode and the sensing layer underneath. In 2009, Zampetti and his group developed a vertical parallel plates-based sensor on very thin (8 µm) polyimide substrate. The sensor was fabricated by spin coating, evaporation of chromium and wet-etching as depicted in Figure 1.7, and its operation was based on the variation of the [bis(benzo cyclobutene)] sensing layer permittivity in presence of humidity [49]. The fabricated sensor showed a sensitivity to relative humidity of 0.38% / R.H. % and a linearity of $R^2 = 0.996$ in the range of 10 – 90 R.H.%. The response time, estimated from 10 to 90% of the response curve was 216 s.

The bendability of the device was assessed demonstrating negligible electrical variations for bending radius down to 1.4 mm. The same group extended the work and reported it two years after in [50]. They developed a whole system composed of three PP sensors using different polymeric sensing layers: poly(tetrafluoroethene) (PTFE), poly(methyl 2-methylpropenoate) (PMMA) and benzocyclobutene (BCB). A ring oscillator circuit, implemented with polysilicon thin film transistors (PS-nTFT), was used to convert the capacitance variations into frequency shifts. The electronic tests show oscillating frequencies of about 211 ± 2 kHz and negligible frequency shifts under different bending radius of curvature. The system response to some concentrations of alcohols (Methanol, ethanol, 1-butanol, and 1-propanol) was reported and data analysis proved that the system was able to discriminate methanol from ethanol.

Getting over the materials limitations imposed by the chemical compatibility between the different printed stack layers, I developed for first time and describe in this thesis report a

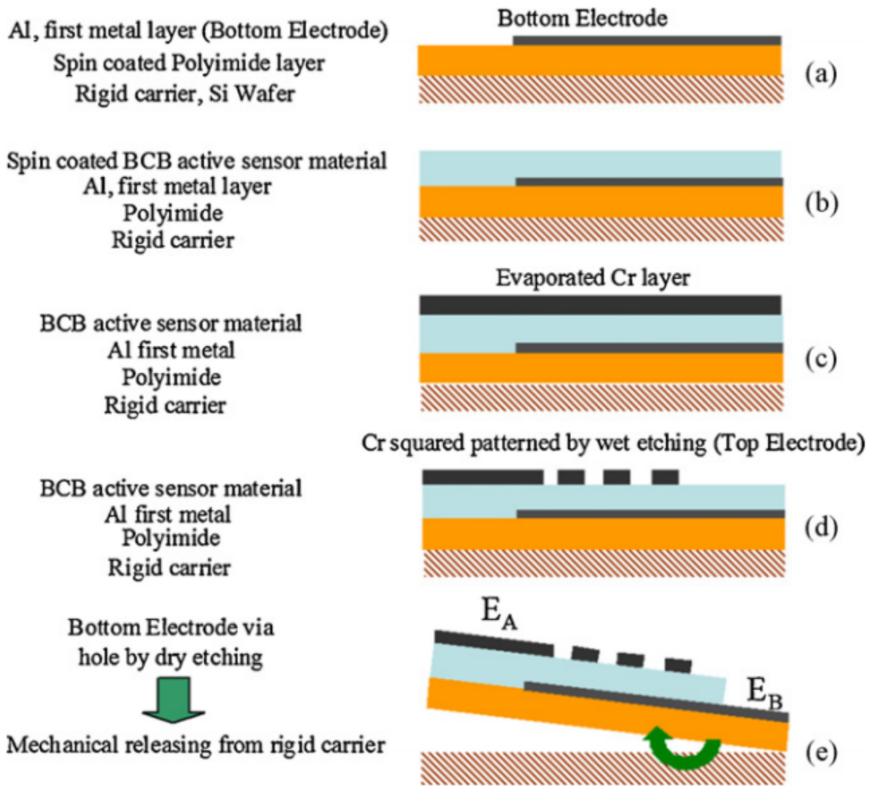

Figure 1.7: (a) Thermal evaporation of a 200 nm-thick aluminum layer on PI. (b) Spin coating of a 800 nm-thick layer of BCB over the sample. (c) Second evaporation of 200 nm-hick chromium layer on the structure, and (d) squares patterned on it by photolithography and wet etching in order to allow humidity penetration into the BCB sensing layer. (e) Finally, through BCB via holes were dry etched for contact bottom electrode and the structure was released from the rigid carrier [49].

fully-inkjet printed PP-based capacitive gas sensors on foil. The sensor had a smaller foot print than their IDE counterparts and presented improved performance for R.H. detection.

1.3.3 Microbeam gas sensors

Another approach to sense gas addressed in this thesis is based on mechanically movable microstructures. The first example of a microbeam-based gas sensors is found in 1994, when Thomas Thundat and co-workers at Oakridge National Laboratory in Tensesse USA started exploring the use of microcantilevers as potential physical and chemical sensors [51]. After that moments MEMS have been broadly investigated for chemical sensing. A thorough review about cantilever-like MEMS for chemical sensing applications was published by Professor Boisen from the Tecnical University of Denmark in 2011 [52]. This review included different operation principles (surface or bulk stress in static deflection mode, or change of mass in resonance mode) of both Si and polymeric beams. However, the great majority of MEMS sensors reported were based on devices fabricated using standard clean room materials (like

silicon) and techniques.

For the case of surface stress-based sensors, one of the two faces of the beam is functionalized with an specific sensing layer, which interact with the target analyte inducing a difference in surface stress of the two faces of the cantilever which deflects the cantilever. This operation mode is based on adsorption. The first example of such sensors is found in 1998, in a work by Christoph Gerber and co-workers from IBM in Zürich (Switzerland) [53].

The considerations of surface stress applies only when the sensing layer is much thinner than the beam underneath. Otherwise, the device operates under a different operation mode based on bulk stress. By opposition to the previous described working mode, the absorption (instead of adsorption) of the target analyte into the sensing layer plays now the main role. The devices basing their operation in bulk stress are modeled as bimaterial beams. Some examples using Si and other metals patterned using conventional clean-room techniques can be found in literature for chemical sensing and humidity sensing [54, 55]. Singamaneni and colleagues published a review dealing with bimaterial microcantilevers as a hybrid sensing platform [56].

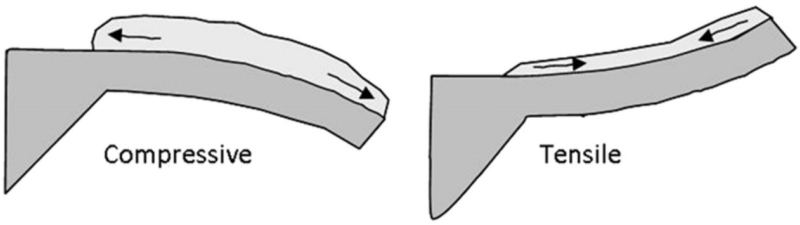

Figure 1.8: Sketch showing the deflection of a single clamped cantilever due to stress induced by a sensing layer coated on top. As the sensing film expands the cantilever bends down. The resulting stress in the sensing layer is compressive as its expansion is hindered and balanced by the bending of the cantilever. Similar and opposite behaviour occurs in contracting films [52].

Finally the third working principle utilized by microbeams is based on their resonant frequency, which drops when the mass of the beam increases, allowing very precise detection of minute amounts of analyte. MEMS resonant cantilevers have been integrated with other transducers and CMOS circuitry for organic and inorganic gas and vapour detection [27, 28]. Unlike in the most part of the previous examples where the sensor read-out was optical, the read-out circuitry used in the the last two references comes integrated in the device, improving its compactness and cost.

Microbeams systems using polymers either as beam or substrate material

Regardless the working principle, the most part of the examples of microbeams described in the literature involve inorganic bridges. Nevertheless, since 1990 there has been an increase in work reporting polymer-based cantilevers. The main driving force to introduce polymers in MEMS is that their Young's modulus is two orders of magnitude lower than silicon, leading to an increase in sensitivity for deflection-based applications (despite low Young's modulus is not

beneficial for resonant-based devices). Another important factor influencing the development of polymer-based MEMS is the possibility to reduce cost of raw material and fabrication [52]. Few of those polymer MEMS have been exploited as chemical sensors.

The first polymeric microbeam was a cantilever fabricated by Pechman *et al.* in 1994 with standard Novolak-based photoresist [57]. Some others authors have used SU-8 photo-resist to fabricate microbeams, taking advantage of its low stiffness (Young's modulus equal to 4 GPa) [58–60]. SU-8 beams have found more recently application as surface stress bio sensors and bio-chemical sensors [61, 62]. Other examples of beams made of different polymers (polyimide, PET, parylene) can be found in [63–70] Despite the previous examples, polymer cantilevers are still in an early phase and there are still many challenges to solve. They could be used in dynamic mode, but they should surmount issues related to material damping and lack of stability with temperature and humidity.

Owing to their flexibility, large-area compatibility and low price, using polymers also as the substrate material of microbeams systems could bring numberless advantages to the field of microbeams-based sensors and actuators. However, these advantages come accompanied of several challenges such as limitations in the process temperature or the lack of a reliable fixed reference position due to the polymer softness. Despite these challenges, some groups have ventured to develop inorganic microbeams using polymers as substrate material. For instance, in the work presented in [71] by Prof. Conde's team from INASC (Portugal) in 2008, microbridges (shown in Figure 1.9) were made of thin films of silicon on PET substrate; resonant frequencies up to 2 MHz with quality factors of 500 under vacuum conditions were reached through electrostatic actuation. An absolute pressure sensor was fabricated between two polyimide foils by means of magnetron sputtering, photolithography and lift-off [72]. The authors created a vacuum-sealed cavity for pressure reference and used piezoresistors for detection. Also, the utilization of polymers as substrate material to fabricate MEMS at large area was exploited in the case of the "smart MEMS sheet" for the electrostatic and thermal actuated displacement of small objects on a flexible foil presented by Ataka *et al.* in 2013 at the group of Prof. Fujita (University of Tokyo) [73, 74]. In this case, as well as in the previous ones, the authors used standard microfabrication technologies to fabricate the movable structures. The reason not to use printed materials is that they are in general less robust than materials deposited from gas phase. On the other hand, as it was mentioned in the Introduction of this chapter, printing techniques present good compatibility with polymers in terms of process temperature, permit a reduction of the fabrication cost and make systems more compatible with large-area and large-scale production . It turns out that not much work has been done in that respect and none was found for gas sensing applications. However, few inspiring works exist utilizing printing technology for physical sensors based on movable structures. They are described in the next section.

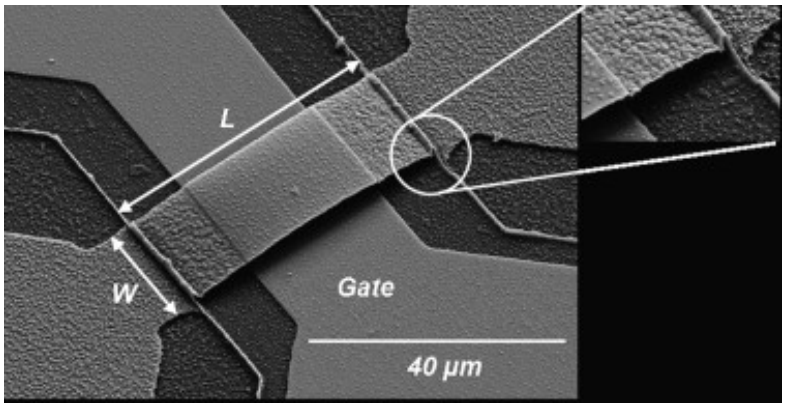

Figure 1.9: SEM-obtained micrograph of thin film silicon bridge on a PET substrate [71].

Microbeams polymeric systems including printing technologies

Among the different micro or milimeter beam-based systems including polymers and printing technologies we can find, for instance, a PP capacitive accelerometer using a suspended structure of inkjet-printed PEDOT:PSS and flexible substrates. The transducer strategy is based on the shift of capacitance of the structure when subjected to acceleration due to the displacement of the suspended electrode [75]. A similar geometry is found in [76], where the authors described another PP capacitive accelerometer fabricated on PET substrate by means of evaporation and etching, but using inkjet-printed polyestyrene-acrylate as etching mask, reducing considerably the number of fabrication steps. In 2008 Someya's group from the University of Tokyo developed two different types of cantilever to be used as MEMS switches using polyimide sheets and inkjet printing of Ag nanoparticles for electrical contact [77, 78]. The first one was a single actuated switch whereas the second one was improved to be double actuated in a complementary way, being able to reach a commutation frequency of 50 Hz at 60 V. They also reported a large-area flexible ultrasonic imaging system on polyimide foil formed by an array of sensing cells. Despite every sensing cell consisted of piezoelectric polymeric actuators, they were driven by an printed organic transistor active matrix [79], demonstrating the compatibility of printing technologies with large-area polymeric systems. Such compatibility was reassured and taken even further by adding roll-to-roll processing in a collaborative work between the National Tsing Hua University in Taiwan, VTT in Finland and Prof. Fujita's group at the University of Tokyo [80]. The authors of the article proposed the use of polyethylene naphthalate (PEN) as substrate and microbridge actuator for a novel MEMS controlled paper-like transmissive flexible display device realized by roll-to-roll printing process for the first time. The roll-to-roll process included flexography printing, gravure printing, lift-off, and lamination techniques, and was proved for high-volume, low-cost, and large-area solutions. Another example of low-cost material beams combined with printing technologies comes from Prof. Whitesides's team in Harvard university, who developed in 2011 a force sensor based on a laser-cut paper cantilever of few millimeters size, which included on its base a screen printed carbon piezoresistor as a detection element for the deflection of the beam [81].

Finally, some authors have built 3D mechanical structures without using polymers as structural support, but by directly printing ceramics or metals to form the structure itself. This is the case of the millimeter-sized screen-printed cantilevers made of ceramics for force sensors [82] or those millimeter-sized cantilevers made by screen printing gold, silver, PZT (lead zirconate titanate) and other dielectric materials, developed at Southampton University for energy harvesting [83].

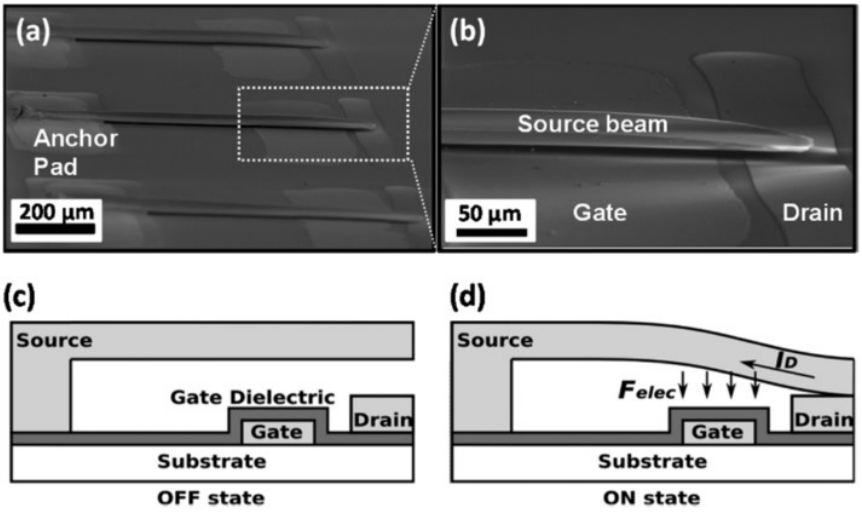

Figure 1.10: SEM-obtained micrographs of (a) several inkjet-printed MEMS cantilever switches and (b) close view of one device. Schematic representation of the operation of the switch in (c) OFF-state and (d) ON-state [84].

Printed movable microstructures are also possible, as it was demonstrated in 2002 by an MIT group that showed 2D and 3D mechanical structures, namely linear and rotary electrostatic-drive motors, and in-plane and vertical electrothermal actuators using inkjet printing of up to 400 layers of insulators, silver and gold with 100 µm feature size and high conductivity, 10:1 vertical aspect ratios and etch-released [85]. A different group also at MIT developed inkjet-printed cantilevers with feature as small as 20 µm for characterization of the printed material itself [86]. On top of that, in 2013 Prof. Subramanian's group in UC Berkeley developed inkjet-printed MEMS cantilevers switches (see Figure 1.10) by means of a relatively complex process involving spin coating and the definition of via-holes also by inkjet-printing [84]. Finally less-standard printing methods such as microcontact have been also used to form free-standing 3D structures [87].

Although the ground floor for printed MEMS is established, there are not examples using fully printed microstructures at a large area. Furthermore, the applications of the devices are limited to physical sensors or switches. No examples have been found for chemical sensing. In this thesis I propose a fully inkjet-printed MEMS bridges system on polymeric foil for gas and vapour detection. The device has been tested for humidity, responding to the bulk stress principle described above, where the polymeric substrate acts a swelling sensing layer upon absorption of ambient moisture.

1.3.4 Thermometers on foil

Whether the detection of gas is based on physical process, such as physisorption into a sensing layer, or on chemical reactions, temperature will always be a big player in the process. This means that the temperature needs to be controlled at every moment during the gas sensing process. For that reason, in this thesis work I will present also the development of thermoresistors along with the printed humidity sensors on foil. In order to enable the integration of both elements together on the same chip, the thermoresistors must be fabricated with the same printing technology that the humidity sensors, i.e. inkjet printing and electrodeposition on plastic foil.

There are different ways to sense temperature using microsystems, but the most popular and straight forward is to use conductive materials which conductivity (or resistivity) varies with temperature [88]. The devices exploiting such property are thus called resistive thermodetectors (RTD). Traditionally, ceramic substrates and platinum resistors have been used to fabricate RTD. Nowadays we can find some RTD using also foil substrate. Among the published work of interest, we can find "cost-effective" thermoresistors made of Pt on polyimide with a temperature coefficient of resistance (TCR) of 0.00291 $°C^{-1}$ [89]; thermoresistors with TCR = 0.00188 $°C^{-1}$ integrated on foil with gas sensors [31]; or miniaturized Ti/Pt/Ti resistors on polyimide working from 0 to 400 °Cwith TCR = 0.00145 $°C^{-1}$ for medical applications [90]. Lichtenwalner *et al.* presented also an array of flexible thermoresistors on polyimide oriented along different directions as depicted in Figure 1.11 and fabricated from Pt and NiCr to be able to measure bi-axial strain fields and temperature simultaneously by comparing the different TCR and gauge factor of both materials as well as the different orientation of the devices [91]. The Pt version presented a TCR of around 0.0020 $°C^{-1}$ whereas the one of the NiCr version was between 0.00230 and 0.00385 $°C^{-1}$. Strain gauge factors of between 1.4 and 1.7 were found in the worse cases.

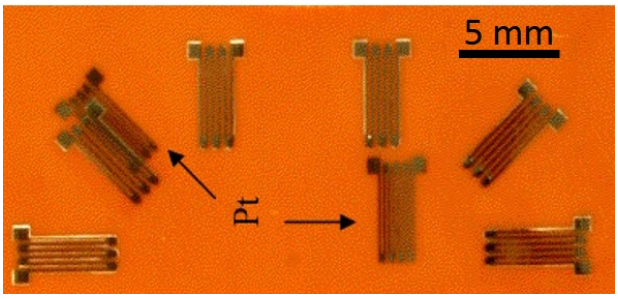

Figure 1.11: Picture of an array thermoresistors and strain sensors fabricated on foil with NiCr and Pt [91].

Even though Pt is commonly used for thermometers due to its high linearity over a wide range of temperatures, temperature sensors made of gold have also been integrated together with humidity sensors on the same polyimide foil in [32]. The sensors, isolated by parylene, presented a TCR = 0.00481 $°C^{-1}$.

It can be observed that the most part of the referenced works rely on expensive polyimide polymer due to its high thermal resistance and on evaporated metals. Felba *et al.* reported in [92] on silver nanoparticles lines inkjet-printed on glass slides and characterized their thermal sintering process. Although the authors did not target at developing an RTD (but at characterizing the printed materials instead), a curve "resistance vs temperature" was presented displaying lines sintered at 240°C with a TCR of 0.00208 $°C^{-1}$. However, inkjet printing can be also compatible with low heat resistance flexible substrate such as PET or paper that could be employed for specific applications that do not require exposure to high temperatures, such as environmental monitoring. The use of printing technologies would also decrease the cost of the fabrication process. The previous reasons encouraged our group to develop an inkjet printed silver RTD on paper in 2011 [37]. The RTD presented however a relatively low TCR of 0.0011 $°C^{-1}$ and suffered high dependence on variations in the relative humidity probably due to the lack of stability of the printed material (sintered at only at 150°C) and the high moisture absorption capabilities of paper.

In spite of the previous issues, there are still plenty of room for improvement and no many works dealing with printing RTD on foil are available nowadays. The feasibility and potential of the field can be however reflected in the success story of the Southafrican-based company *PST Sensors* that has developed its own process to print Silicon for thermoresistive detection.

1.3.5 Processes

Several devices have been described in the sections above where additive methods, mostly printing, were used for patterning. The devices also required the use of a specific sensing layer that is sometimes deposited from liquid phase. This technology is not always at a mature stage and some groups are working to understand and improve it. In this section I review the relevant works related to the technologies that I used in this thesis, namely inkjet printing, electrodeposition and different process existing for deposition of sensing layers for gas sensors.

Inkjet printing (printable materials, parameters and sintering techniques)

Inkjet printing is a very versatile method that offers to the the user many different parameters to tune. The morphology, geometry, mechanical and electrical properties of inkjet properties depend on theses parameters which are at the same time dependent on the working surface and the ink jetted onto it. Various articles have been published trying to understand and describe the control and tuning of different parameters for inkjet printing. Among the different parameters involved in the process, drop-to-drop spacing, temperature of the substrate, surface treatment, firing frequency, etc. are the most important. Another issue that inkjet printing has to deal with is the redistribution of solid materials towards the outer edge occurring on a landed drop as a result of unbalanced evaporation rates of the solvent in the drop. This phenomenon, known as the "coffee ring" effect, was first reported in 1997 and subsequently studied by Deegan $et al.$ [93–95]. The coffee ring effect is responsible for the

difficulty to fabricate printed lines with homogeneous thickness.

The correlation between the drop-to-drop space and the profile and width of inkjet-printed metallic lines was studied in [96]. Also, the influence of the substrate surface energy on printed lines profile and resistivity was described in [97]. Prof. Subramanian's group in UC Berkeley clarified the relation between the aforementioned parameters along with the substrate temperature, firing frequency, etc. in properties of the inkjet-printed line such as the edge quality (see Figure 1.3) or the coffee ring formation [9].

Another aspect that plays a big role in the quality of printed metallic patterns, specially in terms of electrical resistance and mechanical properties is the curing and sintering process. Different ways to cure and sinter metallic ink after deposition have been described in [98]. Thermal treatment is the most common and straight forward way of sintering conductive inks. Nevertheless, when dealing with organic substrates, high temperatures above the glass transition temperature of the substrate (Tg) are not allowed. In that case, near infra-red, microwave radiation, DC and AC current [99], laser beam or other photonic methods become more suitable methods for curing and sintering conductive inks.

In summary, inkjet printing of functional materials is subjected to a many different parameters not fully understood. Although very promising, this method remains challenging and difficult to control especially when it comes to reduce the printing resolution, increase line thickness homogeneity and decrease the resistivity of metallic lines without recurring to high temperature thermal steps. Inkjet is also challenging to create multi-stack layers of different materials due to the low thickness and high roughness of inkjet-printed films, and the need to find chemically orthogonal solvents to not dissolve the bottommost layers.

Electroplating and adhesion treatments

One of the characteristic properties of inkjet printed patterns is their low thickness. In order to increase this thickness, maintaining the additive character of the method, electroplating can be performed using the printed line as seed layer for the growth of the plated material. Electroplating can be used also to create bimorphs or as passivation layer for reactive metals. Kao *et al.* treated the topic for electroless of Cu on inkjet-printed lines in 2010. However, in this work, the substrate was alumina instead of polymer [100]. In the same year, Cauchois and colleagues demonstrated electroless deposition of a 1.7 μm thick nickel layer on top of 600 nm thick printed and sintered silver nanoparticles-based lines for wire bonding using polyimide as substrate [101]. Electroplating can be performed directly on the substrate without need of a metallic sensing layer. Micron- and submicron-scale patterns of copper on Si and polymer surfaces was carried out by selective electroless deposition on the areas defined by colloids that served as catalysts. Such areas were patterned and deposited by microcontact printing [102]. In [103] the authors used microcontact printing of self-assembled silane layers on PEN foil to define the areas where nickel could not directly grow by electroless plating. The nickel lines defined the gate electrode of a thin film transistor on foil. Other similar works describing the

combination of microcontact printing and electroless deposition for fine patterning of metals can be found in [104–107].

Adhesion is a common problem in polymer electronics. Already in 1992, Inagaki *et al.* addressed this issue for polyimide foils and tried to solve it by means of oxygen plasma treatment [108]. Oxygen plasma treatment activates the surface energy improving the adhesion metal-polymer. More recently, many other groups have come back to the issue of using plasma for surface and adhesion improvement of polymers in general [109], and for sputtered [110] or inkjet-printed [111] copper layers. On the other hand, surface treatments can also target to enhance printing quality by lowing the surface energy of the substrate. Smaller ink drops are possible on substrates with lower surface energy.

Sensing layers coating

In order to have sensors for specific gaseous analytes, it is necessary to coat the transducers with an specific sensing layer. These sensing layers are often organic polymers very sensitive to solvent, light and high temperature, reason why they tend to be deposited towards the end of the fabrication process flow. This fact presents certain limitations in the devices geometry. IDE devices are advantageous in that sense since both electrodes are simultaneously patterned, leaving freedom for the deposition of the sensing layer afterwards. On the other extreme, parallel plates structures are not suitable for many sensing layers since the top electrode must be deposited onto the sensing layer, which is "sandwiched" between the two electrodes, and patterned to let the analyte penetrate into the sensing layer. The issue becomes even more challenging for printed devices where the electrodes are deposited from a solvent-based ink. Common methods for coating sensing inorganic layers are normal evaporation, sputtering or screen printing. In the case of organic sensing layers, they are mostly deposited by spin coating or spray coating [112], self-assembly [113], drop coating [13], or inkjet coating [26, 107]. Although spin coating permit a very good reproducibility and fine control of the sensing layer thickness, it is constrained to wafer level and it is not additive, so it lies out of our interest [114].

Spray coating is fairly reproducible, allows good control of the sensing layer thickness and can be considered as additive. Nonetheless it requires a shadow mask for the sensing layer to reach only the areas of interest and it is not appropriate to cover small features. Self-assembly sensing layers applies mostly to organic molecules that self-organize in a very ordered and packed way on top of the device substrate or electrodes. The chemistry of the process limits its application to very specific scenarios, like well-known thiol-gold bonding. Moreover, the thickness of the sensing layer is very small and fixed by the morphology of the used self-assembled molecules, so it cannot be modified. Event though drop coating is a very simple method, it lacks resolution and yields relatively uneven and thick sensing layers. Finally, owing to its non-contact character, inkjet printing makes a good candidate to functionalize fragile structures such as microbridges. On top of that, its digital nature allows simultaneous deposition and maskless patterning of different sensing materials [115], as well as customized combinations of them. Nonetheless, it must be taken into account that as in the case of drop

coating, in inkjet printing the sensing layer is deposited from a solution. Thus it is subjected to the solute reorganization and solvent rheology that causes the formation of coffee ring stain [93–95]. The coffee ring stain yields sensing layers with non-homogeneous thickness and uneven surface. Some effort is being carried out to surmount this problem by mixing solvents with different boiling points and superimposing complementary layouts [116].

1.4 Thesis motivation and structure

Thesis motivation and achievements

Having as future vision the development of ubiquitous gas sensors, during my doctoral work I took advantage of the properties of common polymeric foils and printed electronics for the fabrication of low-cost, environmentally-friendly and flexible gas microsensors requiring low power for wireless applications. The core of the thesis focuses on describing the development of transducers for gas (and vapour) sensing, which includes also the fabrication of temperature sensors and heating microelements. Different geometries of capacitive transducers have been investigated and characterized after functionalization with custom-made test sensing layers, mostly for relative humidity. These geometries include planar interdigitated electrodes (IDE), parallel plates (PP) and movable microbridges.

One of the main flagship characteristics of the *FlexSmell* project is to develop low-cost and environmental-friendly smart systems. Therefore, very low-power consumption devices were conceived with a special concern in minimizing the use of polluting and expensive materials, as well as resources during the fabrication process. Low-power consumption is at the same time compatible with wireless applications, allowing the system to communicate remotely. Capacitive microsensors seem suitable for such systems because they require very low-power consumption. On the other hand resistive microsensors require higher power than their capacitive counterparts, but they offer a larger range of sensing materials, facilitating the enhancement of the system selectivity. Either way, the most part of gas microsensors available nowadays are made using expensive rigid materials and high energy consuming clean-room processes. To make the fabrication of existing gas microsensors comply with the needs of a new kind of low-cost and environmental-friendly systems, it has to be as efficient as possible: the fabrication must involve relatively low temperatures and the use additive techniques (such as inkjet printing and electroplating) to optimize material usage. The former techniques are also suitable for large-scale production methods which potentially leads to a reduction of the fabrication cost. Low temperatures processing is compatible at the same time with the use of a new range of organic materials, otherwise impossible to use at traditional microelectronics process temperatures. Hence, polymers are the main kind of materials to be used in this work for both substrate and sensing layers. Compared to standard inorganic substrates used in microfabrication such as silicon and glass, polymers are very cheap, easy to handle and compatible to large-scale production via roll-to-roll method. Their flexibility is a convenient characteristic for smart packaging, among many other applications. The thesis work presented

here intends to fill the existing technological gap in the field of gas microsensors by developing low-cost performing resistive and capacitive sensors on flexible plastic foil by means of inkjet printing technology.

Figure 1.12 summarizes the required points to be fulfilled in the project and the existing relationship between them.

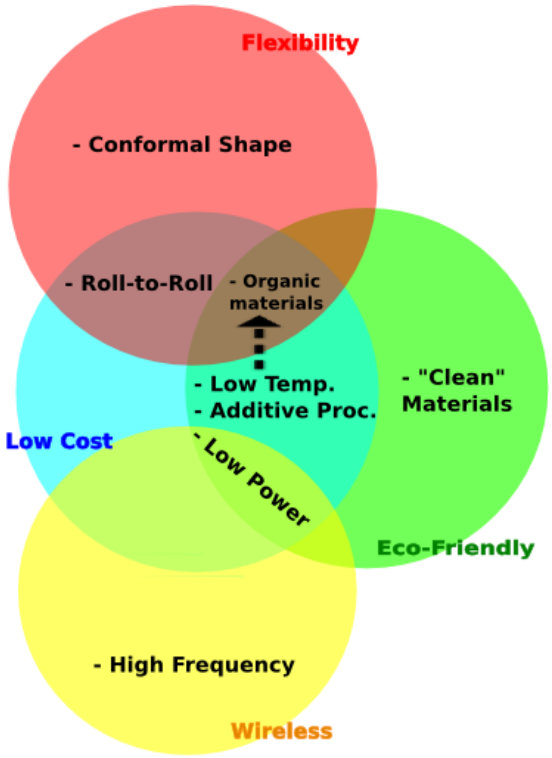

Figure 1.12: General specifications considered in the project. Different characteristics linked to each specification and relations between them.

Although previous reviewed work showed gas microsensors fabricated on both rigid substrate and flexible polymeric foils [1, 49, 50], the fabrication involved mostly expensive clean-room microfabrication techniques at wafer level. In this thesis, I demonstrated devices with comparable performances fabricated exclusively by printing and other additive methods such as electrodeposition, compatible with large-area fabrication. The characterization of the devices have been duly accompanied of theoretical models predicting and explaining in many cases the observed behaviours.

The power consumption of capacitive sensors is relatively low compared to resistive sensors, reason why the core of my thesis was focused on capacitive devices. The first studied devices are IDE capacitive humidity sensors. Firstly, the relationship between the geometry of IDE devices and their sensing behaviour has been theoretically studied generalizing existing models [45], and compared with that of parallel-plates devices. In both cases, the working principle

consists of the diffusion of analyte molecules into a polymeric sensing layer inside a capacitor, modifying its electrical permittivity and thickness, and as a consequence the capacitance value. Then, different strategies to improve the performances of printed IDE transducers have been explored. These strategies include passivation of the electrodes with either a dielectric or a metallic chemical barrier, or miniaturization of the patterned electrodes. Electrodes with a pitch smaller than 60 μm have been achieved, improving the state of the art of printed IDE [35, 36, 38, 39]. Concerning the flexibility of the devices, the influence of bending in the capacitance of IDE devices has been analytically determined and experimentally confirmed for first time, allowing for a better understanding of the physics involved in the process.

Although technologically more challenging to fabricate than their IDE counterparts, parallel plate-based structures are more compact and present certain advantages for gas sensing, such as improved sensitivity and no parasitic influence of the polymeric substrate in the sensing behaviour. The fabrication and characterization of the first fully printed parallel plates capacitive gas sensor on plastic foil is described in this thesis.

In order to add extra functionality to the targeted multisensing platform, we have developed MEMS microbridges arranged in large arrays. Every microbridge behaves as a small parallel plates capacitor where the top electrode is suspended. Thus, every microbridge can be independently actuated, and if connecting many bridges in parallel, the device displays a capacitance value of ~ 1.4 pF. This structure is very versatile and could find multiple applications. We have demonstrated its operation as capacitive humidity sensors subjected to a novel swelling-based working principle inherently different from the one of the standard parallel plates and IDE-based chemocapacitors: upon the absorption of humidity the devices buckle, modifying their capacitance. The fact of exploiting different working principle results beneficial to ameliorate the future selectivity of a sensing platform.

Since the sorption process undergoing on humidity sensing is temperature dependent, a printed thermoresistor has been integrated on the same chip with the IDE humidity sensors for thermal calibration. The sensitivity of the thermometer (or temperature coefficient of resistance, TCR) has been increased in several folds by electroplating it with nickel. Furthermore, the detection of some analytes is not optimum at room temperature with certain sensing layers. Therefore I targeted the development of a heating microelement able to reach ~ 100°C and readily integrable with such high temperature-operating sensing layers. Microhotplates made from silicon in a clean-room are widely known. The transfer of this devices to a low-cost technology, i.e. printed on foil, presents many challenges from the point of view of fabrication and power consumption. Using a different geometry, design and functionalization than in [25], we managed to develop a microhotplate which largely outperformed the previously reported in terms of power consumption. The devices consisted of a meander-shaped heating micro-element, a laminated thin dielectric and IDE on top. Gold electrodeposition has been demonstrated on the IDE to broaden the range of materials choice, facilitating the chemical compatibility during subsequent fabrication steps. Thanks to a novel sensing layer of conductive polyaniline polymer developed by our *FlexSmell* partners in the group of Prof.

Persaud at the University of Manchester (UK), the microhotplate showed reliable resistive detection of ammonia vapour with reduced drift and improved recovery at 95°C (compared to room temperature), what consumed 35 mW. Resistive gas sensors are based on the change of resistivity of some materials due to certain chemical or physical process undergoing inside them in the presence of an analyte gas. They have available a large spectrum of sensing materials such as metal oxides (MOX) or conductive polymers like is the case in this work. The microhotplate could be also compatible with capacitive detection at a fixed high and controlled temperature, as an alternative to the standard but inconvenient thermal calibration necessary in gas sensors.

Finally, complying with the *FlexSmell* project expectations, all the devices (excepting the PP capacitor-MEMS microbridges array which technology is not mature enough yet) have been brought together on the same substrate to create a multisensing platform that was included in an low-cost RFID smart label. The RFID label, developed by our partners at Holst Centre (Holland) was able to store data from the sensors and transmit them wirelessly. The multisensing platform counted with capacitive and resistive channels properly functionalized for simultaneous selective sensing of temperature, relative humidity and ammonia vapour concentration. Detection of alcohol vapour is also planned but has not been totally accomplished yet. More concretely, sensing layers consisting of conductive polymers of polyaninline (PANI) and polypyrrole (PPy) have been developed by our partners at the University of Manchester (UK) for resistive detection of ammonia vapour (already demonstrated) and alcohol vapour (planned), respectively; and sensing layers of poly (ether urethane) (PEUT) and cellulose acetate butyrate (CAB) have been developed by SAMLAB and our partners at the University of Tübingen (Germany) for capacitive detection of relative humidity (demonstrated). Other analytes of interest in food spoilage are detailed in Section 5.4.3 of Chapter 5. The detection of such analytes were the field of research of other partners of the *FlexSmell* project. Overall, this work supposes a step forward in the concept of the "internet of things" where ubiquitous smart systems able to sense their environment will be able to interact between them and with the people around.

Thesis structure

The Chapter 1 of this thesis aims at offering to the reader a general background of the fundamental and technological aspects of this work, as well as the context that motivated it. After presenting the previous works relevant to the development of this thesis, I pointed out the current needs in the field and its challenges. Finally, I informed the reader about the specific motivations and content of this work, highlighting the novelty and advantages that it brought to the field of printed low-cost sensing systems on foil.

The second Chapter deals with the theoretical aspects pertaining interdigitated (IDE) capacitors and their use as gas sensors in general by adding a polymeric sensing layer to the structure. This includes a review of the geometrical parameters that lead to the optimal design of devices, bearing in mind the different fabrication restrictions imposed by the used technol-

ogy, i.e. inkjet-printing on polymeric substrate. It is also described the influence of circular bending on the capacitance value of IDE structures.

In Chapter 3, I describe the design, fabrication (transducer and sensing layer) and characterization of IDE-based capacitive vapour sensors. The sensors consists of silver electrodes inkjet-printed on PET substrate. Electrodeposition of Ni was utilized for silver passivation. Reducing the electrodes pitch was also possible by the introduction of a parylene-C dielectric layer between both fingers combs. Finally, it is explained how the devices, inkjet coated with a customized humidity sensing layer of cellulose acetate butyrate (CAB), were characterized in controlled environments. The performances of the devices are discussed at the end.

Two different configurations of capacitive humidity sensors based on parallel plates (PP) structures and fabricated using printing silver on PET foil are detailed in Chapter 4. In the first configuration, the sensing layer is placed between two standard non-movable electrodes, whereas in the second configuration, the top electrode is an array of suspended MEMS bridges and the sensing layer is the polymeric substrate itself. Some fundamental theory that applies to these structures is revised in this chapter, along with the sensing particularities, advantages and fabrication challenges that every typology of sensor comes along with.

Chapter 5 foresees the fabrication of a multisensing platform by describing different resistive sensors and their integration together. It is a well-known fact that humidity sensing is influenced by temperature variations. This is the reason why Chapter 5 describes first of all the design and fabrication of different resistive thermodetectors (RTD) to be integrated side by side with the humidity sensors described in Chapters 3. Some theoretical aspects of electrical resistance and its dependence with temperature are addressed too. Since high temperature is sometimes beneficial in gas sensing for chemical desorption or increase of sensitivity, an inkjet-printed microhotplate was developed on PEN foil for those sensing layers exhibiting improved performances at temperatures above room temperature. The microhotplate has been tested for resistive detection of ammonia. Finally, I present some multisensing platforms where IDE capacitive and resistive sensors, electroplated RTD and resistive sensors based on stacks of microheater-IDE-conductive polymer are integrated on the same substrate. The sensors were customized for detection of different gases by the $FlexSmell$ partners at the University of Tübingen (Germany) and University of Manchester (UK). The platform was assembled into a printed radio frequency identification (RFID) tag developed by the *FlexSmell* partner Holst Centre (The Netherlands) in collaboration with EPFL-SAMLAB.

Chapter 6 includes a general discussion of the thesis results and compare the performances of the different devices presented in this thesis.

Chapter 7 draws general conclusions and highlights future perspectives of this field of research.

2 Fundamental Concepts of Capacitive Humidity Sensors Based on Coplanar Interdigitated Electrodes (IDE)

2.1 Introduction

Targeting the development of gas sensing systems on flexible substrates, some humidity capacitive sensors on plastic foil were already found in literature and reviewed in the state of the art in Subsection 1.3.2. An important part of these sensors utilizes the ability of certain polymers to first adsorb and then absorb humidity and other gases, modifying the properties of their dielectric layers. To maximize the interaction of the sensing layer and its environment, the most commonly utilized capacitive structure consists of planar combed or interdigitated electrodes (IDE) [31–34] rather than parallel plate structures [49, 50]. The goal of this thesis is to develop printed gas sensors on foil for which I also utilized capacitive devices based on these two geometries. In the next two chapters, I focus on devices composed of IDE and stacked multilayer of polymers (substrate, optional passivation and sensing layer). To offer a complete review of such sensors, I report in this chapter on the fundamental theoretical concepts that determine their behaviour, keeping in mind the limitations of the technology intended for their fabrication, i.e., inkjet printing of silver on flexible polymeric foils. The fabrication and characterization of the devices will be described in the next Chapter 3. A large part of the content of this chapter has been published in peer reviewed journals [117–119].

In general, capacitive gas sensors are based on the ability of certain structures to shift their capacitance in presence of a target gas. Different to parallel plate capacitors (shown in Figure 2.1 (a) and described in detail in Chapter 4) where the electric field lines are confined exclusively in the dielectric material placed between the two electrodes, IDE capacitors generate an electric field in both dielectric layers underneath and on top of the electrodes plane. The layer underneath the electrodes plane is referred as the substrate of the device, since it provides mechanical support; whereas the dielectric/s deposited on top of the electrodes (usually a polymer capable to absorb/adsorb gas) will be called the sensing layer (see Figure 2.1 (b)). In this chapter, I describe a thorough theoretical analysis of the operation principle of IDE-based

gas sensors in terms of their transducing and sensing mechanisms. The theoretical consideration applying to parallel plate capacitors will be addressed in Chapter 4. To understand and optimize the performance of the IDE-based gas sensors fabricated in Chapters 3 and 5 through an optimal design, I first describe the sensing principle, based on the physisorption and diffusion of the analyte into the sensing layer and the substrate (see Figure 2.2), taking previous works [29, 30, 48, 120, 121] as starting point. Chemical interaction between analyte and the sensing layer could also occur in this kind of sensors, but they are not considered in this work. The estimation of the influence of the diffusion process in the capacitance value and sensor time response are addressed as well. Then, I generalize the models presented by R. Igreja and C. J. Dias in [45, 46, 48] and Gevorgian *et al.* in [47] to calculate analytically the capacitance of coplanar IDE structures, and applied them to our concrete materials and geometrical cases. Igreja and Dias made use of the conformal mapping and partial capacitance methods to calculate the capacitance of IDE capacitors with flat thin and regular electrodes, and integrated between a flat substrate and a flat sensing layer. Gevorgian *et al.* introduced a correction for thick electrodes. Apart from applying their model directly to these simplified geometries, I expanded it to another more complex structure consisting of flat quasi-planar IDE, where every comb has a different width and there is an extra dielectric layer between electrodes. The latter structure corresponds to a device in which a new fabrication strategy has been tested to decrease the pitch of its electrodes (distance between the centre of two adjacent fingers) in a reliable and reproducible way (see Figure 2.9), while accomplishing at the same time the passivation of the the substrate against moisture absorption. Gas absorption in the substrate is an undesired effect that I tried to prevent either by performing differential measurements, where a coated device is compared to an uncoated one used as reference, or by passivating the substrate against penetration of the analyte. The fabrication of this device, described in detail in Chapter 3, consists of the deposition of a thin dielectric layer of parylene-C onto the first printed electrode comb prior to the printing of the second comb on top, in such a way that both polarities are electrically insulated and cannot be in contact if printing errors occur. Since each comb was printed on a different material, the fist one on the substrate and the second on the insulating dielectric, the electrodes present two different widths. On top of that, not only flat structures have been analyzed in this chapter. For the case of the regular IDE structure, the model has been completed by including for the first time the analytic evaluation of the capacitance for circularly bent electrodes at different radii of curvature.

2.2 Sensing principle

The sensing mechanism concerning the typology of IDE sensors addressed in this chapter works as follows: the target gas (water vapour in this case) is adsorbed and then absorbed ideally only in the polymeric sensing layer as depicted in Figure 2.2. As a result, the sensing layer swells (increasing thickness) and its dielectric constant ϵ_s changes, modifying the value of the capacitance C. Apart from the obvious difference in mechanical flexibility between

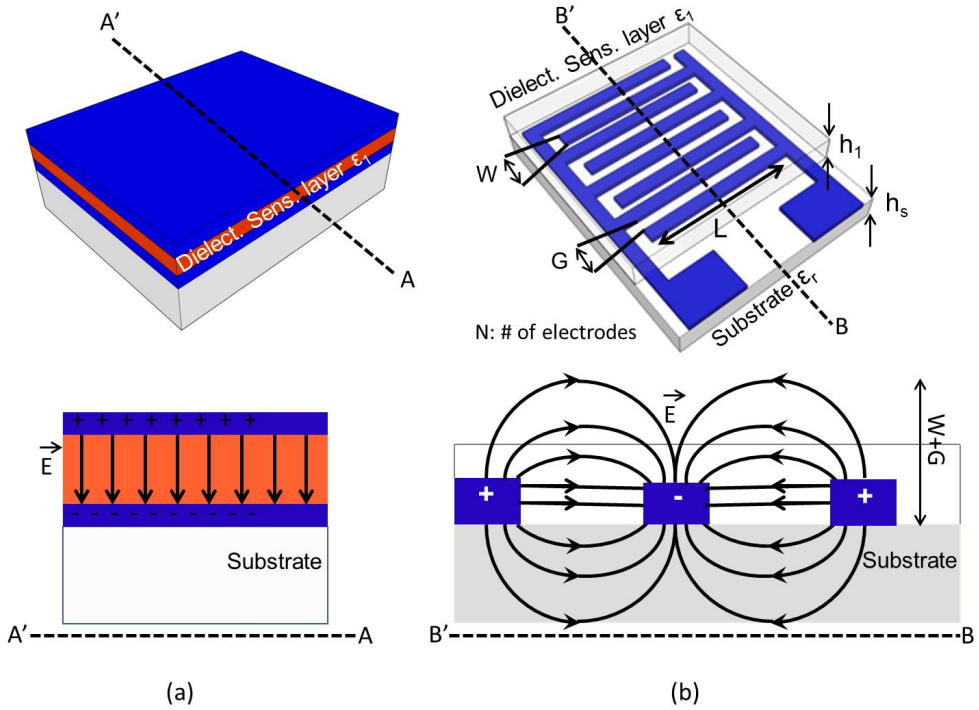

Figure 2.1: (a)Sketch of a typical parallel plate structure(top), along with its cross-sectional view depicting the electric field distribution in the device (bottom). (b) Same sketch for interdigitated electrode (IDE) and its main geometrical parameters.

ceramic and polymer substrates, we encounter at this point the other main difference between rigid and foil devices. Whereas rigid substrates such as silicon or glass do not absorb gases, polymeric substrates do. This behaviour can increase the sensitivity of the device, although this is not always positive since substrates are intended to have merely structural functions rather that being optimized for sensing. This aspect needs to be taken into account when designing polymeric gas sensors.

In any case, when a sensing film (or substrate) of original thickness h_1 swells upon absorption, its new effective thickness, h_{eff}, is [29]:

$$h_{eff} = h_1(1 + Q\phi) \tag{2.1}$$

On the other hand, according to [29], the effective dielectric constant of the sensing film (or substrate) upon absorption of analyte can be expressed as:

$$\epsilon_{eff} = \epsilon_{r1} + \phi[(\epsilon_a - 1) - Q(\epsilon_{r1} - 1)] \tag{2.2}$$

where ϵ_a is the dielectric constant of the analyte in liquid state (76.6 for water), ϵ_{r1} is

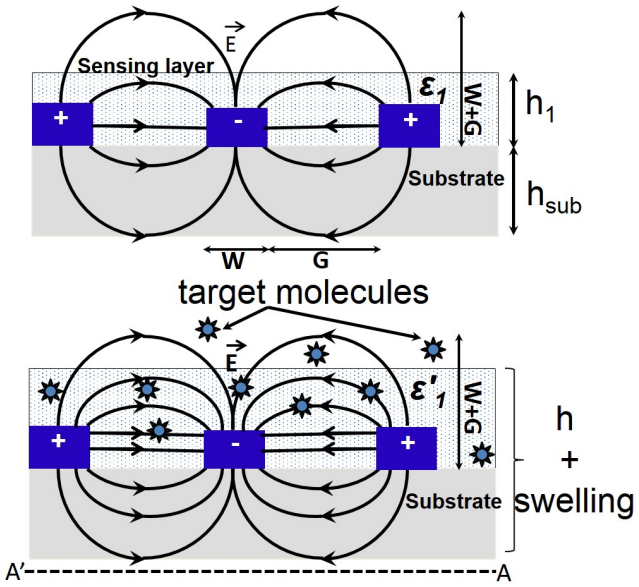

Figure 2.2: Representation of the working principle for the humidity sensor (example for the cross section of three electrodes from Figure 2.1) where the vapour molecules are absorbed into the polymeric sensing layer, which swells and modifies its dielectric properties, shifting the capacitance of the device.

the original dielectric constant of the film, ϕ is the volume fraction of the analyte in the sensing layer and Q is an experimental coefficient representing non-ideal swelling. Q can be considered close to 1 (ideal swelling) for rubbery elastic polymers. Other similar expressions for the effective permittivity of the composite polymer-analyte can be found in [48, 122].

2.2.1 Sensitivity

Therefore, the total variation of the sensor capacitance in presence of gas consists of the addition of two terms, one due to changes in the dielectric permittivity and another due to swelling, represented in the first and second term of the right part of 2.3 respectively:

$$\delta C = \frac{\partial C}{\partial h}\delta h + \frac{\partial C}{\partial \epsilon_r}\delta \epsilon_r \tag{2.3}$$

It is worth noting that during this thesis we test our capacitive gas sensors for relative humidity ($\epsilon_a = 76.6$) by using a customized sensing layer of cellulose acetate butyrate (CAB) ($\epsilon_r \sim 3.5$). Due to the large difference between ϵ_a and ϵ_r and the small size of water molecules, the contribution coming from permittivity changes in the sensing layer surpasses and masks the contribution coming from swelling.

Calculating $\delta h = h_{eff} - h_1$ from 2.1 and $\delta\epsilon_r = \epsilon_{eff} - \epsilon_{r1}$ from 2.2 as:

$$\delta h = h_{eff} - h_1 = h_1 Q \phi \tag{2.4}$$

and

$$\delta\epsilon_r = \epsilon_{eff} - \epsilon_{r1} = \phi[(\epsilon_a - 1) - Q(\epsilon_{r1} - 1)] \tag{2.5}$$

it is possible to obtain the physical sensitivity $\delta C/\phi$ against h for different values of ϵ_a and ϵ_r.

This procedure is easy to apply to parallel plate capacitors as it will be seen in Section 4.2.1 (Chapter 4). However, it is very hard to use with IDE capacitors due to the lack of a close short expression for their capacitance (as it will be shown in the sections below). Kummer *et al.* bypassed that issue in an example of application of Equation 2.3 to a concrete IDE structure presented in [29] . According to the authors, extensive finite element method simulations were performed for their IDE geometry with different sensing layers. The capacitance of the IDE was simulated with polymeric sensing layers of different thicknesses and dielectric constants. The simulated capacitance data set was approximated with a mathematical fit to a function having the sensing layer thickness and dielectric constant as sole variables. This function could be plugged more easily in Equation 2.3. Such procedure could be applied to our concrete IDE geometries, but this point lies out of the work of this thesis.

Partition coefficient and volume fraction ϕ The partition coefficient, K, is a chemical equilibrium constant used to state the thermodynamic equilibrium condition of the the diffusion process of certain analyte in a polymeric sensing layer. K is a measure of the solubility of a gas in the solid sensing layer, and it is related to the volatility (or vapour pressure) of this gas. It is defined as the ratio of the analyte concentration within the polymer $c_{polymer}$ to the concentration of the same analyte on the gas phase c_{gas}:

$$K = \frac{c_{polymer}}{c_{gas}} \tag{2.6}$$

It depends on the standard Gibbs free energy solvation ΔG_s^0, the absolute temperature (in K), T, and the universal constant of ideal gases, R, through the Arrhenius form [15]:

$$K = constant \cdot e^{-\frac{\Delta G_s^0}{2.303 * RT}} \tag{2.7}$$

Very sensitive polymers to certain analyte are the associated to a high K value. The partition

coefficient is related to the parameter ϕ used in Equations 2.1 and 2.2 through the partial pressure of the analyte, P_a, its molar mass, M, its density in liquid phase, ρ, R and T as [29]:

$$\phi = \frac{P_a K M}{RT\rho} \tag{2.8}$$

For the case of relative humidity (R.H.), the partial pressure P_a has been calculated for every $R.H.$ point using the definition of relative humidity (based on partial pressures) $R.H. = \frac{P_a}{P_s}100$:

$$P_a = P_s * R.H./100 \tag{2.9}$$

where P_s is the saturated partial pressure calculated with the correlation presented in [123]:

$$Ps = (1.0007 + 3.46 * 10^{-6} P/100) * 6.1121 * e^{\frac{17.502T}{240.97+T}} * 100 \tag{2.10}$$

with P being the atmospheric pressure in millibars and T the ambient temperature in °C.

Note that in the Equation 2.8 above, M/ρ is associated to the volume, V, of the analyte molecule (1 mol) (do not mistake ρ, the density in liquid phase with the density in gas phase). Hence, according to the equation of ideal gas law, $PV_T = nRT$ (with n being the number of moles and V_T the total volume occupied by the gas):

$$\phi = \frac{n}{V_T} VK = n_v VK \tag{2.11}$$

where n_v is the concentration of analyte (in mol/volume). From the equation above, it can be drawn that the volume fraction is proportional to the size of the analyte molecule, its concentration and its solubility in the sensing layer.

2.2.2 Time response

The sensor absorption process is diffusion based, and assumed to follow Fickian behaviour. Then, the amount (number of moles) of analyte in vapour phase diffused in the sensing layer as a function of time, $n(t)$, can be approached by an exponential behaviour [48]:

$$n(t) \approx n_m \Big[1 - \frac{8}{\pi^2} exp\Big(\frac{-t}{\tau}\Big)\Big] \tag{2.12}$$

where n_m is the total amount of moles in the sensing layer in equilibrium and τ is the absorption equilibrium time or simply the time constant.

As it can be observed in Figure 2.1 (b) and it will be described in Section 2.3.1, IDE generate an electric field that reaches as far as the fingers pitch distance is ($W + G$ in the figure). Therefore in IDE gas sensors, the sensing layer is sensitive only below that distance, which I will call the saturation thickness $h_1 \sim W + G$. For this reason, the amount of analyte absorbed in a sensing layer thicker than the saturation thickness has a proportional influence in the capacitance only when the analyte reaches the sensitive area within the saturation thickness. In equilibrium, such proportionality is given by the factor n_m. Also for this reason, once a sensing layer is thicker than the saturation thickness, to increase further its thickness does not improve the sensor sensitivity (but it slows down its response since the analyte needs more time to reach the sensitive area). Similarly, the swelling of thick sensing layers does not influence the capacitance. On the other hand, thin sensing layers (below the saturation thickness) depends on the amount of analyte at every time $n(t)$ although this dependency is not proportional since the effective swelling of the sensing layer should be taken into account in the capacitive response. In any case, if we define $t = 0$ as the instant when a new R.H. step occurs after steady state is achieved, the shift of capacitance for a sensing layers thinner than the saturation thickness is a function of $n(t)$, as stated by the next equation [48]:

$$\Delta C(t) = f\left(n(t) \simeq n_m\left[1 - \frac{8}{\pi^2} exp\left(\frac{-t}{\tau}\right)\right]\right) \tag{2.13}$$

This function can be approached as linear for many cases where the swelling does not have a big influence as it is the case of humidity sensing or sensing layers which thickness is very close to the saturation thickness. The latter case is interesting because the closer the thickness of the sensing layer is to the saturation value, the larger the amount of molecules that it can absorb and effectively sense under a fixed concentration of ambiance gas, yielding to wider shifts of C and hence to a higher sensitivity.

As it can be appreciated in Equation 2.13, the sensor capacitive signal would stabilize only when the number of moles of analyte in the sensing layer $n(t)$ reaches the limit value n_m. This absorption process has a time constant τ which corresponds to the 63% of the maximum value of capacitance (reached at equilibrium) for every increasing step of R.H. τ depends on the square of the sensing layer thickness and on its diffusion coefficient D as [48] as:

$$\tau = \frac{h_1^2}{0.25\pi^2 D} \tag{2.14}$$

The diffusion coefficient is given by the Arrhenius equation [30]:

$$D = D_0 e^{\frac{-E_a}{RT}} \tag{2.15}$$

where D_0 is the maximum diffusion coefficient, E_a is the activation energy for diffusion, R

is the ideal gas constant, and T is the absolute temperature.

Therefore, a thicker layer implies slower sensor stabilization and a compromise between sensor response time and sensitivity needs to be found. Note that the response time related with the adsorption process can be considered negligible compared with the time scale of absorption for practical thickness (of some microns) of the sensing layer. On the other hand, the substrate of the reported sensors in Chapter 3 is also polymeric and interacts with humidity in a similar way as the sensing layer does. Although this could be translated in an enhance of sensitivity, the characteristics of the substrate are not usually optimized for humidity sensing, so it introduces undesired parasitic effects mostly related with slow diffusion processes such as long time response, hysteresis and non-linearity [31]. Finally, the time constant usually also depends on the R.H. value through the diffusion coefficient D (especially for high values of R.H.), but in our case, this dependence is neglected for practical reasons, since it is smaller than the range of error measured for τ.

2.2.3 Sensing advantages of compact IDE

Sensors based on IDE with reduced pitch present several advantages for capacitive sensing compared with less compact structures. For instance, the sensitivity of such printed sensors improves for two reasons: on one hand, the nominal capacitance increases for the same area, and accordingly the absolute sensitivity. On the other hand, being the electrodes more packed, there would be a maximization of the interaction between the electric field and a thin sensing layer, increasing also the relative sensitivity (since we saw that the electric field of such combed structures extends basically to a height equal to the electrodes pitch [29, 44, 45, 48]). To keep the the sensing layer thin is beneficial for a fast response of the sensor.

Within this thesis work I developed IDE with decreased pitch for gas sensing. The devices had a thin dielectric film placed between the two IDE combs so the electrodes could be very close without the risk of electrical contact and shortcircuit between the combs. In principle the dielectric intermediate layer, considered insensitive to the target gas would decrease the sensitivity of the device because it occupies space filled by the electric field lines. Nevertheless its influence results negligible in practice, due to its thinness, very small compared to the electrodes pitch in every reported case. The previous fact has been supported theoretically by removing the parylene layer from the model presented in 2.3.2 and observing a very small capacitance difference. In the same way, the overlapping portion of the electrodes do not contribute to the shift in capacitance in the presence of the target gas, since the electric field associated to it would be confined in the insensitive dielectric layer. Another sensing advantage of the presented devices with a dielectric inter-layer comes from the fact that both capacitor polarities are insulated. Therefore, the detrimental effect in the sensor signal provoked by condensation of water between electrodes at high relative humidity level, does not occur [17, 120, 124]. Last but not least, the dielectric partially passivates the substrate against moisture so it does not absorb an undesirable high amount of water [32] compared to

PET or other polymeric substrates. The reduced absorption of water into the substrate permit the operation of one single device instead of differential mode measurements [31, 117].

2.2.4 Discussion on the principle of gas sensing using polymeric sensing layers

The process that drive the detection of the sensors described in this chapter has been assumed to be physisorption. Although chemical interactions can occur for certain analyte and sensing materials, these are not considered in this work. It has been established that the higher is the concentration or the volume of the analyte molecules, the higher is the volume fraction of analyte absorbed into the polymeric sensing layer, named ϕ (see Equation 2.11). Both the swelling (Equation 2.4) and the change in the sensing layer permittivity (Equation 2.5) are proportional to the volume fraction, so large shifts of capacitance would be expected for high concentrations of large molecules. The other factor affecting the volume fraction is the partition coefficient K (see Equation 2.6) that determines whether or not a sensing layer shows affinity to certain analyte. The partition coefficient is one of the big players in the sensitivity and selectivity of gas sensors. Furthermore, the change in the sensing layer permittivity is also quasi-proportional to the difference in permittivity between analyte and sensing layer (Equation 2.5), as long as the sensing layer is made of a rubbery polymer (which is the case in this thesis). Due to the high relative permittivity of water compared to the sensing layer or other analyte, capacitive sensors tend to be very sensitive to humidity. The permittivity contribution made by humidity to the sensing signal is high to the point that the swelling contribution can be neglected for most part of moisture detectors. Regarding the response time of the sensor, thick sensing layer result in sensors slower than thin layer. The material of the sensing layer is also a factor influencing the sensor time response through the diffusion coefficient D presented in Equation 2.15.

2.3 Capacitance calculation of interdigitated electrode structures

Interdigitated electrode (IDE) is one of the most employed structures in traditional microelectronics and MEMS, and starts being very popular in flexible electronics as well. In addition to be used in the polymeric capacitive gas sensors cited in the section 2.1, IDE fabricated on flexible polymeric substrates have been used as resistive gas sensors [17, 19, 21–25] and strain sensors devices too [43, 125]. Nonetheless, the IDE structure offers benefits beyond its functionality as sensors; it is also commonly used for the source and drain electrodes in flexible transistors [126–128]. The understanding of the physics behind IDE is a key factor for the right design of devices that use this structure.

The devices studied along this chapter are coplanar interdigitated electrodes (IDE) capacitors as depicted in Figure 2.1. They will be employed as capacitive gas sensors as described in Chapter 3. Compared with parallel plate structures used in other publications [49, 50], IDE devices allow more direct interaction between the sensor and its environment. Moreover, IDE configuration imposes less restrictive requirements than parallel plate in terms of processing

for deposition of the sensing layer, since the sensing layer is the last deposited material and does need to be adjusted for the deposition of an electrode on top.

With the objective of calculating the capacitance value of our functional multilayered IDE structure, the theoretical study developed by Igreja and Dias [45, 46], based on conformal mapping transformations and the partial capacitance method, has been selected as a reference point. Conformal mapping consists on a series of space transformations to bring coplanar electrodes into the shape of parallel plate, possible to solve with a closed formula. Partial capacitance accounts for the partial contribution of every stacked layer to the total capacitance of the IDE structure by superposing all the layers as if each one occupied the whole space with a weighted permittivity at every thickness (see Figure 2.3b). This model is valid for devices where the electrodes length is much larger than the electrodes spacing distance and the electrodes thickness much smaller than their width. A correction for non-planar electrodes was added then as in [47] to account for thicker electrodes (electroplated in our case). Although this model provides a powerful analytical tool to predict the capacitance of the different IDE designs, the transformation are expressed as complex special functions nested into other special functions which are not always obvious to express analytically. The arguments used by these special functions are the dimensions of the device at different steps of the transformation (as it can be seen in Figure 2.4). Therefore, to express the capacitance as a closed equation directly related to the dimensions of the device would result in a very long expression, reason why in this section the capacitance value has been broken down into small equations (from Equation 2.16 to 2.22) instead for the sake of clarity.

2.3.1 Totally coplanar IDE devices

In this section, I mainly reproduce the analytical model to calculate the capacitance of flat, multilayer and planar IDE structures previously reported by Igreja and Dias [45] and I complement it with the model for finite thickness electrodes developed by Gevorgian [47]. The aforementioned theoretical models are based on conformal mapping and partial capacitance techniques, and showed that the total capacitance of a multilayered IDE structure is obtained by adding up the contribution that every pair of fingers makes within each layer. Figure 2.3, obtained from [46] and [45] represents that affirmation.

The simplest case of study corresponds to Figure 2.3a, where the electrodes are patterned on a substrate of finite thickness, surrounded by air and in the absence of a capping layer on top. Then, using the concept of the partial capacitance, the total capacitance of the IDE structure is given by [45]:

$$C = 2C_{air} + (\epsilon_{sub} - 1)C_{sub} \tag{2.16}$$

where $2C_{air}$ is the contribution from the infinitely thick layers of air above and below the IDE structure with a dielectric constant equal to 1, and C_{sub} is the contribution from

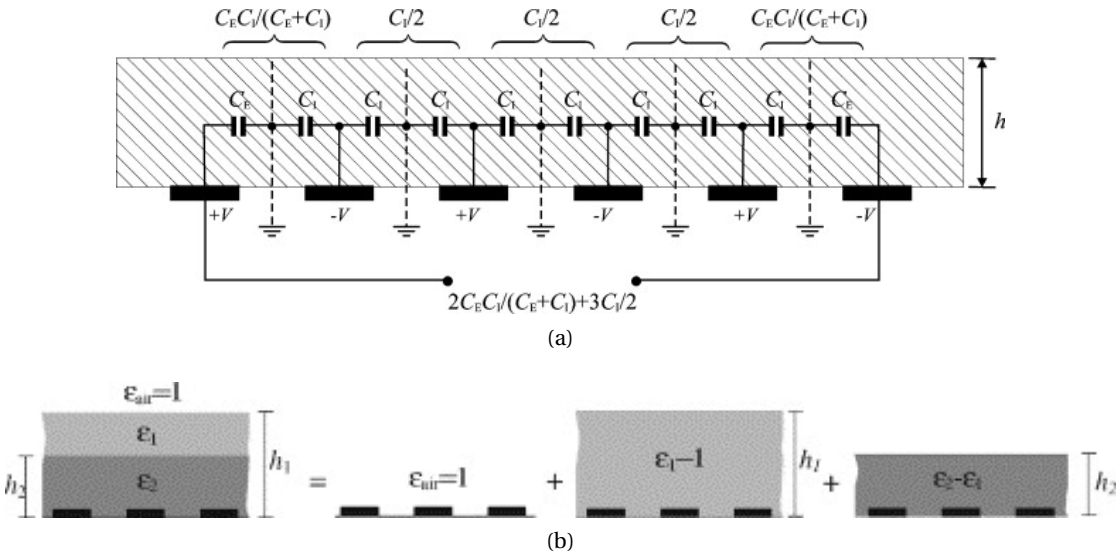

Figure 2.3: Representation of the analytical model developed by Igreja and Dias to calculate the capacitance of planar interdigitated electrode multilayer structures: (a) Equivalent circuit for evaluation of the capacitance of a single layer with six electrodes [46] and (b) Splitting of a two-layered half plane according to the partial capacitance technique [45].

the substrate with dielectric constant ϵ_{sub}. The capacitance provided by each layer, C_x (x representing air or sub), has been proven to depend on its dielectric constant, thickness, and the particular electrode geometry. It is also linearly dependent on the length of the electrodes, L, as well as the number of electrodes, N, and can be expressed as [45]:

$$C_x = (N-3)\frac{C_I}{2} + 2\frac{C_I C_E}{C_I + C_E} \qquad (N > 3) \tag{2.17}$$

In the equation above, C_I refers to the capacitance of the electrodes located in the middle of the IDE structure and C_E refers to the contribution from the two outermost electrodes, situated at the edges of the structure. The calculation of C_I and C_E has been executed using the conformal mapping technique described in detail in [45] and represented by the five consecutive space transformations shown in Figure 2.4.

$$C_I = \epsilon_0 \epsilon_r L \frac{K(k_I)}{K(k'_I)} \tag{2.18}$$

In the equation above, ϵ_0 and ϵ_r are the relative permittivity of the air and the dielectric layer (i.e., air or substrate) respectively; $K(k\_)$ is the complete elliptic integral of the first kind with modulus $k\_$; and $k'\_$ is the complementary modulus expressed as $k'\_ = \sqrt{1-k\_^2}$. On one hand, for a dielectric layer with a finite thickness, such as the substrate in this study [45]: $k_I = t_2\sqrt{(t_4^2-1)/(t_4^2-t_2^2)}$, where the variable $t_i = sn(z_i, k)$ is the Jacobi elliptic function of modulus k; the value of the modulus k is equal to $(v_2(0,q)/v_3(0,q))^2$, where v_2 and v_3 are the

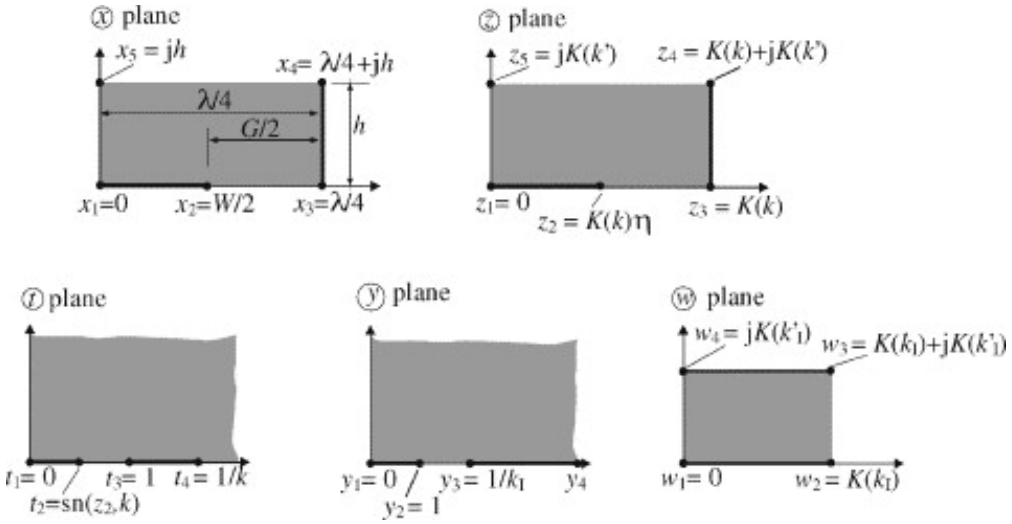

Figure 2.4: Conformal transformations for the calculation of C_I. The fixed equipotential lines and their transformations are marked as solid lines while the dielectric and its transformations are the shadowed regions [45].

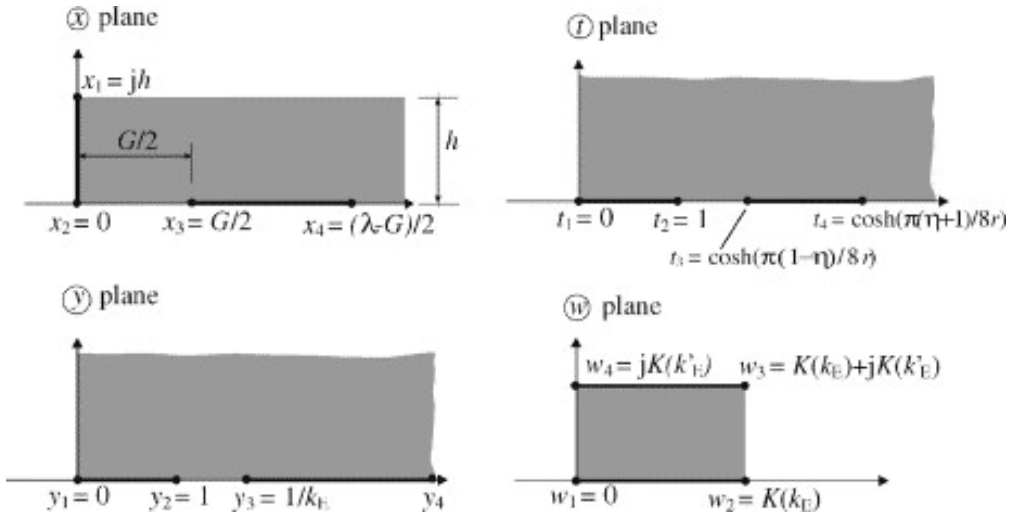

Figure 2.5: Conformal transformations for the calculation of C_E. The fixed equipotential lines and their transformations are marked as solid lines while the dielectric and its transformations are the shadowed regions [45].

Jacobi theta functions; $q = exp(-4\pi r)$; $r = h_s/\lambda$; the parameter $\lambda = 2(W+G)$; and h_s is the substrate thickness. On the other hand, for a dielectric layer with an infinite thickness, such as the air surrounding the substrate and the electrodes, $k_{I\infty} = sin(\pi W/\lambda)$.

The variable z_i is equal to [45]:

$$z_i = 4x_i K(k)/\lambda \tag{2.19}$$

, and the values of x_i can be obtained from the X-plane shown in Figure 2.4. They are: $x_2 = W/2$ and $x_4 = \lambda/4 + i\,h_s$, with i being the imaginary unit.

Similarly, the capacitance contribution of the electrodes in the external positions, C_E, is calculated as [45]

$$C_E = \epsilon_0 \epsilon_r L \frac{K(k_E)}{K'_E}, \tag{2.20}$$

where $k_E = 1/t_3\sqrt{(t_4^2 - t_3^2)/(t_4^2 - 1)}$ and [45]

$$t_i = cosh(x_i \pi/(2h_s)) \tag{2.21}$$

for dielectric layers of finite thickness; $k_E\infty = 2\sqrt{2W/\lambda}/(1 + 2W/\lambda)$ for infinitely thick dielectric layers. In this case, the values of x_i are $x_3 = G/2$ and $x_4 = W + G/2$ as it is shown in the X-plane of Figure 2.5.

Igreja and Dias analized in [45] the capacitance evolution of a typical device coated with a sensing layer of permittivity $\epsilon = 5$, versus the parameter $r = h_1/\lambda = h_1/[2(W + G)]$, which is in reality a normalized thickness of the sensing layer h_1 to the pitch of the electrodes. Their results were compared with those reported in previous works by Gevorgian *et al.* [47] and Wu *et al.* [129] as well as those obtained using finite element methods (FEM) (see Figure 2.6).

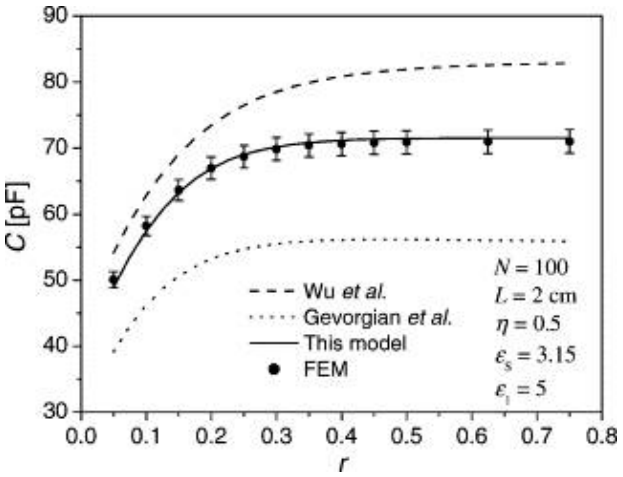

Figure 2.6: Capacitance as a function of r; comparisons between available models and FEM. Simulation parameters are given in the graph. In the legend, $\eta = W/(W + G)$ [45].

In conclusion, we can say that the value of capacitance C is linearly proportional to the number (N) and length (L) of electrodes as well as to the permittivity of the substrate (ϵ_s) and sensing layer (ϵ_1). Although not linearly, C also increases with the ratio W/g and the thickness of substrate (h_s or equivalently r_s) and sensing layer (h_1 or equivalently r_1). However, for the

case of $r_{s,1}$, C saturates above $r_{s,1} \sim 0.5$, i.e., when the thickness $h_{s,1}$ is around the same as the structure pitch $W+G$. Hence, any layer thicker than $W+G$ is considered as infinite in terms of the influence of the electric field. That assumption implies that any change in the dielectric layer taking place at a further distance than $\sim (W+G)$ above or below the electrodes plane will not practically affect the capacitance of the structure.

Finally, we generalized the described model from Igreja et Dias for IDE with certain thickness by following the work performed by Gevogian *et al.* in [47]. They account for the electrodes thickness by modifying the electrodes width before applying the conformal transformations to the IDE geometry. The effective width W_{h_e} of the electrodes with a thickness h_e becomes then:

$$W_{h_e} = W + \frac{h_e}{\pi}\left[1 + ln\left(\frac{8\pi W}{2h_e}\right)\right] \tag{2.22}$$

Validation of the model for coplanar IDE

Finite element method Although the model above is able to predict the capacitance of typical IDE structures, it does not account for the parasitic contribution of the electrodes tip or the sidewall capacitance of thick electrodes. This is the reason why it was established at the beginning of this section 2.3 that the validity of the model was subjected to electrodes much longer than the pitch distance and much thinner than wide. Although these conditions apply to the devices studied in this thesis, the validity of the model cannot be confirmed until the importance of these parasitic contributions to the total capacitance is evaluated for the selected geometries. Finite Element Methods (FEM) is a powerful tool to confirm the theoretical predictions of capacitance for every concrete case applied.

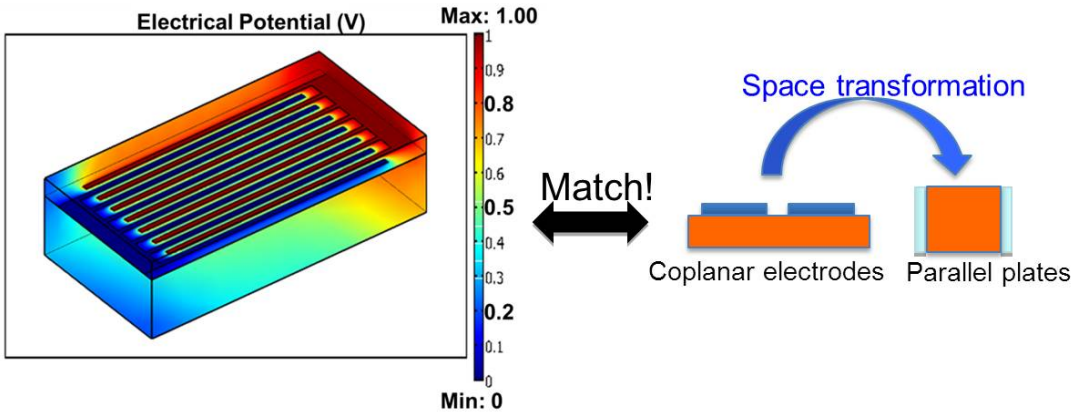

Figure 2.7: Distribution of potential field in a multilayered standard IDE structure, calculated with finite elements methods. The resulting capacitance value for the different studied geometries matched well the one obtained with the analytical method of conformal mapping described in this chapter, confirming that the electrodes tip and sidewall parasitic contribution to the total capacitance can be neglected for every practical example.

Figure 2.7 shows the FEM-simulated distribution of potential field in a multilayer IDE structure. The electrostatics mode of the software *COMSOL 3.5* was utilized to calculate the capacitance of different IDE structures, where the first comb is tied to the ground, the second is defined as a port and the surrounding boundaries are modeled as zero charge/symmetry. Using the port as input and selecting "Energy method" as the input property ensures that a unit voltage is forced on the boundaries of the second comb drive, and the capacitance value is integrated from electric energy density. The capacitance deduced by FEM matches the value calculated with the conformal mapping method for all the fabricated geometries, confirming the validity of the model and the negligible contribution of the parasitics terms mentioned above for the fabricated devices.

Experimental validation Figure 2.8 shows the validation of the model described in this section to calculate the capacitance of flat and totally coplanar IDE capacitors with different thickness, by comparing theoretical values with experimental data points. Details about the design and fabrication of the real devices are given in Chapter 3 Sections 3.2 and 3.3 respectively, however, we anticipate here that they were inkjet-printed and electroplated with different thickness (1, 5 and 10 µm) of nickel. The electrodeposition of the capacitor lines resulted in a capacitance value that evolved as presented in Figure 2.8, assuming isotropic growth of the nickel plated on the silver electrodes. Despite increasing electrodes width (W), and reducing inter-electrode gap (G), electrodeposition of few microns of nickel did not induce a change in the metalization ratio ($\eta = W/(W+G)$) large enough to allow a significant increase in capacitance. On the other hand, the new component of capacitance arising between the lateral walls of the thicker electrodes is not very important neither. The reason for these results is the thinness of the electroplated layer in comparison to the rest of the sizes of the fabricated device (few µm against 100 µm). As an example, according with the theoretical model, a device with bare silver electrodes of 95 µm width separated 105 µm from each other as the fabricated one showed in Chapter 3, would increase its capacitance value in only 13.9% after electrodepositing 10 µm thick metal layer on top. In the same way, to obtain a 52% increase in the capacitance value for the same electrodes, the necessary plated layer would become 40 µm thick. The last choice is not feasible in practice since thicker layers of nickel make the devices less cost efficient and require very good adhesion between lines and substrate to deal with higher induced stresses. Nevertheless, it would still be possible, for instance, to enhance the capacitance value in 43% by electroplating just a 20 µm thick metal layer in 95 µm width electrodes, if we could reduce the inter-electrode distance down to 40 µm. Such a gap reduction is technologically feasible and although challenging, it was achieved towards the end of my thesis work. Finally, the metalization ratio η plays an important role in the reproducibility of plated capacitors. Even though $W+G$ is fixed at 200 µm, the control of electrodes width and gap permitted by inkjet printing process is relatively poor, and introduced important geometrical variations from one batch to another. These η variations influenced in practice the capacitance as much as the extra thickness of the electrodes obtained through electrodeposition. Figure 2.8 also includes the experimental data points for capacitance

measured from the three different fabricated batches of devices, taking into account their measured geometry. The experimental values, with an error of 95% confidence, matched the theoretical prediction for each batch, with their mean differing in less than 10% from the theoretical estimation.

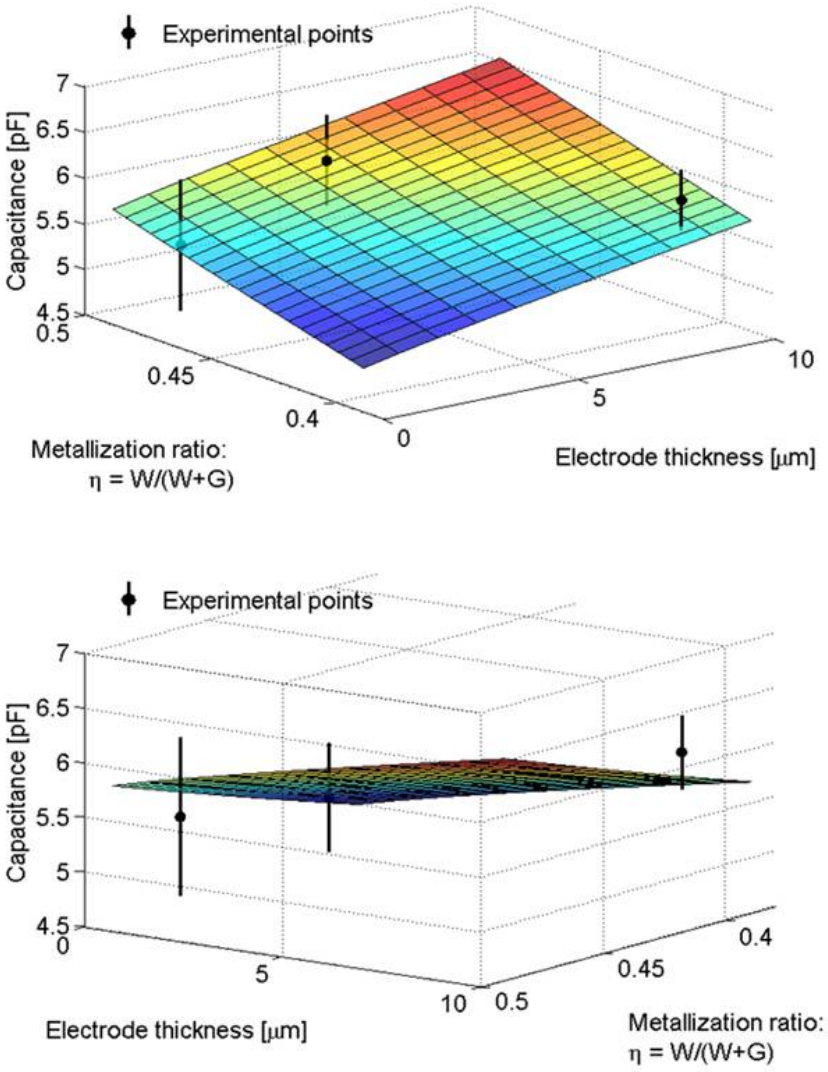

Figure 2.8: Two different views of the curve that theoretically predicts the capacitance evolution with electrodes thickness and metalization ratio $\eta = W/(W+G)$. The experimental points correspond with three different fabricated batches of IDE capacitors and differ in less than 10% from the theoretical prediction. The top graphic highlights the change in capacitance with the metalization ratio and the electrode thickness, while the graphic on the bottom has been tilted to reveal that all the experimental data coincides with the theoretical values within their range of error [117].

2.3.2 IDE devices with a dielectric layer between the combs

In the previous section a model for the capacitance calculation of standard coplanar IDE structures was presented. According to this model, and considering the best resolution safely achieved in this thesis for inkjet-printed lines, i.e. ~ 60 µm, the fabrication of IDE devices with a readable value of capacitance of few pF would require few mm^2, a surface area relatively high for a single microsensor. Therefore, a new strategy has been investigated to increase the capacitance per surface area of IDE by decreasing the electrodes pitch: Figure 2.9 sketches the geometry of an IDE gas sensor with a dielectric inter-finger layer serving to reduce electrodes pitch without risk of electrical contact. Both, first (bottom) and second (top) combs can be distinguished in the figure, as well as the thin separating dielectric layer. Being the thickness of the dielectric layer very thin compared to the width and gap of the electrodes, it is reasonable to assume that both combs are practical coplanar. As previously commented, the spreading of the ink on the substrate is related to the interfacial energies of the system, which depend on ink solvent, substrate material, roughness and applied surface treatments. As a result, the fingers width is different for every comb. More details about the design and fabrication of these devices is given in Sections 3.2 and 3.3 of Chapter 3.

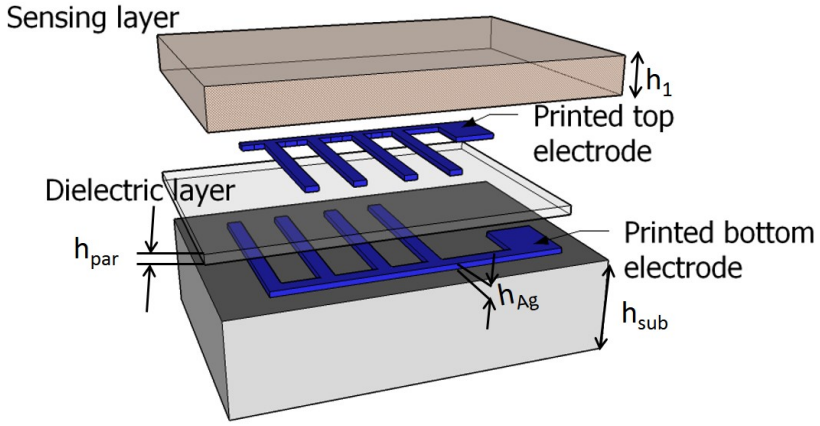

Figure 2.9: Exploded view of the IDE gas sensing device utilizing a dielectric interlayer between combs to decrease electrodes pitch while avoiding shortcuts [118].

It is possible to use the conformal mapping and partial capacitance technique described above (section 2.3.1), to analytically estimate the capacitance value of this new geometry. A suitable model would serve to evaluate the potential of the fabrication strategy and to optimize the design of the devices fabricated in Chapter 3. Thus, I adapted the described model to our concrete case of comb electrodes with two different widths and a thin dielectric layer in between the combs. In this way, I expanded the original model in [46] and [45], generalizing its capability for other geometries as described below. The equivalent electrical circuit of the device (by analogy with Figure 2.3a) is shown in Figure 2.10. For the sake of simplicity, the dielectric layer is modeled so that it shifts its position abruptly in the midpoint between electrodes, letting the electrodes lie on the same plane as if there were grooves etched in

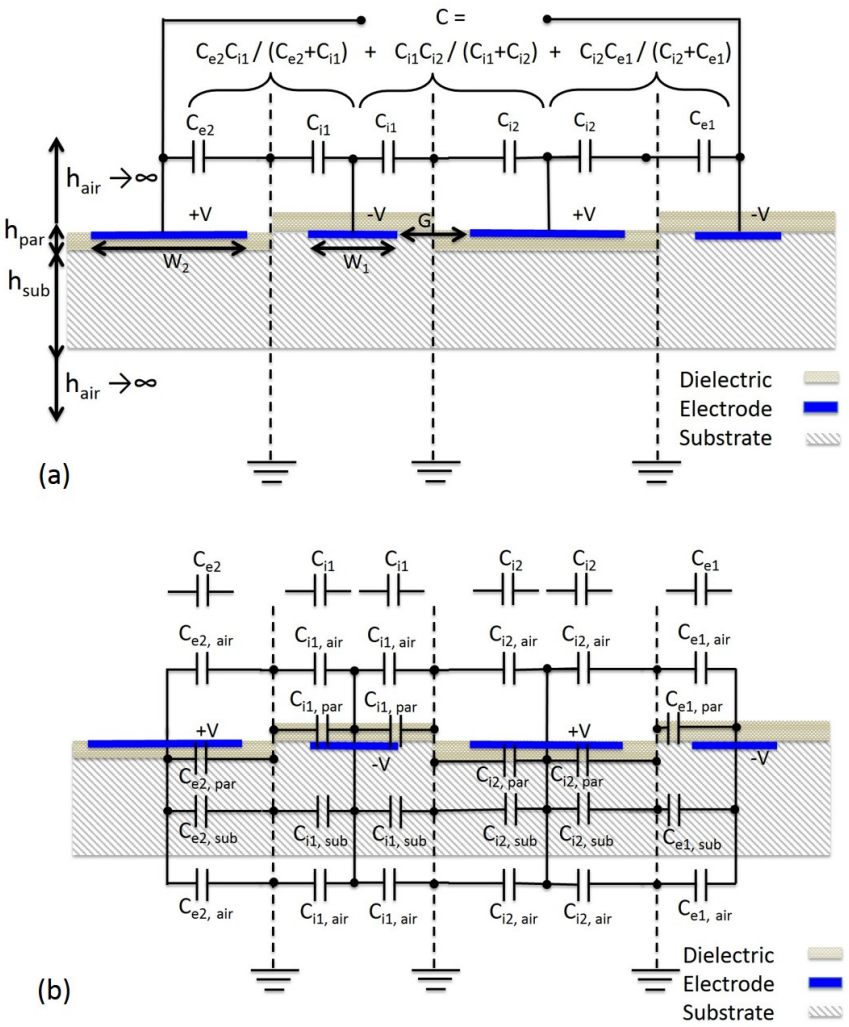

Figure 2.10: (a) Electrical equivalent of the device based on the partial capacitance technique. (b) Detail of the contribution to the total capacitance of every material layer. Adapted from [118]

the substrate. Such structure is just a simplification to facilitate the analytical modeling, since the original surface flatness was not really altered. Because the dielectric layer is very thin compared to the pitch of the fabricated electrodes, 2 µm against 40–120 µm, we do not expect it to modify significantly the symmetry of the system, so that virtual ground walls can be still placed in the mid-plane between electrodes. Therefore, the total capacitance of the device, C, is calculated as the parallel of a group of capacitances formed by (see Figure 2.10(a)): capacitance of the external first comb electrodes (of width W_1) C_{e1}; capacitance of the external second comb electrodes (width W_2) C_{e2}; half capacitance of the internal first comb electrodes C_{i1}; and half capacitance of the internal second comb electrodes C_{i2}.

In general for a device with an arbitrary even number N of electrodes, the total capacitance

would be expressed by analogy with Equation 2.17 as:

$$C = (N-3)\frac{C_{i1}C_{i2}}{C_{i1}+C_{i2}} + \frac{C_{e2}C_{i1}}{C_{e2}+C_{i1}} + \frac{C_{i2}C_{e1}}{C_{i2}+C_{e1}} \tag{2.23}$$

Since we are dealing with a multilayer structure where the outer layers possess a higher electrical permittivity than the inner layers, every capacitance component in Equation 2.23 can be expressed as the parallel of the contribution from every different layer - air, dielectric (parylene-C), substrate and air - using the partial capacitance technique as in Equation 2.16. In the hypothetical case where the permittivity increases while moving to the outer layers, the method described in [46] should be used instead. The contribution to the total capacitance of every layer depends of its thickness, h. Then

$$C_{i1} = 2C_{i1,air}(\infty) + (\epsilon_{par}-1)C_{i1,par}(h_{par}) + (\epsilon_{sub}-1)C_{i1,sub}(h_{sub}) \tag{2.24}$$

$$C_{e1} = 2C_{e1,air}(\infty) + (\epsilon_{par}-1)C_{e1,par}(h_{par}) + (\epsilon_{sub}-1)C_{e1,sub}(h_{sub}) \tag{2.25}$$

$$C_{i2} = 2C_{i2,air}(\infty) + (\epsilon_{sub}-1)C_{i2,sub}(h_{sub}) + (\epsilon_{par}-\epsilon_{sub})C_{i2,par}(h_{par}) \tag{2.26}$$

$$C_{e2} = 2Ce2,air(\infty) + (\epsilon_{sub}-1)C_{e2,sub}(h_{sub}) + (\epsilon_{par}-\epsilon_{sub})C_{e2,par}(h_{par}) \tag{2.27}$$

In the four equations above, the subscript i, e, 1, 2, air, par and sub, stand for internal electrode, external electrode, first electrodes comb, second electrodes comb, air layer, dielectric layer (parylene-C) and substrate layer respectively. The estimation of every contribution value is not straightforward and conformal mapping technique needs to be used as in section 2.3.1.

Note that while Equation 2.17 provides the capacitance contribution of a single dielectric layer C_x (C_I and C_E refers to the contribution of internal and external electrodes through a single layer of dielectric), Equation 2.23 provides the total value of capacitance ($C_{i1,i2}$ and $C_{e1,e2}$ refers to the contribution of internal and external electrodes through all the dielectric layers through Equations 2.24 to 2.27).

Validation of the model for IDE with dielectric interlayer

Figure 2.11 shows that the model for IDE with dielectric interlayer (2 µm-thick) and two different widths (first comb 40 µm-wide and second comb 60 µm-wide) fits very well the experiments except for the devices with the smallest pitch.

The reason is that there is overlapping between bottom and top electrodes for those last mentioned devices, making impossible the theoretical capacitance estimation with the described model. In any case, it is demonstrated that reducing the electrodes pitch leads to significant enhancements of capacitance per unit area. More details about the measured

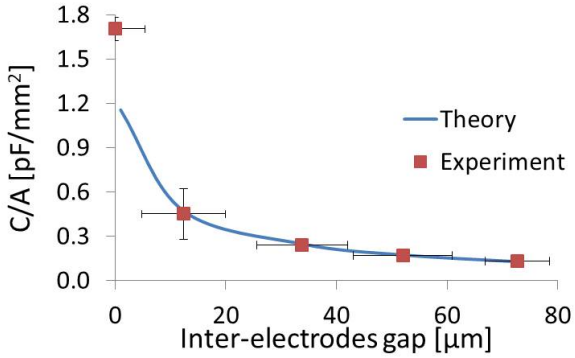

Figure 2.11: Comparison between theoretically estimated and measured capacitance per surface area versus inter-electrode space for IDE with dielectric interlayer [118].

geometry of the fabricated devices and the parameters introduced in the model are given in Section 3.5.3 of Chapter 3.

2.3.3 Bent IDE devices

The introduction of plastic substrates in the microfabrication of IDE has suggested a high potential for the development of functional flexible devices. However, in order to ensure proper functionality of flexible IDE structures subjected to bending strains, the variation of their electrical and mechanical properties upon bending must be fully understood and quantified. Although some previous works have studied mechanical aspects related to stress and failure modes of flexible electronics [130–132], no many studies exist on electrical characterization of bendable devices. Some groups have studied the resistivity of conductive lines patterned on polymeric substrates [133] or the influence of bending on the resistance of conductors such as ITO [134]. Regarding capacitors, in [49] the authors observed experimentally the effect of bending a parallel plate capacitor fabricated on flexible foil, but to the best of our knowledge there was no experimental data or theoretical model addressing capacitance changes of bendable IDE capacitors prior to this thesis work. In this section, I present a new theoretical model to predict the capacitance changes of uncoated IDE microstructures subjected to circular bending. The proposed model published in [119] accounts for the electric field redistribution taking place when changing the shape of the device from planar to cylindrical, as well as the modification of the device geometry due to the surface strain caused by bending. The results are supported by experiments on IDE microdevices fabricated with several dimensions on different substrates. The devices were bent along the axis perpendicular to the electrodes (see Figure 2.12) using an ad-hoc set-up. Because the model predicts the behaviour of bendable IDE devices, it provides information to adapt the design of IDE structures to a targeted application, by either maximizing (of interest for strain sensors) or minimizing (desirable for gas sensors, transistors, or flexible passive devices) their capacitance variation during bending.

When IDE structures are subjected to circular bending, either outward or inward (Fig-

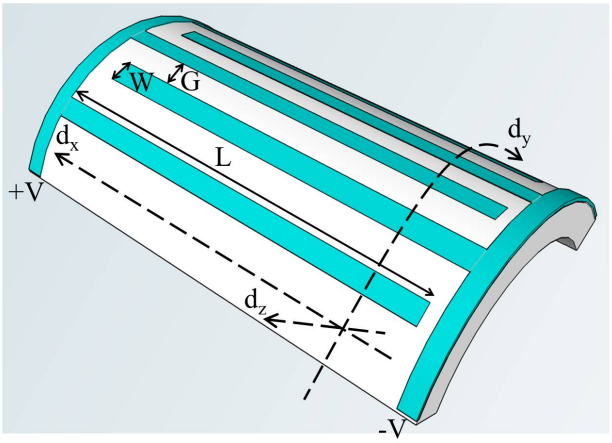

Figure 2.12: Sketch depicting outward bending of an IDE structure along the axis perpendicular to the electrodes (d_y in the picture). Inward bending refers to the case where the electrodes are placed on the underside of the substrate [119].

ure 2.12), two effects must be taken into account in the calculation of their capacitance: (i)redistribution of the electric field due to the change of the electrode shape from coplanar to cylindrical (ii) and the modification of the ratio between the electrode width and the inter-electrode spacing due to mechanical strain on the surface of the substrate. The first part of this section deals with the change of capacitance due to the redistribution of the electric field. Then, in the second part of this section, the real dimensions of the bent electrodes are predicted using solid mechanics. Finally, the model will be validated with experiments.

Calculation of the capacitance for circular bent IDE capacitors

To figure out the changes in capacitance provoked by the redistribution of the electric field between electrodes while circular bending, the new following space transformation must be implemented prior to those in Equations 2.18 and 2.20, presented in the previous section (2.3.1):

$$x_i = (R + \Delta R_{NP}) log\left(\frac{l_i}{R + \Delta R_{NP}}\right) \tag{2.28}$$

The application of 2.28 is shown in Figure 2.13. The suggested transformation maps circles in the first L-space to straight lines in the second X-space while preserving the distance of the neutral plane [135]. By doing so, the distances in the X-plane corresponds to the dimensions of a flat device having the same capacitance value as the circularly bent devices in the L-plane. l_i are the coordinates of the space (L-plane) corresponding to the real bent dimensions and x_i represent their equivalents in the flat space (X-plane). R is the radius of curvature (defined on the plane of the electrodes) and ΔR_{NP} is the distance between the electrodes plane and

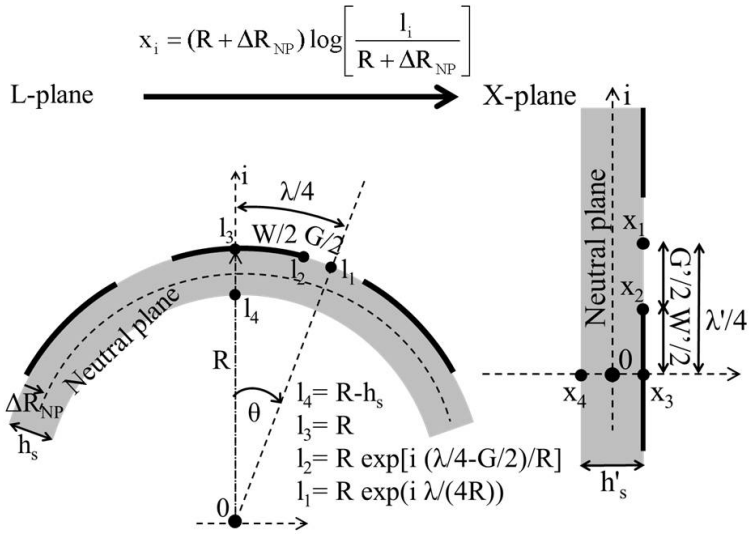

Figure 2.13: Proposed conformal mapping transformation to pass from circularly bent to flat geometry. The example shown is for outward bending of IDE [119].

the neutral plane, which is positive for inward bending and negative for outward bending. In general for bending of a beam-like bilayer, the neutral plane is located on a distance from the interface equal to [136]:

$$|\Delta R_{NP}| = 1/2 \left| \frac{E_s h_s^2 - E_f h_f^2}{E_s h_s + E_f h_f} \right| \tag{2.29}$$

with h_s, h_f, E_s and E_f standing for the thickness and the Young's modulus of substrate and coating film, respectively. In the current application, the coating film (the electrodes) is not continuous and is mostly considered infinitesimally thin, so that the neutral plane is practically located in the middle of the substrate.

Within this study, the parameters describing the device geometry under bending constraints are defined as: W for the electrodes width, G for the inter-electrodes gap, L for the electrodes length, and h for the dielectric substrate thickness. Likewise, the set of parameters representing the dimensions of the unstrained, flat IDE structure will be W_0, G_0, L_0, and h_0. Finally, W', G', $L'(= L)$, and h' are auxiliary parameters used to describe the geometry of the virtual flat structure resulting from the space transformation described by Equation 2.28. Note the difference with the notation in the section 2.3.1, where there were no distinction between these three parameters sets ($X = X_0 = X'$).

For convenience reasons, the distribution of the coordinates x_i in Figure 2.4 (used also in Equations 2.19 and 2.21), is different from the one in Figure 2.13. However, looking at the figures it is straight forward to correlate both coordinates sets. Calling the former set ξ_i

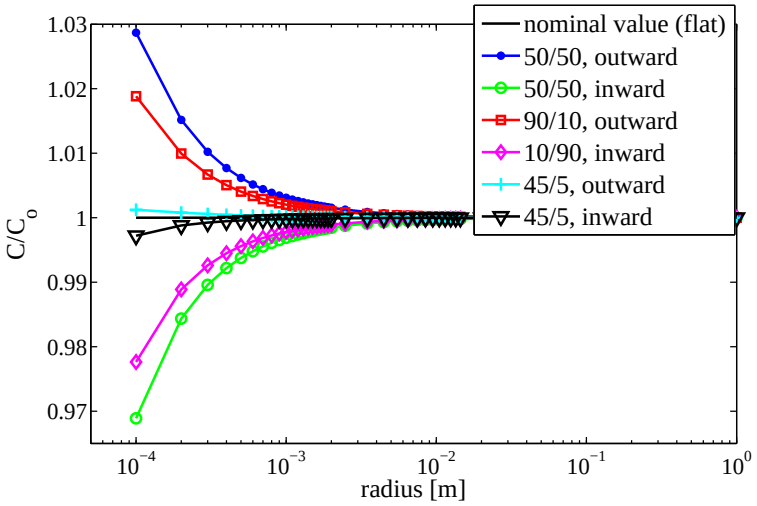

Figure 2.14: Theoretical estimation of the bending influence (inward and outward) in the capacitance of IDE structures due exclusively to the geometrical distortion of the electric field. Comparison with the nominal (flat state) value. In the legend, m/n represents the ratio W_0/G_0 presented in µm. All the structures are simulated on a 50 µm thick substrate [119].

and maintaining the notation x_i for the latter, ξ_2 in Equation 2.19 is for instance equal to $Im(x_2) = W'/2$ or $\xi_4 = Im(x_1) + i(x_3 - x_4) = \lambda'/4 + ih'_s$. The values of x_i can be calculated from the real geometry of the bent structure using Equation 2.28.

Figure 2.14 depicts the calculated effect produced by outward and inward bending on the capacitance of typical IDE structures, due exclusively to the geometrical distortion of the electric field. The behaviour of some of the structures are shown only for one bending direction for the sake of clarity. The parameters varied were: the electrodes width (ranging between 10, 45, 50, and 90 µm), and separation spacing between them (5, 10, 50, 90 µm), resulting in width/spacing ratios of 0.1, 1, and 9. All the structures are considered as being on a 50 µm thick polymeric substrate. The dielectric of the substrate and the electrodes length are kept invariable.

The capacitance value is observed to increase for outward bending and decrease, almost symmetrically, for inward bending. A comparison with the nominal (flat state) value is shown as well. It is worth noting that the maximum capacitance variation occurs for devices exhibiting a width-to-gap ratio equal to 1. In addition, for every studied structure, the capacitance variation is very low for radii of curvature higher than the electrodes pitch. This is also the case for substrates which are thicker than the electrodes pitch (see as an example the structure with 45 µm-wide electrodes, separated by a gap of 5 µm). Even though these results are of general interest, the two last conditions apply for practical reasons to all of the experiments realized in this work where large capacitors with small electrode pitch were required to observe a capacitance change when bending. On one hand, it was not possible to bend large devices to radii smaller than the pitch in the used set-up. On the other hand, the commercial foils used

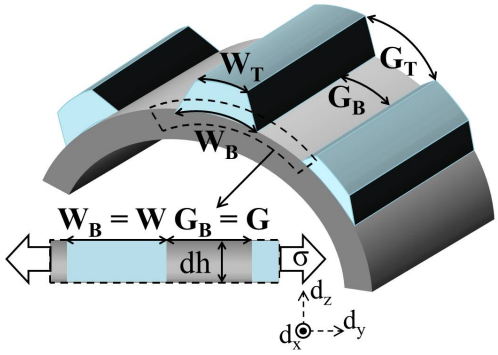

Figure 2.15: Graphical representation of IDE deformation while bending. Only the plane containing the interface electrode/substrate, represented with a dashed line, is taken into account in the capacitance computation. This plane is considered to be an infinitesimally thin composite layer containing alternating portions of electrode and substrate [119].

as substrate in this work are also thicker than the pitch. Therefore, the contribution of the bending-driven electric field distortion to the capacitance variation is very small and could be neglected in the majority of practical cases.

Geometrical deformation of the electrodes due to the bending strain

To evaluate the influence that the bending-drive geometrical deformation of the electrodes has on the total capacitance, we considered the geometry of the electrodes only in the plane containing the interface between the metallic electrodes and the substrate. It is precisely in this plane that the electrodes width and gap were taken into account for the previous capacitance calculation. Figure 2.15 represents this aspect by showing a bent IDE structure where the electrodes, with a finite thickness, experience maximum strain at the interface, where they are constrained by the stretched substrate. Two different values of width and gap spacing are defined: one of them at the bottom of the electrodes (W_B and G_B) and the other at the top (W_T and G_T). However, only the size of the bottom part of the electrodes counted for the calculation of capacitance using the Equations 2.19 and 2.21. The side wall contribution of the electrodes to the overall capacitance is negligible for every practical case, because the electrode thickness is much smaller than its width.

The plane containing the boundary between the electrode and the substrate was considered to be an infinitesimally thin layer that can be seen as a composite material formed by well bonded alternating parts of thin polymer and a thin metal film. However, the "thin metal film" is in reality the interface between the polymer and metal (see Figure 2.15). For this scenario, it is suitable to follow the "iso-stress" assumption [137], $\sigma = \sigma_s = \sigma_m$, where the subscripts s and m correspond to the substrate (polymer) and the "thin metal" film, respectively. Using Hooke's law for continuous media, $\sigma = E\epsilon$ (with E being Young's modulus and ϵ strain), and the fact that $\Delta(W+G) = \Delta W + \Delta G$, it is easy to obtain the effective Young's modulus of the

surface along the d_y axis using Equation 2.30

$$E_{eff} = \frac{(W_0 + G_0)E_s E_m}{E_m G_0 + E_s W_0} \tag{2.30}$$

W_0 and G_0 are, respectively, the IDE original (non-stretched) width and inter-electrodes spacing and E_s and E_m are the Young's moduli of the substrate and the "thin metal film". The stiffness in the bending direction is dominated by the substrate modulus whereas the stiffness in the perpendicular direction, i.e. along the electrodes (d_x axis), $E^{\perp}_{eff} = (E_m W_0 + E_s G_0)/(W_0 + G_0)$, is dominated by the "thin metal" modulus. In the composite material, there are two in-plane Poisson ratios as well. One along the d_x axis, $\nu^{\perp}_{eff} = \nu_m W_0 + \nu_s G_0/(W_0 + G_0)$, and one along the d_y axis

$$\nu_{eff} = \nu^{\perp}_{eff} \frac{E_{eff}}{E^{\perp}_{eff}} \tag{2.31}$$

where ν_s and ν_m represent the Poisson coefficient of substrate and "thin metal film" [137], respectively.

The strain in the electrode plane due to bending is according to [130–132] $\epsilon = h_s(2R)$ and is distributed along the electrodes and the polymeric gap. The previous expression refers to a radius of curvature defined at the neutral plane. Equivalently, for a radius defined at the surface of the electrodes like the one shown in Figure 2.13, $\epsilon = h_s/(2R - h_s)$. Both expressions are nevertheless equivalent in the current study since $h_s \ll R$. Referring again to Hooke's law and the "iso-stress" assumption, $\sigma = E_s \Delta G/G_0 = E_m \Delta W/W_0 = E_{eff}\epsilon = E_{eff} h_s/(2R)$, which combined with Equation 2.30 makes it straight forward to obtain the following equations:

$$\Delta W = W_0 E_s (W_0 + G_0)/(E_m G_0 + E_s W_0) h_s/2R, \tag{2.32}$$

$$\Delta G = G_0 E_m (W_0 + G_0)/(E_m G_0 + E_s W_0) h_s/2R \tag{2.33}$$

Despite the fact that the plastic substrate does not change its total width when bent along its length, it contracts above the neutral plane and compensates by expanding below the neutral plane. Therefore the electrodes, conformal to the surface of the substrate, are also subjected to a modification in their length L_0, which depends on the Poisson's ratio ν_{eff}. Solving the following integral $\int_{L_0}^{L_0-\Delta L} dL/L = -\nu_{eff} \int_{y_0}^{y_0+\Delta y} dy/y$, with $y = W + G$:

$$\Delta L = L_0 \left[1 - \left(\frac{W_0 + \Delta W_0 + G_0 + \Delta G_0}{W_0 + G_0} \right)^{-\nu_{eff}} \right] \tag{2.34}$$

Thus, the dimensions of the IDE in the bent state can be figured out from the original flat

geometry and Equations 2.32,2.33 and 2.34 as $W = W_0 + \Delta W$, $G = G_0 + \Delta G$, and $L = L_0 + \Delta L$. Note that the electrode deformation was assumed elastic with no failure modes occurring. Utilizing the previous geometrical values as the variables l_i of Equation 2.28 and performing the transformations described along section 2.3.1, we obtained the capacitance of the IDE structures under bending conditions.

Validation of the bending model for IDE

Design of the IDE test samples for the bending model evaluation Figure 2.16 depicts an optical image of one of the devices used to evaluate the bending model for IDE described above. The IDE and the shape of the contact pads were specially designed to be clamped in the bending set-up shown in Figure 2.17. The total surface area of the devices were 15 mm x 40 mm. Maximization of the IDE nominal capacitance was a critical design aspect for the bending experiments. A high nominal value was desirable to minimize the influence of parasitic contributions compared to the capacitance variation due to bending. The nominal capacitance value was maximized by making the electrodes as long as possible, given the clamping mechanisms of the set-up (i.e., 15 mm) and by including in the device as many electrodes fingers as possible to fill an Arc_{min} = 6 mm (see Figure 2.17): this is 120 fingers for IDE with a pitch of 50 µm, and 150 electrodes for IDE with a pitch of 40 µm. The IDE with a pitch of 50 µm included electrode widths of 40 and 45 µm with a corresponding inter-electrode spacing of 10 and 5 µm, respectively. The IDE with a pitch of 40 µm had both width and a gap spacing of 20 µm. Such structures resulted in a capacitance value ranging from 40 to 120 pF. The samples were fabricated by means of evaporation and lift-off technique by our partner Dr. T. Kinkeldei from the Electronics Laboratory at ETHZ (Switzerland). The substrates used were 50 µm-thick polyimide (PI) (*Kapton®-E* from *Dupont Teijim Films*™), and 125 and 250 µm-thick polyetherimide (PEI)(*ULTEM* from *Ajedium* ™). More details about the fabrication process of the sample can be found in [138]. Furthermore, one of the samples was electroless-plated with ~ 1 µm of Ni to increase the electrode stiffness.

Bending set-up A customized set-up was fabricated by our partners in EHTZ [119] and used to clamp the test samples for validation of the model. The bending set-up consisted of two plates, mechanical clamps mounted on them and a micrometer screw to precisely control the distance between the two plates. As the two plates got closer, the strip-like IDE structures that were mechanically clamped on the plates, buckled as depicted in Figure 2.17. Therefore, a correlation exists between the displacement of the plates and the radius of curvature of the sample. Figure 2.17 also depicts the set-up structure and the situations of maximum (not counting the flat state) and minimum radius of curvature, 7.86 and 2.47 mm, respectively. As it can be appreciated in Figure 2.17, it was possible to fit a circle to the middle part of the bent foil for every distance between the plates. From optical images, we could easily measure the resulting radius of curvature of the sample as well as the distance of the straight line (A in the Figure 2.17) connecting both ends of the circular foil arc. Using basic trigonometry,

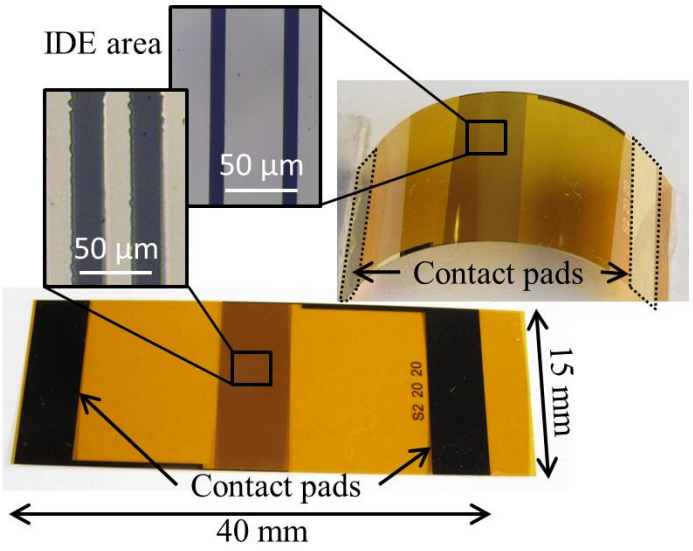

Figure 2.16: Optical image of one of the devices measured in flat and bent state, indicating its size and showing a magnified view of two examples of IDE geometry (W_0/G_0 = 20 µm / 20 µm and 45 µm / 5 µm) [119].

the distance of the resulting arc can be expressed as $Arc = 2Rsin^{-1}(A/(2R))$. The minimum arc distance, Arc_{min}, occurred for the minimum radius of curvature and was 6 mm in the experiments. Therefore, Arc_{min} became the maximum limiting dimension of the test devices along the d_y axis (perpendicular to the electrodes), allowing the electrodes to bend circularly at every radius. The values of capacitance were registered at 100 kHz using an LCR-meter (*Agilent E4980A*), which was connected to small wires soldered to the contacts pads of the samples. Despite the fact that all the metallic parts of the set-up were duly grounded, a small parasitic capacitance was still present for every radius of curvature and had to be subtracted after measurements. The zero parasitic calibration was performed by measuring the parasitic capacitance between the clamps in the absence of any clamped IDE structure. The measurement was repeated for the distances between the plates that corresponded to each radius of curvature used when a sample was clamped.

General validation Figures 2.18 and 2.19 demonstrate the high degree of correlation which was found between the predicted and measured capacitance values. The behaviour of some structures is shown for both outward and inward bending whereas for others the signal is represented only for one bending mode for the sake of clarity. Although the capacitance values have been normalized to compare the different cases, the nominal values fit equally well the model. The Young's modulus of the substrate/electrode interface, E_m, has been used as the only fitting parameter for all cases. The results show how the capacitance value increases for smaller radii of curvature during inward bending whereas it decreases for outward bending. This behaviour is the opposite of the one found in Figure 2.14, and as discussed previously, it

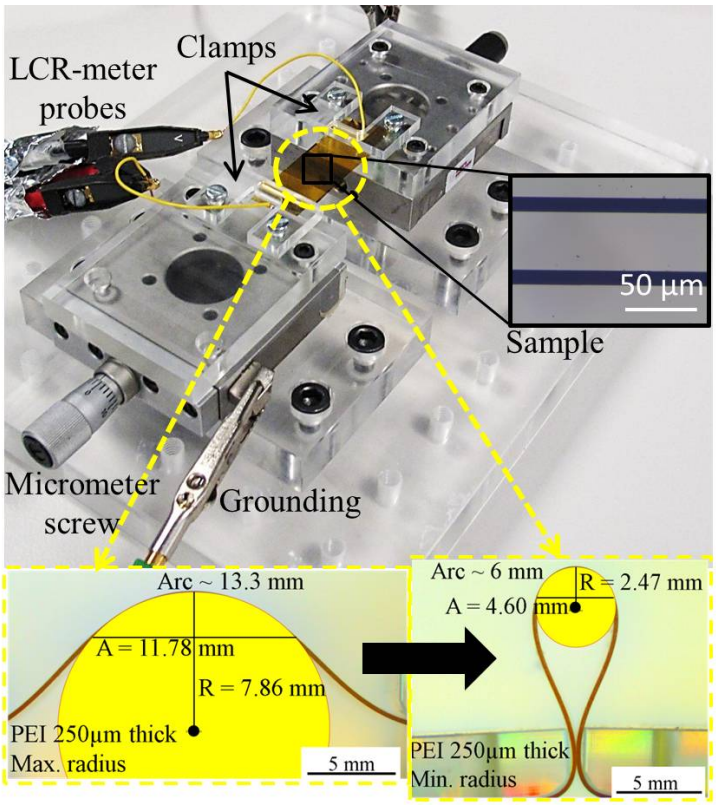

Figure 2.17: An optical image of the bending set-up with a device clamped in place along with a magnified view of one electrode edge, and two optical images taken from the side showing the maximum and minimum measured radii of curvature and the length of the longest fitted circular arc for each case [119].

can be entirely attributed to the geometrical deformation of electrode width and gap spacing. The influence of bending increases in every case with the substrate thickness, and although not shown in Figure 2.18 the model also predicts an increase in the bending influence with the ratio W_0/G_0.

Thin electrodes: Even though the Young's modulus of a thin film of Cr is known to be around 140 GPa, such values do not correspond with the physical meaning of E_m in this work because as the stress is applied to the substrate, E_m refers exclusively to the substrate/metal interface stiffness, as opposed to the electrode stiffness as a whole. This layer was treated as an infinitesimally thin metal film in the model (see Figure 2.15). The value of E_m which fits best with all the experimental cases on the polyetherimide (PEI) substrate is 620 MPa. For polyimide (PI) substrate E_m was 1 GPa. Although those values are much lower than the reported stiffness values for Cr, they are similar to those observed during direct stretching of some samples under the microscope, where the electrode and the gap strains were compared.

The other numerical values used in the model were E_s = 2.77 GPa for PEI and 5.55 GPa for PI, ν_s = 0.32 for both substrates and ν_m = 0.21, according to the substrates manufacturers

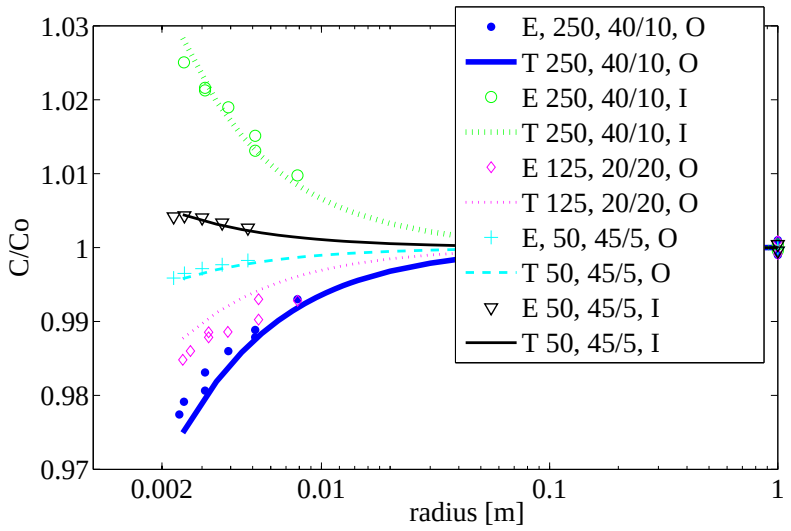

Figure 2.18: Theoretical and measured influence of circular inward and outward bending on the capacitance of IDEs fabricated on three different substrates: 250 and 125 µm thick PEI and 50 µm thick PI. In the legend: E stands for experimental points and T for theoretical values; 250, 125, and 50 are the substrate thicknesses in µm; m/n represents the electrodes W_0/G_0 ratio in µm; and I and O represents inward bending and outward bending, respectively [119].

and a typical Poisson ratio value of thin Chromium films. Figure 2.18 shows how the bending influence for thin electrodes remains small (few %) even for the minimum tested radius of curvature of ~ 2.5 mm, regardless of the geometry of the IDE or the substrate thickness. The largest tested variation of capacitance at the minimum radius corresponds with the case of W_0/G_0 = 40 µm / 10 µm for thin electrodes placed on a 250 µm thick substrate. The change in capacitance is slightly below 3%. This situation leads to electrode width, gap, and length strains of $\Delta W/W_0$ = 4.05%, $\Delta G/G_0$ = 9.09%, and $\Delta L/L_0$ = 1.02%, respectively. It would be possible to decrease even further the capacitance variation, for instance, using thin electrodes with a small ratio W_0/G_0 = 5 µm / 45 µm and fabricated on thin 50 µm substrates. The capacitance variation would be less than 0.5% in this last case when bent to a radius of 2.5 mm. If a coating layer were added to the substrate, the capacitance variation would become even smaller as the electrode plane would move closer to the neutral plane.

Thick electrodes: In order to expand the validity of the model for stiffer electrodes, one of the samples has been electroless-plated with ~1 µm-thick Ni. The Ni layer conformally covered the thin electrodes, adhering to the metal but not to the plastic substrate, hence forming an extra layer on the sidewalls of the electrodes that provides additional stiffness. The plated material is also believed to induce extra stress in the electrodes, which could also act to rigidify them. The selected value of E_m for the Ni plated electrodes was the Young's modulus of bulk Ni, 200 GPa. In any case, the bending behaviour varies only a little for any E_m much bigger than the plastic substrate modulus. As shown in Figure 2.19, the capacitance variation is enhanced by stiffening with plating the electrodes while keeping the rest of the pa-

rameters unchanged: W_0/G_0 = 40 µm / 10 µm on a 250 µm thick substrate. For the mentioned geometry, the enhancement was of more than two folds, from ~3% to ~7%, after plating the electrodes with Ni. The strain values became $\Delta W/W_0$ = 0.33%, $\Delta G/G_0$ = 24.02%, and $\Delta L/L_0$ = 0.94%, confirming that the increase in electrode stiffness results in a larger difference between polymer and electrode strains and hence larger variations of W/G. A capacitance variation of up to 10 or 15% could be achieved by modifying W_0/G_0 to 45 µm / 5 µm or W_0/G_0 = 48 µm / 2 µm, respectively. These high numbers are relevant for the development of strain sensors. Further thickening of the electrodes would lead to even higher capacitance variations due to the appearance of non-negligible sidewall capacitance contributions [125]. However, this aspect is outside the scope of this thesis study.

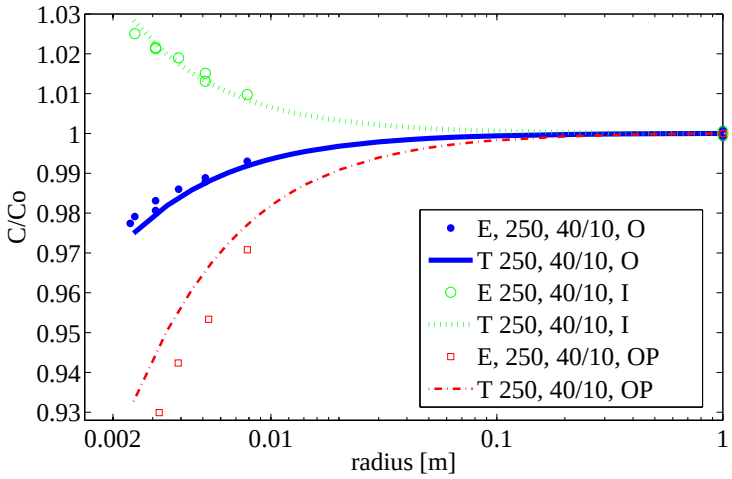

Figure 2.19: Theoretical (T in the legend) and experimental (E in the legend) comparison of the influence of circular inward (I) and outward (O) bending on the capacitance of IDEs fabricated on 250 µm thick PEI with an electrode ratio of W_0/G_0 = 40 µm / 10 µm. In the legend, OP represents outward bending of plated devices [119].

2.4 Conclusions

In this chapter the geometries investigated in this thesis work for capacitive gas detection were introduced, with emphasis in interdigitated electrode (IDE) structures which are theoretically more complex and less understood than common parallel plate capacitor. Motivated by the need of modeling IDE-based gas sensors, I presented the theory related to the sensing principle capacitive gas sensors in general. Then I continued the study by focusing on the the calculation of the capacitance of the different IDE structures utilized in this thesis and their behaviour upon bending. The models based on conformal mapping and partial capacitance principle have been validated by means of FEM and experimental measurements.

In the first part of the chapter it was pointed out that the higher the difference between the analyte permittivity and the sensing layer/substrate permittivity, the greater the sensitivity

is due to changes in the total effective permittivity. In the same way, the higher the volume of the analyte molecules is, the higher the sensitivity due to swelling of the sensing layer. For the case of humidity detection, the permittivity of water is so high (ϵ_a = 76.7) that the swelling component can be usually neglected. Due to the complex analytical expression of the capacitance of IDE structures, quantitatively determine the sensitivity of IDE-based sensors is not straight forward and lies out of the scope of this thesis. On the other hand, in Chapter 4 the equation describing the sensitivity of parallel plate structures is expressed mathematically. However, qualitative estimations of the sensitivity of IDE-based capacitive gas sensors are drawn through this chapter. It has been established that thick sensing layers are advantageous for sensitivity through both swelling and permittivity contributions, but only up to a limit thickness equal to the distance between two adjacent fingers. Beyond this thickness, the value of capacitance and the sensitivity saturates. Nonetheless, since the time necessary to reach concentration equilibrium in diffusion-based process depends quadratically on the thickness of the medium where diffusion takes place, thicker sensing layer yield much slower sensor time response than thin layers (see Equation 2.14).

The model described in the literature, [45–48], has been adopted to calculate the capacitance of multilayer planar IDE structures utilizing the conformal mapping and partial capacitance methods. Then, the same model was adapted for a new geometry of quasi-planar IDE with a dielectric interlayer in between the combs. The outcome of the models is that the capacitance value increases (not necessarily linearly) with the permittivity and thickness of the substrate and sensing layer (up to a thickness equal to the fingers pitch), electrodes thickness and ratio width to inter-finger space. The capacitance also increases linearly with the number of finger electrodes (for a large number of fingers only) and their length. The validity of the described model is limited to devices formed by long and planar electrodes. Therefore finite element methods have been used to evaluate that the model is valid and accurate for the real geometries developed in this thesis. Finally, the model has been expanded to adapt it to the practical case of quasi-planar IDE fabricated during my thesis, where both combs are separated by a thin dielectric film. The width of every comb was different. The evaluation of the model was carried out by comparing theoretical prediction with experimental data coming from fabricated devices with different electrode width, separation space and thickness. The agreement between data obtained from fabricated devices and model confirm the validity of the latter for design and optimization of the former.

Since this thesis deals with devices fabricated on flexible substrate, the influence of circular bending in the capacitance of IDE microstructures has been theoretically and experimentally established as well. The theoretical model, accounting for the coupling between electric field distortion and the geometrical changes on the devices due to bending strain, predicted results in good agreement with each of the experimental cases considered, including different substrate materials and thickness, different IDE geometries, and different electrode stiffness. The modification of the electric field distribution while bending has been determined by introducing an extra conformal mapping transformation prior to the previously reported in literature used to model flat IDE structures. On the other hand, fundamental solid mechanics was used

to determine the strain-driven deformation of the IDE. The proposed model provides, in this way, information to adapt the design of IDE structures to either maximize their capacitance variation during bending, of interest for strain sensors, or minimize it, which is desirable for gas sensors, transistors, or flexible passive devices. Although all the cases presented in this thesis deal with bending around the electrode axis, the developed method could be easily expanded to account for bending around the perpendicular axis too. The model could also be used for IDE devices coated by another polymer layer, a common situation in many gas sensors or embedded devices. In the worse case scenario of bending circularly the electrodes down to a radius of 2.5 mm (around the axis perpendicular to them) has a small influence in the capacitance value of few %, for typical structures. This value would however introduce a rather large inaccuracy of few % R.H. in the response of the gas sensors fabricated in this thesis and described in Chapter 3 (the sensors have a relative sensitivity of around 0.07 %/1% R.H. in the best case). Nonetheless, the influence of bending can be dramatically reduced by design to ~ 0.5% for ~ 2.5 mm radius of curvature. Furthermore for gas sensing applications a coating layer needs to be added to the substrate, moving the neutral plane closer to the electrodes so that less stress would be induced on them, and smaller capacitance variations would occur. The presented model could also allow to design a sensing layer geometry that brings the neutral plane exactly to the electrodes plane, minimizing the effect of bending on the capacitance value. Although it has not been studied, it is expected from theoretical estimations that bending the electrodes around their axis (instead of around their perpendicular axis) does not have a big influence in the capacitance neither.

The current work supposes a general predictive framework that can be applied to any kind of material, inorganic, or organic, and deposition method, to determine the performances of truly flexible electronic gas sensors based on IDE transducers. In the next chapter, these points will be put into relief through the design, fabrication and characterization of different printed IDE R.H. sensors on foil.

3 Inkjet-Printed Capacitive Humidity Sensors on Foil Based on Coplanar Interdigitated Electrodes (IDE)

3.1 Introduction

This chapter describes the realization and characterization of humidity sensors based on inkjet-printed interdigitated (IDE) capacitors fabricated on flexible polymeric substrate. A large part of the content of this chapter has been published in peer reviewed journals [117–119].

Compared with the previous works on IDE gas sensors on foil developed at the Institute of Physical Chemistry at the University of Tübingen (Germany) [112] or in their following collaboration with SAMLAB described in [31], polyethylene terephthalate (PET) has now substituted polyimide (PI) as substrate material due to its advantageous price and current use in the field of goods packaging. These properties suit the goals of the *FlexSmell* project. Furthermore, inkjet printing of silver and electrodeposition of nickel have also now replaced clean-room standard processes and materials. Inkjet printing and electrodeposition are both additive processes [1, 2], which optimize the use of material by depositing it only on required locations on the chip. Consequently, the fabrication of this type of electronics becomes potentially more material and cost effective than traditional silicon electronics. Furthermore, because inkjet printing is a non-contact and localized process, it makes possible the fabrication of arrays of different sensing materials in such a way that the deposition of each sensing material does not affect the other surrounding materials. This last property is of crucial importance when developing multsensing platforms. The sensors presented in this chapter are based on IDE capacitors to allow for the ultra low power consumption typical in capacitive-based devices, compared to resistive ones. The IDE structure allows easy functionalization of the sensor with a sensing layer directly deposited on top. This geometry also maximizes the interaction of the sensing layer with its environment. The design of the sensors was carried out according with the theory described in Chapter 2, targeting relative small features and a geometry able to provide suitable values of capacitance (few pF), sensitivity towards relative humidity (R.H.) (of around some fF / 1%R.H.) and response

time (few minutes). The sampling and operation times imposed by food logistics are such that few minutes response time and few weeks or months of working life are enough for the developed sensors to fulfill the requirements of the *FlexSmell* application. The design of the IDE sensor depends on the selected inkjet printing parameters [9, 96–98] and the possibilities of electroplating nickel with different thickness on top of the electrodes.

In this chapter, I also evaluated the influence of electrodeposition of a thicker metal layer on the stability of the sensor, its absolute sensitivity and its capacitive nominal value. This last point is worth considering the low resolution and low thickness allowed by inkjet printing inks with metallic nanoparticles, which makes it difficult to obtain very packed and tall electrodes providing large capacitance values per surface area. Regarding long-term stability, nickel could also help reducing drifts of the sensor response coming from chemical instability of silver. Another of the strongest points of this printing/electrodeposition process is that it enables the simultaneous fabrication of a humidity and temperature sensing platform by simply including a resistor in the original layout of the capacitor. This last point is developed more in detail in Chapter 5.

An important aspect in solution-based electronics is the adhesion of the ink to the substrate once it dries. This aspect is specially critical when the substrate is flexible since bending generates extra interfacial stress between the deposited material and the substrate, that can result in delamination. The adhesion of printed silver on PET and PI foil and the effect of substrate pre-treatment with oxygen plasma have been previously proven important [111, 139]. They will also be addressed here for our concrete case of materials. A good adhesion of the printed layer onto the substrate is a key point for successful electrodeposition without delamination.

Although the IDE devices could be already used as humidity sensing using their polymeric substrate as sensing layer [40, 112], the substrate is not optimum for sensing. Commercially available plastic substrates (such as PET or PI) are highly hydrophobic and designed to present low moisture intake, specially when their main application is packaging. Low moisture intake is equivalent to low partition coefficient and hence low sensor sensitivity (see section 2.2). Furthermore, since the substrate's main role is to offer mechanical support to the sensor, its thickness is usually selected to be too thick to allow a quick sensor response time. As it was discussed in Section 2.2, this problem is specially acute for printed IDE where the fingers pitch can not be reduced as much as on non-printed devices. The reason is that the electric field will reach into the substrate and sensing layer as deep as the fingers pitch distance is. Low printing resolution implies large pitches and thus a large zone of interaction between electric field and substrate. In the case of substrates thinner than the pitch distance, the electric field would interact also with the material underneath the substrate, modifying the sensing behaviour for every experimental scenario (see Figure 2.1 in Chapter 2, Section 2.1). If the substrate is thick enough to contain all the electric field lines, the sensor may be relatively sensitive, but the analyte will need long time to diffuse into the thick substrate, delaying the response of the sensor. To overcome the sensing disadvantages of the substrate as sensing material,

following the electrodeposition step of nickel on the printed silver electrodes, a solution of cellulose acetate butyrate (CAB) has been customized and inkjet-printed on the capacitive structures to act as a thin humidity sensing film. To conclude, measurements of capacitance value against changes in ambient relative humidity are presented. The performance of the sensors (response time, linearity, hysteresis and sensitivity) are analyzed and qualitatively explained for both single and differential mode, in which the parasitic component of the substrate was subtracted from the complete sensor operation signal [31].

IDE with reduced size As it was mentioned above, increasing the nominal value per surface area of IDE sensors is challenging due to the typical low resolution attainable by common printing methods. Such resolution remains still far below the one allowed by photolithography. This is a limiting factor in the miniaturization of printed devices, and also partly the reason why the price of the technology has not reached its minimum yet. In printing processes in general, and inkjet in particular, the active material (ink) is deposited on the substrate in liquid phase. There exists a limitation concerning the minimum volume that can be ejected from the printing nozzle to be deposited on the substrate; moreover, the ink spreading on the substrate depends on the system interfacial energies and the drop impact [8]. Hence the minimum area occupied by the functional ink is limited and depends on every concrete used material, making difficult the control of the process. Due to their usual geometry, well-packed parallel long electrodes occupying a large area, to realize IDE with high capacitance value implies the fabrication of one of the most challenging structures to be printed. Much care during fabrication and design is needed in order to print comb electrodes structures in a reliable way. The level of care is critical if the devices are to be used actually as capacitors, since shortcircuits between electrodes would turn the devices into resistors instead. Nonetheless, many authors still point out the need of printing closely packed electrodes (see for example [35, 38, 43]). The typical electrodes width and inter-electrodes gap included in the papers referenced above ranged from 100 to 200 μm; only with special care and recurring to different treatments to modify the substrate surface energy, a top resolution of 40 μm is reachable. More compact devices would present several advantages, not only related to decreasing the foot print of the devices and the corresponding material use and fabrication cost, but also in terms of sensing performances; offering more flexibility in design parameters, supplying higher values of nominal capacitance for a given surface area and allowing higher interaction between electric field and sensing layer (see Section 2.2), which yield altogether to a larger sensitivity. For all the exposed reasons, during this thesis work I tried to soothe the limitation in resolution of printed IDE devices through the development of an alternative fabrication strategy conceived to decrease the electrodes pitch (centre to centre distance of adjacent fingers) in a reliable and reproducible way, and without creating shortcircuits between adjacent fingers. In this way, I could increase the nominal value per surface area of the devices as well as the fabrication yield. The strategy consists of the deposition of a thin dielectric layer onto the first printed electrodes comb prior to the printing of the second comb in such a way that both polarities are electrically insulated and cannot be in contact if printing errors occur. This technique renders

the printing process less demanding and more reliable. The method is demonstrated by using parylene-C as dielectric interlayer, whose deposition does not involve high temperatures so that it is compatible with the utilization of inexpensive plastic substrate. Parylene-C is a extremely chemically stable and tightly organized compound, so it acted at the same time as a barrier against the undesired absorption of moisture into the polymeric substrate. In collaboration with the Universtiy of Tübingen (Germany), our group has previously reported on inkjet printed IDE capacitive humidity sensors based on silver ink on PET substrate, using parylene-C as substrate passivation layer [140]. The use of parylene-C made unnecessary the electroplating of the electrodes or the use of differential measurements to get a stable and fast sensor output signal. In this work, I selected inkjet printing of silver nanoparticles based ink as deposition method for proof of concept, and also because inkjet printing is one of the most challenging printing methods to reliably reach a small resolution, emphasizing the usefulness of the described strategy. Nevertheless, the exposed fabrication strategy remains suitable for every printing process dealing with the deposition of liquid phase ink on a substrate.

Summarizing, I present the fabrication of very low cost and mechanically flexible IDE capacitive devices on foil, which operation was demonstrated, but not limited, to humidity detection. The fabrication process involves mostly additive steps (inkjet printing and electrodeposition), minimizing the waste of material. On top of that, a process to reduce the IDE pitch down to fifteen folds while improving at the same time the fabrication yield was developed to increase the capacitance value per surface area. In order to ameliorate the sensor performance, two strategies were investigated: either plate the Ag IDE with Ni and subtract the parasitic effect of the substrate layer, or extra anneal of the Ag IDE and utilize a parylene-C moisture barrier to coat the substrate. The results of this work foresee applications requiring capacitive gas sensors on plastic foil, where low cost, mechanical flexibility and very low power consumption are needed.

3.2 Design

Using the theoretical model described in Section 2.3.1 of Chapter 2 and considering the available materials as well as the typical features size allowed by inkjet printing and electroplating technologies, IDE transducer were designed to obtain sensors with a desired value of capacitance (few pF) and dynamic range (few fF) appropriate for reading the output signals with standard electronic circuits such as the $\Sigma\Delta$ capacitance-to-digital converter AD7745, AD7746 [31, 112], the capacitance-to-digital AD7150 from *Analog Devices*, or the microcontroller MSP430 from *Texas Instruments*. All that while keeping the foot print of the device as small as possible.

Standard IDE devices For standard IDE devices like the one sketched in Figure 3.1, a capacitance of about 5 pF (before the electrodeposition step) was obtained including 20 pairs of planar electrodes of 7 mm length each, occupying a total surface area of 8 mm × 8 mm and

similar width than gap of ~100 µm. This width and gap size is a safe value permitting good fabrication yield. Smaller resolution was achieved in non-standard IDE or in later versions of IDE devices presented in the multisensor platform described in Chapter 5.

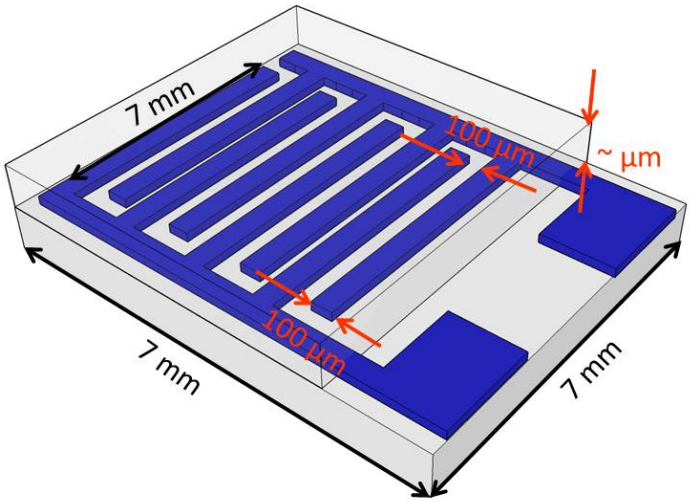

Figure 3.1: Sketch of standard IDE with designed dimensions.

IDE devices with reduced size The geometry of the devices using a thin layer of parylene-C between the two combs was described in Figure 2.9 of Section 2.3.1 of Chapter 2 to support the validation of the theoretical model to predict their capacitance. The structure is repeated in Figure 3.2 including the thickness of the substrate, parylene-C and sensing layers. Five different geometries have been fabricated, labeled from A to E; the number of electrodes and pitch (defined as the distance between the centre of two contiguous electrodes) corresponding to every different geometry is summarized in Table 3.1. The sensing surface area of every device is 3 mm × 3 mm.

Table 3.1: Summary of the design parameters for the printed IDE devices with dielectric interlayer.

Device	Pitch (µm)	Number of electrodes
A	40	74
B	60	50
C	80	37
D	100	30
E	120	25

Sensing layer The surface area of the sensing layer was slightly larger than the IDE in every case to ensure its total coverage. This is, slightly larger than 8 mm × 8 mm for standard IDE devices and than 3 mm x 3 mm for IDE with reduced size. The thickness can be selected

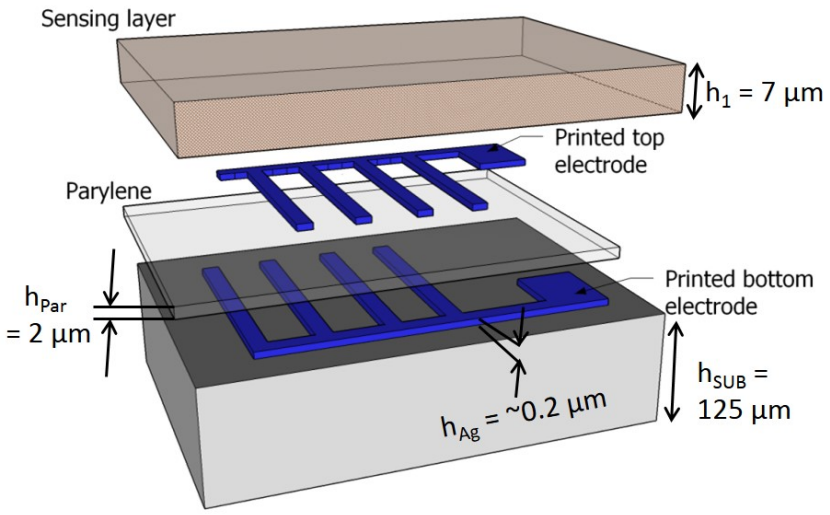

Figure 3.2: Sketch of the exploited view of IDE fabricated with a thin dielectric layer of parylene-C between combs to prevent electrical shortcircuits between them. The thickness of every layer is indicated in the figure.

according to Figure 3.17, depending on whether high sensitivity or fast response is favoured, as it was discussed in the Section 2.2 of Chapter 2.

3.3 Fabrication

The devices developed in this thesis are based on silver nanoparticles-based ink and polymer solutions, inkjet-printed on plastic commercial polymeric foils. Due to the narrow window for printing parameters imposed by the used printer (viscosity ~ 10 mPa*s (or cP) and surface tension ~ 30 mN/m) commercially available silver ink or carefully tuned polymer solutions were used to pattern the sensors and the sensing layers respectively. The printer used for all the devices described in this thesis was the *Dimatix Fujifilm DMP-2800*™ shown in Figure 3.3, with 10 pl drops cartridges.

Temperatures below 150°C were kept during the whole fabrication process to keep unaltered the properties of the PET polymer used as substrate, which maximum processing temperature is 150°C according to the manufacturer. In this section, I describe in detail the fabrication process flow, materials and equipment used to fabricate printed IDE gas sensors on foil.

3.3.1 Substrate preparation and parylene deposition

Standard IDE devices We fabricated printed and electroplated humidity sensors using flexible foils as substrate. Polyimide (PI) *Kapton*®-*E* of 50 µm thickness from Dupont™and

Figure 3.3: Commercial inkjet printer Dimatix Fujifilm DMP-2800™ for printed electronics.

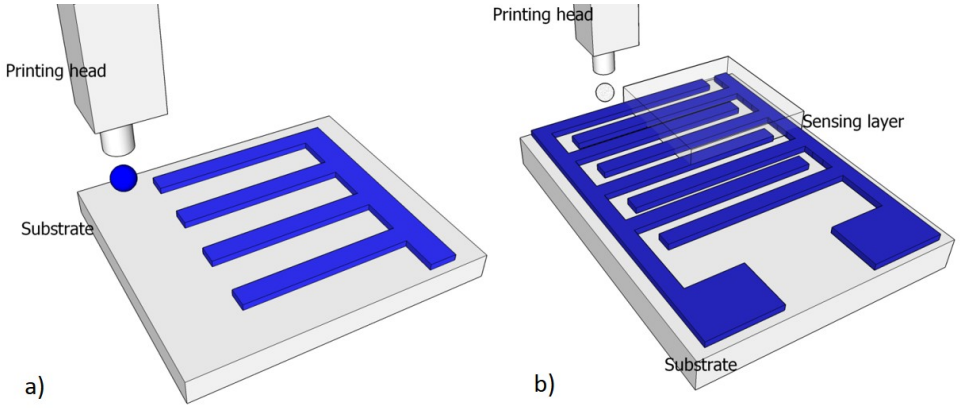

Figure 3.4: Fabrication process flow of printed standard IDE sensors: (a) PET substrate treatment and inkjet printing of the silver electrodes combs and (b) inkjet printing of the CAB humidity sensing layer.

polyethylene terephthalate (PET) *Melinex® ST506* of 125 µm thickness, from *Dupont Teijim Films*™, have been investigated as substrate candidate materials. Eventually, PET foil has been chosen due to its low moisture absorption rate, low cost, commercial availability and good adhesion/printing results. Furthermore, PET is currently used in the field of goods packaging. The substrates were cleaned by immersion in acetone, isopropanol and deionized water. Right after the cleaning process, the substrates were dried with nitrogen, dehydrated them for a minimum of 1 h in an oven at 120 °C, and finally subjected them to microwave (2.456 GHz) oxygen plasma treatment for 4 min at 400 W and 560 mTorr pressure, under a flow rate of 400 sccm in a plasma system *PVA TePla PS210*. The oxygen plasma treatment served to smooth the polymer surface by slightly etching it and to modify its chemistry, resulting in an improvement of wettability control of the silver ink on the substrate [110, 111]. The power and flow rate used for the substrate plasma treatment were standard values used for "descum" process on silicon wafers at low temperature. After several tests, I found 4 minutes the minimum necessary time to obtain optimal printing results on the polymer.

IDE with reduced size The substrate used in this case was only PET, and it was prepared as in the standard IDE case with the exception that only 15 seconds of oxygen plasma were enough to yield good printing results and to improve ink wettability and printability on the substrate. The difference in time compared to the standard IDE case is due to the use of a different silver ink to print the lines as it is described below. Afterwards, the samples were introduced again in the oven for 30 min at 120 °C to slightly attenuate the influence of the plasma on the ink wettability in order to obtain narrower printed lines. We believe that heating up the polymer fulfills some bonding sites reducing the surface energy. To decrease the fingers pitch of this improved generation of IDE capacitors, a layer of parylene-C was deposited between the two combs of IDE and served as electrical isolation and a moisture barrier for the substrate (see Figure 3.5(b)). The parylene layer was formed by chemical vapour deposition at room temperature and under vacuum (few µm bar) in a *Comelec C-30-S* deposition system. The deposited layer was very conformal, chemically tight and its thickness could be very finely controlled. After the parylene-C was deposited on the first comb, we performed again a short oxygen plasma treatment on the parylene under the exact same conditions used for the substrate but for a longer time of 30 s. Then, the samples were brought back to the oven for 30 min at 120 °C. The second plasma/oven treatment had as goal not only the improvement of silver printability by adjusting wettability, but also the adhesion enhancement of the CAB sensing layer onto the parylene-C layer.

3.3.2 Inkjet printing patterning and optional electroplating

Previous to the printing step of the transducers, we made use of DoE (design of experiments) methods to find the optimum printing parameters to achieve the best trade-off between conductivity, edge smoothness and minimum line width and pitch [9]. The used DoE technique was full factorial design. The most relevant printing parameters resulted to be: number of printed layers, temperature of the substrate while printing, inter-drop space, drop jetting speed, drop jetting frequency and the pre-treatment of the substrate with oxygen plasma. The printing parameters were optimized for the printed electrodes on the treated substrate.

Another highly influencing factor is the type of ink used. Two commercially available silver nanoparticles-based inks were tested onto the the substrates: *DGP 40LT-15C* from *Anapro* (*Advanced Nano Products*) was used for standard IDE, and *SuntTronic Jet EMD506* ink from *SunChemical* was used for electrodes with reduced size. Whereas *DGP 40LT-15C* had a Ag solid content of 30 to 35% and uses triethylene glycol monomethyl ether (TGME) as solvent, *SuntTronic Jet EMD506* had 20% of Ag solid content dispersed in ethanol and ethanediol. The *DGP 40LT-15C* was more stable and presented less firing problems, however *SuntTronic Jet EMD506* allowed the patterning of narrower lines, a key aspect to achieve devices with reduced size. The waveform of the potential applied to the piezoelectric nozzles to eject the drops of ink is usually provided by the ink suppliers. Otherwise, it has to be tuned to obtain round drops without tail. Figure 3.6 is an example of the waveform used to print *SuntTronic Jet EMD506* ink, where all the different segments are marked. The role of each segment is described next:

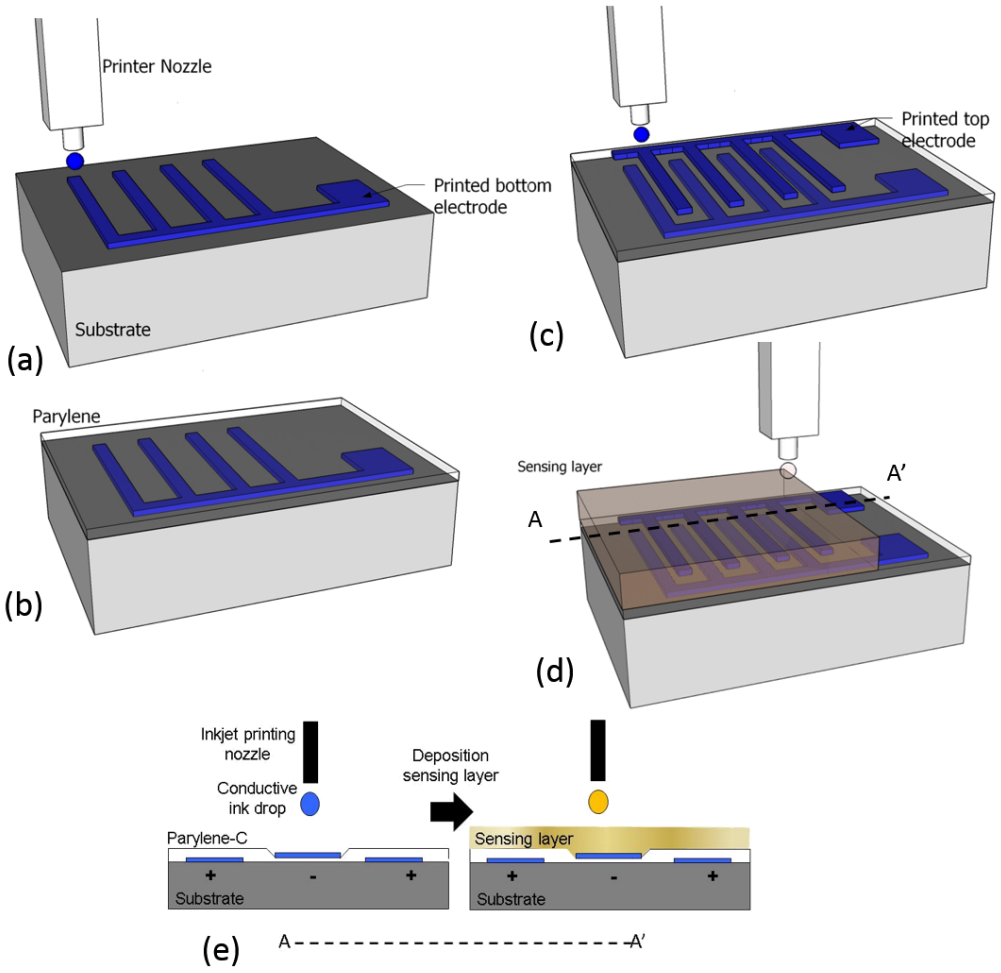

Figure 3.5: Fabrication process flow of printed IDE with reduced size: (a) PET substrate treatment and inkjet printing of the first silver electrodes comb. (b) Chemical vapour deposition of a thin parylene-C layer. (c) Inkjet printing of the second electrodes comb. (d) Inkjet printing of the CAB humidity sensing layer. (e) Cross section view of steps (c) and (d) [118].

1. Negative voltage is applied to the piezoelectric material (PZT), drawing ink from the cartridge into the pumping reservoir. A settling time follows afterward.

2. An increase in voltage deflects the PZT and eject the the ink out of the nozzle. The steeper the first part of this segment is, the faster the ink is ejected. A hold period follows.

3. Dampening segment used to prevent the printed head from sucking air back in. The PZT is brought back to its original position.

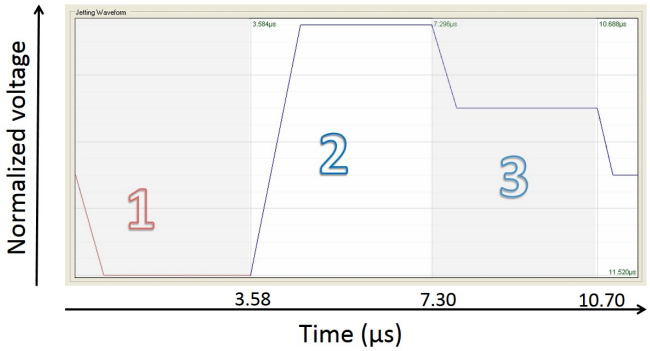

Figure 3.6: Waveform of the potential applied to the printer nozzle over time, used to print round and tail-less drops of SuntTronic Jet EMD506 silver ink. Every segment of the waveform is highlighted in the figure.

Standard IDE devices The patterning of standard IDE on PET by inkjet is depicted in Figure 3.4(a)). The lines were formed by printing two consecutive layers of *DGP 40LT-15C* ink onto a substrate at 52 °C, using a drop-to-drop space of 40 µm and jetting with one single nozzle at 3 m/s and 1 kHz.

Afterwards, the optimized printed devices (in terms of adhesion, geometry and conductivity) were introduced in an oven at 150 °C for 40 min in air atmosphere to thermally cure and sinter the conductive ink. These thermal conditions were the recommended by the supplier. Once the conductive ink was properly sintered, the devices were optionally subjected to electrodeposition process in a nickel sulfamate bath at 54 °C , under an electrical current density of 20 mA/cm^2. The growth rate was 185 nm/min at a current density of 10 mA/cm^2. Nickel was considered as a good potential candidate for electrodeposition metal because it is inexpensive, easy to electroplate on silver and induces lower stress than copper. Nickel will bring also sensitivity advantages not only to the sensors (as it is described in Section 3.5.5) but to the thermoresistors included in the multisensing platform described in Chapter 5, owing to the higher temperature coefficient of resistance (TCR) of Ni than of printed silver.

IDE with reduced size For the IDE with reduced size and parylene interlayer, the first electrode comb was inkjet printed on the PET substrate (see Figure 3.5 (a)) using the *SuntTronic Jet EMD506* ink. The selected printing parameters were: two consecutive layers printed with a single nozzle (four nozzles to print the contact pads) on a heated substrate at 45 °C , using a drop speed and frequency of 6 m/s and 5 kHz respectively while keeping a distance between drops of 40 µm and between printing head and substrate of 1 mm. Following printing, the ink was sintered in a normal convection oven at 150 °C for 3 h. This extra long-time step was needed to merge the nanoparticles together [98] and completely remove the organic content inside the ink rendering the ink electrically conductive. Organic residual would yield to sensing instability [140] otherwise. After the parylene deposition on the first comb, we proceeded to the printing of the second comb of electrodes using the same ink, printing parameters and

annealing process as for the first one (see Figure 3.5(c)). In order to improve the alignment of the second comb, it was necessary to use the "thermal scaling" option of the printer (along the direction perpendicular to the electrodes), which allows for the compensation of the pattern size variation after subjecting the first comb to high temperatures during annealing. The utilized scaling factor was 2500 ppm.

3.3.3 Sensing layer: preparation, tuning and printing

Cellulose acetate butyrate (CAB) was selected as humidity sensing material because it is well known for its sensitivity towards humidity and its easiness of processing [112, 141–143]. On the other hand, it is soluble in hexyl acetate, which is a non-toxic solvent that presents values of surface tension (26.2 nN/m) and boiling point (171.5 °C) appropriate for inkjet printing with our printer. The CAB humidity sensing layer was inkjet-printed onto the IDE capacitors as represented in Figures 3.4(b) and 3.5(d). For its preparation, cellulose acetate butyrate (molecular weight ~ 70000) with 13.5 wt% acetyl and 37% butyryl content from *Sigma–Aldrich* was dissolved over several days in hexyl acetate 99% also from *Sigma–Aldrich*. The surface tension of the ink was measured with a tensiometer *Kibron Aqua Pi*. The concentration of the prepared ink was also adapted to match the dynamic viscosity required for inkjet printing as explained in Section 3.5.4. A viscometer *Brookfield DVII+Pro* was utilized for that purpose. Once the solution was tuned to be inkjet printable (surface tension of 26.2 mN/m and viscosity of 10.2 cP), it was necessary to adjust the voltage waveform applied to the piezoelectric nozzles in the printing head until round ink droplets were formed and jetted. Then, the printing parameters needed to be optimized to obtain non-clogged nozzles and a homogeneous printed layer. In this case, special attention needed to be put in intensifying the nozzles cleaning cycles because the CAB ink was prone to dry and clog the nozzles.

The printing parameters were the the same for all the developed devices: four nozzles were fired on a substrate at 38 °C, using a drop jetting speed around 8 m/s, a jetting frequency 2 kHz, a drop-to-drop space of 20 µm and a distance between printing head and substrate of 1 mm. When printing polymers, I observed a high dependence of the jetting quality with the temperature of the ink when it is jetted, probably due to strong variations in viscosity. The temperature of the cartridge head was set at 50°C. The number of printed layers was defined in accordance with the desired thickness of the final dry CAB layer as depicted in Figure 3.17 in Section 3.5.4. I printed 24 layers, which corresponded with a dry layer 8 ± 3 µm in thickness. This thickness ensured a relative quick sensor response and a value of sensitivity large enough to detect capacitance shifts with the available electronic equipment. On top of that, 24 layers did not make the printing process too time consuming. Figure 3.7 presents a picture, taken with a white light interferometer, of a portion of the sensing layer coating an IDE capacitor.

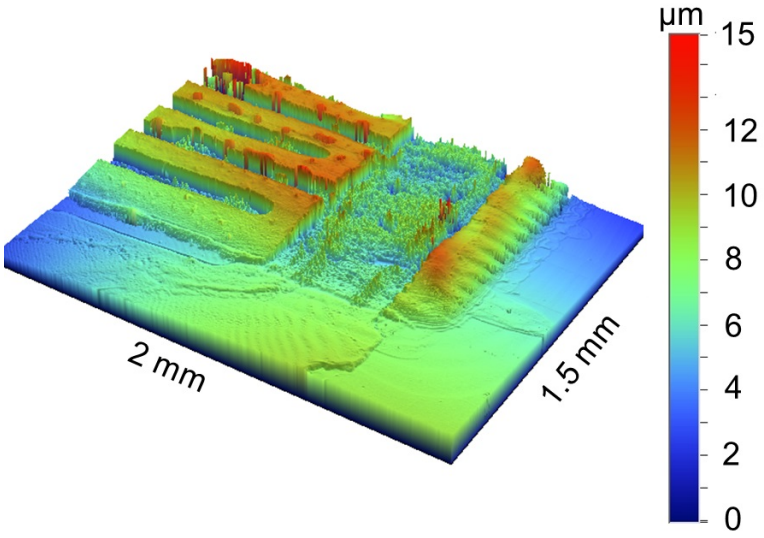

Figure 3.7: Image of a sensing layer of CAB inkjet-printed onto an IDE capacitor. The image was taken with a white light interferometer. The silver part was much more reflective than the CAB, so the CAB did not appear on the areas with silver underneath [117].

3.3.4 Contacts opening

Since the parylene layer covered the whole substrate, before connecting the devices for characterization, the contact of the bottom electrode must be opened. For the time being, a manual scratching was done, but is large scale production is faced, plasma oxygen treatment could be applied through a mask to remove the parylene-C above the contact, while leaving unaltered the rest of the device. The stripping ratio of parylene-C in the oxygen plasma oven used for substrate surface modification at 500 W was estimated in 129 ± 16 nm/min.

3.4 Characterization methods

3.4.1 Adhesion tests

In order to assess the level of adhesion between the silver lines and the different substrates (PI and PET), two different tests have been carried out. The tests took place at ambient conditions. The first test corresponded basically with the standard *ASTM F 1842-09*, where six squared cuts, spaced 2 mm apart, were made on a printed (and sintered as in 3.3) silver layer of around 200 nm thick. Both *Anapro DGP 40LT-15C* and *SuntTronic Jet EMD506* inks were tested on PET and only the *Anapro* on PI. Then, adhesive tape Scotch Magic, 19 mm wide from 3M (green) was stuck to the cuts for 90 s by applying uniform pressure with the fingers, and finally removed without jerking. A bare eye evaluation was enough to classify the results according to the scale in the standard. On three of the six samples of PI that were tested, microwave oxygen plasma treatment was performed on the substrate before printing the silver on it.

In the case of PET substrate, the removal strength of the adhesive tape was not enough to peel the printed metal layer off at all, making impossible the evaluation of the influence of plasma on this substrate. Therefore, a second approach represented in Figure 3.8 was tried, but only on the *DGP 40LT-15C* ink, since it was the one used to pattern standard IDE with thick electrodeposited layer on top, and thus the one requiring the best adhesion. In this approach, the silver was inkjet-printed between two square pieces of clean PET of 1 cm^2, forming a multilayered structure. In this case, the sintering of the ink took place overnight at 150 °C to ensure the total removal of the solvent inside the "sandwiched" silver layer. Afterwards, an adhesion test dolly was perpendicularly stuck to each outer side of the structure using instant glue from *Pattex* which was let to dry overnight. Finally the dollies were pulled apart using an *Instron* pulling set-up at a speed 0.06 mm/min. The force and displacement of the pulling dollies necessary to separate the two PET films was registered so the fracture stress was easily calculated from the area occupied by the layer of ink. Among all the tested devices, we selected 13 representative samples for the non-plasma treated substrate and 6 for the plasma treated substrate.

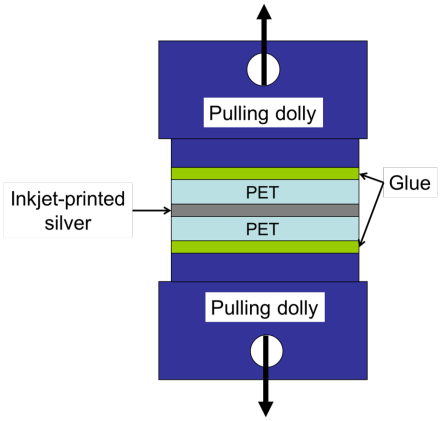

Figure 3.8: Sketch showing the distribution of layers for one sample of the tensile pull test, performed to assess the adhesion between PET substrate and inkjet printed silver ink [117].

3.4.2 Evaluation of the sensor geometry

After their complete fabrication, the devices geometry was evaluated using an optical microscope and a scanning electronic microscope (*ESEM XL 30 FEG* working at 2.0 kV). The profile and thickness of the metallic lines and the sensing layer were analyzed using a white light interferometer (*Wyko NT 110* from *Veeco*) and an alpha-step system (from *Tencor*). The resistivity of the lines was obtained from their geometry and resistance, which was measured by means of the four wires method to eliminate the probes and contacts parasitic resistance.

3.4.3 Humidity measurements

For static measurements (capacitance versus R.H.), I used a climatic chamber (Bench-Top Temperature and Humidity Chamber, *Espec*) able to reproduce controlled temperature and humidity conditions with a precision of 0.5°C and 2% R.H. respectively. The climatic chamber was larger and more user-friendly than the customized chamber. Therefore, although it facilitated the handling and connection of the devices inside, its stabilization time was too large to permit transient measurements.

The transient response of the capacitive sensors was tested against changes in the humidity level. For that purpose, the devices were first degassed at 85 °C under vacuum conditions for 4 h. This step served to desorb residual gases trapped in the sensors, providing a reliable starting point for differential measurements. Then, the devices were connected to the electronic measurement equipment via a special connector (*39-53-2144 - Socket FFC/FPC, ZIF*, 1.25 mm, 14 way from *Molex*) suitable for clamping foil-shaped devices. Finally, for dynamic transient measurements the sensors were introduced in a customized humidity measurements set-up, which allowed for the automatic control of wet and dry airflow inside a small gas chamber at room temperature. The small size of the chamber (~ 170 ml) allowed a quick stabilization of the R.H. conditions inside the whole chamber. The total air flow was 500 ml/min.

Two LCR-meters (*HP 4284L* and *Agilent E4980A*) were used to measure the corresponding capacitance values after every 5 to 7 s. at the same time that R.H. and temperature values were registered by a commercial sensor (*Sensirion SHT15*). The data points were then stored using a PC interfaced with a GPIB cable and a LabView program. The employed frequency, 100 kHz, was easily compatible with standard read-out equipment [31, 50], and was not too high to hinder the polarization of the dielectric layers of the structure. Post-measurements data treatment was carried out with a PC to obtain differential values of capacitance.

3.5 Results and discussion

3.5.1 Adhesion between printed silver and substrate

Figure 3.9 shows the optical picture of two representative samples of PI and PET, pre-treated or not with oxygen plasma, after the first adhesion test (*ASTM F 1842-09*) was performed. This method did not give a quantitative value of adhesion strength, but it was valid for a qualitative comparison between the different cases of study. It can be observed that when applying the adhesive tape to the PI substrate, some damage appeared on the surface of the metallic layer. This surface damage seemed to be independent of whether or not the substrate was previously treated with oxygen plasma, and it corresponded with the classification 2B of the standard. Hence, oxygen plasma pre-treatment on the PI substrate did not improve the adhesion performance. On the other hand, when performing the same test on PET substrate, the metallic surface did not present any modification or damage, demonstrating that the adhesion of the sintered silver ink on PET was significantly better than on PI. No differences

between plasma treated and non-treated PET samples were observed in this first test neither.

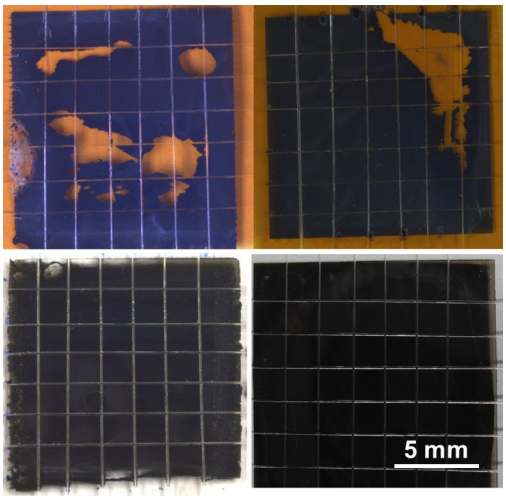

Figure 3.9: Optical pictures of (top) polyimide and (bottom) PET samples after adhesive tape test was performed to evaluate the adhesion strength between the substrate and the silver layer. Two different cases were considered, substrate pre-treated (on the left) and no pre-treated (on the right) with plasma oxygen, yielding similar peeling results. In the case of PET, the good adhesion prevented the observation of any damage on the metallic surface [117].

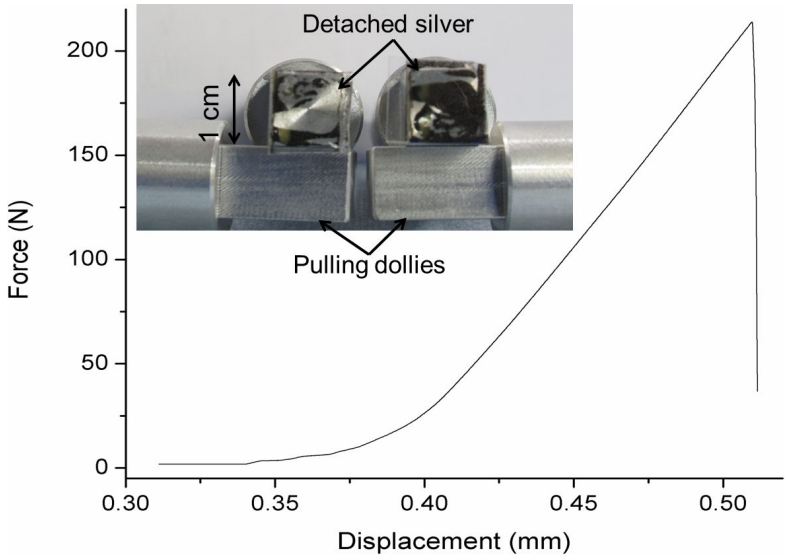

Figure 3.10: Graphic of force versus displacement for an adhesion test measurement in which two samples of PET were stuck together by a layer of sintered silver ink and then, tensile pulled apart until they separated. In this graphic, the fracture point corresponds with a displacement of 0.5 mm at an applied force of 214 N. The inset shows the optical picture of the inner surfaces of two PET foils after they split apart in the pulling machine. We can observe how the ink was detached almost completely from either of the two foil surfaces indistinctly [117].

The second adhesion test used for PET substrate consisted of a tensile pulling test. Figure 3.10 shows the curve "pulling force versus displacement" of a PET/*DGP 40LT-15C* silver/PET sample until splitting in the interface PET/silver occurred. The inset of Figure 3.10 is an

optical picture showing the inner surfaces of two PET foils after they were split apart in the pulling machine; the foils are stuck to the pulling dollies. We can observe how the silver was detached almost completely from either of the two foils surfaces indistinctly. The total area covered by the detached silver layer should ideally be the same as the area of the printed ink onto the substrates, i.e. 1 cm^2. However, this area was usually smaller for many of the samples, indicating that at some spots the two foils separated at the middle of the metal layer instead of at the interface PET/silver. Because the values of fracture stress provided hereafter were calculated considering the totality of the printed ink area, they might be underestimated. Nevertheless, this method remains suitable as a first quantitative approach and for comparison between cases of study. The results showed that the plasma treatment did not improve the adhesion of the printed silver on the PET substrate: the final mean tensile fracture stress was 2.4 ± 0.4 MPa for the treated substrate and 2.4 ± 0.1 MPa otherwise (standard error of the mean). To statistically confirm this result, a t-test was performed for the two ensembles of data (plasma treated and untreated PET), which happened to be normally distributed. The result of the t-test (assuming different variance for every ensemble) was 0.981, confirming that all the samples belonged to the same population with a certainty of 98.1%.

3.5.2 Fabrication of standard IDE capacitors

Using the optimized printing parameters described in Section 3.3.2, we got standard IDE printed on PET with a minimum line width and gap size of 95 ± 3 µm and 105 ± 3 µm, respectively (see Figure 3.11), with a line thickness of about 180 nm. The coffee ring effect [93–95] was decreased significantly with the addition of the second printed layer of ink as depicted in 3.12(b). The achieved resistivity was approximately 100 µΩ*cm. Despite the fact that microwave oxygen plasma treatment did not help to improve the metal-to-substrate adhesion (see Section 3.5.1), it showed advantageous results in improving the smoothness of the lines edges (see Figure 3.12(a)).

Afterwards, we successfully accomplished the electrodeposition of IDE with thickness ranging from ~100 nm to 15 µm on PET and up to 5 µm on PI. This limitation in thickness was due to the increasing stress induced in thick layers, which eventually forced the metallic lines to delaminate from the substrate. The better adhesion between printed silver and PET substrate (see section 3.5.1) permitted the growth of thicker layers of Ni on PET than on PI. We chose 1, 5 and 10 µm as representative values of thickness for the evaluation of the fabricated IDE structures. Figure 3.12(c) is a micrograph, obtained by the secondary electron detector of a scanning electronic microscope (SEM), presenting a capacitor line after electrodepositing 13 µm of nickel onto it. The rounded-shaped edges and irregularities on the surface of the device resembled the typical shapes found on the original printed structure, despite the coffee ring effect was significantly reduced. This fact suggests isotropic growing of nickel along the three directions. Figure 3.12(d) depicts the profile of another electroplate line of ~ 1 µm thick, obtained with a white light interferometer. Once 1 µm thick layer of nickel was electrodeposited on the silver lines, their resistivity was about 14 µΩ*cm. This resistivity is

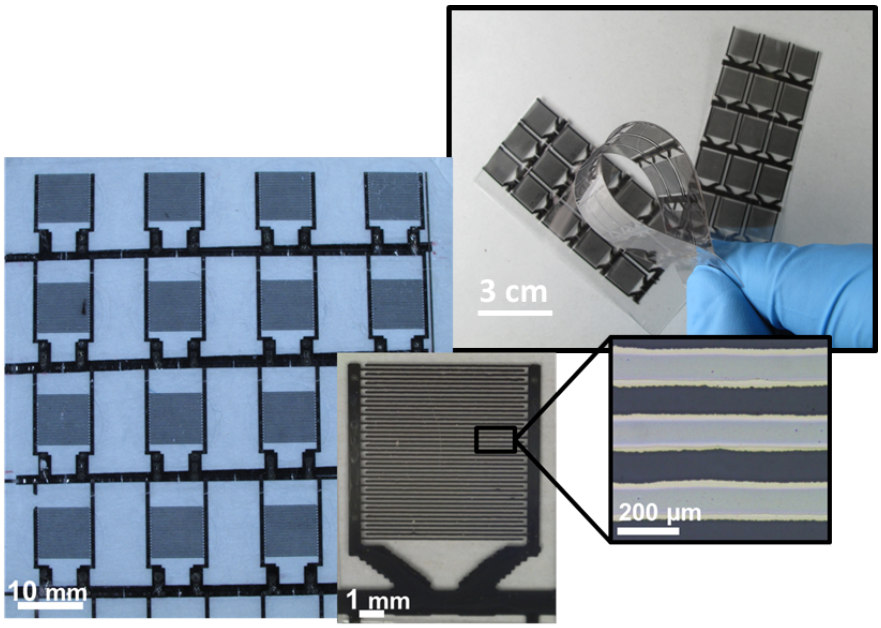

Figure 3.11: Optical pictures of flexible arrays of silver inkjet-printed IDE capacitors on flexible PET foil, and magnified views of a similar device and its electrodes. The devices in the array were short circuited to allow the subsequent electrodeposition step. The electrodes width and pitch are 95 ±3 µm and 105 ±3 µm, respectively.

close to the one of thin film nickel [144].

The capacitance value of the different fabricated devices was presented in Figure 2.8 in Section 2.3.1 and they were 5.41 ± 0.72 pF for ~0.92 µm-thick electrodes, 5.87 ± 0.50 pF for ~5.2 µm-thick electrodes and 5.95 ± 0.34 pF for ~8.75 µm-thick electrodes.

3.5.3 Fabrication of IDE capacitors with parylene interlayer between combs

Different IDE capacitors were successfully fabricated on flexible PET foil with a dielectric parylene-C layer between both capacitor polarities. As expected, even when both electrode combs overlapped due to printing defects (see Figure 3.13), the combs were not electrically in contact so the devices remained fully functional and conserved their capacitive nature. The geometry and resulting capacitance values of the different fabricated devices are shown in Table 3.2. Note that the experimental geometry was very similar to the expected one, summarized in Table 3.1 in Section 3.2, evidencing a relative good control during the fabrication process. Figure 3.14 consists of optical pictures of the devices at two different fabrication steps: right after parylene deposition, where only one comb was printed; and after aligning and inkjet printing the second comb onto the parylene layer.

Figure 3.15 (a) was already used in Chapter 2, Section 2.3.2 to validate the theoretical model used to calculate the capacitance of IDE with parylene interlayer. Since it contains the data

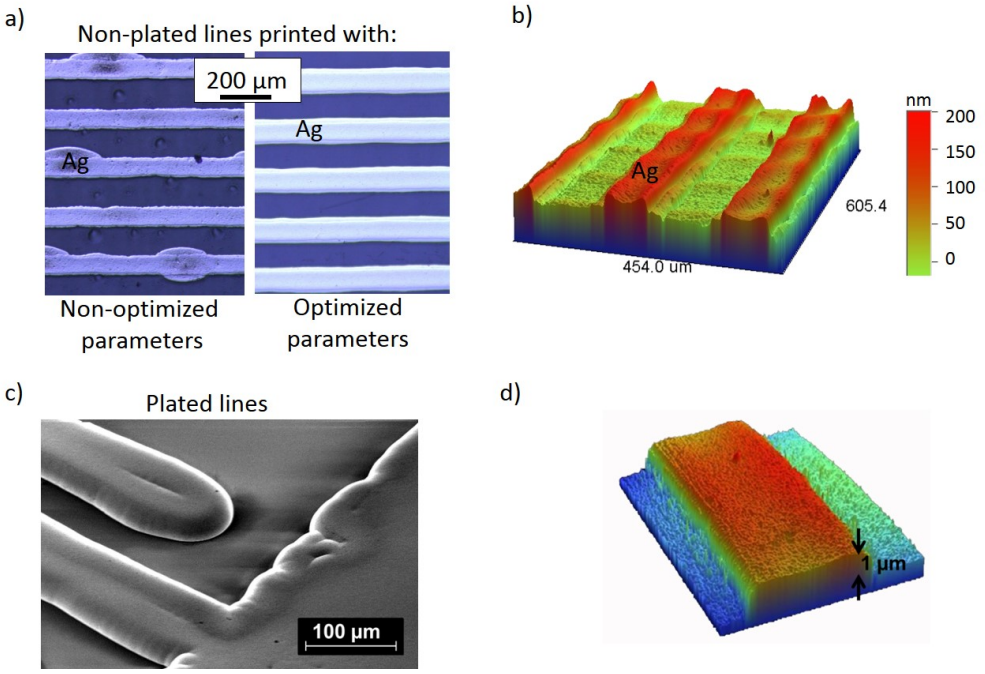

Figure 3.12: (a) Difference between the edge of lines printed with optimal and non-optimal parameters. (b) White light interferometer-obtained image of printed lines. The reduced but still present "coffee ring" effect is visible.(C) Micrograph (obtained by secondary electron detector of a SEM) presenting a printed device electroplated with 13 µm *of nickel. (d) Image of an electroplated capacitor line around 1* µm *thick obtained with the interferometer. The width of the line is around 100* µm *[117].*

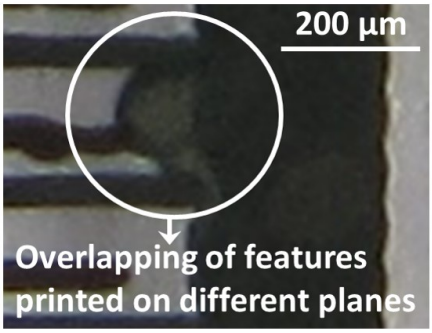

Figure 3.13: The overlapping of two electrodes with different polarity due to a typical printing defect. This situation would normally shortcircuit the device, but it did not affect the functionality of this capacitor because the two different polarities were insulated by a thin layer of parylene-C [118].

summarized in Table 3.2, the graphic is presented here again to demonstrate the potential of the exposed fabrication method to increase the capacitance value per surface area of inkjet printed IDE devices. Such value got an enhancement of 4 folds for non overlapping electrodes and a factor 15 for overlapping electrodes, compared to the IDE with 120 µm pitch (case "E" of Table 3.2) which was the closest geometry to the standard IDE. But the potential of the method reaches even further: according to the theoretical estimation, if we were able

Table 3.2: Different IDE fabricated with reduced size with their experimental geometrical parameters and capacitance value.

Device	Pitch (μm)	Gap 1^{st} comb (μm)	Gap 2^{nd} comb (μm)	$C_{experim}$ (pF)	C_{theory} (pF)
A	40 ± 1	43 ± 3	Overlap: 7 ± 3	15.3 ± 0.7	-
B	60 ± 3	81 ± 6	12 ± 7	4 ± 2	4.24
C	81 ± 3	124 ± 7	34 ± 8	2.1 ± 0.2	2.23
D	99 ± 4	160 ± 8	52 ± 9	1.5 ± 0.1	1.56
E	120 ± 2	201 ± 4	73 ± 6	1.18 ± 0.04	1.15

to achieve non-overlapping electrodes with gaps as small as 1 μm, it could be possible to enhance the capacitance value per surface area to almost a factor 10. The theoretical curve in the graphic was obtained including the measured geometry of the devices: the electrodes were considered bidimensional (they were about 200 nm thick); the width of the bottom electrodes, printed on PET, was measured and its mean value was 38 μm with a standard deviation of 2 μm. On the other hand, the top electrodes, printed on parylene-C were 56 ± 4 μm wide. The inter-layer of parylene-C between combs was 1.8 ± 0.4 μm. The electrical permittivity at the frequency range of interest (around 100 kHz) for the parylene-C layer was considered 3 and the one for the PET substrate 2.9, according to the fabricant. The model fit very well the experimental values for every geometry except for the devices with smallest pitch, labeled as "A". The reason is that for "A"devices, there is overlapping between bottom and top electrodes, making impossible the theoretical estimation with the model described in 2.3.2. Figure 3.15 (b) shows a series of optical pictures of the top and both electrodes combs for each geometry. Even though the positioning reproducibility of the utilized printer was rather poor, ± 25 μm, I managed to have a proper alignment of the top comb after few trial-and-error iterations for the printing head placement, in combination with the implementation of the thermal scaling option mentioned in the Section 3.3.2. For a less manual process, other commercially available printers could be used, offering better alignment of about ±5 μm as it is the case of the *Dimatix™DMP3000* or even ±3 μm achievable by the printers *Ceradrop X-Serie* or *PIXDRO IP410*.

3.5.4 Tuning CAB sensing layer for inkjet printing deposition

CAB has been inkjet-printed onto the printed capacitive structures and worked as the sensing layer. In order to obtain an inkjet printable solution, different concentrations of CAB were dissolved in hexyl acetate. According with the manufacturer of the inkjet printer, the surface tension and the viscosity of a printable fluid need to be in the ranges 28–33 mN/m for the former and 10–12 cP for the latter. The surface tension of the CAB solution was measured and it did not show significant dependence with concentration, its value being always 26.2 mN/m. On the contrary, the measured viscosity value of the solution depended on the CAB concentration as depicted in Figure 3.16. An empirical fit has been applied to the experimental

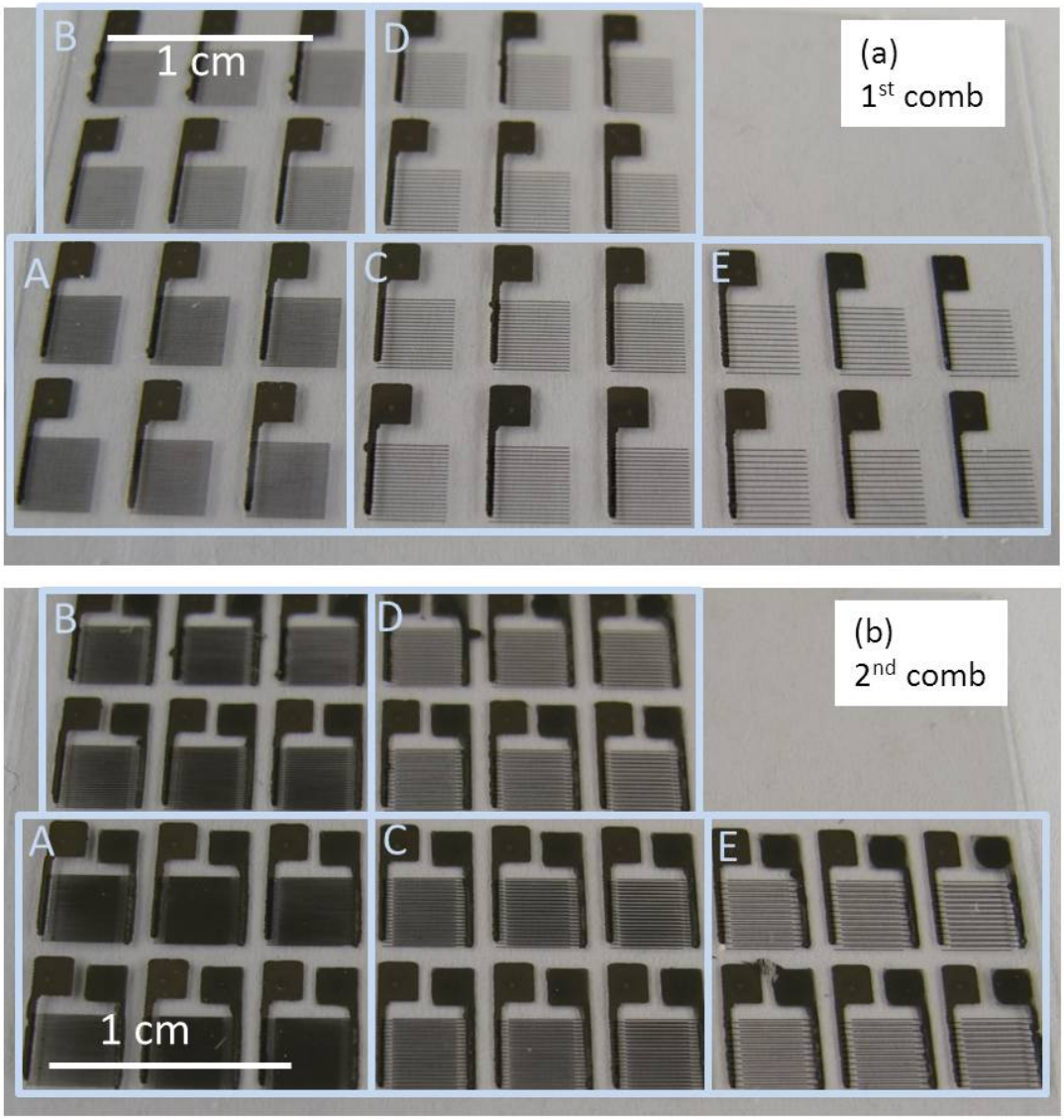

Figure 3.14: Optical picture showing an array of devices with the different geometries described in Table 3.2, at two different fabrication steps: (a) After printing the bottom electrodes comb on PET substrate, and (b) after printing the top comb on parylene-C [118].

data points, giving the following relation:

$$\nu = 2.104e^{0.0969C} \tag{3.1}$$

where ν is the dynamic viscosity of the solution, C the concentration of CAB and the constant 0.0969 has units of liter/gram. According to the fitting on Figure 3.16, the concentration of the CAB ink chosen for inkjet printing the sensing layer should be ~16.25 g of CAB per liter of solution, corresponding to a viscosity of 10.17 cP.

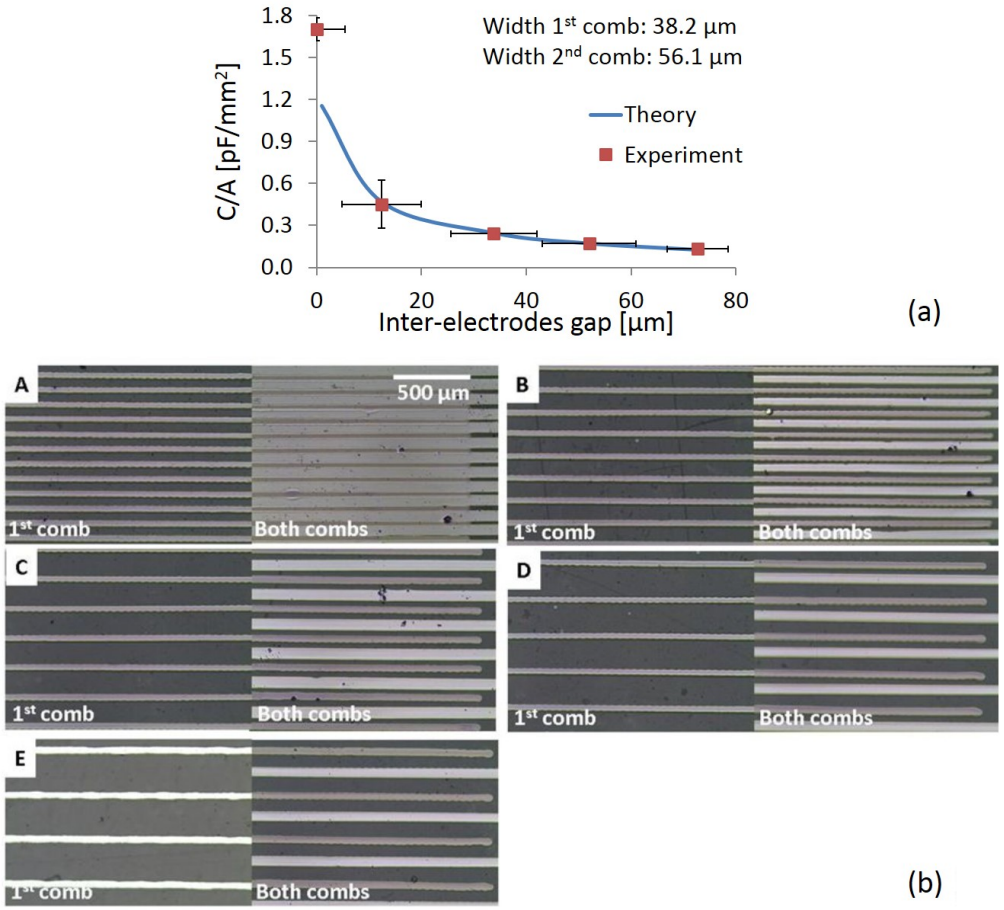

Figure 3.15: (a) Comparison between theoretically estimated and measured capacitance per surface area versus inter-electrodes space. (b) Optical pictures of only the bottom, and both printed combs for every different printed geometry [118].

It is possible to estimate the contribution to the total thickness made by every single layer of printed ink. For this calculation, we can assume that the substrate surface area equivalent to d^2, being d the drop-to-drop space, is occupied by the volume of one single drop of ink, V_D (or four quarters of drop as sketched in the inset of Figure 3.17). This assumption allows making calculations without knowing the total surface area of the layout [145]. However, it requires the surface of the layout to be large enough to neglect the inaccuracy provoked by ink spreading at the edges of the patterns. The thickness of the dry sensing layer corresponding with one printed layer of ink comes then from the next expression:

$$h_{s,1layer} = \frac{V_{CAB}}{d^2} = \frac{CV_D/\rho_{CAB}}{d^2} \tag{3.2}$$

where V_{CAB} is the volume of dry CAB existing over a certain surface d^2, V_D is the volume of one single drop of ink, C is the concentration of CAB in the ink and ρ_{CAB} is the density of dry

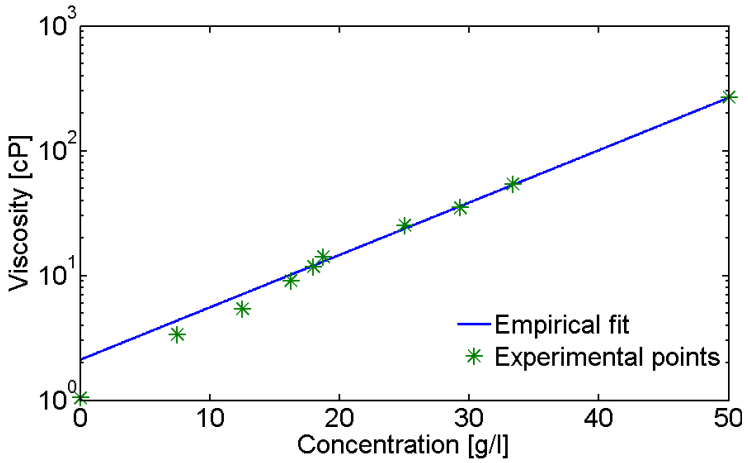

Figure 3.16: Variation of the viscosity of the CAB solution with CAB concentration (experimental points and empirical fit [117].

CAB. Substituting the parameters in the equation above for the following numerical values: 20 µm drop-to-drop space, 10 pl drop volume, 16.25 g/l concentration of CAB in the ink and 1.25 g/cm^3 density of CAB; $h_{s,1layer}$ resulted 325 nm. Figure 3.17 presents the sensing layer thickness against the number of printed layers, assuming that the thickness of every single layer adds up linearly. Experimental data corresponding with the average thickness of several coated devices are also included in the same figure along with their standard error with a 95% of confidence. Both experimental and theoretical data matched well overall.

3.5.5 Humidity measurements

As discussed in the introduction, although the fabricated devices could be readily used as gas sensors using only their polymeric substrate as sensing layer, the lack of optimization of the substrate for sensing applications would lead to poor performance in terms of sensitivity and response time. Therefore, the IDE were coated with an appropriate gas sensitive layer. For the sake of simplicity, we functionalized the devices for relative humidity (R.H.) detection by inkjet printing a test sensing layer of CAB. After the sensing layer deposition, the sensors experienced an increase in their nominal capacitance of ~8% and larger sensitivity to R.H. In this section, I review the response of the different fabricated IDE capacitive sensors against changes in R.H. at room temperature. First I will show the behaviour of standard IDE devices, their stabilization by electroplating and the improvement of their signal by using differential methods. Then, I will present the R.H. sensing response of the IDE sensors with decreased size and parylene interlayer, highlighting their sensing advantages.

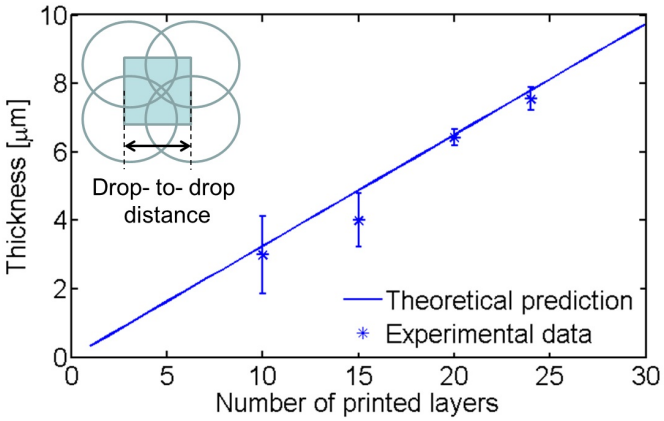

Figure 3.17: Dry sensing layer thickness versus number of printed layer, theoretical model and experimental data averaged from different measured devices. The inset is a top view sketch showing the substrate surface area occupied by a printed ink drop [117].

Standard plated IDE devices: Single mode operation

Sensors based on IDE electroplated with 1 µm of nickel were measured under different humidity steps (from 20 to 80% R.H.) obtained directly from the wet and dry air flow balance into the chamber. The R.H. level were programmed to change every 25 min. Both, uncoated and coated (with 7.5 ± 0.4 µm thick CAB layer) capacitors reacted to these changes in humidity as depicted in Figure 3.18. In Figure 3.18 (a), it is shown the static behaviour of the sensors (capacitance versus R.H.). It can be observed that, as expected, the coated device supplied higher value and larger variations of capacitance. However, both sensors presented non-linear response and high hysteresis. This behaviour is associated to the slow response of the substrate, which is far from stabilization at the end of every R.H. step, as it can be seen in the transient response of the sensor depicted in Figure 3.18 (b). The output of the devices was normalized here to their nominal value of capacitance, C_0. The explanation for slow response of the substrate is found in its large thickness (and the large sensor spatial wavelength, $2(W+G)$, that rendered the most part of this substrate sensitive to the analyte). Considering the absorption of vapour molecules in the substrate layer as a diffusive-based process (see theory in Section 2.2 of Chapter 3), the thicker the absorbing layer, the longer the time it would require to reach concentration equilibrium with the ambiance. The 25 min-long steps used in this experiment were thus not long enough to attain the equilibrium of the water molecules inside the 125 µm-thick PET substrate. Quantitative predictions of the sensor response time would require a deeper study of the interaction between the analyte and the polymeric layers of the sensor and goes beyond the scope of this work. However, the sketch in Figure 3.19 aims at explaining in a qualitative way the evolution of the diffusion process: the cross section of an uncoated two IDE device is shown in three different relative humidity conditions at different moments. Arrows represent the net diffusion gas flux flowing through every virtual layer in the substrate. The diffusion flux in one dimension (the vertical direction z) is usually given by the Fick's first law of diffusion as

$J = -D\delta C/\delta z$, where D is the diffusion coefficient and C is the concentration of gas at every z point.

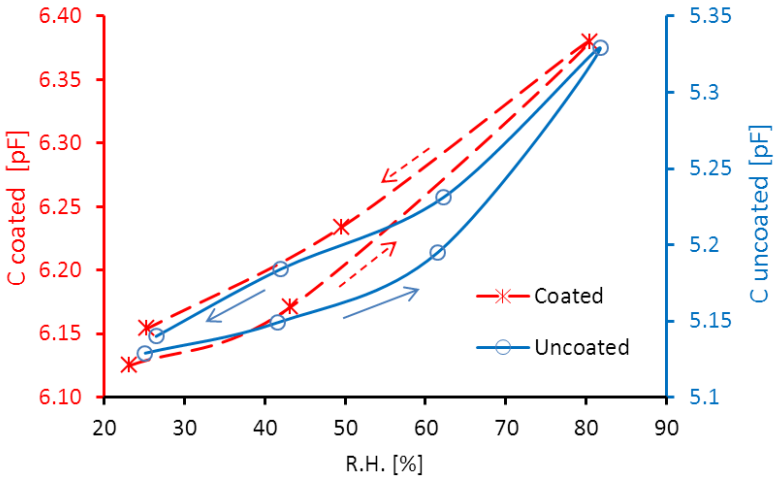

(a)

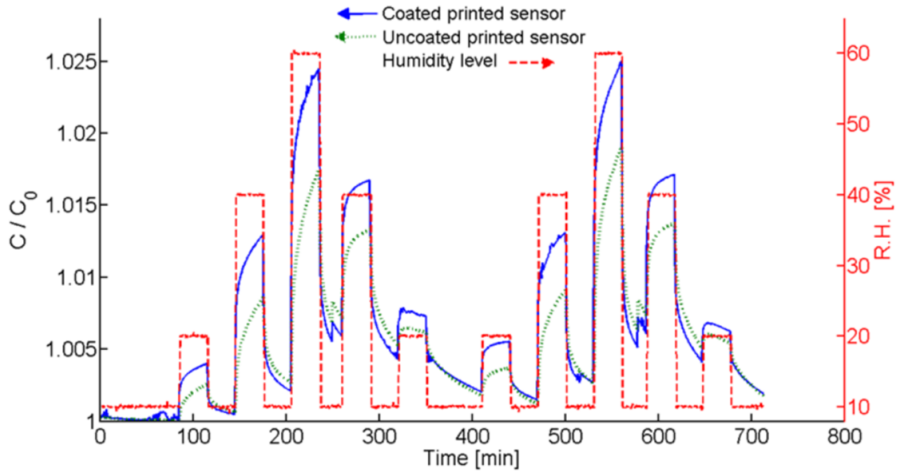

(b)

Figure 3.18: (a) Capacitance versus R.H. (up to 80% R.H.) for a pair of IDE capacitors (one uncoated and one coated with CAB) electroplated with 1 µm of nickel. It can be observed that as expected, the coated device supplied higher values and larger variations of capacitance. However, both signals are non-linear and present hysteresis. This behaviour is associated to the non-stabilization of the signal at the end of every step of R.H. observed in (b). (b) Transient response of the pair of IDE capacitors of (a) for different steps of R.H. The signal is normalized to the nominal value of capacitance C_0, and the values of R.H. (10-20-10-40-10-60-10-40-10-20-10%) are taken directly from the wet and dry air flow balance [117].

By analogy, in this example the number of drawn crosses represents the concentration C, and every layer in the substrate should be considered as having a infinitesimal thickness δz. The time step between every situation is too short ($t_{i+1} - t_i = \delta t$) to allow the equilibrium of gas concentration inside the whole substrate (considered infinitely thick), and only contiguous

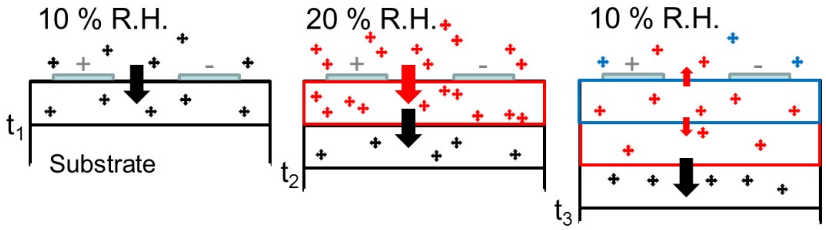

Figure 3.19: Sketch explaining the influence of the large substrate thickness in non-linear response and hysteresis phenomenon in the R.H. sensor output: the cross section of a small two IDE device is shown in three different situations corresponding to three different ambient relative humidity conditions at different moments. Arrows represent the net flow of gas flowing through every virtual layer in the substrate. The time step between every situation is too short to achieve the concentration equilibrium of gas inside the whole substrate (considered infinitely thick), and only contiguous layers interact at every time [117].

layers interact at every time step. This situation corresponds to the one sketched in Figure 3.18. At every time step, when changes in R.H. occur, only the most superficial layer (top layer) of the substrate reaches equilibrium with the ambiance. In the second situation, R.H. increases from 10 to 20%, the molecules in the top layer at time t_1 (black crosses) continue diffusing into the substrate while the top layer reaches a new equilibrium with the outside (following Henry's law) at t_2 (red crosses). It is possible to observe at this point that the total number of molecules around the electrodes plane at 20% R.H. exceeds the double of molecules at 10% R.H., which justifies the faster-than-linear increase in capacitance shifts presented in the first steps of Figure 3.18. In the last situation, the R.H. comes down to 10%; "black crosses" are not affected for this change so they continue their diffusion into the substrate whereas "red crosses", in the top layer at t_2, simultaneously diffuse inside the substrate and flow outside the device to reach equilibrium with the ambiance. Counting the crosses around the electrodes at time t_1 and t_3, it is easy to realize than even though R.H. is 10% in both cases, the number of crosses is higher at the last moment. This effect can explain the hysteresis phenomena and is also observed in Figure 3.18. It is straight forward to expand the same reasoning to the situation in which a sensing layer is placed on the substrate. For this scenario, the electrodes plane would lie underneath this first layer, making the shift of capacitance slower at the beginning, when the analyte is far from the electrodes, and accelerating it progressively as the analyte approaches the electrode plane. After this point, the process would present an analogous behaviour to the above described.

Standard plated IDE devices: Differential mode operation

As it has been explained, the large thickness of the substrate involves very high stabilization time and masks the actual contribution of the thin sensing film. Differential measurements, in which the signal of an uncoated device, C_0, is subtracted from the whole sensor signal, C, can be used to solve this parasitic effect. Note that for the devices presented in this work, the printed sensing layer is thin enough to let us assume that the diffusion process of gas into

the substrate occurs as in the uncoated device, justifying the use of the differential method. Figure 3.20 shows differential measurements of capacitance, normalized to the differential nominal value $(\Delta C)_0 = (C - C_0)_0$. As before, the measurements were taken over time under different steps of humidity level ranging from 10 to 70%. Figure 3.20 (a) corresponds to a pair of non-electroplated devices. Despite the fact that the differential signal looks saturated and linear for low R.H. steps, it is not stable over time or at high R.H. levels. On the other hand, Figure 3.20 (b) shows the signal from the same devices presented in Figure 3.18, where 1 µm of nickel was electroplated on the electrodes. Despite the signal remaining noisy for high levels of humidity, an important improvement in stability could be observed.

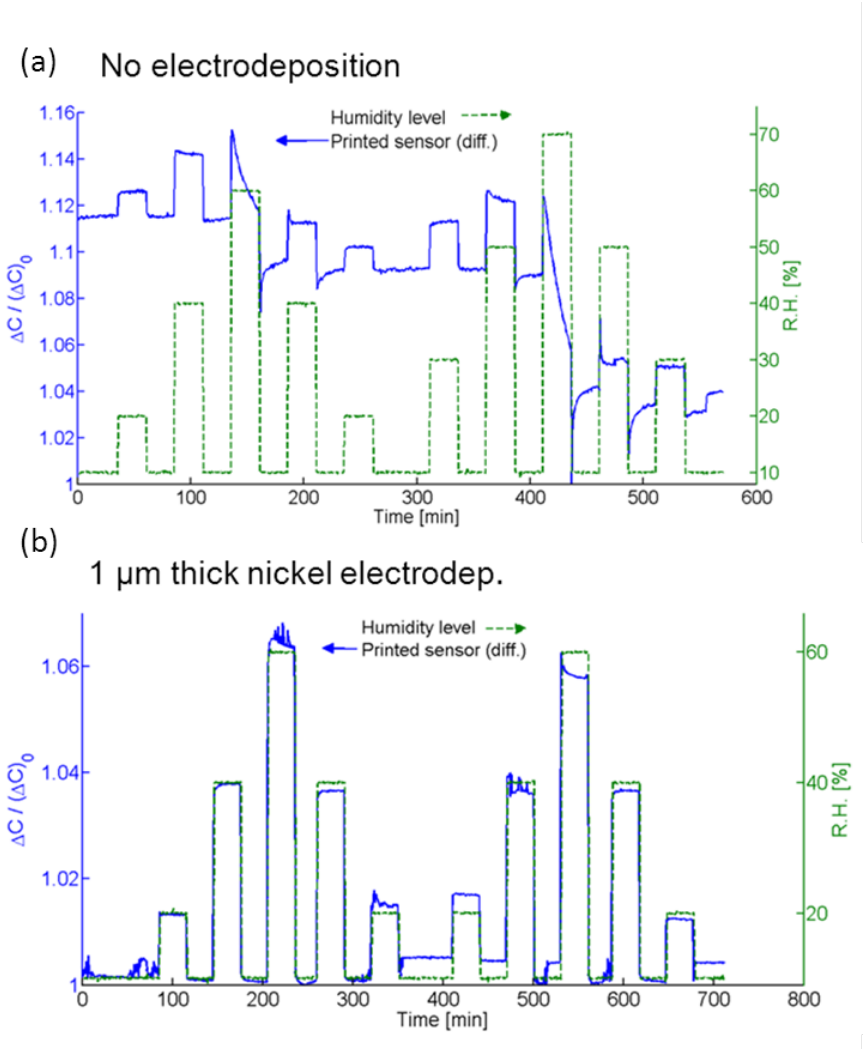

Figure 3.20: Differential measurement of capacitance normalized to the differential nominal value $(\Delta C)_0 = (C - C_0)_0$. *The measurements were taken over time under different humidity steps (from 10 to 70%) for (a) a pair of non-electroplated devices; and (b) the same devices presented in Figure 3.18, where 1 µm of nickel was electroplated [117].*

The sensitivity tested over different devices resulted 0.86 ± 0.07 fF per 1% R.H. (or equiva-

lently 0.078 ± 0.006% of $(\Delta C)_0$ per 1% R.H.) for bare silver electrodes; and 1.5 ± 0.3 fF (or 0.14 ± 0.03% of $(\Delta C)_0$ per 1% R.H.) for 1 µm thick plated nickel electrodes. The applied error is the standard with 95% of confidence.

Finally, we measured a last pair of devices with 5 µm-thick nickel electroplated layer. The sensor response is presented in Figure 3.21 and shows a high degree of stability over time and along different measurement cycles. The sensor signal was practically saturated and as a result, the linearity and stability of the sensor were sensibly improved. In this case, the output of the printed sensor is presented along with a commercial sensor (see experimental in Section 3.4.3) and the performances are comparable. The achieved sensitivity is 2.36 ± 0.08 fF per 1% R.H. (2.3 ± 0.5 fF / 1% R.H. for several measured devices) corresponding with 0.216 ± 0.007% of $(\Delta C)_0$ = 1.09 pF per 1% R.H., or 0.040 ± 0.001% of the nominal value C_0 = 5.87 ± 0.25 pF per 1% R.H. The applied errors were again the standard with 95% confidence. The coefficient of linearity was 0.9971. The hysteresis was calculated from the maximum mismatch encountered between increasing R.H. steps (represented as "up" in the figure) and decreasing R.H. steps (representing as "down" in the figure) data; its value was found to be less than 4.4 fF or 0.4% of $(\Delta C)_0$.

The final response time, associated with the absorption process, was calculated according to the equation 2.13 described in Section 2.2 of Chapter 2, corresponding with the 63% of the maximum value of capacitance (reached at equilibrium) for every increasing step of R.H. shown in Figure 3.21 (a), and is equal to 24 ± 3 s (standard error with 95% confidence). Equivalently, we can define the response time for desorption, as the one corresponding with the 37% of the maximum value of capacitance for every decreasing step of R.H. Its value was similar to the absorption time, 22 ± 4 s. The response time can be defined as well in an alternative manner as the time necessary to rise from 10% to 90% of the stable maximum value of capacitance. In this case, both absorption and desorption time response resulted in ~4.5 min. In any case, apart from the dependence of the response time with temperature (the temperature is kept constant in these experiments), it also depends on the R.H. value (specially at high values of R.H.) through the activation energy term E_a in the diffusion coefficient D (see Equation 2.15). Nonetheless this dependence is neglected here because it is smaller than the range of error encountered for the response time τ. For more precision in the determination of τ, a faster sampling of time needs to be performed during the measurement of capacitance. The experiments leasing to the results in Figure 3.21 were realized between 10 and 70% R.H. Beyond this level, CAB loses stability as a consequence of the clustering of molecules of water in its interior. This problem has already been treated somewhere else [142] and solved by cross-linking the CAB [143].

Passivation of the printed silver electrodes with nickel could be a justification for the improvement in the stability of the electroplated sensors. Although this phenomenon is not totally understood and more studies are needed, we hypothesize that when the printed electrodes are in direct contact with the ambiance, silver is likely to interact with humidity, oxidizing and/or releasing some possible trapped organic residual from the ink. Further

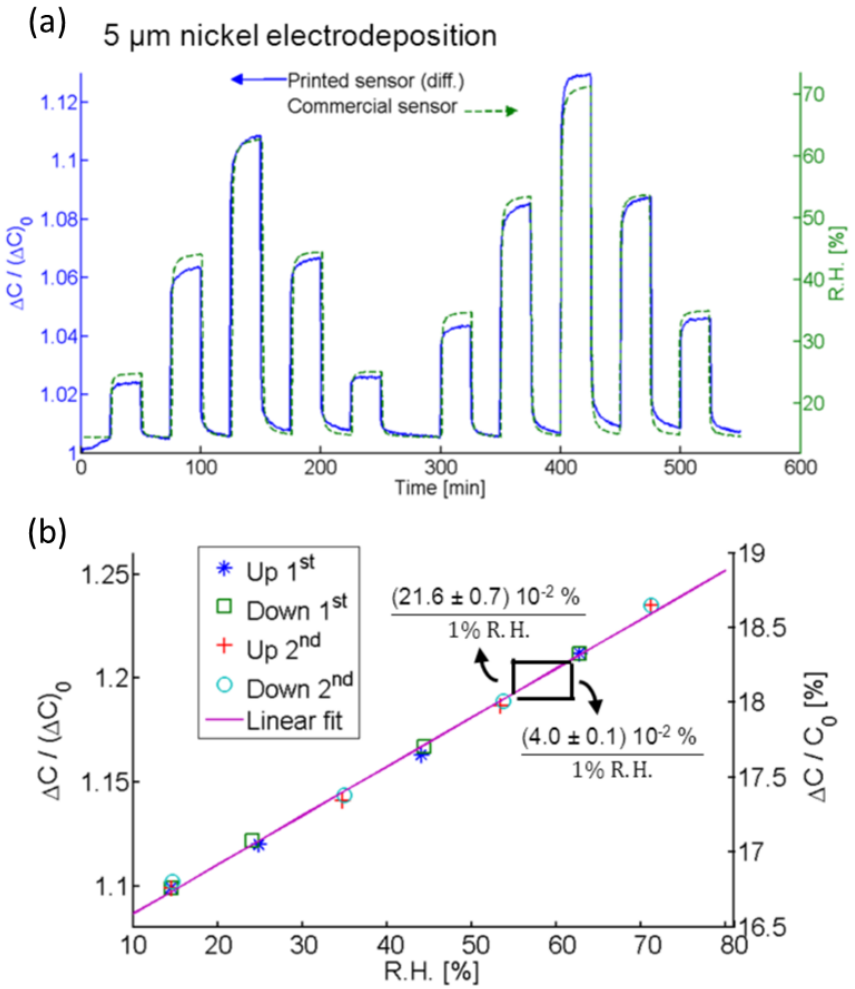

Figure 3.21: a) Differential measurement of capacitance normalized to the differential nominal value $(\Delta C)_0 = (C - C_0)_0$ *versus time. Measurements were taken at room temperature for a device with 5 µm-thick layer of nickel over a period of time divided into two cycles of different humidity steps (from 10 to 70%). In this case, the output of the printed sensor is presented along with a commercial sensor. (b) Normalized differential values of capacitance against R.H. "up" ("down") stands for increasing (decreasing) humidity level.* 1^{st} *and* 2^{nd} *indicate the measurements cycle. The slope of the line gives the normalized sensor sensitivities corresponding with every axis [117].*

studies made on similar IDE structures in collaboration with the Institute of Physical Chemistry from the University of Tübingeng in Germany [140], demonstrated that the stability of the devices could be improved by extra annealing, supporting the hypothesis of the presence of organic residual trapped into the silver ink. In any case, the stability of IDE has been studied only for the short-term. In the long-term, plating could prevent oxidation and migration of silver in presence of water. Indeed, I observed oxidation and change in colour of non-plated IDE after some months in ambiance conditions while the devices plated with Ni did not show any sign of oxidation or deterioration. Besides, extra stiffness provided by a thicker metal layer

could reduce strains arising on the electrodes plane due to polymer swelling at high humidity levels. Since the printed silver layer is very thin and porous [101, 146], non-electroplated electrodes would result especially vulnerable to all these effects. Reviewing the performance of every device exposed above, we conclude that the absolute sensitivity (in farads) as well as the sensitivity relative to the baseline differential value, $(\Delta C)_0$, increased sensibly with the thickness of the electrodeposited layer. This would not be the case if we consider the sensitivity relative to the nominal value of the capacitor C_0, because C_0 would increase with the thickness of the electrodes faster than $(\Delta C)_0$, impeding the rising of sensitivity. In any case, it would be possible to drastically increase the sensitivity of the devices by reducing their size, making $W + G$ comparable to the thickness of the sensing layer, and this is exactly what I am addressing in the next section.

3.5.6 Single mode operation for device coated with parylene-C (reduced size)

In order to evaluate the performances of IDE with decreased size and parylene-C interlayer, and demonstrate their improved performances compared to the standard IDE, the sensors were measured in similar conditions. Figure 3.22 represents the steady state measurements (after sensors stabilization) of capacitance versus R.H. value up to 80%. The response was linear, with a coefficient of linear determination R^2 of 0.992 ± 0.012 up to 70% R.H. and 0.987 ± 0.012 up to 80% R.H.

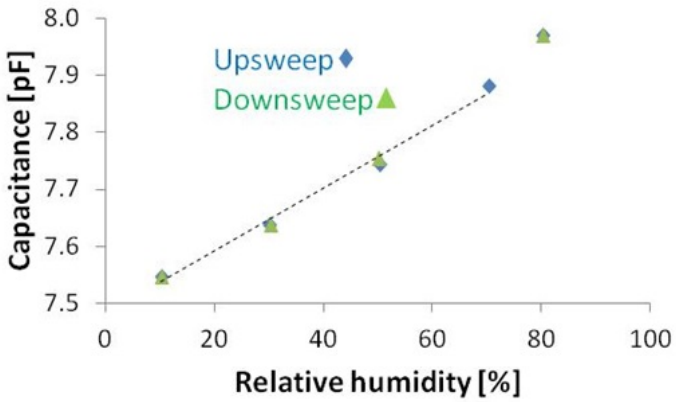

Figure 3.22: Steady state response of the capacitive humidity sensor for different upsweep and downsweep values of relative humidity, and linear fitting up to 70% R.H. [118].

The absolute sensitivity, obtained as the slope of the curve in Figure 3.22 is 5.5 ± 0.2 fF / 1% R.H., much above the 0.86 ± 0.22 fF / 1% R.H. (bare silver electrodes), 1.5 ± 0.3 fF / 1% R.H. (1 µm thick nickel electrodes) or 2.36 ± 0.08 fF / 1% R.H. (5 µm thick nickel electrodes) encountered in the the standard IDE devices with similar surface area represented in the previous Section. The relative sensitivity was 0.073 ± 0.003% / 1% R.H. for a nominal capacitance value of 7.548 pF, almost twice the value of standard IDE case (0.040 ± 0.001% / 1% R.H. of 5.87 pF). It can be observed that the hysteresis, i.e. the difference between the

R.H. upsweep and downsweep curves is negligible, making the sensor highly reversible. Figure 3.23 shows the transient behaviour of the sensor, which has been subjected to two different groups of increasing and decreasing R.H. pulses. The sensor response time, defined as the necessary time to move from 10% to 90% of the maximum stable signal during absorption, was found to be ~ 4.5 min (comparable to the response time of the standard IDE devices). Contrary to the case of standard IDE devices, the sensor was stable in time without the need of electrodeposition, probably due to the barrier effect that parylene-C has for the substrate, or to the extra annealing (3 hours instead of 40 minutes at 150 °C) of the silver patterns that favored their complete sintering and removal of any organic residual coming from the ink formulation [140]. Nonetheless, the top electrodes on non-coated samples, which were exposed to the air, showed oxidation after few months. Furthermore very long annealing times may not be suitable for some low heat resistant polymeric substrates, keeping the option of electroplating appealing for certain applications. The IDE sensors with parylene interlayer also came back well to the baseline value and presented reproducibility along the different pulses cycles to which it was subjected.

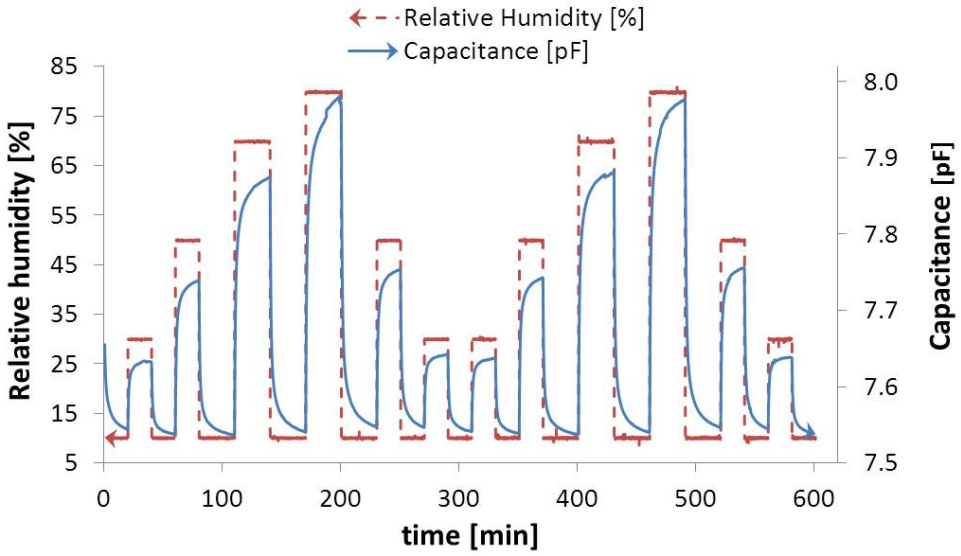

Figure 3.23: Transient response of the sensor (on the right axis) against two cycles of upsweep and downsweep pulses of relative humidity from 10 to 80% (left axis) [118].

3.6 Conclusions

As a conclusion of this chapter, capacitive-based humidity sensors have been fabricated on flexible foil by means of only additive methods. The sensors could be separated in two categories. The first category (standard IDE) consisted of an interdigitated electrode structure made of silver nanoparticles, inkjet printed on a PET substrate and electroplated with a thicker layer of nickel. The selected silver ink exhibited better adhesion performances on PET than on PI regardless of pretreatment with oxygen plasma, which was however useful to increase the

smoothness of the printed lines edges. In the second category of sensors (IDE with decreased size), I targeted the fabrication of IDE fabricated using similar technology but with decreased size and improved fabrication yield thanks to the introduction of a thin parylene-C film between both electrode combs. The parylene-C layer worked as electrical insulation, allowing printing very compact electrodes without any risk of shortcircuits. The value of capacitance per surface area obtained for devices with well aligned and non-overlapped electrodes was increased by a factor 4 compared to standard IDE, reaching a value of 0.45 pF/mm^2 for an electrode pitch of 60 µm and an inter-electrodes gap as small as 12 µm.

Afterwards, the potential of the aforementioned devices for sensing has been evaluated for relative humidity capacitive sensing, by inkjetprinting on top a test layer of customized CAB, whose electrical permittivity and thickness is sensitive to relative humidity. For the standard IDE I utilized another uncoated device as a reference for differential measurements of relative humidity in an atmosphere of air. An analysis of the working principle of the differential mode showed that differential measurements drastically improved the linearity and hysteresis of the sensor output, since they enabled the cancellation of the parasitic influence of the substrate, which is usually too thick to allow a quick stabilization of the sensor response. High sensor stability has been obtained only for nickel electrodeposited devices. Moreover, it is worthwhile to remark that electrodeposition on inkjetprinted patterns is a smart solution for the simultaneous fabrication of temperature and gas sensing platforms. The temperature sensor performance would also benefit from the electroplated layer. Chapter 5 addresses this point. This plating technology could also be used in general for chemicapacitors and chemiresistors, widening the choices of functional sensing materials and transducers able to discriminate different gases by using an array of printed gas sensors.

Last but not least, even though electrodeposition did not significantly increase the nominal value of capacitance, it also played a role in improving the relative differential sensitivity. In any case, further reduction of the device size would yield to an important increase in the sensor sensitivity and this is what I demonstrated with the IDE devices with decreased size. The improvement of the sensitivity is due to two reasons: increase of nominal capacitance per surface area, and maximization of the interaction between the electric field and the thin sensing layer. The characterization of the sensors in both steady and transient state offered devices with linear behaviour up to 70% r.h., stable and reproducible signal, and an improved absolute sensitivity of 5.46 fF/1% R.H. for devices smaller than the standard IDE. It is worth noting that the parylene-C layer acted at the same time as a passivation barrier for the substrate, lessening the need for differential mode measurements. The step electrodeposition for stabilization of the devices was substituted in the case of IDE with decreased size for extra annealing time of the electrodes [140]. However, we observed oxidation on non-plated lines after few months in contact with the air. Furthermore very long annealing times may not be suitable for some low heat resistant polymeric substrates, keeping electrodeposition or deposition of a second layer of parylene-C on printed lines interesting options for some applications requiring long-term use.

In future efforts, the width of the inkjet printed electrodes could be further decreased by using 1 pL ink drops instead of 10 pL, or alternative printing methods such as microcontact printing [87, 102] or hydroelectrodynamic inkjet printing [147, 147]. In the same way, the gap between electrodes could be even smaller than the 12 μm achieved in this thesis (see Table 3.2). In this case, the decrease in thickness of the parylene-C layer to few hundreds of nanometers should be needed in order to keep the validity of the model, which is perfectly feasible. The described technique could be applied for other kind of sensors, such as sensors for other gases or mechanical strain. In this work and for sake of simplicity, we functionalized our sensors for relative humidity (R.H.) detection with a test CAB sensing layer. However, the sensing layer can be optimized for R.H. by cross linking CAB [143], or its composition can be modified to sense other gases.

4 Inkjet-Printed Capacitive Humidity Sensors on Foil Based on Parallel Plates

4.1 Introduction

In this chapter, I present the realization and characterization of fully inkjet-printed gas microsensors on flexible plastic foil based on parallel plate (PP) capacitive structures. Two different structures have been developed: the first one is the standard PP capacitive gas sensor configuration where the gas sensing layer is "sandwiched" between the top and the bottom electrode [146]. The second one is based on a large array of PP-MEMS microbridges where the polymeric substrate act as swelling-driven sensing layer [148]. The differences between both structures and their advantages compared to prior works on capacitive sensors is highlighted and discussed.

Fully printed standard PP R.H. sensors The majority of capacitive gas microsensors reported in the literature are fabricated on rigid substrate and based on interdigitated electrode (IDE) structures [27–29]. The reason is that IDE structures are better adapted to CMOS process because they usually make use of only one metalization layer from the CMOS stack on top of which the specific sensing layer can be deposited during a simple post-processing step. The company *Sensirion* has commercialized sensors produced with such technology. However, in IDE structures, the electric field lines pass trough the insensitive substrate, creating a capacitive contribution in parallel to the contribution from the sensing layer that seriously degrade the sensitivity of the device. This phenomenon was explained in [122] where the authors proposed to use a parallel plate structure to increase the sensitivity of the humidity sensor. This sensor was also integrated in a CMOS stack where an empty layer was formed by etching between parallel conductive plates and filled afterwards with a polyimide sensing layer using inkjet printing through a small window on the top plate. They measured a sensitivity of 0.31% of change in capacitance per 1% relative humidity (R.H.). Nevertheless, the authors also encountered a high temperature sensitivity of the sensor of 0.19% $°C^{-1}$ and hypothesized

that unfilled regions within the sensing layer and deflection of the top membrane due to thermal expansion could be the reasons. The top electrode needed to be patterned to let the analyte reach the sensing layer and diffuse laterally, determining a sensor response of ~ 70 seconds. Other example of parallel plate humidity sensor involving a complex patterning of the top electrode was presented in [149]. The sensor was optimized for a fast response time of 1 second and had integrated a polysilicon heater to measure high levels of R.H.

The situation of gas sensors made on foil is similar in terms of the sense that the most commonly used geometry is IDE. Although some articles describe PP humidity sensors on foil [49, 50], the most part of the groups opted for fabricating IDE structures [1] to benefit from the easy deposition of the sensing layer and its full exposure to the analyte without complex top electrode patterning. However, the issue of the interaction of the electric field with the substrate for IDE described on silicon structures can be worsened when using plastic substrate. The reason is that polymers absorb gas in a similar way as the sensing layer does, so the contribution of the substrate to the total capacitance is not constant anymore, but varies with the presence of analyte. While this can be seen as an advantage in terms of sensitivity, the substrate is not always optimized for sensing so its sensitivity may degrade the sensor performances in terms of selectivity and specially response time. As mentioned in Section 3.1, the described situation is more critical for printing technologies where the patterning resolution is usually limited to ~ 100 µm. To eliminate this influence of the substrate, differential measurements have been successfully performed before in [31] and evaluated for printing devices in Section 3.5.5, yielding good results. However, they required an extra uncoated device as reference. Another approach evaluated in Chapter 3 to reduce the degradation of the sensor signal due to the substrate consisted of utilizing a thin sensing layer and a thick substrate passivated against moisture. Although the elicited two strategies were proven successful to obtain relatively fast sensors, they both yielded low sensor sensitivity. Another implication of using printed IDE structures is that they require many electrodes to get a reasonable nominal value of capacitance, resulting in large devices of several squared millimeters. PP capacitors could be used to eliminate the undesired interaction of the substrate on the sensor output because in this geometry the electric field lines are fully confined into the sensing layer between the electrodes (see Figure 2.1 in the introductory section of Chapter 2). This situation reverts also in a high sensitivity. Moreover, by reducing the thickness of the dielectric between the parallel plates, the nominal capacitance of PP structures is increased. However, the fabrication of fully printed PP structures is specially challenging due to usual chemical incompatibilities between the sensing layer and the solvent of the ink used to define the top plate electrode. This solvent can affect the sensing layer modifying its sensing behaviour. Even worse, the solvent of the ink can render the device non-operational by dissolving the sensing layer, creating electric paths between the top and the bottom electrode.

In the first part of this chapter, I demonstrate the fair chemical compatibility between the electrode ink and the sensing layer through the fabrication and characterization of fully inkjet-printed PP capacitive humidity sensor on PET foil (see Figure 4.1 (a)). It was also highlighted that the use of inkjet-printed PP structures for gas sensing drastically reduces the

patterning requirements for the electrodes compared to IDE geometries or PP fabricated by means of clean-room technologies. The reason is that the porosity and uneven surface of the inkjet-printed silver top electrode makes them non-continuous and permits the penetration of the analyte into the sensing layer, making unnecessary the patterning of complex combed electrodes or grids onto the sensing layer. This low demanding patterning resolution facilitates the miniaturization of the inkjet-printed sensors, very challenging for the case of printed IDE. Smaller devices have smaller footprint and involve less material usage. The utilization of inkjet printing allows the deposition and fine patterning of a broad range of materials in very thin layers, introducing significant improvements in the nominal value, sensitivity and response time of PP capacitive sensor. Finally, the printed sensing devices were characterized against pulses of relative humidity (R.H.) and their performances were analyzed. The fabricated devices, with a surface area as small as 1 mm^2, were able to supply a nominal capacitance value of around 3.5 pF and a offered 5 to 8 times better sensitivity than the IDE devices reported in Chapter 3 without the need of performing differential mode measurements or depositing moisture barriers on the substrate.

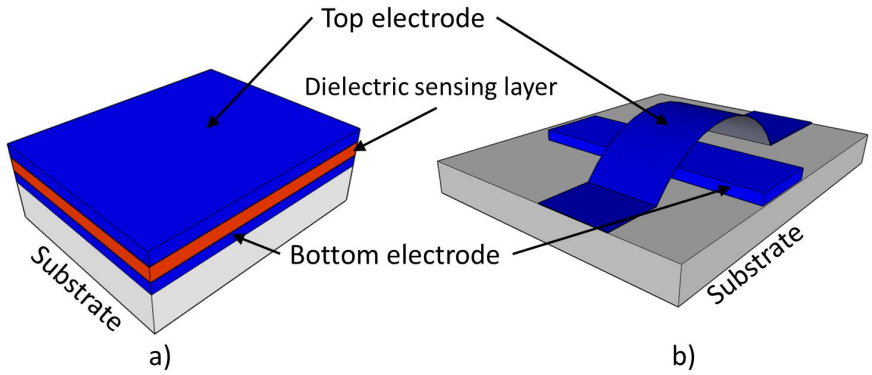

Figure 4.1: Sketch comparing a (a) standard and (b) a MEMS-based parallel plates capacitive gas sensor.

Fully printed PP-MEMS R.H. sensors In the second part of this chapter, I report on a second approach for capacitive sensing of R.H. consisting on the development of fully printed suspended MEMS microbridges on PET substrate. I call this devices PP-MEMS to differentiate them from the standard PP devices presented at the beginning of this chapter. Contrary to standard PP devices where the sensing operation is based mainly on changes in the permittivity and thickness of a sensing layer in the presence of gas, the PP-MEMS are based on a new working principle for gas sensing based on the swelling of the polymeric substrate which acts as the sensing element. This principle complements well the IDE and the PP sensors described in Chapter 3 and in this chapter since it shows no dependence with the analyte permittivity. While the former sensors are good to detect molecules with high permittivity (such as water), the second is more sensitive to large molecules that occupy more volume and induce higher swelling in the substrate.

In spite of the fact that inkjet printing on plastic substrate has been investigated as a promising technique to develop bi-dimensional and non-movable devices at high throughput, low-cost and large area, the technology has been barely exploited for surface micromachining of movable structures. Few previous works can be found where inkjet-printed movable microstructures were fabricated on rigid substrate: merely to characterize the mechanical properties of printed metals [86] or briefly presented as MEMS [85] without electrical characterization. Only very recently, in 2013, an inkjet-printed MEMS has been reported in [84], where the authors described the fabrication of cantilever-based switches through a relatively complex process involving also spin coating and the definition of via-holes. On the other hand, MEMS are gaining interest in the field of large-area or flexible systems due to the possibility to employ them in many new applications. In these scenarios, polymers need to be used as substrate material. For example, the fabrication of a "smart MEMS sheet" for the displacement of small objects on a flexible foil was recently presented by Prof. Fujita's team at the University of Tokyo [73]. However, these MEMS were fabricated using clean room processes which limit their realization on a large-area and increase their production cost. The application of printing techniques to the fabrication of large-area and flexible MEMS production has been introduced in a work combining inkjet-printed organic transistors with millimetric polymeric actuators on a large-area reported in [79, 150] by Prof. Someya's group at the University of Tokyo, for the fabrication of flexible ultrasonic systems. In that case, the inkjet printing was applied only to fabricate the organic transistors, but not the actuators.

In the second part of this chapter, I take advantages of inkjet printing to develop arrays of fully printed MEMS microbridges on polymeric foil through four steps, all of them occurring at temperature lower than 120 °C. As in the case of standard PP, the PP-MEMS devices were realized using a surface micromachining process based on inkjet printing of every necessary layer, sacrificial, electrical and structural. The geometry of the microbridges could be adapted through simple modifications in the printing layout and number of printed layers. Extra bridge stiffness was also obtained by electroless plating Ni on the silver printed bridge. Every microbridge was electrostatically deflected for characterization and finally their operation as capacitive sensors for relative humidity (R.H.) has been demonstrated. The application of the device as a capacitive sensor became possible owing to the high capacitance value of 1.5 pF provided by many microbridges connected in parallel. The PP-MEMS microbridges were arranged in arrays of 2 mm x 2 mm surface area formed by 80 individual microbridges of 120 μm x 80 μm size each.

Compared to a membrane-like device providing an equivalent capacitance, the array developed here finds advantages in terms of fabrication simplicity and mechanically robustness. On top of that, due to the small mass of every independent microbridge, the device would present smaller sensitivity to accelerations than a large membrane.

4.2 Fully printed humidity sensors on foil based on standard parallel plate (PP) structure

4.2.1 Design and theory of standard printed PP humidity sensor on foil

The geometry and design of the fabricated standard PP relative humidity (R.H.) sensors is depicted in Figure 4.4 (d). The devices consisted of a thin dielectric sensing layer "sandwiched" between two square-shaped electrodes. The bottom electrode is directly printed on the substrate whereas the top one is printed on the dielectric sensing layer. A grid was initially patterned on the top electrode as in [49] to let the environmental moisture to reach the sensing layer. This kind of standard PP sensor is named type I. In the section 4.2.3 below I demonstrate that the porous nature of the inkjet-printed silver along with the uneven profile of the top electrodes make unnecessary the top electrode patterning. Standard PP sensors with an non-patterned continuous top electrode were also fabricated for comparison and named type II sensors, simplifying the printing process and permitting the development of smaller devices. As it was stated in the introduction to the chapter, one of the biggest advantages of such PP devices is that the electric field is confined within the thin sensing layer between top and bottom electrode, making them insensitive to dielectric changes in the substrate. Therefore, the behaviour of the standard PP gas sensors is intrinsically different from that of interdigitated devices described in Chapter 2 and Chapter 3. Contrary to the case of interdigitated electrode capacitors, the calculation of the capacitance, C, of parallel plate capacitors is straight forward. If the surface area of the electrodes (plates) is A and they are separated by a dielectric of thickness h and dielectric constant (or relative permittivity) ϵ_r then:

$$C = \epsilon_0 \epsilon_r \frac{A}{h} \tag{4.1}$$

where ϵ_0 is the dielectric constant of the vacuum.

Applying Equation 4.1 to Equation 2.3 (Section 2.2 of Chapter 2), and combining with Equations 2.4 and 2.5 from the same section, it is possible to deduce the variation of the standard PP sensor capacitance in presence of gas (in steady state) by taking into account the two main physical effects occurring in the device: change in the dielectric constant and thickness of the sensing layer due to absorption of the analyte (see Figure 4.2).

$$\delta C = \frac{\partial C}{\partial h}\delta h + \frac{\partial C}{\partial \epsilon_r}\delta \epsilon_r \tag{4.2}$$

$$= -\frac{\epsilon_0 \epsilon_r A}{h^2}\delta h + \frac{\epsilon_0 A}{h}\delta \epsilon_r \tag{4.3}$$

$$= -\frac{\epsilon_0 \epsilon_r A}{h} Q\phi + \frac{\epsilon_0 A}{h}\phi[(\epsilon_a - 1) - Q(\epsilon_r - 1)] \tag{4.4}$$

where ϵ_a is the dielectric constant of the analyte in liquid phase (76.6 for water), ϕ is the volume fraction of the analyte in the sensing layer and Q is an experimental coefficient representing non-ideal swelling. Q can be considered close to 1 (ideal swelling) for rubbery elastic polymers like is the case of the cellulose acetate butyrate (CAB) polymer used as sensing layer in the presented device.

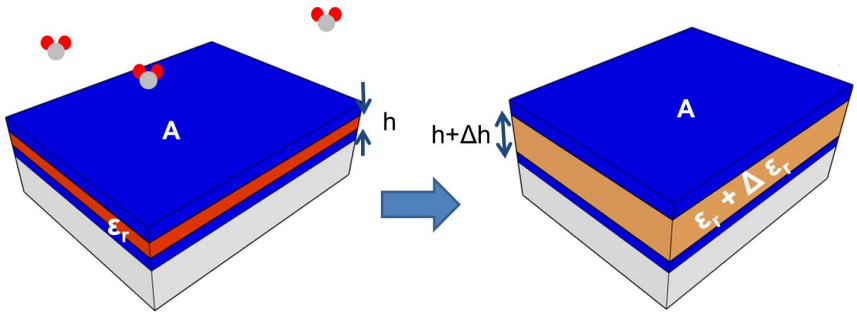

Figure 4.2: Sketch describing the working principle of standard parallel plate (PP) capacitive humidity sensors.

Making use of Equation 4.4, it is possible to plot the physical sensitivity $\Delta C/\phi$ against h for different values of ϵ_a and ϵ_r. The physical sensitivity refers to the normalized sensitivity of the sensor regardless the amount of present analyte, reflected in the term ϕ. ϕ affects equally the swelling an the dielectric constant contributions as it can be seen in 4.4. Figure 4.3 (a) shows the physical sensitivity for a dielectric constant $\epsilon_r = 3$, which is a typical value for polymers used as sensing layer like the CAB used in here, and for two different analytes with typical example values of permittivity $\epsilon_a = 1.5$ and 4 [29]. If a third analyte with $\epsilon_a = \epsilon_r = 3$ were plotted, only the swelling component would be present. In the same way, for an analyte of $\epsilon_a \simeq 6$, the dielectric and swelling components would cancel out and the analyte would appear as "transparent" for the sensor. It can be noticed in the graphic that the swelling component is independent of the analyte because the influence of the analyte molecular volume has been canceled by dividing ΔC by the volume fraction ϕ . It can be also observed that in general, the sensitivity increases for thin dielectric layers, which are also advantageous for reducing the sensor response time according to the theory stated in Section 2.2 of Chapter 2. The graphic in Figure 4.3 (b) shows similar results to the graphic in (a) but for the permittivity of water, i.e., $\epsilon_a \sim 80$, which corresponds to our experimental situation for R.H sensing. The dielectric constant of R.H. is so high that the swelling component can be neglected.

4.2.2 Fabrication of standard printed PP humidity sensor on foil

The fabrication process flow of the sensors is represented in Figure 4.4. It started with a polyethylene terephthalate (PET) foil, 125 µm-thick, *Melinex® ST506* from *Dupont Teijim Films* ™ that was cleaned with standard solvents: acetone, isopropanol and deionized water. The substrate was then dehydrated in a convection oven at 120°C for one hour. Afterwards, the bottom electrode was inkjet-printed using a *Dimatix DMP 2800*™ printer from *Fujifilm*

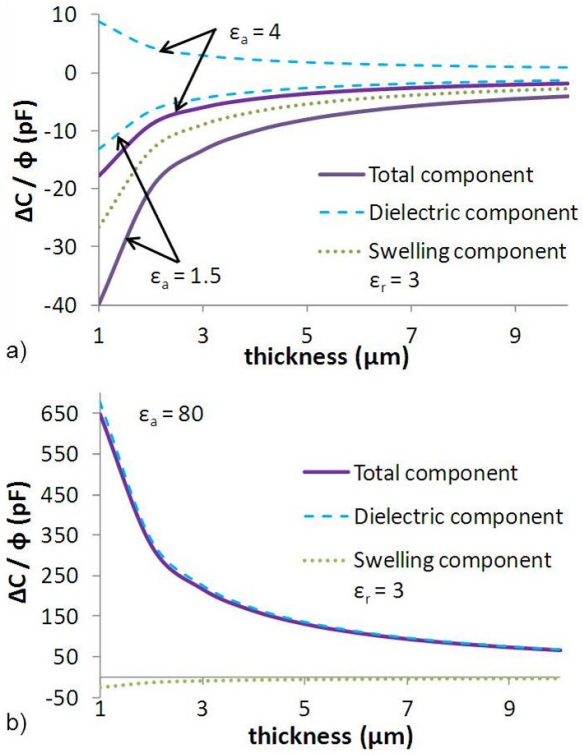

Figure 4.3: Theoretical estimation of the change in capacitance per analyte volume fraction against different thickness of the dielectric sensing layer for a) analytes with similar permittivity, and b) water [146].

with a 10 pl drops cartridge (see Figure 3.3 in Chapter 3) and nanoparticles-based silver ink *DGP 40LT-15C* from *Advanced Nano Products* (Figure 4.4 (a)). The silver ink was sintered in a convection oven at 150°C for 30 minutes. Figure 4.4 (b) shows the subsequent inkjet printing of the R.H. sensing layer of cellulose acetate butyrate (CAB) on the bottom electrode. The sensing layer was developed as in Section 3.3.3 of Chapter 3 and was dried in the oven for 20 minutes at 90°C. Finally, the top electrode was aligned with the bottom electrode and inkjet-printed onto the sensing layer as depicted in Figure4.4 (c). The silver of the top electrode was thermally sintered by introducing the device in the oven for 1 hour at 90°C. Such low temperature was adopted to not alter the properties of the CAB sensing layer.

Figure 4.5 shows different views of the PP R.H. sensors. Two kinds of configurations were fabricated: the type I included a grid patterned on the top electrode for gas intake and the type II possessed a continuous top electrode, without any patterning. The dimensions of the fabricated sensors were in agreement with the design excepting the width of type II devices, which resulted ~ 850 µm instead of 1 mm (see Figure 4.4 (d)). The CAB sensing layer was 7.5 µm-thick. Thinner sensing layer would be beneficial for sensitivity (Figure 4.3) and response time (Equation 2.14 in Section 2.2), but lead to fabrication yields problems as it is explained below. The resulting capacitance values at room temperature were 3.8 ± 0.2 pF (at 40%

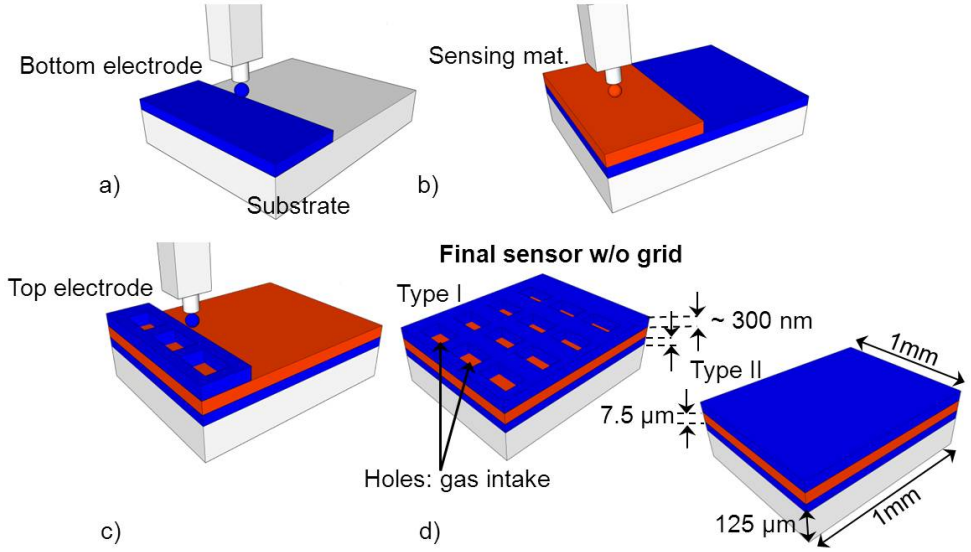

Figure 4.4: Process flow of the fabrication of fully inkjet-printed parallel plate capacitive gas sensors: a) inkjet printing of the bottom Ag electrode, b) inkjet printing of the CAB sensing layer, c) inkjet printing of the top Ag electrode, d) final design with dimensions of the two types of sensor, with (type I) and without (type II) patterned grid on the top electrode for gas intake [146].

R.H.) for type I devices and 3.6 ± 0.2 pF (at 35% R.H.) for type II devices. Our goal for the fabrication of the two types of sensors was to asses the real need of a patterned top electrode by demonstrating that the used nanoparticles-based silver, inkjet-printed on a uneven layer (CAB in this case), had enough defects and pores to let the water molecules reach the CAB sensing layer without the need of any patterning.

It can be observed in Figure 4.5 that the surface of the top electrode is full of ridges, probably due to the high roughness of the CAB sensing layer underneath and/or chemical interaction between the CAB and the solvent of the ink (partial dissolution of the CAB by the solvent). Figure 4.6 contains a white light interferometer (*Wyko NT 110* from *Veeco*) image of the top electrode where the ridges can be seen with more detail, on top that an *ZEIS LEO 1550* scanning electron microscopy (SEM) was used to observe the microscopical morphology of the top electrode. A high porosity and the presence of voids can be observed. Finally, several images of the cross section of the PP device can be seen on the bottom part of the Figure. The cross section images of the PP structure obtained with the SEM reveal that the ink of the top electrode partially penetrates into the sensing layer, probably because of holes and other defects existing on the surface of the CAB layer and because of the partial dissolution of the CAB by the solvent on the top electrode ink. The dissolution of CAB may have occurred in spite of the small amount of solvent deposited at every printed drop and the efforts realized to find a commercial silver ink chemically orthogonal to the CAB layer. The previous reasons were in any case the limiting factor to the thickness of the sensing layer, that could not be reduced much below 7.5 µm maintaining a fair fabrication yield. Very thin layers are desirable to enhance the nominal capacitance, sensitivity and response time of the sensor, but they would

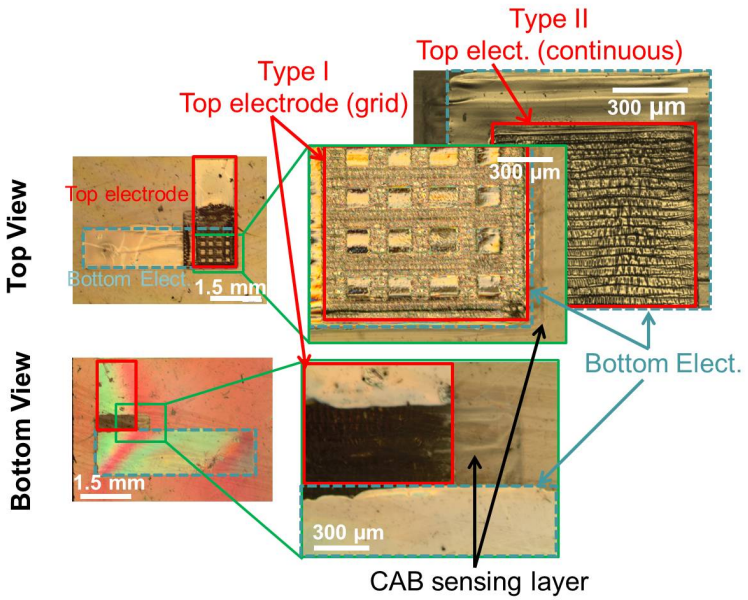

Figure 4.5: Optical pictures (top view) of the fully inkjet-printed humidity sensors. Top and bottom (trough the transparent PET substrate) views, magnifications and details of every different layer, including type I (grid) and type II (no grid) configurations [146].

facilitate shortcircuits between top and bottom electrode. In this sense, some work needs to be made to increase the yield and reproducibility of devices by improving the homogeneity of the sensing film surface, decreasing the amount of solvent used to deposit the top electrode or increasing the chemical stability of the sensing material by cross-linking it. The cross-linking of CAB was reported in [143].

4.2.3 Characterization of standard printed PP humidity sensor on foil

The fabricated devices were characterized against increasing and decreasing staircase and pulses of R.H. (of 15 minutes of duration) ranging from 15% to 85 ± 2% in the customized gas mixing system presented in Section 3.4.3 in Chapter 3, where a total 500 ml / min flow of a controlled mix of dry and wet synthetic air flowed inside a small gas cell at room temperature. The value of capacitance was registered at a frequency of 100 kHz with a LCR meter *E4980A* from *Agilent*. A commercial sensor *Sensirion SHT15* was used for comparative purposes.

The sensors signal against upsweep and downsweep changes in R.H. at room temperature is presented in Figure 4.7. Both types of sensors responded almost linearly to R.H, especially below 60% R.H. for which range the R^2 coefficient was 0.97. Clustering of water molecules in the CAB layer can be one of the reasons of the lack of linearity at high R.H. [143]. No significant hysteresis was observed between upsweep and downsweep cycles, suggesting quick stabilization of the sensing layer and good reversibility of the sorption process. The sensor time response can be extracted from its transient response represented in Figure 4.8 for

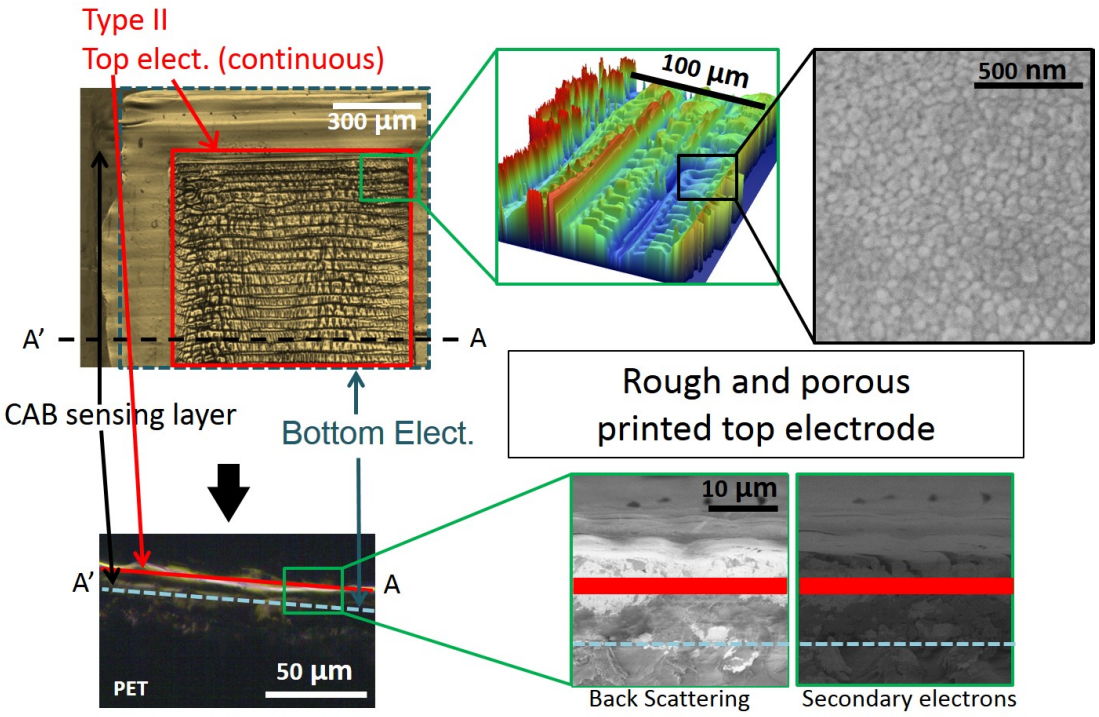

Figure 4.6: Different images of the inkjet-printed top electrode of PP device including top view optical picture of the electrode (top left), optical picture of a cross section of the device (bottom left), profile of the top electrode taken with a white light interferometer (top middle) and images obtained with a SEM of the top view (top right) and cross section views (bottom right) of the device.

the type II sensor. A comparison with a commercial sensor is also included in the graphic. The average time constant of every kind of sensor was 25 ± 2 seconds for type I devices and 17 ± 2 seconds for type II. The time constant was defined in Section 2.2 of Chapter 2 as the necessary time to rise from 0 to 63% of the maximum signal (stabilized). The time response of the sensors, defined as the necessary time to rise from 10 to 90% of the maximum stable sensor signal is 50 ± 20 and 70 ± 30 seconds for type I and type II devices respectively for the step 15 to 30% R.H. Therefore, there is not a real difference in response time between type I and II devices. The mismatches should be rather attributed to the low fabrication reproducibility between the different tested devices. The sensitivity of the sensors is 11.3 ± 0.4 fF / % R.H. for type I and 8.8 ± 0.4 fF / % R.H. for type II devices. This mismatch resulted from the different nominal value of both configurations since the relative sensitivity (in the 100% R.H. range) is 33 ± 3% for type I and 27 ± 3% for type II. Compared to the IDE sensors developed in Chapter 3, these sensors are around 3 times faster, maybe due to total lack of parasitic effect of the substrate. They also present twice higher absolute sensitive than the most sensitive IDE fabricated (those with a dielectric interlayer characterized in Section 3.5.6) for 9 times less surface area, and their relative sensitivity is around 4.5 times greater.

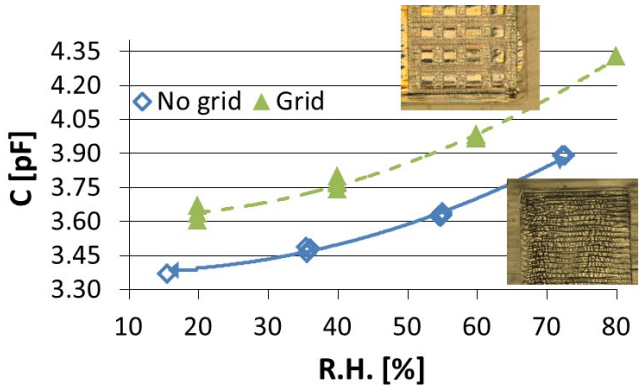

Figure 4.7: Measurements of capacitance against upsweep and downsweep variations of R.H. at the sensor steady state. Comparison between type I and type II devices [146].

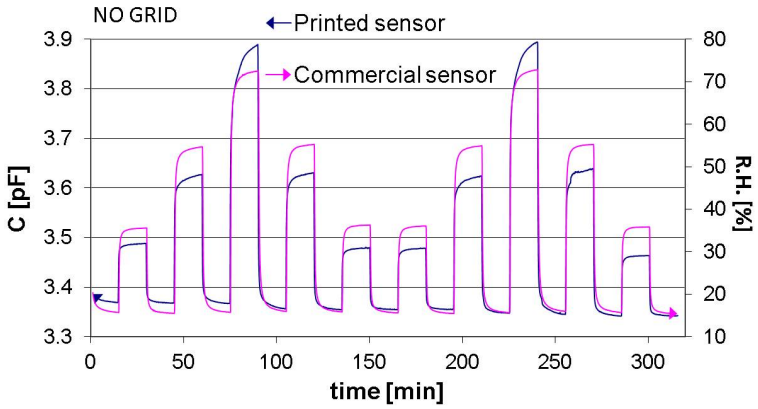

Figure 4.8: Capacitance (left axis) of the type II devices versus time for different cycles consisting of upsweep and downsweep R.H. pulses (right axis) registered with a commercial sensor [146].

Calculation of the partition coefficient

In Section 2.2 of Chapter 2 it was introduced that the partition coefficient, K (Equation 2.6), quantifies the capability of a polymer to absorb certain gas. Its relationship with the volume fraction ϕ (Equation 2.8) was also highlighted. Now, it is straight forward to extract ϕ at every experimental point of R.H. from the ΔC data in Figure 4.7 and Equation 4.4. Hence it is possible to calculate the experimental value of K for our particular interaction between water and the 7.5 µm-thick CAB layer executing Equation 2.8:

$$\phi = \frac{P_a K M}{R T \rho}$$

where the molar mass of water has been considered $M = 18$ g/mol, its density in liquid phase, $\rho = 1000$ Kg/m^3, the absolute temperature (in K), $T = 298$ K, and the universal constant of ideal gases, $R = 8.314$ J/(mol K). The partial pressure P_a of water has been calculated for every $R.H.$

point using the definition of relative humidity (based on partial pressures) $R.H. = \frac{P_a}{P_s}100$ as in Equation 2.9 in Section 2.2. P_s is the saturated partial pressure calculated with the correlation presented in [123] (see Equation 2.10):

$$Ps = (1.0007 + 3.46 * 10^{-6} P/100) * 6.1121 * e^{\frac{17.502T}{240.97+T}} * 100$$

where P is the atmospheric pressure in Pa and T the ambient temperature in °C (25 °C).

Figure 4.9 shows the calculated partition coefficient of water in our inkjet-printed CAB layer, K, at room temperature and different values of R.H. for type I and type II devices. No clear trend was observed with R.H. for the levels tested so K was assumed R.H. independent. Thus K was equal to 420 ± 50 for type I devices and 350 ± 30 for type II devices. Both values lay in the same error margin, proofing no influence of the grid in the concentration of analyte absorbed in the sensing layer and no interference of the printed silver top electrode in the sorption process. Hence, we can establish a final common K calculated from the totality of the experimental points equal to 390 ± 50.

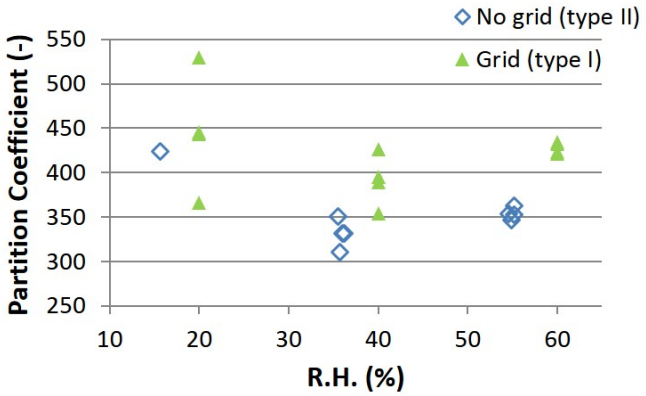

Figure 4.9: Partition coefficient of water in the inkjet-printed CAB sensing layer at room temperature for different level of R.H. Comparison between type I and II devices.

Summarizing, from the obtained values of response time, sensitivity and partition coefficient for type I and II devices, it can be inferred that contrary to evaporated metals, the porosity of the inkjet-printed silver employed in the top electrode makes further patterning unnecessary to allow the penetration of analyte into the sensing layer. However, the variability of the inkjet printing process utilized to deposit the sensing layer, as well as the limited batch of tested devices introduced an error range which was too large to be totally conclusive. In any case, it can be stated that the difference between both types is not significant for our practical purposes. If more precision were required, other printing methods such as flexography or screen printing could be used at least for deposition of the sensing layer. Due to the high surface roughness that it induces, inkjet printing also limits the minimum sensing layer thickness needed to get reasonably high fabrication yield. The reported sensors have proven robust enough to withstand the typical handling and bending occurred during all the tests without

special precautions.

4.3 Fully printed humidity sensors on foil based on parallel plate MEMS (PP-MEMS) microbridge structure

4.3.1 Design and theory of printed PP-MEMS humidity sensors on foil

The PP-MEMS R.H. sensor presented in the second part of this chapter consisted of an array of 80 microbridges like the one sketched in Figure 4.10. The bridges could function separately or could be connected in parallel to operate together. Each bridge was designed to be formed by a 200 nm-thin, 65 µm-wide silver bottom electrode; and a thicker (~ 2 µm) 80 µm-wide suspended silver top electrode that acted as well as movable microbridge. This thickness was selected to provide the bridge with certain mechanical robustness, critical during the step of photoresist release. The suspended microbridge was fabricated with the help of a sacrificial layer of photoresist placed in between the two electrodes and removed afterwards as described in the Section 4.3.2 below. The thickness of the sacrificial layer was expected to be ~ 5 µm, and corresponded with the height of the microbridge before being released. Sacrificial layers thinner than 5 µm resulted in poor fabrication yield due to the collapse of the bridge during the removal of the sacrificial material (stiction). The expected capacitance value of every single bridge was of ~ 20 fF, calculated using the Equation 4.1 as if every bridge were a parallel plate capacitor. This assumption is valid since the bridge is metallic and has a rectangular bottom electrode below. The surface area of the equivalent PP capacitor is thus the superposed area of the bridge with its bottom electrode, i.e. $A = W_B * W_T$ in Figure 4.10.

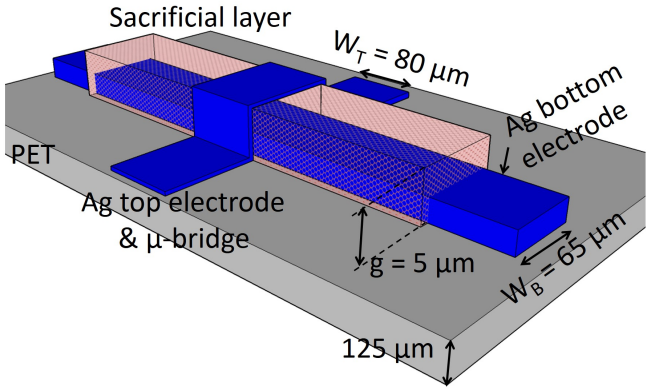

Figure 4.10: Sketch of the structure, materials and dimensions of the developed PP-MEMS R.H. sensor on foil before being released [148].

In the fabricated array that can be seen in Figure 4.13, the bridges were arranged in 10 columns separated by a distance of 200 µm. Each column was composed by 8 rows of microbridges placed in line and separated by a distance of 240 µm. The bottom electrode was a continuous line shared by the 10 microbridges in the same row. In order to reach a capacitance

value easily readable with standard laboratory instruments, the 80 bridges in the device were connected in parallel. All the bottom electrodes were connected together by large pads placed at both sides of the array. Similarly, all the bridges were contacted by pads placed above and below the array. The size of the contact pads was 1 mm x 1 mm. The total expected capacitance was of 1.5 pF.

The presented microbridge was shaped as a beam. Thus, standard beam-theory can be applied in first approach to model its deflection. Also, since the structure can be treated as a parallel plate structure, the parallel plate model for MEMS can be used to model its electrostatically-driven deflection. This model states that in static mode, the mechanical force on the bridge F_M is equal to the electrostatic one F_E. Assuming that the deflected beam is subjected to an elastic deformation, its behaviour can be assumed as the one of a spring. Then, the mechanical force applied on the bridge is given by the Hook's law

$$F_M = k_{eff} d \tag{4.5}$$

where d is the deflection of the beam and k_{efff} is the effective spring constant of the beam. On the other hand, the electrical force exerted on each of the two parallel plates charged with a total charge Q is defined as:

$$F_E = \frac{1}{2} EQ \tag{4.6}$$

where E is the total electric field existing between the plates, and the term $1/2$ accounts for the fact that the electrostatic force exerted on one plate (the suspended in this case) is generated by the electric field generated exclusively by the other plate i.e. $E/2$.

The total electric field between two parallel electrodes subjected to a total difference of potential V is by definition

$$E = \frac{V}{g - d} \tag{4.7}$$

where d is the deflection of the bridge and g the original gap in between the plates (see Figure 4.10). Then, isolating Q from the definition of capacitance ($C = Q/V$), and combining it with Equations 4.5 and 4.7, we obtain:

$$F_E = \frac{1}{2} \frac{CV^2}{(g - d)} \tag{4.8}$$

Considering that the capacitance of every microbridge depends on its geometry according to Equation 4.1, and looking at the geometry in Figure 4.10, we have that for every deflection

$C = \epsilon_0 \epsilon_r W_B W_T / (g - d)$, and Equation 4.8 becomes:

$$F_E = \frac{1}{2} \frac{V^2}{(g-d)^2} \epsilon_0 \epsilon_r W_B W_T \tag{4.9}$$

with ϵ_0 and ϵ_r being respectively the dielectric constants of vacuum and the dielectric between the plates, air in our case (ϵ_r = 1); and W_B and W_T being the width of bottom and top electrode as depicted in Figure 4.10.

According to the condition stating that in static deflection, the mechanical force on the bridge F_M (from Equation 4.5) is equal to the electrostatic one F_E (Equation 4.9), the next relationship must be prevail at every potential applied to the bridge:

$$k_{eff} d = \frac{1}{2} \frac{V^2}{(g-d)^2} \epsilon_0 \epsilon_r W_B W_T \tag{4.10}$$

The effective spring constant k_{eff} is proportional to EI/L^3, where E is the Young's modulus of the bridge material, I is the bending moment of inertia of the microbridge and L its length.

If the microbridge were to be used as a resonator, the resonance frequency could be computed as:

$$f_r = \frac{1}{2\pi} \sqrt{\frac{k_{eff}}{m_{eff}}} \tag{4.11}$$

where m_{eff} is the effective mass of the microbridge.

4.3.2 Fabrication of printed PP-MEMS humidity sensor on foil

All the chemicals employed during the fabrication of the MEMS array were purchased from *Sigma-Aldrich* and used without further modifications unless otherwise stated. The fabrication of the device along with an optical picture after every step is sketched in Figure 4.11. It started with a 125 µm-thick PET substrate *Melinex® ST506* from *Dupont Teijim Films* ™ that was cleaned by successive immersion in acetone, isopropanol (both VLSI grade) and deionized water baths for 10 minutes. After drying with nitrogen, the substrate was subjected to a thermal treatment for 30 minutes at 140 °C for dehydration and thermal stabilization. Then, we treated the substrate with low frequency (13.56 MHz) oxygen plasma for 35 seconds at 50 W to increase the substrate surface wettability. An undesired side effect of the oxygen plasma treatment was a large spreading of the ink on the substrate, resulting in very wide printed lines. This effect was considerably reduced while maintaining good wettability by heating up again the substrate in the oven for 5 minutes at 120 °C. After plasma treatment, the bottom electrode was inkjet-printed through two layers of silver-nanoparticles ink (*SuntTronic Jet EMD506* from

SunChemical) with 20% solid content using a drop-to-drop space of 40 um (Figure 4.11 (a)). The utilized printer was a *Dimatix Fujifilm DMP-2800*™ with 10 pL drop volume cartridges (see Figure 3.3 in Chapter 3).

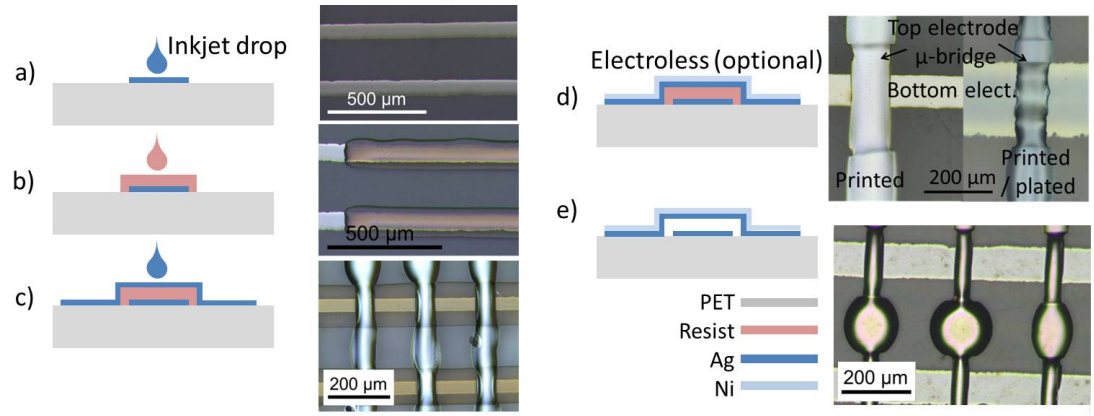

Figure 4.11: Sketch (left) and corresponding optical image (right) of every step of the PP-MEMS microbridges fabrication process [148].

After sintering the printed bottom electrode at 140°C for 30 minutes in a convection oven, the sacrificial layer was formed by inkjet printing two layers of commercial photoresist *Microposit® 1813®* from *Shipley* diluted 90:10 (% weight) with propylene glycol monomethyl ether acetate (PGMEA) to make it inkjet-printable by the utilized printer (see Figure4.11 (b)). The drop-to-drop spacing used to form the sacrificial layer was 20 µm, the temperature of the ink in the nozzle was 55°C, and the speed and frequency of the firing were 9 m/s and 7 kHz respectively. Special care was taken during the alignment of the resist on the bottom electrode to ensure its total coverage and to avoid future shortcircuits between the top and the bottom electrodes. After the resist was annealed on a hot plate at 115 °C for 10 minutes, the previous silver ink was inkjet-printed on it to form the top electrode-microbridge. The annealing of the resist served to render it chemically resistant to the solvent of the silver ink. Nine consecutive layers with a drop-to-drop space of 20 µm were printed to form the microbridge, which was afterwards sintered on a hot plate at 115°C for 30 minutes (Figure 4.11 (c)). Although this sintering temperature was rather mild and led probably to bridges with poor mechanical properties, difficulties to dissolve the resist when it underwent temperatures higher than 115°C impeded me to increase the sintering temperature. Optional electrodeposition of Ni was also demonstrated at this point to thicken the bridge if necessary (Figure 4.11 (d)). Finally, the sacrificial layer was removed by dissolving it in acetone (Figure 4.11 (e)). Stiction problems were avoided by performing freeze-drying process: the acetone under the bridge was progressively replaced by isopropanol and finally by cyclohexane (HPLC grade), which was frozen on a Peltier element (freezing point 6.47°C) and sublimated under nitrogen atmosphere, avoiding capillarity forces that could pull down the bridge.

Using inkjet printing made it easy to control the geometry of the microbridges. For instance, the height of the bridge as well as its thickness were controlled by selecting the number of

printed photoresist or top electrode layers respectively. Figure 4.12 shows the relationship between the thickness and the number of printed layers for the sacrificial photoresist layer and the silver microbridge. The final selected values were ~ 5 µm-thick photoresist and ~ 2 µm-thick top electrodes. The previous values were chosen based on empirical observations, seeking to maximize the fabrication yield. Although Figure 4.12 (bottom) indicates that 6 printed layers were sufficient to print ~ 2 µm-thick top electrode, the flow of the ink toward the pillars made necessary to print 9 layers as indicated in the process flow above. The final released bridges had a typical height of ~ 2.5 µm-thick, which is smaller than the thickness of the sacrificial layer. The reason is that the bridges moved down after being released. The length of the bridges was 120 µm and the width ranged from 60 to 80 µm. The bottom electrode was 65 µm-wide.

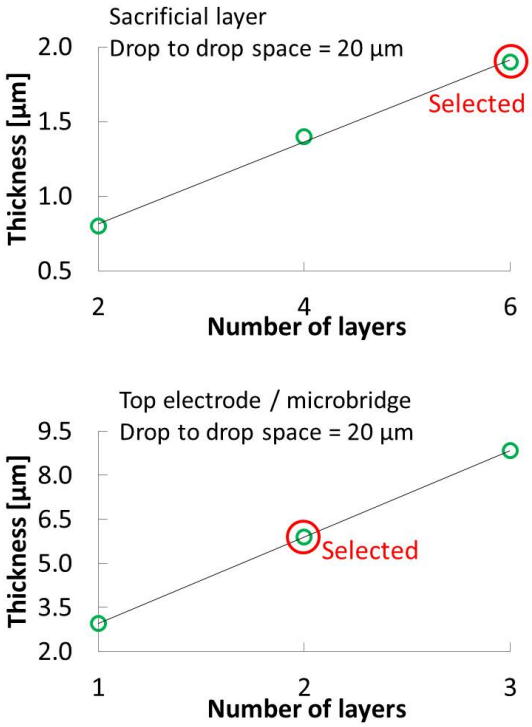

Figure 4.12: Thickness of the inkjet-printed sacrificial layer and consequently of the height of the unreleased microbridge (top) and thickness of the bridge (bottom) versus number o printed layers [148].

Figure 4.13 shows images of several arrays of MEMS microbridges successfully inkjet-printed on PET foil. The figure contains optical image and magnified view of an array of printed PP-MEMS microbridges (left). SEM-obtained image of the array with magnified view (top right) and white light interferometer-obtained image view (bottom right) of the same array showing its 3D topography. The SEM used was a *ESEM XL 30 FEG* and the interferometer a *Wyko NT 110* from *Veeco*. The accumulation of ink between the bridges during the printing process formed pillars-like structures which were not found to be unfavorable for the proper operation of the device.

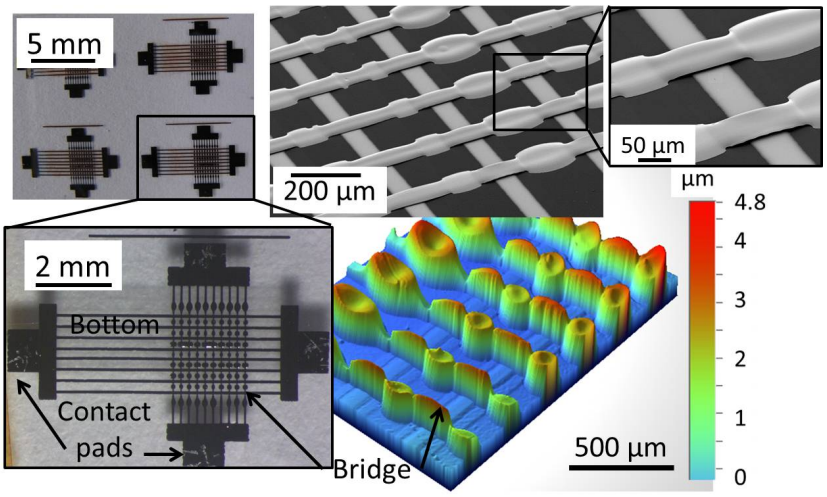

Figure 4.13: Optical image and magnified view of an array of printed PP-MEMS microbridges (left). SEM-obtained image of the array with magnified view (top right) and white light interferometer-obtained image view (bottom right) of the same array [148].

4.3.3 Characterization of printed PP-MEMS humidity sensor on foil

Electrostatic deflection of the PP-MEMS

In order to confirm that the microbridges were properly released and that they could be operated as suspended structures, a voltage was applied between the bottom electrode and the microbridge itself to electrostatically deflects it. The deflection of the bridges was measured using a white light interferometer *Wyko NT 110* from *Veeco*.

Figure 4.14 shows these experimental data for a bridge presenting a distance of 1.6 µm between its top and its base. The experimental data were plotted along with a theoretical estimation of the bridge deflection with the applied voltage obtained by solving the Equation 4.10. The effective spring constant k_{eff} was used as the only fitting parameter of the curve. It was considered constant for all the deflections, and its best fitting value resulted k = 76 ± 4 N/m. This value takes into account the material of the bridge, its sintering conditions, the bridge geometry and anchoring effects. That value can be changed by varying all those parameters, making possible to adjust the stiffness of the bridge to the required application. The effective spring constant of the printed microbridge was expected to be lower than for a microbridge fabricated using standard metalization methods (such as evaporation), due mainly to the lower Young's modulus found for printed silver (22 GPa [86]) compared to evaporated thin film silver (74.8 GPa [151]) or to bulk silver (83 GPa). The difference is likely a result of the nanostructure of the printed film.

With the dimensions indicated in the Section 4.3.1 and the determined k_{eff}, the expected resonance of frequency for the microbridge would be, assuming the density of printed silver to be 10.45 g/ml [152], is ~ 133 kHz.

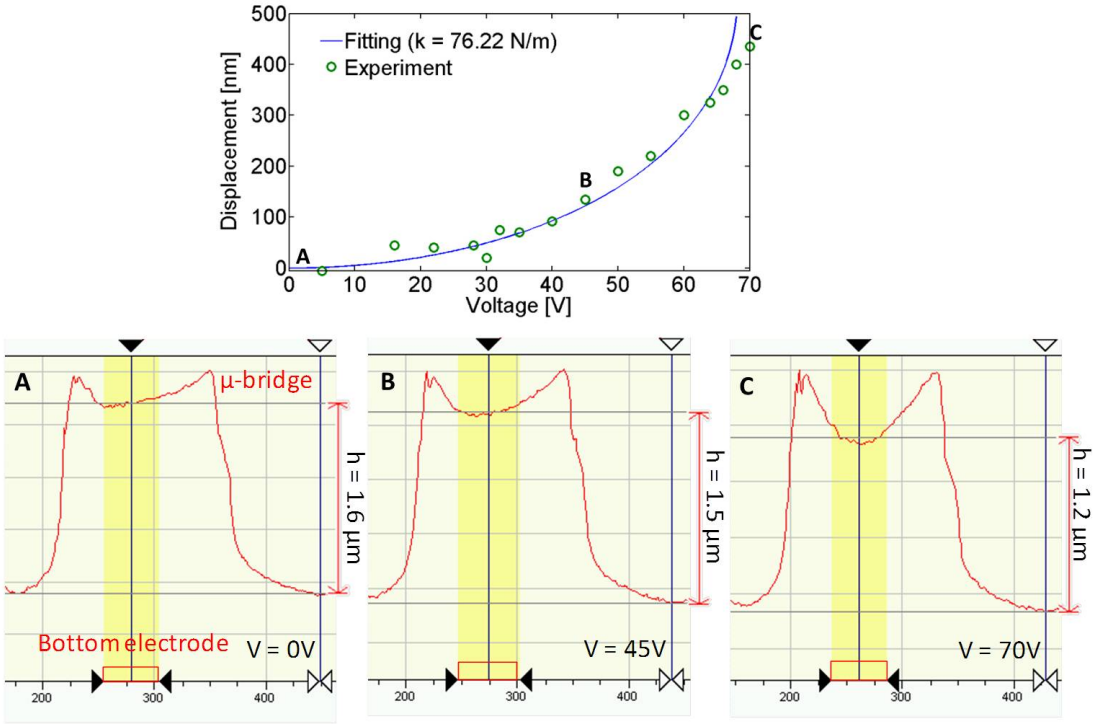

Figure 4.14: Deflection of a PP-MEMS microbridge against different voltages applied between top and bottom electrode: experimental points and fitting curve with deduced effective spring constant (top). Profile of the microbridge measured with a white light interferometer at some selected values of applied voltage [148].

PP-MEMS used as relative humidity sensors

As mentioned in the Introduction, the PP-MEMS sensor working principle is inherently different from the one of standard PP capacitive sensors. The PP-MEMS sensor makes use of its polymeric substrate that swells upon gas absorption. Our hypothesis is that when the substrate swells, it bends and the bridges buckle up increasing the distance between the bottom and the top electrode as depicted in the inset of Figure 4.15. The capacitance value of the array should therefore decrease accordingly offering a mean for gas sensing. The results shown in Figure 4.15 (where C' < C) seem to agree with our assumptions. The tests were carried out for relative humidity for the sake of simplicity but the principle applies to every gas in general that could penetrates in PET. Indeed, according to Equation 2.4, the swelling of a polymeric layer is proportional to the volume fraction ϕ, which would be higher for larger molecules. Therefore, we would expect the sensor to be more sensitive to large molecules such as volatile organic compounds (VOCs) than to small molecules like water. On top of that, PET has low moisture intake. Since there is not sensing layer between top and bottom electrodes where the electric field is distributed, and the dielectric constant of dry and humid air is always almost the same and equal to 1, the PP-MEMS bridges capacitance is not influenced by the permittivity of the analyte. Although it has not been tested, this fact suggests a big advantage compared to standard PP or IDE gas sensor, based on changes of permittivity, where water is usually a

big interference even at small amounts due to its high permittivity. In that way, PP-MEMS sensors are a perfect complement for standard PP or IDE capacitive sensors. The functionality of the sensor towards more specific analytes could be expanded by coating the bridge with a customized sensing layer. This would induce stress on the bridge itself too. Non-contact printing methods such as inkjet or laser induced forward transfer (LIFT) would be suitable methods for such purpose. Alternatively, the substrate could be functionalized or passivated at the same time to tailor the selectivity of the sensor.

As it was mentioned, for the sake of simplicity to proof the concepts, in this thesis work the sensing tests were carried out for R.H. To perform the tests, the device was introduced in a climatic chamber (see Section 3.4.3) able to provide controlled steps of relative humidity (25%, 45% and 65% R.H. in this case) at a fixed temperature of 30°C. After sensor stabilization for 30 minutes, the capacitance value was registered at 100 kHz for every step using an LCR-meter. The device was tested for two downsweep cycles and one upsweep cycle, displaying a linear behaviour with a coefficient R^2 = 0.9757 with a precision due hysteresis of 4.3% R.H. The sensitivity of the sensors was -1.92 ± 0.14 fF / 1% R.H. These values indicate a performance poorer than the one of standard PP devices. However, as explained above, R.H. may not the best analyte for the PP-MEMS device to display their best performance. With the characterization of the PP-MEMS sensor for R.H., I just intended to show a proof of concept of this novel sensing principle

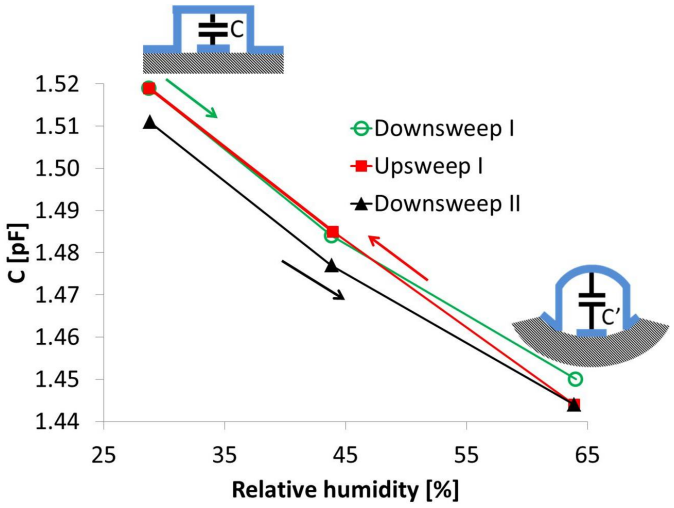

Figure 4.15: Capacitance value versus relative humidity displayed by the PP-MEMS array operating as a humidity sensor, along with a sketch of the hypothesized bridge behaviour [148].

According to the first term of the right part of Equation 4.3, $-\frac{\epsilon_0 \epsilon_r A}{h^2}\Delta h$, the smaller the microbridge height, the higher the sensitivity of the PP-MEMS gas sensor. Such equation is still valid since we are still dealing with a PP structure. Nonetheless, the term Δh needs to be defined for the swelling-buckling-based operation through a suitable theoretical model.

Compared to equivalent devices based on the deflection of a continuous membrane, the array developed here is easier to fabricate, more robust and more insensitive to accelerations,

owing to the small mass of every independent bridge.

4.4 Conclusions

Parallel plate (PP) capacitive structures have been used for gas sensing, concretely for relative humidity (R.H.) detection. Two different geometries based on two different working principles were described. The first one consisted of standard PP capacitor where the dielectric between the electrodes/plates is the sensing layer. Changes in dielectric constant and thickness of the sensing layer upon absorption of R.H. are translated in capacitance shifts. The second geometry is based on large arrays of PP-MEMS microbridges. The polymeric substrate acts in this case a swelling-driven sensing layer that makes the devices to buckle up splitting apart the PP electrodes. Hence, the capacitance of the device is decreased as a result. Although not proven yet, changes in permittivity are not expected to have any influence in the capacitance of the PP-MMES devices. A theoretical study of the working principle of the transducers and the sensing principle is presented for both geometries, elucidating the differences between parallel-plate, IDE and PP-MEMS capacitive gas sensors.

The sensors have been fabricated in both cases by means of inkjet printing of silver on flexible PET foil, and have been characterized for R.H. variations. For standard PP sensors, their geometry along with the large porosity of the printed top electrode permitted the fabrication of simpler and more miniaturized devices than in the case of their IDE counterpart reported in Chapter 3. The presented devices showed also better performances than IDE R.H. sensors: high linear response up to 60% R.H., 30% relative sensitivity for full R.H. range and time responses shorter than 30 seconds were achieved without the need of differential methods. Thinner sensing layer would improve further the performance of the device. However, the practical minimum film thickness permitting a good fabrication yield is in this case limited to few μm by the nature of the inkjet printing process and the lack of homogeneity of inkjet-printed films. Since the top electrode is deposited from liquid ink, the ink may have partially dissolved the sensing layer or penetrated trough voids or defects reaching the bottom electrode. The occurrence risk of top and bottom electrodes shortcircuit gets higher when the sensing layer is thinner. Some future work should be carrier out to decrease the thickness of the sensing layer and to increase the fabrication yield by improving the sensing layer homogeneity and/or the chemical resistance of the CAB sensing layer through cross-linking it [143]. Inkjet-printed CAB was used here as a test sensing layer for proof of concept, and despite the fact that it offered good performance in terms of sensing and fabrication compatibility, the sensor performance could be improved even further by using an optimized sensing material, or a deposition method permitting good thickness control, such as flexography or screen printing. Another mean to achieve good chemical compatibility between the top electrode ink and the sensing layer would be to modify the solvent of the ink. Different nanoparticulate metals like gold or copper are commercially available in solutions with different solvents. Ultimately, microcontact printing could be used to patter the top electrode without worrying about solvent compatibility, since it allows the transfer of thin dry layers making use of Van der Waals

forces [87, 102–106].

For PP-MEMS sensors, the electrostatic actuation of independent bridges was first of all confirmed, then I demonstrated the possibility of interconnecting the 80 bridges of the array in parallel to provide readable capacitance values of 1.5 pF. The potential of the array MEMS microbridges was evaluated for capacitive detection of humidity. However, an increase in sensitivity would be expected for larger molecules. By coating the bridges with a customized sensing layer or by functionalizing/passivating the substrate, the operation of the sensor could be expanded to detection of others analytes. Non-contact printing methods such as inkjet or laser induced forward transfer (LIFT) would be suitable methods for such purpose. However, a theoretical model to predict the sensor response to gases is currently missing and should be elaborated for future improvements. The model developed in [153] to predict the bending of flexible substrates coated with a metallic layer due to thermal mismatch could be adapted to this scenario. Finally, by optimizing the pull-in voltage of every microbridge or tailoring their geometry, the device could also find application as an array of MEMS switches, sensors or actuators.

The work reported int this chapter suggests the potential of combining different sensing layers in several PP structures for fabrication of selective sensors arrays. The presented technology enables the development of very low cost, low power flexible gas sensing devices. Chapter 5 will expand and materialize this concept through the fabrication of a multisensing platform to be in integrated in a wireless smart label.

5 Inkjet-Printed Multisensing Platforms on Foil for RFID Applications: Integration of Capacitive and Resistive Sensors with Thermodetector and Microhotplate

5.1 Introduction

I present along this chapter the development of an inkjet-printed multisensing platform compatible with a radio frequency identification (RFID) label for monitoring of perishable goods. Both the multisensing platform and the tag were fabricated on a foil substrate. Their integration can be achieved using foil-to-foil integration techniques. The multisensing platform takes advantage of the know-how developed during this thesis in printing standard IDE structures on foil (see Chapter 3), and utilizes this know-how for developing capacitive and resistive IDE sensors, as well as fabricating printed resistive meanders to be used as temperature detectors (RTD) and microheaters. All these elements are integrated on the same substrate to address the simultaneous detection of different gas analytes (humidity, ammonia and other volatile organic compounds) and temperature, owing to the combination in the same array of different transducing principles (capacitive, resistive and hotplate), sensing layers and measurement approaches such as differential read-out. The typical characteristics of inkjet printing pointed out in Section 1.1, namely its maskless, contactless, localized character and its easiness for lab scale prototyping, resulted to be especially advantageous in the fabrication of this multisensing platform, on which the integration of many diverse transducers and sensing layers need to be accomplished. Capacitive IDE relative humidity (R.H.) sensors with same architectures to those described in Chapter 3 but with improved stability and resolution are included in the tag. Since the ambient temperature plays an important role in gas sensing in terms of both sensitivity and response time, it should be monitored or controlled during operation at every moment. Therefore I first describe in this chapter the development of a simple platform where a RTD is integrated with an IDE R.H. sensor as reported in [154]. The RTD resulted useful

to calibrate the capacitive R.H. sensing as well as to obtain information about the ambient temperature as a sensing parameter itself. Compensating the influence of temperature in gas sensing is possible in some cases by monitoring the ambient temperature during gas measurements and comparing the measured parameters with the data obtained in a previous thermal calibration. In other cases however, it is required to actively control the temperature by heating up the sensing layer above room temperature, in order to modify the kinetics of interaction between the analyte and the sensing layer for enhanced sensing performances. Furthermore, heating up the sensing layer could be used as well as a mean to cancel the influence of ambient temperature on the response signal of gas sensors, simply by maintaining a higher-than-room temperature during the entire sensing process. For that reason, the inkjet-printed resistive structure developed for the RTD has been adapted to operate as a microhotplate as described in the second section of this chapter. The microhoplate has been combined with the resistive read-out of a sensing layer (chemiresistor), adding extra versatility to the sensing system by generalizing its operation for resistive gas detection (besides capacitive). The operation of the microhotplate in combination with the chemiresistor has been demonstrated for detection of ammonia using a conductive polymer (polyaniline) sensing layer developed by our *FlexSmell* partners from the research group of Prof. K. Persaud at the University of Manchester (UK) [155]. At the end of the chapter the different elements mentioned above have been integrated on a common substrate forming a multisensing platform composed of two IDE capacitors, one to be left uncoated and one to be coated for differential mode detection (see Section 3.5.5 in Chapter 3), a RTD for temperature detection and compensation, a small IDE structure chemiresistive detection operating at room temperature and a microhotplate integrated with a second chemireresistor using a polyaniline (PANI) layer for ammonia detection at 80 - 95°C. The multisensing platform is fully compatible and readily integrable on a flexible RFID label for perishable food monitoring, accomplishing the goal of the *FlexSmell* project.

Resistive temperature detector (RTD) for temperature detection and thermal compensation of relative humidity (R.H.) sensors Both the temperature and the humidity conditions of perishable goods should be tightly controlled during their distribution to ensure their freshness. Besides being temperature a very important parameter to control by itself, the influence of temperature in gas sensing is a well known fact. In Section 2.2 it was described that temperature is a factor that affect both sensitivity and response time of capacitive sensors through the thermal dependence of the partition (Equation 2.7) and diffusivity (Equation 2.15) coefficients respectively. Some people have studied the influence of temperature in R.H. sensing and the influence of the measuring frequency on it [40]. We have reported on the topic in [154]. The first subsection of this chapter presents the simultaneous fabrication of arrays of R.H. sensors and RTD, both of them inkjet-printed on flexible substrate. The R.H. sensors are based on the planar standard IDE described in Chapter 3 with optimized resolution (120 µm instead of 200 µm pitch) and with the same inkjet-printed CAB sensing layer. The RTD rely on the variation of electrical resistance with changes in temperature shown by some metals [88]. They were formed by meander-shaped lines as for the flexible RTD realized by standard microfabrication

methods reported in [32, 90]. Although silver inkjet-printed line-shaped resistors have already been presented in the literature [92], the substrate used was glass and the authors did not target sensing purposes, but the study of the thermal sintering of silver nanoparticles ink. The authors found a temperature coefficient of resistance (TCR) of 2080 ppm/°C for lines sintered at 240°C.

The combination of printed RTD with IDE R.H. sensors allowed the compensation of the R.H. signals variations at different temperatures through an appropriate calibration. The whole fabrication of the system is carried out at foil level and involves exclusively the utilization of additive methods, namely inkjet-printing and electrodeposition. The electrodeposition of nickel described in Section 3.3.2 was demonstrated to improve the RTD sensitivity (or TCR). On the other side, an extra annealing of the IDE capacitors [140] made unnecessary their plating for stable operation as in Section 3.5.5, at least for short to medium-term operation. For long-term operation, plating of a passivation material such as nickel onto the inkjet-printed silver electrodes still remains a better option since it prevents oxidation.

After inkjet deposition of the CAB sensing layer on the IDE, the sensors have been characterized for R.H. and temperature sensing and their performances analyzed. Single mode operation has been used for R.H. sensing characterization for simplicity, since the focus here is not on the IDE sensing performance for R.H., but on its combination with the RTD. The final sensors have been encapsulated at foil level and the encapsulation was shown not to modify the sensors performance in terms of sensitivity or response time. Further details about the fabrication of the encapsulation can be found in [154], or as a part of the thesis work of my colleague A. Vásquez Quintero.

Microhotplates for chemiresistive sensors In the second part of this chapter I report on the design, fabrication and characterization of an inkjet-printed silver microhotplate integrated on polyethylene naphthalate (PEN) foil with an inkjet-printed IDE. The microheater was separated from the IDE by a thin insulating organic layer. The features of printed microheaters were improved through the development of different generations where the thermal performances have been optimized through careful redesign of the heater shape and dimension. Improved long-term stability of the sensors could be enabled by electrodeposition of nickel on the heater [156] or gold on the silver IDE. The IDE was used then as a chemiresistor by placing on top a layer of polyaniline (PANI) (a conductive polymer which conductivity changes in the presence of ammonia) doped with poly(4-stryenesulfonic acid) that was synthesized and deposited on the IDE by vapour-phase deposition polymerization by our *FlexSmell* partner E. Danesh at the University of Manchester (UK) [157]. The proper operation of the PANI layer to detect ammonia in air required high temperature of 80 to 100°C, supplied by the microheater underneath, demonstrating the functionality of the presented device in particular and the feasibility of low-cost and low power consumption printed micro-hotplates on polymeric foil for gas sensing applications in general.

Some works have reported on how integrated heaters improve the performance of capacitive humidity sensors fabricated on silicon [149]. Some other publications reported on integrated heaters in the domain of Metal Oxide (MOX) micro gas sensors. MOX gas sensors with on-chip heater have been fabricated on traditional rigid substrates [13], and few works can be even found dealing with MOX micro gas sensors fabricated on flexible substrate [1,20]. Since MOX sensors usually require high temperatures (about 200-300°C) to achieve a good performance, heat resistant and relatively expensive polyimide was chosen as the substrate material for the reported MOX on foil. They were also fabricated using standard clean-room technology, which are costly and require special clean-room facilities. Other foil-like chemiresistors were already based on PANI and a heating element for ammonia detection (some of them even fabricated by printing techniques). In all the cases, high temperature was necessary to facilitate the ammonia desorption from the PANI. For instance, Crowley *et al.* presented in 2008 screen printing of silver electrodes using inkjet-printed polyaniline nanoparticle films as sensing layer for conductimetric detection of ammonia [23]. They used a commercially available external foil heater to improve the sensing performances at 60 to 80°C but the continuous heating resulted detrimental for the nominal conductivity. E. Danesh and Prof. Persaud developed in 2012 sensitive (sub-ppm) and reversible ammonia sensors using a polyaniline/carbon black composite sensing layer on polyimide substrate. They used a ceramic sub-miniature heater to heat it up to 80°C [158]. More recently, Claramunt and colleagues have reported in [25] an ammonia sensor consisting of a polyimide flexible substrate, onto which an array of silver interdigitated electrodes was inkjet-printed on one side, and a common heater on the backside. The interdigitated electrodes were coated with carbon nanofibers decorated with metal nanoparticles. The heater was used to clean the nanofibers and make the sensors reversible. The large surface of the heater (few mm^2) and the high thickness (50 μm) of the foil separating the heater from the sensing layer, resulted in a relatively high power consumption of around 150 mW to achieve the optimal sensing temperature of 110 to 120°C. Nevertheless, the sensor showed only 3% change in resistance upon exposure to rather high concentrations of ammonia (500 ppm). In this work we improve the state of the art by fabricating inkjet-printed microhotplates of 1 mm^2 with a novel sensing layer able to sense sub-ppm concentration of ammonia at 80-95°C, requiring only 25-35 mW.

In summary, in this chapter low-cost sensing systems consisting of two IDE capacitors to detect R.H. and a RTD to detect temperature and allow thermal compensation of the capacitor, have been firstly fabricated on flexible PET foil by using only additive methods, namely inkjet-printing and electrodeposition. The devices have been encapsulated at foil level for protection and eventually characterized. Then, I described the development of two generations of inkjet-printed microhotplates on PEN substrate consisting on silver heater and IDE, separated by a thin layer of patternable dry photoresist. The whole process was compatible to large mass production at sheet-to-sheet level. Their suitability for resistive detection of very low concentrations of ammonia in sub-ppm range has been demonstrated in dry and humid conditions using a polymeric acid-doped PANI sensing layer developed by our *FlexSmell* partners at the University of Manchester (UK). The thermal performance

of the hotplates was examined using micro-thermocouples in collaboration with FEMTO-ST Laboratory in Besançon (France). Finally, all the previous elements have been integrated on a common PEN substrate to build up a multisensing platform to be functionalized by our *FlexSmell* partners at the University of Tübingen (Germany) and University of Manchester (UK). The multisensing platform is compatible and was integrated with a flexible RFID label developed by our *FlexSmell* partners at Holst Centre (The Netherlands) in collaboration with EPFL-SAMLAB. We will shortly succeed in that way to fulfill the goals of the *FlexSmell* project by developing a smart sensing system compatible with wireless communication for smart food packaging applications.

5.2 Printed RTD for temperature detection and thermal compensation of relative humidity (R.H.) capacitive sensors on foil

5.2.1 Design of RTD and R.H. interdigitated electrode (IDE) sensors

A meander-shaped resistive thermodetector and a R.H. IDE capacitive sensor have been simultaneously patterned on foil using inkjet-printed silver nanoparticles-based ink and electroplated nickel as shown in Chapter 3. The geometry and dimensions of the platform are represented in the sketch of Figure 5.1 (a) along with an optical picture of the final printed device in (b). The expected resolution of the patterned lines were 100 µm and 20 µm for width and gap respectively. The better expected resolution compared to standard IDE in Chapter 3 can be attributed to the use of a different ink as described later in 5.2.2. The IDE capacitors were formed by 28 fingers of 4 mm length each, occupying a surface area of 4 mm x 3.5 mm without taking into account the contact pads. It was designed to supply a capacitance of ~ 3.5 pF according to the theoretical model in Section 2.3.1. The meander-shaped resistive thermodetector (RTD) had a total length of 317.9 ± 1.6 mm, designed to supply a resistance of ~ 7 kΩ. It occupied a surface area of ~ 11 mm x 3 mm.

5.2.2 Fabrication of RTD and R.H. IDE sensors

The fabrication of the R.H. and temperature sensing platform is based on the fabrication process used for the standard printed/plated IDE on foil as described in Section 3.3. The process flow along with an extensive study of the encapsulation can be found in [154].

Experimental

Substrate preparation The fabrication of these devices is very similar to that of the standard IDE devices described in Section 3.3 of Chapter 3. The fabrication started with a polyethylene terephthalate (PET) *Melinex® ST506* foil, 125 µm-thick, from *Dupont Teijim Films*™ that was cleaned by successive immersion and rinsing in acetone and isopropanol (purity > 99.9%) for 5 min, followed by immersion and rinsing in deionized water for other 5 min. After cleaning,

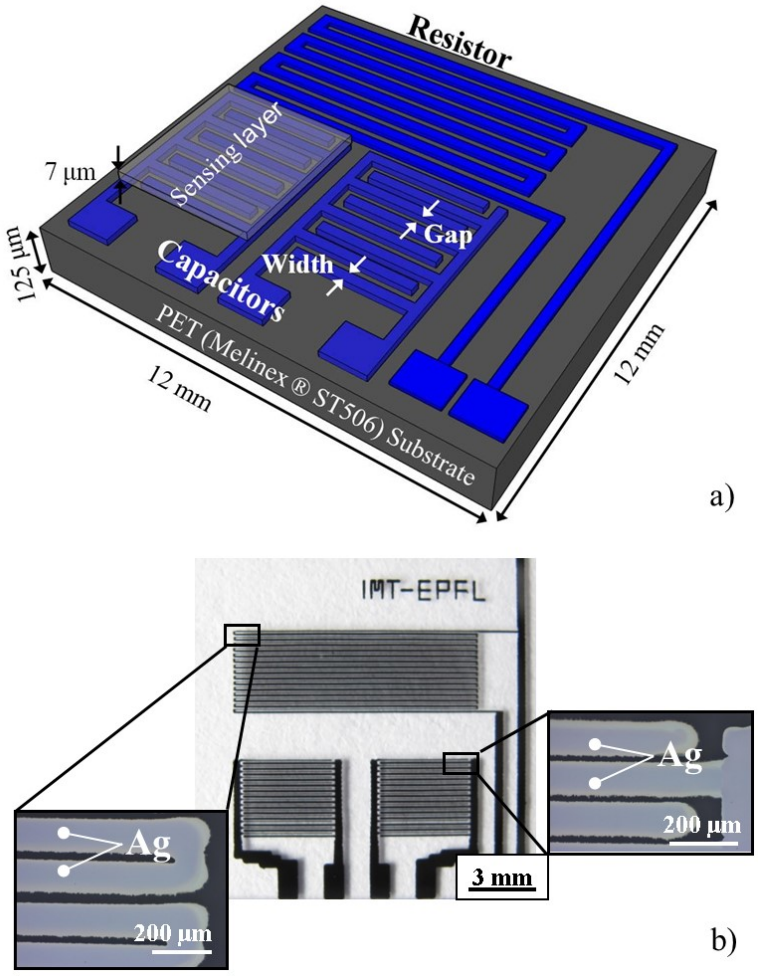

Figure 5.1: (a) Sketch and (b) optical image of the printed sensing system of foil including two IDE capacitor for R.H. detection and a thermoresistor. The materials and dimensions of the system are sketched in (a) [154].

the substrate was dried with nitrogen and dehydrated in a convection oven for 1 hour at 120°C. Finally, low temperature 2.456 GHz microwave oxygen plasma treatment was applied to the substrate for 1 minute at 400 W under a flow of 400 sccm and 560 mTorr pressure in a system *PVA TePla PS210* to achieve enhanced surface wettability and improved printability.

Inkjet printing of transducer and sensing layer To form the IDE and the meander RTD, silver nanoparticles-based ink *SuntTronic Jet EMD506* from *SunChemical*) with 20% Ag solid content was printed on the substrate heated-up at 45°C using a *Dimatix Fujifilm DMP-2800*™ printer with 10 pL drops cartridges. The optimum printing parameters were: two printed layers with drops ejected at 5 kHz with a speed of 7 m/s and spaced 40 µm one from each other (drop-to-drop space). The silver was sintered in a convection oven at 150°C for 3 hours. The selected temperature was recommended by the ink manufacturer, and coincided with the

maximum process temperature of the PET foil. However, we chose an extra long annealing time to ensure the removal of the organic residual contained in the silver lines, seeking to increase their chemical stability [140]. Afterwards, the lines corresponded to the RTD were subjected to electrodepostion of nickel in a nickel sulfamate bath at 54°C, under an electrical current density of 20 mA / cm^2. Finally, a humidity sensing layer of cellulose acetate butyrate (CAB) was fabricated by dissolving 65 mg of CAB in 4 ml of hexyl acetate (purity > 99%) as stated on Section 3.3.3, and by subsequently inkjet printing the solution on the IDE. After printing, the solution was dried for 30 min at 85°C in a convection oven forming a solid thin film of CAB. The CAB sensing layer served to test the functionality of the IDE transducers for R.H. detection. The fabricated sensors were optically evaluated with an optical microscope and their profile measured using a white light interferometer *Wyko NT110* from *Veeco* and an alpha-step system from *Tencor*.

Encapsulation The developed sensors were further fully encapsulated using lamination techniques following a process developed by the Ph.D. student A. Vásquez Quintero at our laboratory [154]. The encapsulation layers were also flexible polymers to comply with the flexibility of the system. The encapsulation process took place at low temperature of less than 85°C, compatible with the limited thermal stability of the polymeric materials employed. The encapsulation was important since it served as protection of the sensors (especially of the sensing layer) against dust particles, liquid droplets, handling, scratches, etc. Two different strategies were investigated for the encapsulation of the sensor (see 5.2).

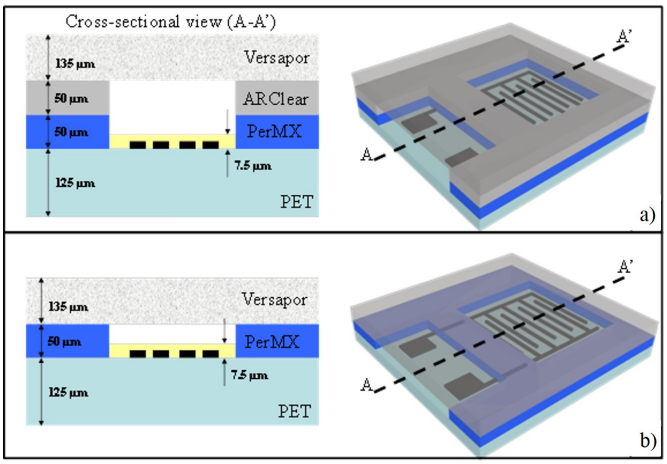

Figure 5.2: Sketch of the different strategies investigated to encapsulate the sensing platform: (a) using dry photoresist + adhesive + porous membrane and (b) without using dry adhesive [154].

The first one consisted of the stack of 50 µm-thick dry film photoresist *PerMX2050*™ from *Dupont*™ combined with 50 µm-thick dry adhesive *ARClear® 8932*. Both layers are deposited and patterned as a frame around the sensors. Finally, a top 135 µm-thick acrylic copolymer porous membrane was laminated on top of the frame (*Versapor® 10000R* from *PALL*). The porous membrane was gas-permeable. The second encapsulation strategy omitted the use

of the dry adhesive, saving one lamination step and reducing the total thickness of the stack. However, oxygen plasma surface treatment was needed to achieve good adhesion between the top membrane and the dry film photoresist without the use of the intermediate dry adhesive.

Results of fabrication

Figure 5.1 (b) depicts an optical picture of the fabricated platform with close views of the IDE and the meander lines. The profile of the bare-printed silver lines and printed-plated silver-Ni lines is shown in Figure 5.3. The images were taken with a withe light interferometer and showed printed lines with a thickness of 230 ± 30 nm and bell-shaped cross section; and printed-plated lines of a thickness of 1.0 ± 0.5 µm and quasi-rectangular shape.

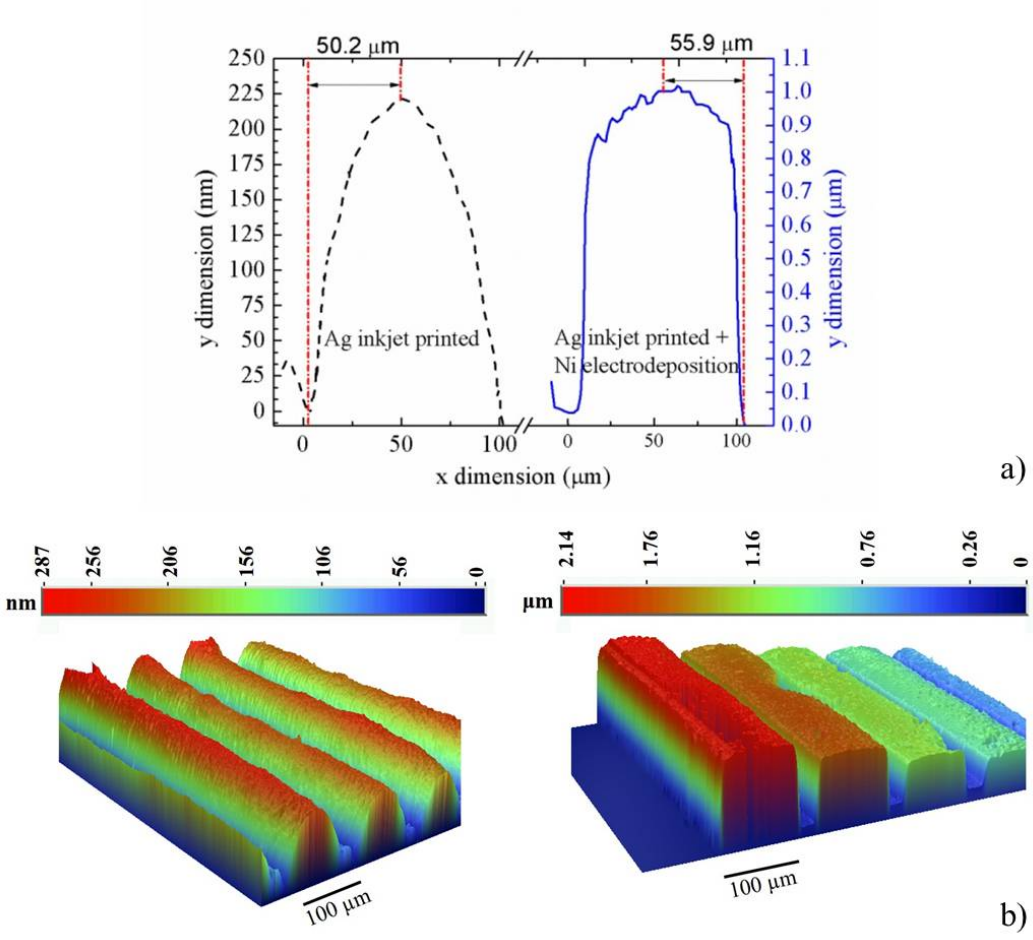

Figure 5.3: Images obtained with a white light interferometer displaying the profile of the bare-printed IDE capacitor (left), and the Ni-electroplated thermoresistor lines (right) in (a) perpendicular cross section view [154] and (b) 3D surface mapping view.

The smallest width achieved for the printed lines was 99.1 µm with a standard deviation of 2.3 µm and the smallest separation between them was 20 ± 5 µm (see Figure 5.1 (b)). Compared

to the standard IDE printed with the silver ink *Anapro DGP40LT-15C* presented in Section 3.5.2, the lines width is similar but the fingers pitch has been decreased from 200 um to 120 µm owing to the reduction of the inter-electrodes space. As a consequence, the capacitance per surface area was also enhanced from 0.11 (or 0.12 for plated electrodes) to 0.23 pF / mm^2. Compared to the first IDE comb printed with the same *Suntronic Jet EMD506* ink in Section 3.5.3 for IDE with reduced size, the width of the lines presented here was higher (99.1 µm against 38 µm) due to a more extensive use of the oxygen plasma treatment. This effect was pursued to increase the ratio width to gap and hence the capacitance value per surface area (see Figure 2.8 in Chapter 2).

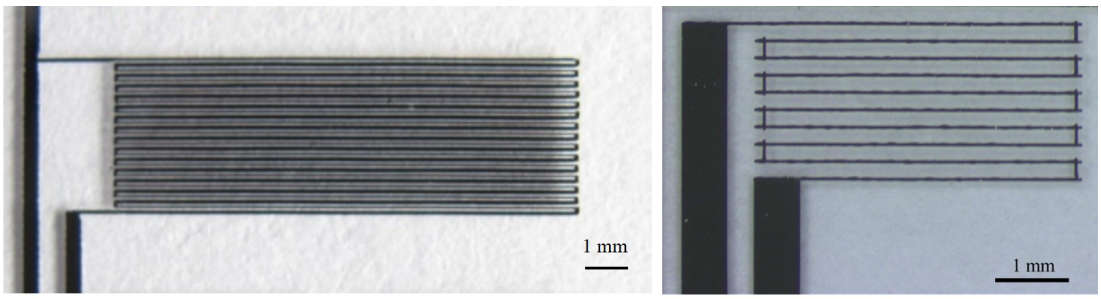

Figure 5.4: Optical pictures of (a) the printed RTD used in this section and (b) the printed RTD used with improved line resolution used in the multisensing platform in Section 5.4.

The measured resistivity for the printed and printed-plated lines was 50 ± 9 µΩ*cm and 90 ± 40 µΩ*cm, respectively. The high deviation in the resistivity of the plated lines is the result of the poor control of the plated layer thickness achieved during the electrodeposition process due to the relative large voltage drop occurring across the resistance. Thus, the outermost meanders are progressively thicker than the innermost ones. This situation is clearly represented in the right graphic of Figure 5.3. This issue could be easily solved in the future by adding more contact points for electrodeposition towards the middle part of the meander. Figure 5.4 consists of two optical pictures of different RTD based on the same meander-shaped structure. The one of the left corresponds to the one included in the described platform whereas the one on the right has improved resolution and was used in the multisensing platform described below in Section 5.4.

The measured resistance and capacitance of the printed devices at ambient conditions (room temperature and 45%R.H.) were 7.0 ± 0.3 kΩ and 3.69 ± 0.9 pF, respectively. In spite of the increase in resistivity of printed-plated lines compared to bare-printed lines, their resistance decreased to 2.78 ± 0.18 kΩ due to the increase in the lines thickness. Finally, the measured thickness of the dry CAB sensing layer was 6.7 ± 0.2 µm. The top and bottom view of an array of complete platforms (including encapsulation) is shown in the optical pictures of Figure 5.5. The transparent substrate permitted to see the structures from the bottom.

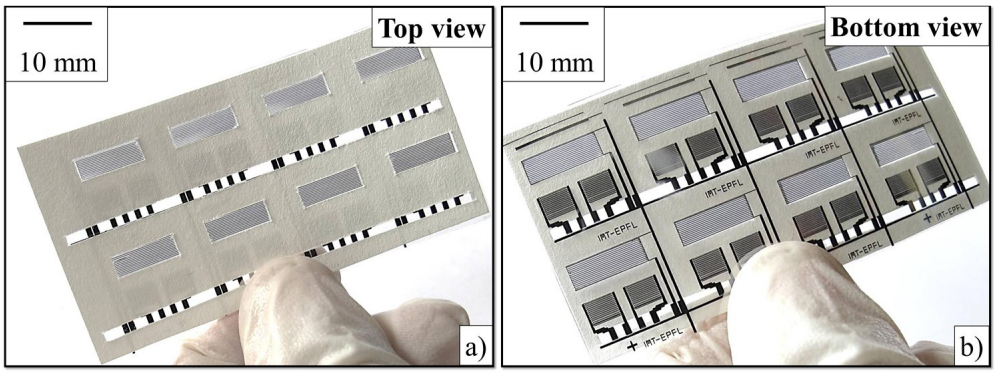

Figure 5.5: Optical pictures of an array of encapsulated temperature and R.H. sensing platforms: (a) top view and (b) bottom view [154].

5.2.3 Characterization of RTD and R.H. IDE sensors

The printed thermoresistors were characterized within a climatic chamber (Bench-Top Temperature and Humidity Chamber, *Espec*) able to reproduce controlled temperature and humidity conditions with a precision of 0.5°C and 2% R.H. respectively. The sample resistance was acquired using the four-wires technique, in order to eliminate any possible resistive contribution due to contact and probes resistances. The measurement protocol used was the following: First of all, the R.H. was fixed at 40 ± 2% while sweeping the temperature up and down between -10 and 60°C corresponding to typical ambient conditions. Then, the temperature was fixed at 40.0 ± 0.5°C while the R.H. was ranged between 20 and 80% (also corresponding to typical ambient conditions). The printed IDE capacitors were characterized within the same climatic chamber described above under similar typical ambient conditions. The measurement protocol was as followed: the R.H. ranged from 40 to 80% at different fixed selected temperatures (15, 35 and 45°C). The limitation in the minimum temperature and R.H. were imposed by the operation of the chamber. Data points were taken after 7s. The customized gas mixing system of Section 3.4.3, allowing quick humidity variations by the automatic gas flow control of dry and wet air into a small chamber of ~ 170 ml at room temperatures was used to measure the transient response of the IDE R.H. sensors.

5.2.4 Results of the operation of the RTD and R.H. IDE sensor

Theoretical considerations As described in [91], the temperature, T, is known to affect the resistance of a metal, R, through the temperature coefficient of resistance TCR as follows:

$$R(T) = R_0[1 + TCR * (T - T_0)] \tag{5.1}$$

, where R_0 refers to the resistance at a reference temperature T_0 (usually equal to 0°C). If the resistor is also subjected to mechanical strain ϵ, then R depends as well on ϵ through the

gauge factor GF:

$$R(T) = R_0[1 + TCR * (T - T_0) + GF * \epsilon] \tag{5.2}$$

Calculation of the temperature coefficient of resistance (TCR) Figure 5.6 shows the thermal response of the printed/plated RTD as the normalized resistance (to the resistance at 0°C, R_0) versus temperature. The tests were performed at a fixed value of R.H. of 40 ± 2%. The experimental data in the graph are represented by discrete markers and the linear interpolation fitting is represented by a continuous line. The TCR was extracted from the slope of the best fitted line and was (6.52 ± 0.05)*10^{-4} °C^{-1} (or equivalent 652 ± 5 ppm/°C) for non-plated devices and (1.82 ± 0.06)*10^{-3} °C^{-1} (or equivalent 1820 ± 60 ppm/°C) for Ni-plated devices. This increase in sensitivity in 3 folds is one of the benefits that plating brings to the system. The coefficient of determination to a linear fit R^2 was higher than 0.999 in both cases. The hysteresis of the devices (defined as the normalized maximum difference between the upsweep and the downsweep curves) was smaller than 1% for both cases.

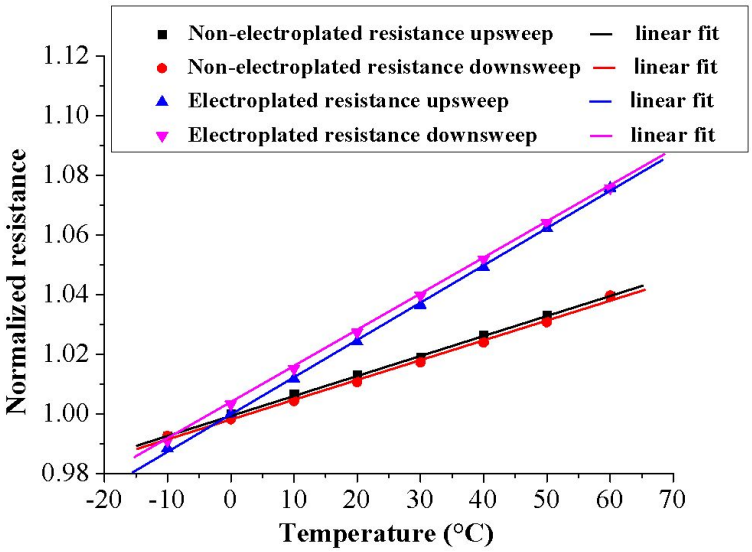

Figure 5.6: Normalized resistance versus temperature of printed/electroplated resistors at R.H. = 40 ± 2% for two different upsweep and downsweep cycles. The points show experimental data and the lines the mathematical fittings by linear interpolation [154].

Influence of R.H. in the RTD The results presented in Figure 5.6 demonstrate the proper operation of the RTD at 40% R.H. However, in logistic the devices will be subjected to different values of R.H. as well. Therefore, the influence of R.H. in the resistance of the RTD must be analyzed. Figure 5.7 displays the results of the tests performed to asses this dependence in the most performing RTD fabricated (those plated with nickel) at a fixed temperature of 40.0 ± 0.5°C. Figure 5.7 (a) shows the results of subjecting the plated RTD to low (44 ± 2%) and

high (84 ± 2%) values of R.H. for 20 hours. The resistance increased in both cases with time. However, whereas little influence (< 0.5% variation) was found after 20 hours in the RTD at a low R.H., a high influence of 2.5% variation was observed at high R.H., suggesting interaction of humidity with the organic residual inside the silver lines and/or oxidation of the silver lines. In spite of the silver lines being plated with Ni on their top side, the water molecules could have reached their bottom after diffusing into the substrate.

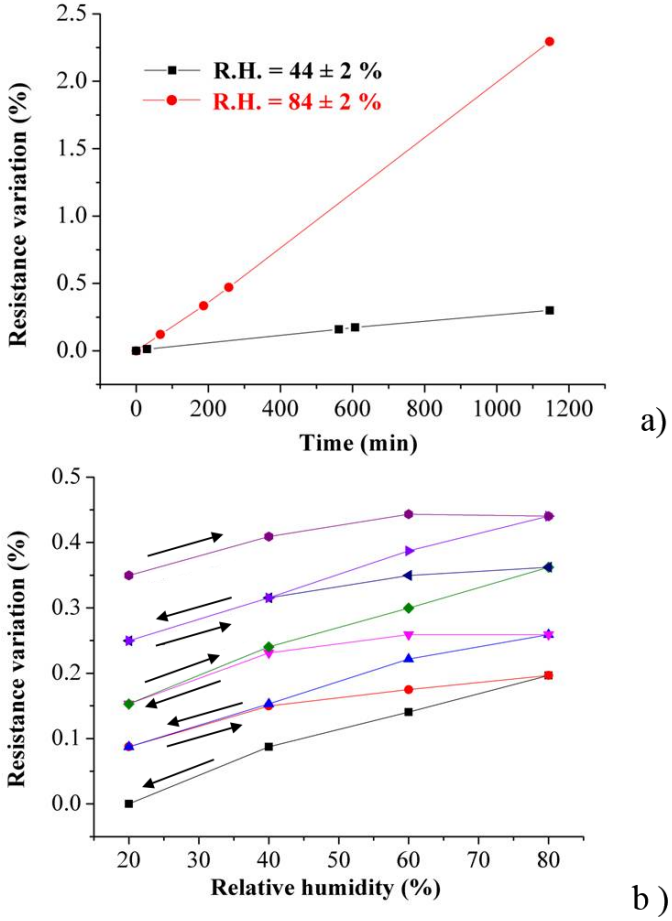

Figure 5.7: (a) Evolution as a function of time for the normalized resistance of the thermometer for two different values of R.H. at 40.0 ± 0.5°C. (b) Resistance versus R.H. for two different upsweep and downsweep R.H. cycles at the same temperature [154].

In Figure 5.7 (b), I show the resistance variation against changes in R.H. varying from 20 to 80 ± 2% R.H. every 40 minutes in successive up and downsweep cycles at a fixed temperature of 40.0 ± 0.5°C. The influence of R.H. could be separated in two contributions: one of them induces a decrease in the resistance after every up and downsweep cycle (with a sweeping range of 60 ± 4% R.H.). The drift in resistance becomes progressively smaller at every cycle. The other contribution is associated to a resistance fluctuation that follows well the upsweep and downsweep R.H cycles. The maximum variation of R.H. in one cycle introduced a resistance shift of only 0.2% in the worse case (corresponding to the first cycle). Such error in resistance

corresponds to only ~ 1°C of error in the temperature determination considering the measured TCR of 1820 ± 60 ppm/°C. Hence, the devices could be still suitable for applications in which the R.H. does not reach high levels or where the required working time is limited to few days. Even though the origin of the R.H. dependence is not understood, we hypothesize that the fact that the resistance follows the R.H. cycles both up and downsweep could be associated to strain generated in the silver lines as a result of substrate swelling upon R.H. absorption, according to Equation 5.2. The decreasing stress during the downsweep cycle would force the resistance to decrease as well. Another possible explanation could be the penetration of water molecules into the silver lines, interacting with (chemically or inducing swelling in) the possible organic residual. The steady drift due to oxidation mentioned if Figure 5.7 (a) should still be present in the situation shown in Figure 5.7 (b), but this effect is now superposed and mostly masked by the other phenomena associated to R.H. cycling. The predominance of the cycling contribution becomes specially obvious when considering the fact that the RTD resistance actually dropped after every cycle, suggesting that somehow the process of sorption and desorption of water into the lines could have assisted the removal of the organic residual from the line. Therefore, the sintering process should be improved by using for instance infrared or photonic sintering that can locally induce high temperature in the metal lines to calcine the organic residual material into the silver lines without damaging the substrate. Another possibility for the drop of resistance after every R.H. cycle could be the reorganization of the nanostructure of the RTD when subjected to small mechanical strains due to substrate swelling. In any case, more studies, including long term operation, need to be carried out to define possible interactions between the silver/nickel lines and humidity, as well as the influence of the substrate on the resistor value due to stress generated upon swelling during humidity absorption.

Humidity sensor measurements at different temperatures I characterized the signal of the printed capacitive R.H. sensors against changes in R.H. ranging from 40 to 80% at three different temperature points, 15, 25 and 45°C. The results are included in Figure 5.8.

It can be observed that the moisture intake and the associated capacitance increased for high temperatures for the same R.H. point. This result was expected considering the Arrhenius expression of the partition coefficient given in Equation 2.7 in Section 2.2 and the demonstrated independence of the partition coefficient with R.H. encountered in Section 4.2.3 of Chapter 4. The dynamic behaviour (evolution with time) of the sensor is presented in Figure 5.8 (a). On the other hand, Figure 5.8 (b) depicts an almost linear behaviour of capacitance versus R.H. for every temperature.

The performances of the sensor (coefficient of linear determination R^2, sensitivity and hysteresis) are shown in Table 5.1 with their standard deviation for all the cases except for the sensitivity, where the maximum between the standard deviation and the error of the linear fitting in Figure 5.8 (b) has been used as error. The response time of the sensor has been calculated as the necessary time to rise from 10 to 90% of the maximum stable signal at room

Table 5.1: Performances of the printed IDE R.H. capacitive sensor as function of temperature.

Temperature (°C)	Linearity (R^2)	Sensitivity (pF/100% R.H.)	Hysteresis
15 ± 0.5	0.997 ± 0.002	0.32 ± 0.01	-
25 ± 0.5	0.981 ± 0.017	0.40 ± 0.05	~ 2% R.H.
45 ± 0.5	0.985 ± 0.005	0.47 ± 0.04	~ 1% R.H.

temperature. The time response (from 10 to 30% R.H.) resulted 360 ± 60 s. Encapsulated devices were measured too and no difference in the response time was observed between encapsulated and non-encapsulated devices.

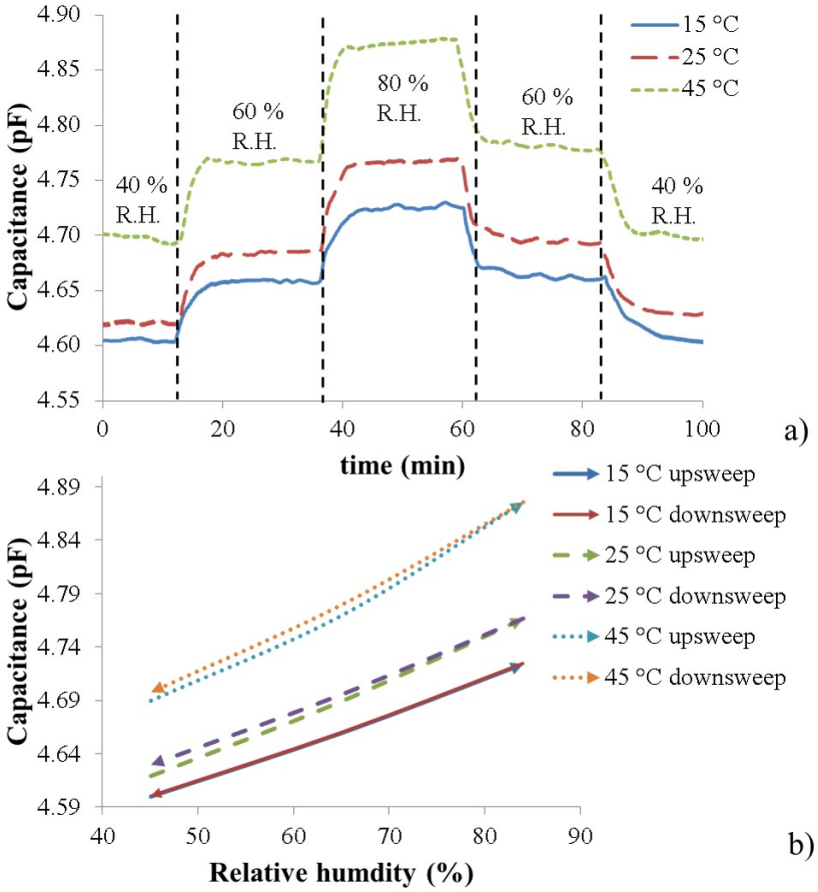

Figure 5.8: Response of the capacitive R.H. printed sensors to upsweep and downsweep R.H. stair case levels at different temperatures: (a) dynamic response and (b) static response [154].

5.3 Printed microhotplates on foil for chemiresistive sensors

5.3.1 Design of the microhotplate

Two different generations of microhotplates were designed and fabricated by inkjet printing silver nanoparticles-based ink on polyethylene naphthalate (PEN) foil. PEN has been selected as substrate material because it presents the best trade-off between price and heat stability compared to others commonly used polymeric substrates in printed electronics, such as polyimide (PI) or PET. Heat stability is important to keep the polymer properties unaltered during fabrication and especially during the operation of the heater at up to 120°C. On one hand, PI has higher glass transition temperature than PEN (400°C against 155°C), but its price in the market is much higher. On the other hand, PET is cheaper than PEN, but its glass transition temperature ranges from 80 to 120°C and its maximum process temperature is only 150°C. Despite the glass transition temperature of PEN being only 155°C, its maximum process temperature is higher so that we can anneal the silver ink at 180°C for some hours before altering the substrate. Temperatures as high as 150°C are not expected anyway during the normal operation of the heater. For the second generation, two versions corresponding to different heater designs were also defined. Both microhotplate generations consisted of similar structures composed of the following layers stacked from bottom to top (see Figure 5.9): PEN substrate, meander-shaped heater, dielectric layer, interdigitated electrodes and sensing layer. Nevertheless, the second generation differed from the first one in that it was 24 times smaller (1 mm^2 instead of 24 mm^2), used thinner substrate (50 µm instead of 125 µm) and also thinner dielectric film between heater and combed electrodes (14 µm instead of 50 µm). This reduction in device size and dielectric layer thickness led to smaller thermal inertia and less heat dissipation. As a consequence, better performances were expected for the second generation of microhotplates than for the first one in terms of thermal and sensing behaviour. On top of that, the version II of the second generation has been developed by modifying the heater shape from a single to a double meander shaped as a square spiral, as depicted in Figure 5.10, while maintaining the same surface area of ~ 1 mm^2. The purpose of redesigning the heater was to improve the thermal homogeneity. Electrodeposition of nickel on the heater is a possibility to increase its thermal stability [156].

Figure 5.10 depicts sketches of the two generations of the heaters included in the microhotplates. The heater from the first generation and the version I of the second generation were designed as simple meanders for the sake of simplicity whereas the version II of the second generation presented a symmetrical double meander (square spiral) shape to improve thermal homogeneity. The optimization of each design to easily achieve the targeted temperature of ~ 100°C at low power consumption, as well as the thermal distribution of every design were firstly obtained by our colleague at EPFL-SAMLAB Dr. Malick Camara using finite element methods (FEM) [155]. The software used for FEM simulation was *COMSOL* (version 4.2). During these simulations, the thermal conductivity of both polymeric films (PEN substrate and dielectric layer covering the heater) was fixed at 0.78 $W*m^{-1}*K^{-1}$, according to a literature survey and the data base of the *COMSOL* software. A coefficient accounting for the overall heat

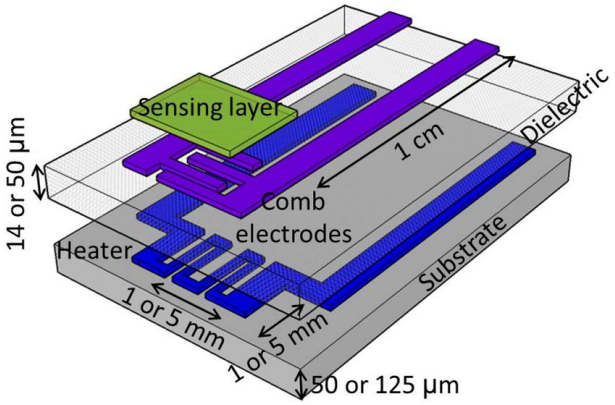

Figure 5.9: Sketch of the structure of the printed microhotplate including from bottom to top: polymeric substrate, inkjet-printed heater, thin dielectric layer, inkjet-printed IDE and conducting polymeric sensing layer [155].

losses was applied to the 2D FEM model to fit the thermal measurements. This coefficient was at 2.6 10^7 W*m^{-3}*K^{-1}. The results are shown in Figure 5.11. The outcome of the FEM simulation indicated that whereas the first generation of heaters required around 150 mW of power to achieve the targeted temperature, the second needed less 35 mW at identical conditions. Furthermore, the thermal homogeneity was very poor for the first generation compared to the second. Regarding the improvements introduced by the double meander version of the second generation of heaters, the simulation envisaged better heat distribution, with less heat concentrated at the centre, and lower thermal gradient toward the edges than its single meander-shaped counterpart.

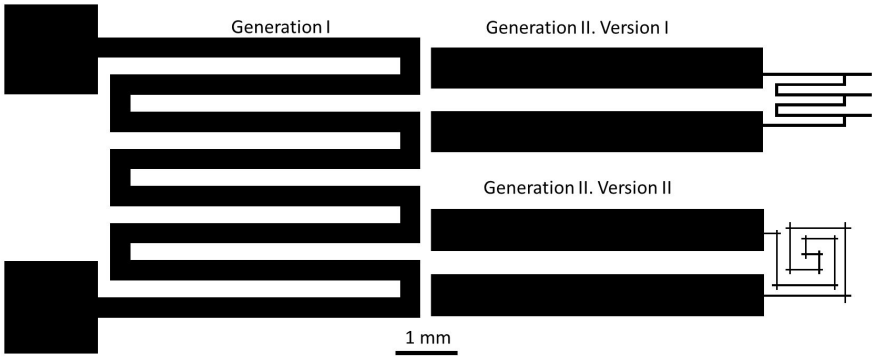

Figure 5.10: Layout of the different designed heaters: The first generation (on the left) was designed as a large meander for reasons of printing simplicity. The second generation (on the right) presented smaller size than the first one and was designed either as a single meander (on the top right), or as a double meander shape for improved thermal performances (on the bottom right).

The first generation of the heater was designed as a meander of a total length of ~ 41 mm placed on a 125 µm-thick substrate. The meander shape was chosen for proof of concept due

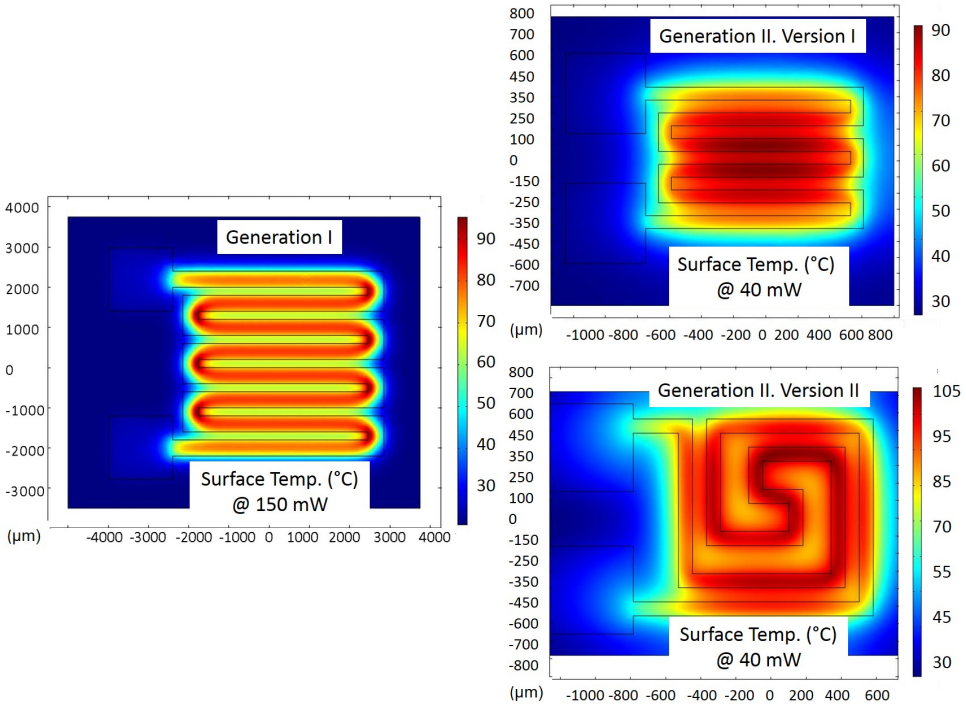

Figure 5.11: Thermographic simulation obtained by finite elements method (FEM) of the temperature achievable by the first (left) and second (right) generations of heaters at identical conditions (courtesy of Dr. M. Camara).

to its simplicity to be inkjet-printed. Adjacent tracks were widely spaced by a pitch of 600 µm to further facilitate the printing process, and they were also relatively large: 300 µm-wide on the layout. The heater thickness was designed to be 1 µm, resulting on a expected heater resistance of 25 Ω. The total surface area of the device was ~ 24 mm^2.

The version I of the second generation of heaters was as a meander of a total length of ~ 7.5 mm placed on a 125 µm-thick substrate. Adjacent lines were designed to have a pitch of 160 µm. The expected net resistance of the heater, i.e. subtracting the residual resistance of the contact pads, was 40 Ω. In the version II of the second generation, the meander-shaped heater was replaced by a heater in the form of a double meander, with a total length of ~ 7.75 mm. The substrate was in this case only 50 µm-thick. The double meander shape was intended to increase the symmetry of the heater, hence homogenizing the temperature over its surface. To further decrease the thermal gradient, adjacent lines were placed closer to each other at the outermost part of the device than at the innermost part (160 µm against 240 µm), compensating for the larger heat dissipation occurring at the edge of the heater, compared to at its centre. The square shape of the meander was chosen because round shapes are challenging to inkjet print. The total expected resistance of the second generation of heaters was also 40 Ω.

For both versions of the second generation of heaters, the line width was designed to be

around 70 µm. The minimum space between patterns was of 90 µm and the line thickness 0.5 µm. The total surface area of the device was ~ 1 mm^2.

On top of the heater, a dielectric film was laminated. The film was targeted to be patternable and as thin as possible to optimize the heat transfer from the heater to the sensing layer onto the film. A dry photoresist was chosen as described in [155]. Combed electrodes were printed then on the dielectric film to complete the structure of the transducer. The combed electrodes were similar for the two generations of hotplates, and were used as resistive transducer for the conductive polyaniline (PANI) sensing layer deposited on top of them. To ensure a good thermal homogeneity along the whole sensing area, we tried to align the electrodes with the heater and kept their surface area slightly smaller than the surface of the heater. The electrode consists of two interdigitated combs. The pitch of the electrodes was designed to be 120 µm, corresponding to 60 µm width and inter-fingers gap space. The total expected thickness of the electrodes was 250 to 300 nm. Silver is known to oxidize, presenting some limitations in terms of chemical compatibility with many sensing layers. Therefore the electrodeposition of a thin film of gold of ~ 500 nm on top of the printed electrodes was targeted to ameliorate the long-term operation of the device while broadening the utilization of sensing materials. Gold is a noble material which is more chemically stable than silver.

The devices from the first generation were directly measured on using standard probes. Therefore, their contact pads were simply squares of 1.5 mm-long side. However the devices from the second generation were designed to be measured using a zero insertion force (ZIF) connector (see Section 3.4.3), suitable for devices on foil. The utilization of the ZIF connector required the contact pads to be as long as 1.4 cm to facilitate their insertion. In order to minimize the heat dissipation on such long contact pads due to Joule effect, they were designed to be much wider and thicker than the heater lines. The designed pads width and thickness of the second generation of devices was 700 µm and 1 µm respectively corresponding to an expected resistance of < 5 Ω, which is negligible compared to the heater resistance. Moreover, the insertion in the ZIF connector required all the pads to be on the same plane (the substrate in this case). Therefore, the contact pads of the IDE needed to cover the step formed by the patterned dielectric film laminated underneath.

5.3.2 Fabrication of the microhotplate

Experimental

The fabrication of the heaters along with some optical images is represented in Figure 5.12 and consisted of inkjet printing (using a *Dimatix DMP 2800*™ printer) of silver nanoparticles-based ink (*SuntTronic Jet EMD506* from *SunChemical*) on 50 µm-thick (2^{nd} Generation) or 125 µm-thick (1^{st} Generation) PEN foil (*Teonex®Q65FA* from *Dupont Teijim Films*™). PEN was selected as substrate material due to its good thermal properties, as explained above in Section 5.3.1. It was cleaned by immersion for 5 minutes in acetone, isopropanol and deionized water, dried in a oven for 30 minutes at 150°C and subjected to (13.56 MHz) oxygen plasma surface

treatment for 35 seconds at 50 W. To optimize the wettability of the substrate by the ink (as described in Section 4.3.2), the substrate was heated up again in the oven for 5 minutes at 120 °C. Two layers were printed selecting a drop-to-drop of 25 µm for the first generation of heaters, and three layers at a drop-to-drop space of 40 µm were printed to fabricate the second generation. The difference in the drop-to-drop space between generations was due to the different resolution targeted for each one; small resolution of around 70 µm was not possible to achieve using 25 µm drop-to-drop space. An extra layer of silver was printed for the second generation of heaters to compensate for the loss in line thickness associated to highly spaced printed drops. When printing the version II of the second generation of heaters, it had to be considered that the printing quality is better along the printing head movement than perpendicularly to it. Therefore, to maintain the symmetry of the layout, all the lines were printed along the printing head (which moved horizontally) as follows: the horizontal lines of the spiral were printed and dried first, and then, the substrate was rotated 90° and aligned to print the vertical lines also along the printer head movement. The patterns were then sintered in a convection oven for 3 hours at 180°C. The sintering temperature was higher here than in the case of the other printed silver patterns described in this thesis to ensure a good thermal stability of the printed heaters. Thermal stability is a must in this application since the device is meant to work at temperatures up to ~ 100°C. Eventually, we demonstrated the possibility of electrodeposition a thin layer of Ni or gold on the silver heater for improved robustness.

Afterwards, photo-patternable dry photoresist 50 µm (1^{st} Generation) or 14 µm-thick (2^{nd} Generation) (*PerMX*™ 3050 from *DuPont*™) was used as the dielectric film for the first and the second generations, respectively. It was laminated onto the heater at 85°C and 2 bars by our EPFL-SAMLAB colleague A. Vásquez Quintero (Ph.D. student). This dry photoresist was selected because of its thermal stability, its mechanical flexibility, the fact that it can be laminated at foil level and subsequently patterned by photolithography, and the good performance that it offered in terms of printability and chemical stability. The dry photoresist was patterned via photolithography to open contact windows on the pads of the device (see Figure 5.12 (b)). On top of the dielectric foil, the electrodes were fabricated by inkjet printing the same silver ink used to print the heater, and they were thermally annealed for 2 hours at 180°C. Annealing the IDE at high temperature was shown be be beneficial for their adhesion to the dielectric foil and chemical compatibility with the sensing layer. Figure 5.12 (c) shows optical images of the second generation of microhotplates right after printing the IDE). Two layers were printed to form the electrodes, using a drop-to-drop space of 40 µm. Special care was taken during printing the pads of the IDE from the second generation to ensure a good step coverage of the dry photoresist. Figure 5.13 shows optical images of microhotplates examples from both generations, before deposition of the conductive polyaniline sensing layer. A device with combed electrodes plated with gold is also depicted. The measured dimensions of the device are indicated below in the part dedicated to the results of fabrication.

The vapour deposition polymerization method was developed to form a thin polymeric acid-doped PANI sensing layer on the polymeric hotplates (see Figure 5.12 (d)). The PANI sensing layer was developed and deposited by our *FlexSmell* colleague E. Danesh at the

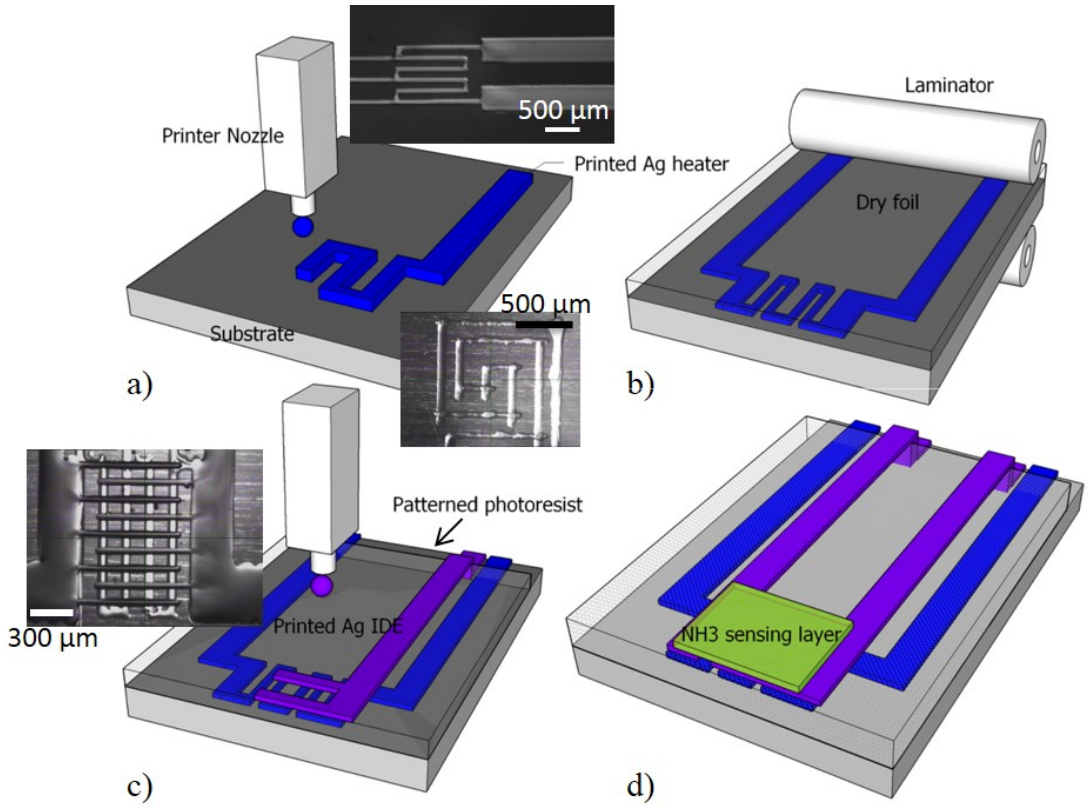

Figure 5.12: Sketch of the microhotplates fabrication process flow (example for the second generation): (a) Inkjet printing of the heater on the PEN substrate. The insets show optical images of the two versions of the printed heaters after thermal sintering of the silver ink. (b) Lamination of a thin dielectric film on the heater for electrical isolation. (c) Inkjet printing of the IDE onto the thin dielectric and optical picture of the device in the inset. (d) Deposition of the polyaniline sensing layer.

University of Manchester (UK). More information about the sensing layer and results can be found somewhere else [155, 157].

Results of fabrication

The meandered line of the first generation heaters resulted 397 ± 6 µm-wide on the fabricated devices. The uncertainty of the measurements corresponds to the standard deviation. The printed lines were wider in the real device than on the layout (300 µm) due to the lateral spreading of the ink. The heater thickness measured 1.2 ± 0.2 µm and it resistance 25 ± 3 Ω, corresponding to a resistivity of 22 ± 3 µΩ*cm.

The version I of the second generation of heaters measured 36 ± 3 Ω of resistance, close to the expected value. On the contrary, the total resistance of the version II was 95 ± 7 Ω. The

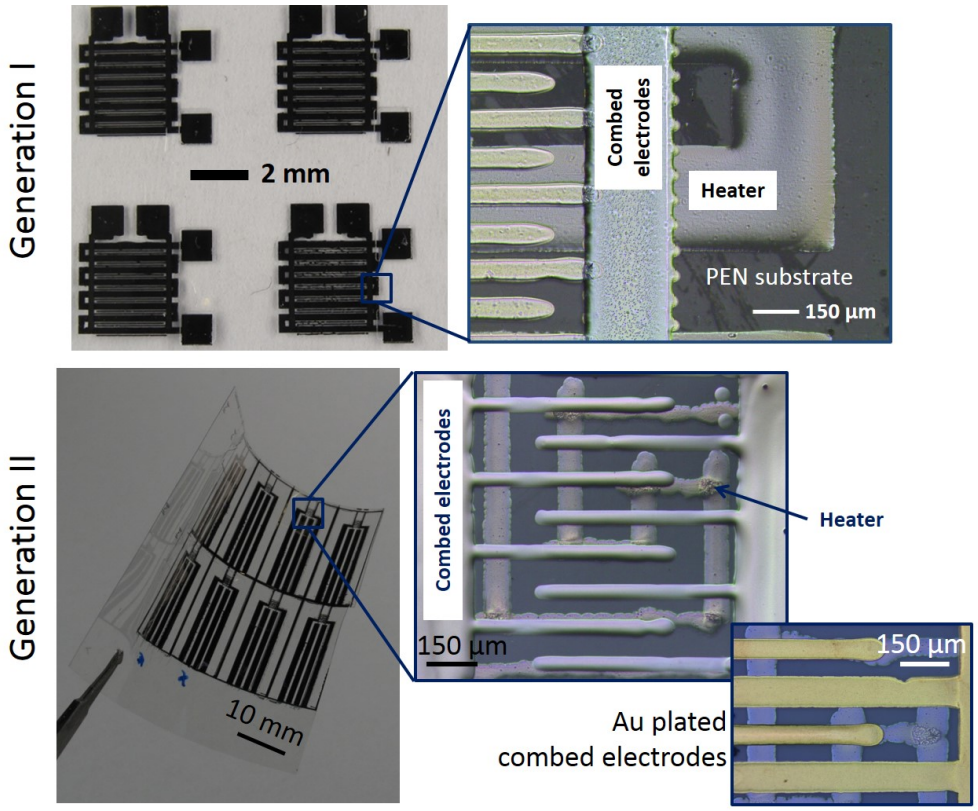

Figure 5.13: Optical images of the two generations of microhotplates depicting examples including a flexible array of the second generation, single devices and close views for both generations and an improved device with gold-plated combed electrode.

mismatch between the experimental and the expected resistance, 40 Ω, can be attributed to cracks observed at the corners of the spiral, appearing during the thermal annealing. We believe that the reason of the cracks formation was the fact that the horizontal lines were printed and annealed first and then the vertical lines were printed on top of them. Since the horizontal lines were already dry when the vertical lines were printed on top, both patterns did not merge properly, resulting in cracks formation during the final thermal annealing. This problem could be solved by skipping the pre-drying of the horizontal lines prior to the printing of the vertical lines on top. Nonetheless, the cracks and the increase of resistance did not affect the good performances of the heater and the devices could be used without further improvements.

For both versions of the second generation of heaters, the experimental line width ended up being 68 ± 8 µm and the thickness of the lines 530 ± 90 nm. Both parameters were averaged over nine devices, and the standard deviation was used as uncertainty. The measured resistivity was 18 ± 7 µΩ*cm.

The IDE printed on top of the dry photoresist had a pitch of 120 µm, corresponding to a measured width of 68 ± 8 µm and a measured inter-finger spacing of 52 ± 8 µm. The electrodes

total thickness was 260 ± 50 nm. To prevent silver from oxidation, the electrodeposition of 400 ± 270 nm of gold on top of the printed electrodes was demonstrated.

Finally, the measured average resistance of every contact pad was 2.3 ± 0.3 Ω as aimed in the design to minimize heat losses.

5.3.3 Results of the operation of the microhotplate

Microheater

Comparison of power consumption between generations The heating elements of the microhotplates were characterized to assess their thermal efficiency in terms of power dissipation, as well as the temperature distribution at the surface of the dielectric layer laminated on the heater. The characterization was carried out by our partners at FEMTO-ST Laboratory in Besançon (France). Type S micro-thermocouples of 1.3 µm of diameter were brought in contact to different points of the device area for a reliable experimental mapping of the surface temperature [159], while DC currents were supplied to the heater using a source *Agilent B2901A*. The power consumption was measured with the same source whereas the parameters of the thermocouples and the room temperature were measured with multimeters *Keithley 2700* and *Keithley 2000* respectively. The results were compared to the finite element methods simulations carried out by our colleague Dr. M. Camara. Figure 5.14 shows the curve temperature versus power for the two generations of the fabricated heaters. The line for the second generation includes both versions because their behaviour is practically identical. The power ranges from 0 to 350 W for the first generation and up to 80 mW for the second generation, enough in both cases to achieve operational temperatures up to 100°C for the former generation and 200°C for the latter. The reported temperature corresponds to the one measured at the centre of the device, on the surface of the dielectric laminated on top of the heater.

The data set corresponding to the first generation of heaters fit a straight line with a coefficient of determination R^2 = 0.9960 and the relation between temperature T in °C and power P in mW was $T = (0.248 \pm 0.008)P + (28.5 \pm 0.7)$. This data set corresponded to a thermal efficiency of 0.248 ± 0.008 °C / mW. On the other hand, for the second generation of heaters, the data fit a line with R^2 = 0.9973 and the relation between temperature T and power P is $T = (1.93 \pm 0.02)P + (27.7 \pm 0.8)$. The thermal efficiency was then 1.93 ± 0.02 °C / mW. Comparing the slopes of the two lines, we can conclude that the second generation of heaters is 7.8 better than the first one in terms of the power dissipation needed to increase the temperature of the sensor. The intercept corresponded to the room temperature at which the devices were measured, and was almost identical for both generations. The results in Figure 5.14 matched very well the FEM simulation depicted in Figure 5.11 for the second generation of devices, but the simulated power was slightly underestimated for the first generation.

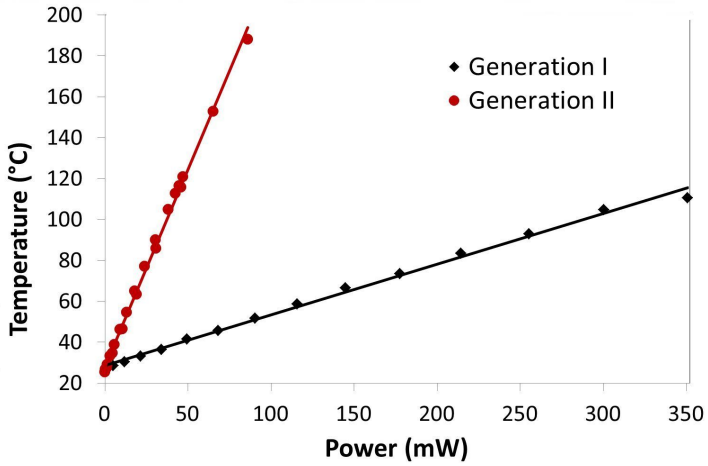

Figure 5.14: Comparison of the temperature achieved at the centre of the heaters as a function of the dissipated power for the first and the second generations of devices. The curve is similar for the two versions (I and II) of the second generation (raw data courtesy of FEMTO-ST, Besançon (France)).

Improvement of the thermal gradient by using double meander heater Once being established the superiority in terms of thermal performances of the second generation of heaters compared to the first generation, we studied the differences between its first (double meander-shaped) and second (single meander-shaped) version in terms of thermal distribution over the device surface. Although both versions displayed similar power consumption as stated above, the second version showed better thermal distribution than the first generation. The surface temperature of the microhotplates was registered following two perpendicular lines, along the x and y axes, that crossed the device and passed by its centre. Figure 5.15 depicts the outcome of the measurements, taken at 50 mW and 40 mW, for the first and the second version respectively. The slightly higher power applied to the first version of heater explains why it reached higher temperature than the second version.

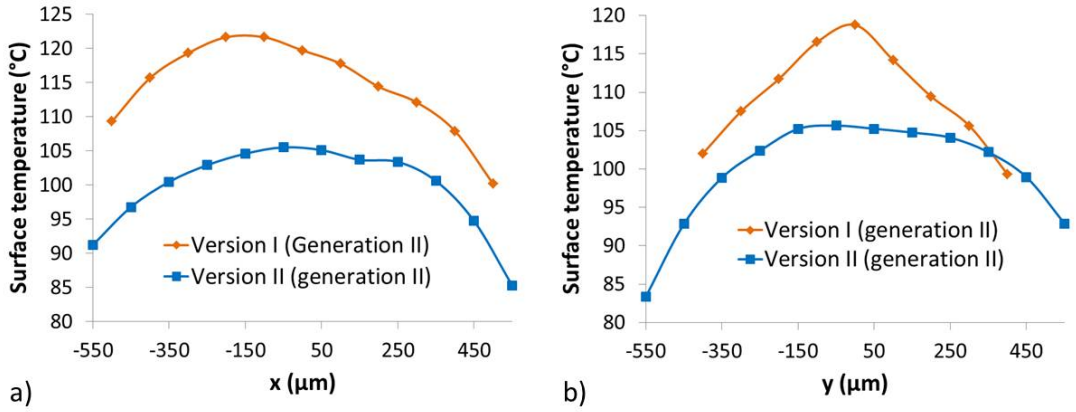

Figure 5.15: Comparison of the thermal profile of the surface for the 1st and 2nd versions of the 2nd generation of micro-hotplates along (a) axis x and (b) axis y (raw data courtesy of FEMTO-ST, Besançon (France)).

The range of temperatures reached by the first type of device corresponded to 100 to 123°C along the x axis and 98°C to 118°C along the y axis, whereas for the second type, the temperature range along the x and the y axes was 85°C to 105°C and 83°C to 105°C , respectively. The figure confirms the better thermal distribution of the double meander-shaped heaters, compared to the single meander-shaped, especially along the y axis and toward the middle of the device. As predicted in the FEM simulation presented in Figure 5.11, the first design lead to much higher temperature generation at the centre of the device than at the edges, resulting in a non-homogeneous thermal profile. As an example, the maximum temperature difference within the space of 600 µm corresponding to the central zone of the single meander-shaped device resulted in 10°C (between 112°C and 122°C) in the x direction and in 13°C (between 105°C and 118°C) in the y direction. The thermal gradient is not so high in the double meander design, which presents a close-to-flat profile in the middle of the device along both x and y axes: maximum temperature interval of 2°C (between 103°C and 105°C) in the x direction and of 4°C (between 102°C and 106°C) in the y direction. This selected zone (600 µm at the middle of the device) is meaningful since it mostly corresponds to the sensing area where the combed electrodes were placed.

Owing to its superior performance, we further characterized the thermal behaviour of the version II of the second generation of microhotplates over its whole surface by adding two profile lines more to the one presented in Figure 5.15, as it is detailed in Figure 5.16 (a). The FEM simulation image of the version II of heater, presented in Figure 5.11, is re-used for the sake of clarity. Figure 5.16 (b) and (c) contain the three profile lines along x and y directions respectively. Both the measurements and the simulations were carried out at 40 mW. The experimental results fitted very well the FEM simulation, which accurately predicted the nominal value of generated temperature, as well as the thermal distribution over the whole surface. We observe that in general the temperature reached a maximum in the middle of the device and decayed nearly symmetrically as the points get further from the centre. Thus, the lines crossing the device at its centre, i.e. A and D, corresponded to the highest temperatures. A maximum temperature of ~ 107°C was registered at the centre of the device. The lowest temperatures corresponded to the corners of the device and ranged between 73°C and 97°C. Clear differences were not found in the thermal distribution between the profiles along the different axes.

Demonstration for ammonia sensing

The application of the microhotplate was demonstrated by our partner E. Danesh at the University of Manchester (UK) by depositing a sensing layer of PSSA-doped PANI on the top IDE electrodes using vapour deposition polymerization process. Figure 5.17 shows an example of the results for the 1st generation of microhotplates where the resistance (normalized to the baseline resistance R_b) is plotted upon exposure to different vapour concentration of ammonia over the range of 250 ppb to 3.65 ppm in dry air at different temperatures (from 20°C to 80°C) generated with the heater.

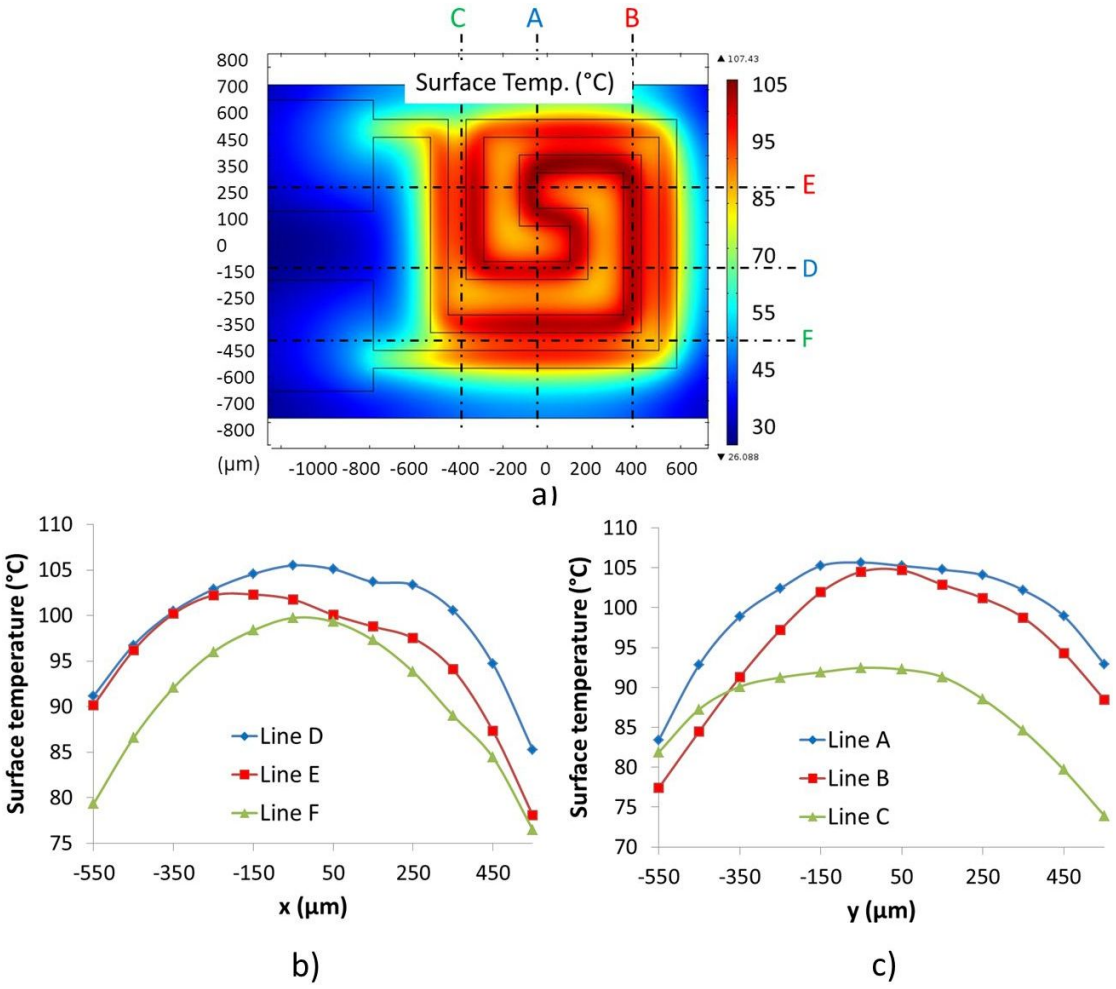

Figure 5.16: (a) Thermographic simulation, obtained using FEM, of the version II of second generation of microhotplates powered at 40 mW. Thermal mapping of the heater surface along three different lines (one centered on the device and two at the edges) in (b) the x direction and (c) the y direction. The measurements were performed by micro-thermocouples while operating the devices at 40 mW (FEM and data courtesy of Dr. M. Camara (EPFL-SAMLAB) and FEMTO-ST, Besançon (France)).

The largest response magnitude was found at room temperature and decreased as the temperature increased. However, elevated temperatures promoted the recovery of the signal. The maximum required power to achieve good performance, at 80°C, was rather high ~ 220 mW.

The second generation of microhotplates have been proven to ameliorate the power consumption by operating well at 35 mW, which corresponded to a sensing temperature of ~ 95°C. These devices were functional and performing also under 50% R.H. conditions. More details about the ammonia sensing experiments can be found in [155] and are expected to be published soon by our partners [157].

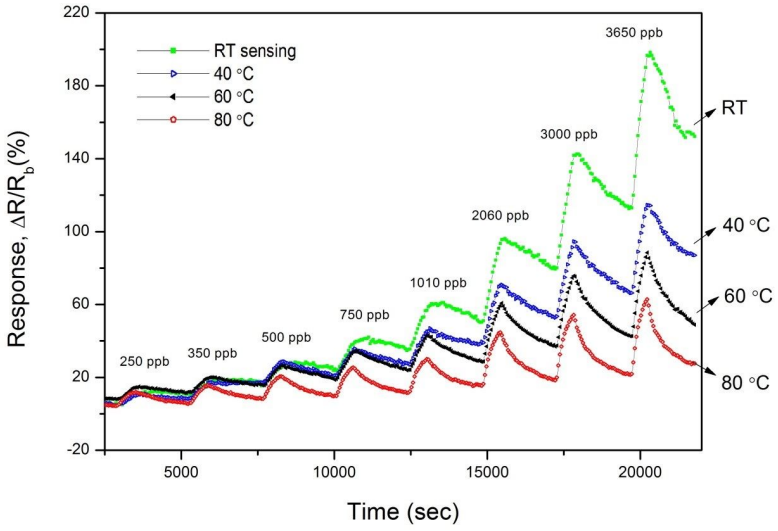

Figure 5.17: Normalized resistance of the hotplate (generation I) versus different concentration of ammonia vapour from 250 ppb to 3.65 ppm in dry air, at four temperatures: 20, 40, 60 and 80 °C (max. 220 mW) with exposure and recovery time of 10 min and 30 min, respectively [155].

5.4 Printed multisensing platform on foil for RFID applications

The printed IDE R.H. capacitive sensors with integrated thermodetector and the microhotplates presented along this chapter in Section 5.2 and 5.3 respectively were combined on the same substrate to form a multisensing platform. In this way, the multisensing platform combined capacitive detection for R.H., along with three resistive channels: one for temperature sensing, one with heating capability for ammonia gas detection and the last one for detection of other volatile organic compounds such as alcohols. The multisensing platform was designed to be integrated in a flexible and printed RFID tag developed by our *FlexSmell* partners at Holst Centre (The Netherlands).

5.4.1 Design of the platform

Design of the platforms

The sensing platform was fabricated on a 200 µm-thick foil for reasons related to their integration, described in Section 5.4.2 and consisted of: 2 large IDE capacitive devices for R.H. detection, 2 small IDE resistive devices (one with heater for ammonia detection and one without heater for other VOCs sensing), and a RTD (see Figures 5.18 and 5.20).

The large IDE capacitors were designed for R.H. detection; one of them was coated with a specialized sensing layer and the other, uncoated, was used as reference for differential measurements. The large IDE devices were composed of 36 fingers 5 mm-long, spaced with a pitch of 120 µm and occupying a total effective surface area of 5.1 x 4.2 mm^2. The microhotplate was, as the one described in the previous section, composed of a double meander heater of

7.5 mm length, dielectric layer 14 µm-thick and one of the small IDE formed by 8 fingers of 0.8 mm in length with a pitch of 120 µm. It occupied a total effective surface area of 1 mm^2. The other small IDE device consisted of 14 fingers (1 mm-long) with a total surface area of 1.2 x 1.6 mm^2, to be used for resistive gas detection without heater underneath. Finally, the resistive temperature detector (RTD) was designed with 6 meanders composed of 240 µm pitch lines of 6.7 mm in length each, adding up to a total length of 83.3 mm and occupying an effective surface area of 7.3 x 2.7 mm^2. Figure 5.18 is a sketch describing the distribution and size of every component on the platform as well as relevant cross sections of the platform indicating the material and thickness of every layer. The fabricated platform (excepting the IDE to be printed on top of the microheater) can be found in Figure 5.20. The figure depicts also a close view of every element,including the IDE over the microheater. The contact pads of this IDE can be seen on the left side of the microheater.

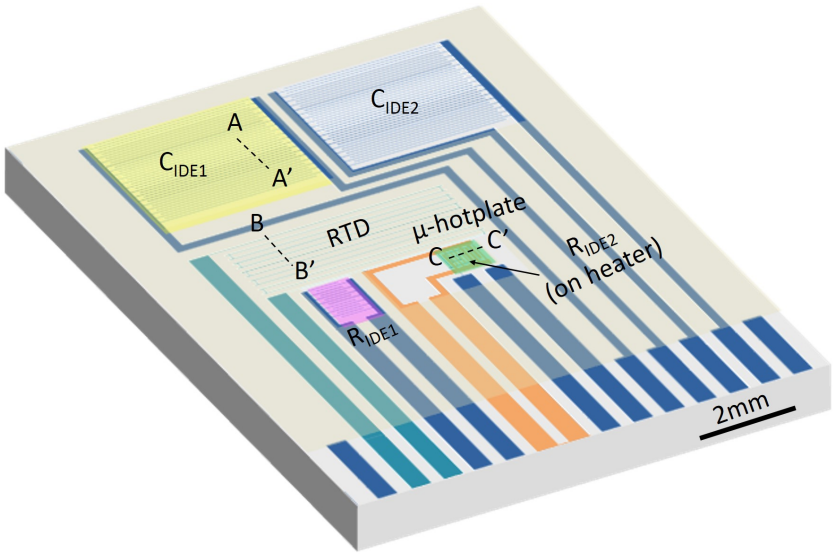

(a)

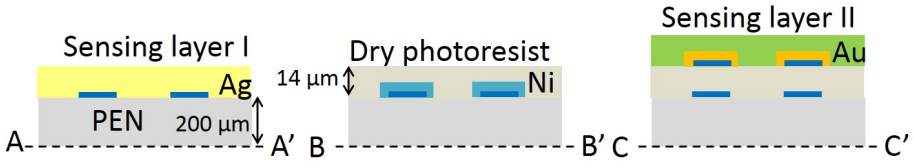

(b)

Figure 5.18: (a) Sketch of the multisensing platform functionalized with 3 different sensing layers. Every component device is labeled. (b) Cross-section sketches of the platform at three representative parts, indicating the different component layers, materials and thicknesses.

The large IDE for capacitive detection were designed to provide a capacitance of 3.5 pF before coating, according to the model in Section 2.3.1. Such capacitance nominal value was selected to optimize the sensor read out by the RFID tag microcontroller. The RTD should be of 1 kΩ before plating and ~ 500 Ω after plating it with 1 µm-thick layer of nickel. The

microhotplate was designed, as before, to have a 40 Ω heater. The capacitance value of the small IDE to be used as chemiresitor should be 0.5 pF. This value was relevant only for testing purposes since the devices were intended to be coated with a conductive polymeric film developed by our partners. A final resistance in the range of 10 kΩ to 1 MΩ was expected for the coated IDE.

As we can see in Figure 5.18, the pads of the platform are compatible with the zero insertion force (ZIF) connector described in Section 3.4.3. Although the platform will be eventually integrated on the RFID tag by means of foil-to-foil techniques, the use of a ZIF connector permitted to clamp and unclamp the platform in the tag as many times as necessary, facilitating the characterization tests.

The platform was covered with a 14 µm-thick dry photoresist film that covered the whole surface except for the IDE active area, the electrical contact pads and a trench around the heater, where the top IDE must be patterned. The trench was defined to reduce the conductive heat losses through the film.

5.4.2 Fabrication of the platform

Experimental

The development of the platform benefited from the expertise acquired throughout the fabrication of the sensing devices described before; it utilized the same fabrication techniques, namely inkjet printing, electrodeposition, lamination and photo-patterning. However, the versatility of inkjet is brought forward by patterning all the transducers in one metallization step, except for the microhotplate that required a second metallization on top of the laminated dry photoresist. The resolution of inkjet printing was improved compared to some of the previous reported devices by employing the substrate treatment and printing parameters described in Section 5.3.2. Although inkjet was used due to its compatibility with quick prototyping, the fabrication of the platform could be readily expanded to other printing methods. We also found that the dry photoresist used between the heater and the IDE in the hotplate could act at the same time as protection layer for the platform and support frame for the subsequent device encapsulation as described in Section 5.2.2 and [154]. The microhotplates imposed the most demanding conditions in terms of silver ink sintering (3 hours at 180°C) and thermal stability during operation. Therefore, the utilized substrate was also PEN (*Teonex®Q65FA* from *Dupont Teijim Films*™) as described in Section 5.3.1. The PEN substrate was this time 200 µm-thick instead of 125 µm-thick to fulfill the requirements of the novel self-assembled method based on water capillarity developed at Holst Centre (The Netherlands), envisaged for the integration of the platform on the RFID tag [160].

The fabrication process flow of the multisensing platform is depicted in Figure 5.19 and consisted of: a) first metallization using inkjet printing of Ag nanoparticles to pattern the following transducers: two large IDE for capacitive detection, RTD, heater, small IDE for

resistive detection (without heater) and contact pads compatible with ZIF connector. b) After annealing the silver ink for 3 hours at 180°C, the RTD was nickel-electroplated as described in Section 5.2.2 to improve its sensitivity (see Figure 5.6). The Ni plating of the IDE was optional and subjected to chemical compatibility issues between the IDE material and its sensing layer. In the same way, the heater could be plated if the current density and operation time intended for the heater were to be very high. c) Lamination, exposure to UV light through a Cr mask and development of the dry photoresist as described in [154, 155, 157]. The photoresist acted as a protection barrier for the platform against chemical and physical agents. We believe that it would also contribute to improve the adhesion of the devices underneath and to ameliorate the robustness of the platform upon bending, reasons why the dry photoresist was laminated at first on the whole platform surface. Afterwards, the photoresist was patterned to open windows only on top of the IDE for their subsequent functionalization, as well as to uncover the electrical contact pads of the platform and to define a trench around the area onto the heater where the top IDE must be patterned (see Section 5.3.1). The RTD remained covered with the intention of minimizing its interaction with moisture, avoiding the chemical and mechanical instabilities reported in 5.2.3. d) Inkjet printing and sintering of Ag IDE on top of the photoresist above the heater as in Section 5.3.2. e) Optional Au electrodeposition of the microhotplate Ag IDE to improve its chemical stability. f) Functionalization of the different transducers by inkjet printing, drop coating or spray coating performed by our different *FlexSmell* partners. One large IDE was not functionalized to be used as reference in differential measurements. Finally the electrodeposition contact pads are cut to make the platform contact pads ready for integration using the ZIF connector or the foil-to-foil integration based on the self-assembly reported in [160].

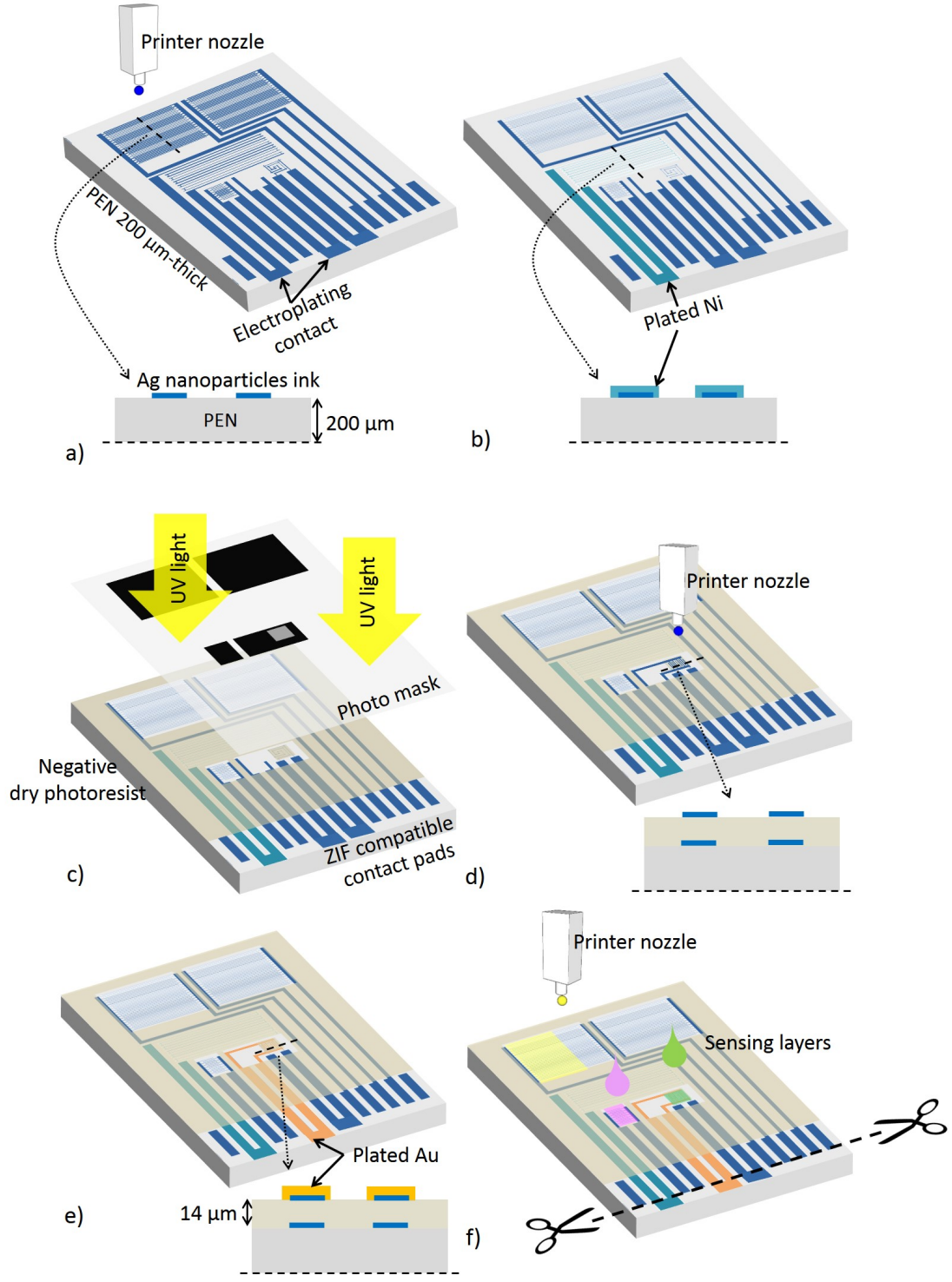

Figure 5.19: Sketch of the fabrication process flow for the multisensing platform: a) inkjet printing the first metallization of transducers using Ag nanoparticles ink; b) Ni electrodeposition of the RTD (small IDE and heater optional); c) lamination, exposure to UV light through a chromium mask and development of the dry photoresist to open windows for the functionalization of the different transducers and interconnection of the platform; d) inkjet printing of Ag IDE on top of the photoresist above the heater; e) Au electrodeposition of the microhotplate IDE; f) functionalization of the different transducers by inkjet printing, drop coating or spray coating, cutting the electrodeposition contact pads.

Results of the fabrication

Figure 5.20 consists of optical pictures of the platform with close view of every component. Compared to the IDE capacitive devices in Section 5.2.2, the width and the gap space of the fingers in this platform varied, 49 ± 4 µm and 71 ± 4 µm respectively (instead of ~ 100 µm and 20 µm), due to the different surface treatment applied to the substrate. However, the pitch was maintained at 120 µm and the lines consisted in both cases of single drop rows. Higher ratio width to gap results in higher value of capacitance (see Figure 2.8 of Chapter 2). However, we were not constrained by surface area limitations in the platform and printing large gaps facilitated the maximization of the fabrication yield. The IDE thickness was 260 ± 60 nm, the RTD thickness was 330 ± 120 nm (before plating) and the microheater thickness was 530 ± 90 nm.

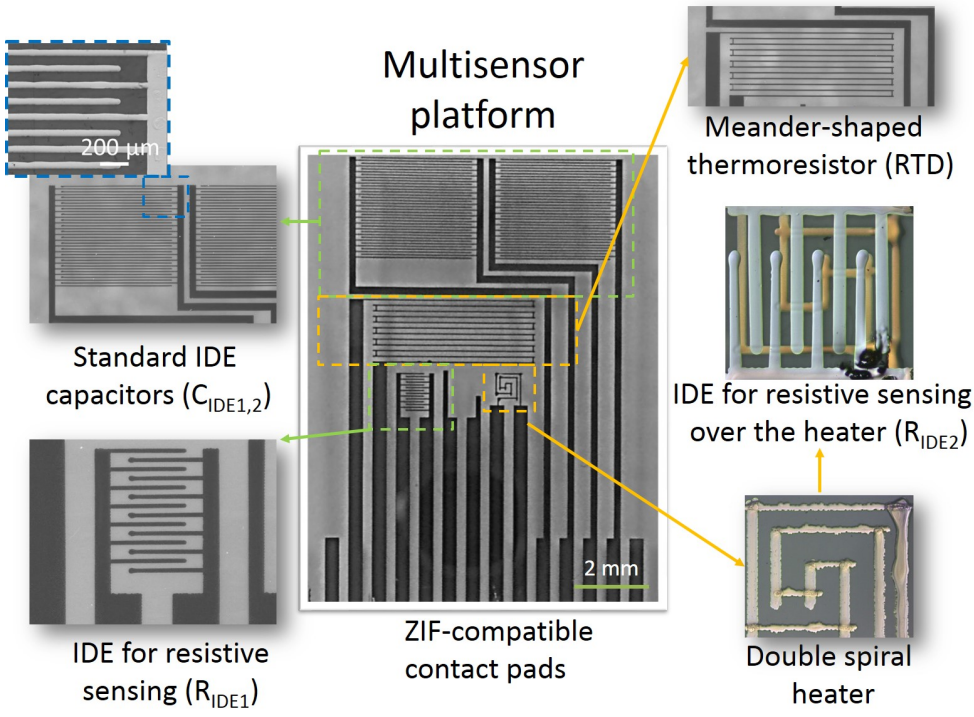

Figure 5.20: Optical pictures of the printed multisensing platforms on PEN foil with close view of every transducing component.

Figure 5.21 shows optical pictures of an array of the flexible printed multisensing platform. The measured nominal values at ambient conditions of the different components of the platforms are summarized in Table 5.2. The two large IDE are uncoated and their capacitance is represented by $C_{IDE1,2}$; the RTD resistance, represented by R_{RTD}, includes bare-printed and Ni-plated devices; the small IDE for resistive sensing are represented by $R_{IDE1,2}$; and the value of the heater is represented by R_h.

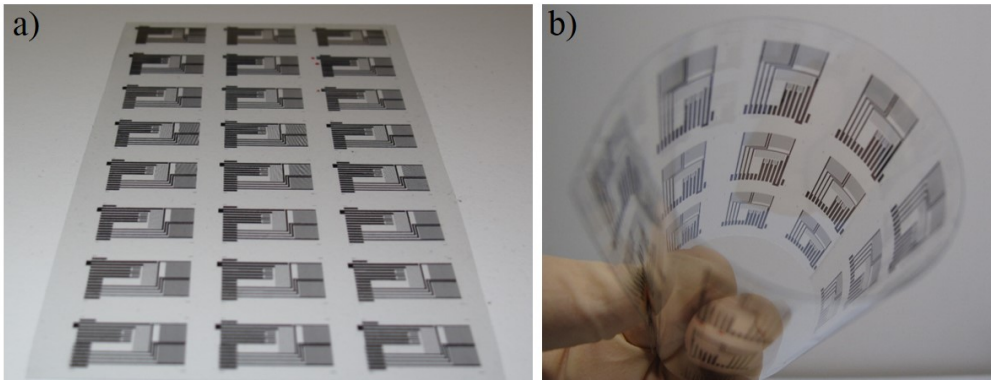

Figure 5.21: Optical pictures of an array of flexible printed multisensing platforms on PEN foil (a) flat and (b) rolled.

Table 5.2: Nominal value of capacitance and resistance for the different components of the multisensing platform.

C_{IDE1} (pF)	C_{IDE2} (pF)	R_{RTD} (Bare Ag) (kΩ)	R_{RTD} (Plated) (kΩ)	R_{IDE1} (pF)	R_{IDE2} (pF)	R_h (Ω)
3.7 ± 0.2	3.66 ± 0.15	0.74 ± 0.09	0.56 ± 0.04	0.52 ± 0.07	0.61 ± 0.02	84 ± 12

5.4.3 Characterization of the multisensing platform and its integration in the RFID tag

Figure 5.22 (a) is an optical image of a multisensing platform with two large IDE (C_{IDE1} and C_{IDE2}), two small IDE (R_{IDE1} and R_{IDE2} without heater), and a RTD. The transducers described above has been functionalized by our *FlexSmell* partners to detect R.H. and ammonia in gas phase. C_{IDE1} and C_{IDE2} were employed to detect R.H. in differential mode (see Section 3.5.5 in Chapter 3) by coating C_{IDE1} with an specific R.H. sensing layer and leaving C_{IDE2} as a reference. The R.H. sensing layer material was either cellulose acetate butyrate (CAB) or poly(ether urethane) (PEUT). These sensing layers were developed by Dr. A. Oprea and the Ph.D. student S. Pandule at IPC-University of Tübingen (Germany), and deposited by spray coating through a shadow mask. R_{IDE1} was coated with polyaniline (PANI) for ammonia sensing by E. Danesh, Ph.D. student at the University of Manchester (UK), using vapour-phase polymerization deposition as in [155, 157]. R_{IDE2} was coated also by our partners at the University of Manchester (UK) with a third sensing layer of polypyrrole for future detection of alcohol. Ammonia is typically released during the spoilage process of fish [161], whereas alcohols such as ethanol are strongly related to the spoilage of poultry and other meats [162]. Other examples of analytes relevant for food spoilage and the kind of food with which they are associated are the following:

- Aldehydes: fruits, spices, essential oils, fried foods [163].
- Alcohols: Poultry and other meat [162].

- Ammonia: Fish [161, 164], eggs [165].
- Esters: Fruits, abundant in apples [166]
- Limonene: Citrus fruits [167].
- Pyrazines: Roasted nuts, chocolate, bread, cocoa, coffee and browned meats, eggs, dairy product and fish [168].
- Sulfure containing compounds: Garlic, onion, beer, putrid odor of spoiled meat [167, 168].

One of the main challenges existing in the field of gas sensing is the ability of a sensor to distinguish, at different temperatures, certain analyte when several of them (including water vapour) are present at the same time. This is the reason why a platform with many sensors integrated and operating together is necessary to increase the selectivity towards the targeted analytes. Figure 5.22 (b) is an example of the success of the multsensing platform approach; it depicts two graphics of the characterization of the functionalized platforms: the image on the left presents the capacitive response of the PEUT-coated IDE (C_{IDE1}) against R.H. for different temperatures (to be measured with the RTD), whereas the image on the right is the variation of resistance of the small IDE coated with PANI in presence of different concentrations of ammonia at room temperature in dry (0% R.H.) and humid (50% R.H.) air. Both the picture and the measurements in Figure 5.22 are courtesy of Dr. A. Oprea and the Ph.D. student S. Pandule from IPC-University of Tübingen (Germany).

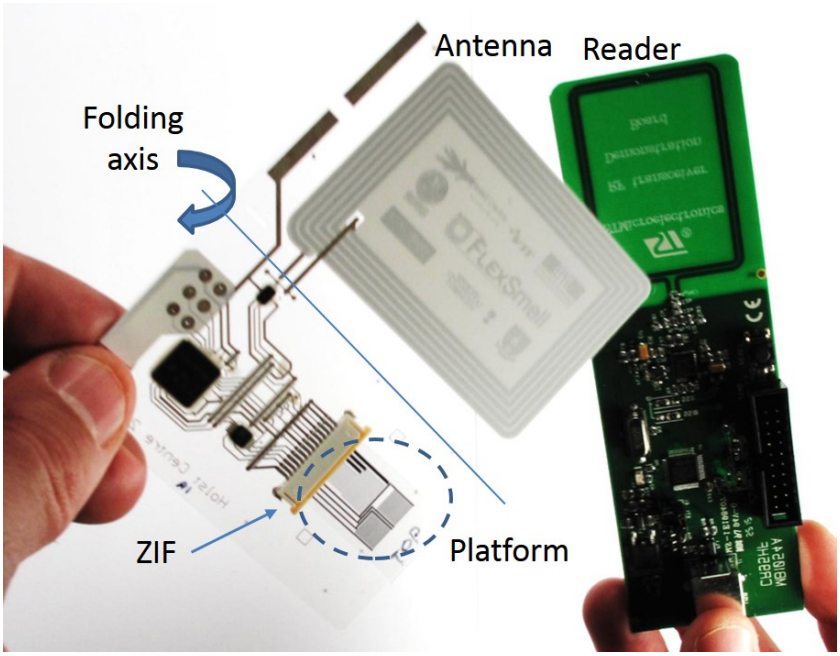

Figure 5.23: Optical picture of the flexible RFID label developed by Holst Centre (The Netherlands) and EPFL-SAMLAB (Switzerland), with the multisensing platform integrated in it by clamping in a ZIF connector. A commercial reader was used to read-out the sensor data wirelessly.

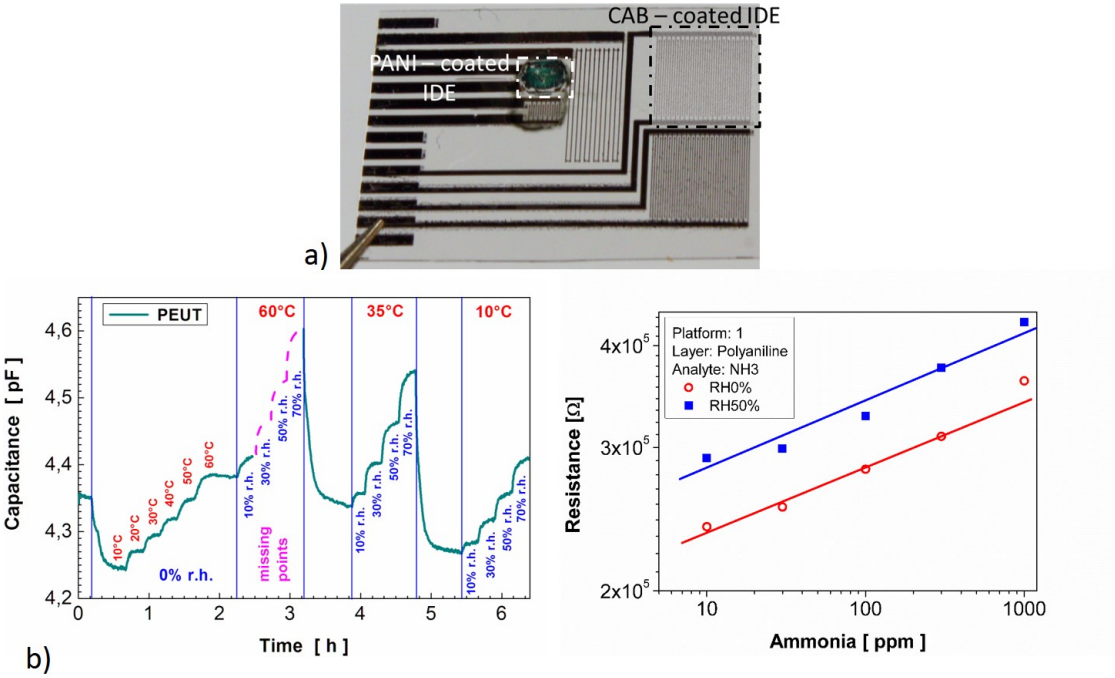

Figure 5.22: (a) Optical image of a multisensing platform with two large IDE ($C_{IDE1,2}$), two small IDE ($R_{IDE1,2}$) (no heater) and RTD. C_{IDE1} is functionalized with an specific R.H. sensing layer (CAB in this case) whereas C_{IDE2} is kept uncoated for reference, R_{IDE1} is functionalized with PANI for ammonia detection and R_{IDE2} is functionalized with polypyrrole. (b) Characterization of the multisensing platform for R.H. (using PEUT as sensitive material) and temperature (left), and ammonia (right) (Picture and measurements courtesy of Dr. A. Oprea and Ph.D. student S. Pandule from IPC-University of Tübingen (Germany)).

Figure 5.23 is an optical picture of the RFID label developed by Holst Centre (The Netherland) which includes an screen-printed antenna and PCB; an analog-to-digital (ADC) Si chip (*AD7150* from *Analog Devices*) as a front-end chip for the capacitive sensors; an RFID Si chip (*M24LR64-R* from ST Microelectronics) for wireless communication; a Si microcontroller (*MSP430F1611* from *Texas Instruments*) to read-out the resistive channels, store data in data logging mode and manage the RFID and ADC chips. The label is designed to be folded in its middle, accommodating a thin film battery inside. A commercial reader (*MB1054A* RF transceiver Demonstration Board from *ST Microelectronics*) was used to read-out the data from the sensors. The multisensing platform is clamped in the label using a ZIF connector for quick prototyping. However foil-to-foil integration is to be performed afterwards using a method developed in Holst Centre (The Netherlands) [160] to self-align the platform, followed by mechanical and electrical interconnection strategies developed by our EPFL-SAMLAB colleague A. Vásquez Quintero, which consists of through-foil vias definition in dry photoresist filled with isotropic conductive adhesive [169].

The implication of the platform design and the RFID label architecture on the gas sensing process need to be taken into account in the future by establishing a logic measurement

protocol managed by the microcontroller of the RFID label. For instance:

- In order to have an accurate value of ambient temperature and due to the close proximity of the RTD to the microheater, it would be preferable to measure the temperature before activating the microheater for ammonia sensing.
- If the power available in the label is not enough to simultaneously activate several sensing blocks, one block should be switched off before the next one is switched on. In this case the capacitive read-out should be activated right after the RTD so the former can profit from the the recent temperature measurements obtained by the latter.
- The sampling time should be adapted to the demands of the application while trying to minimize the overall power consumption.
- Etc...

5.5 Conclusions

I presented in this Chapter the design, fabrication and characterization of different inkjet-printed sensing elements on foil and I demonstrated the potential of combining them in the same multisensing platform to detect temperature, R.H. and ammonia gas. Moreover, the multisensing platform is readily integrable in a flexible RFID label with sensing capabilities. The multisensing platform includes two IDE devices for capacitive gas detection, a third IDE for resistive gas detection at room temperature, a microhotplate formed by a heater and a fourth IDE on top for resistive gas detection, and a resistive temperature detector (RTD) for environmental temperature control. In this chapter I described how every transducing element was individually fabricated using inkjet printing and electrodeposition on plastic foil, and subsequently characterized (with test sensing layers for validation). Then, I showed how all the individual elements were eventually combined on the same sensing platform compatible with integration on a RFID label for food freshness and quality traceability control. The label was developed in collaboration with the *FlexSmell* partners at Holst Centre (The Netherlands). My role in this work was the fabrication of the transducers by means of only additive processes, namely inkjet-printing and electrodeposition, compatible with large-area production. These transducers were functionalized for the detection of R.H. and ammonia by deposition of customized sensing layers developed by different *FlexSmell* partners at the University of Manchester (UK) (responsible for coating the IDE resistive sensors) and IPC-University of Tübingen (Germany) (responsible for functionalization of the IDE capacitive sensors).

Regarding the IDE capacitors and the RTD, I have presented their combined design, fabrication and characterization as R.H. sensors and thermometers respectively. It was also mentioned that the devices were encapsulated at foil level and low temperatures. The meander-shaped RTD served as on-foil thermal compensation for the IDE capacitive humidity sensors.

The R.H. sensors were characterized for different R.H. and temperature values ranging from 10% to 80% and from 15°C to 45°C , evidencing the need of thermal compensation during the R.H. sensing process. The response of the bare-printed capacitive R.H. sensors was stable and reproducible after several weeks, close to linear and reversible (little hysteresis). Compact devices have been achieved by improving the printability of the ink on the polymeric substrates, which also presented good enough adhesion to permit the electrodeposition of Ni on the silver seed. Electrodeposition was desirable because the printed RTD increased their TCR in almost 3 folds after electrodeposition of nickel on them. They displayed linear variation with temperature, but also interaction with R.H. which was not fully understood. However, the devices were still suitable for the most part of practical applications dealing with environmental monitoring where high values of humidity and temperature are not kept for long time. For future improvements, the time consuming thermal annealing utilized could be substituted by flash photonic or near-infrared sintering to increase the reliability of the sintering process and the throughput of the fabrication. Passivation of the RTD against moisture using chemical barriers, along with photonic sintering could contribute to an enhancement of its stability.

In regards to the microhotplates, the devices consisted of fully inkjet-printed silver heater patterned on a PEN substrate and IDE on top of the heater, both elements separated by a thin patternable dry photoresist. The power consumption and thermal gradient of the heaters were optimized through the development of two different generations. The second generation of devices outperformed the first one owing to their smaller size (1 mm^2 versus 24 mm^2), thinner substrate (50 μm instead of 125 μm) and thinner dielectric film (14 μm instead of 50 μm), demonstrating the crucial importance of good printing resolution and structure design. The second generation of heaters was further improved in terms of thermal distribution through the development of a second version, which involved the redesign of the heater geometry from a single meander to a double meander shaped as a square spiral, while keeping the same device footprint. Finally, the operation of the microhotplates as sub-ppm ammonia chemiresistors was demonstrated through coating the IDE with PSSA-doped polyaniline by means vapour-phase deposition polymerization. Both generations of microhotplates displayed better performance at elevated temperatures generated by the heater than at room temperature. Although not shown in this report, the second generation outperformed the fist one and permitted fast and selective detection of ammonia in both dry and wet air when operated at ~ 95 °C, which required ~ 35 mW [157]. The electrodeposition of gold on the microhotplate IDE was demonstrated for better chemical stability and compatibility of the IDE with the sensing layer.

The capability of the multisensing platform to detect relative humidity at different temperatures and ammonia vapour at different values of humidity have been demonstrated. Inkjet printing has been proven to be very convenient for the fabrication of this kind of systems that include several devices with different line thickness and coatings, but that share a common substrate. Inkjet printing also makes possible a quick redesign of the platform to add or remove funcionalities.

6 Discussion

This chapter aims to discuss the outcome of the different chapters of this thesis as a whole. The results of each chapter are related and the implications of the utilized technology on every developed device and its inclusion in the final multisensor platform is analyzed.

6.1 Theoretical considerations

Some theoretical models were developed by adapting the existing theory to our specific case of materials and geometries in order to define the working principle of every fabricated sensor and to optimize their design. The sensing principle of capacitive gas sensors is known to be based on the diffusion of the analyte into the polymeric sensing layer. As a result, the analyte modified both the sensing layer permittivity and its thickness. For an optimum design of both IDE and PP capacitive sensors, the next points were highlighted as important: The higher the difference between the analyte permittivity and the sensing layer permittivity, the greater the sensitivity is (for a fix absorbed volume of analyte) due to larger changes in the total effective permittivity. In the same way, the higher the volume of absorbed analyte is (either due to the presence of a higher concentration or to larger analyte molecules) the higher the change in permittivity and the swelling of the sensing layer is. Thick sensing layers enhance sensitivity in IDE structure (until reaching a thickness equal to the fingers pitch, after which the value of capacitance and the sensitivity saturates) but decreases sensitivity in PP structures owing to larger separation between the parallel plates. In any case, for the case of humidity detection, the permittivity of water is so high (ϵ_a = 76.6) that the swelling component can be usually neglected. On the other hand, as in every diffusion-based process, time response increases quadratically with the thickness of the absorbing layer so a compromise between sensitivity and time response needs to be found in IDE capacitive sensors, unless IDE can be fabricated with very small pitch, which is challenging using standard printing technologies. For PP gas senors, thin sensing layer are advantageous for both high sensitivity and fast response. Regarding PP-MEMS sensors using the substrate as swelling-driven sensing layer, the sensitivity only depends on the absorbed volume of analyte, but it is independent of the permittivity of the analyte. This marks a fundamental difference with the rest of the sensors

presented, opening the door to the investigation of new sensing strategies leading to increased selectivity. If a large volume of analyte is absorbed into the substrate of a PP-MMES sensors, it would experience a large swelling that induces high stress in the MEMS bridge, making it buckle up as a result. In terms of time response, the same considerations applying to standard PP and IDE sensors apply to the PP-MEMS sensor as well, i.e., thick sensing layer (substrate in this case) yields slow response.

In terms of the implications of making IDE gas sensors on foil, it has been described that IDE generates electric field below and above the plane where they are contained, interacting with the substrate and the sensing layer. Contrary to Si-based IDE gas sensors where the Si substrate is insensitive to gas and thus does not affect the sensing process, the polymeric substrate of our devices absorbs gas. If the substrate is considered as a sensing layer, this effect is in principle beneficial for sensitivity. Nevertheless, the role of the substrate is usually to provide mechanical support; hence it is not optimized for sensing and its contribution considered as a inconvenience most of the times. Mainly, commercial substrates are usually too thick to allow a fast sensor response time and they lack selectivity. The undesired influence of the substrate has been circumvented by performing differential measurements where the response of one IDE coated with a specialized sensing layer is compared to the response of another uncoated IDE for reference. Differential measurements allowed fast response time but did not result in high sensitivities. Moreover, the use of two devices and post measurement signal treatment became necessary. Larger sensitivities could be achievable by adjusting the ratio of sensing layer thickness to IDE pitch, by either increasing the sensing layer at expenses of increasing the time response, or ideally by reducing the electrodes pitch as much as possible, which is very challenging with printing techniques. As an alternative to differential measurements, we have demonstrated passivation of the the substrate against absorption of the analyte using a barrier layer. In PP structures, the electric field is exclusively contained in the sensing layer "sandwiched" between electrodes so it does not reach the substrate. As a result gas sensors based on PP present higher sensitivity and smaller response time than their IDE counterparts without the need of differential measurements or substrate passivation.

Concerning IDE capacitive transducers, an analytical model has been developed to calculate their capacitance and the influence of bending. The outcome of such models could be summarized in the next two main points: 1) The capacitance value of IDE capacitors increases with the permittivity and thickness of the substrate and sensing layer (up to a thickness equal to the fingers pitch), number of electrodes, electrodes thickness, electrodes length and the ratio width to inter-finger space; 2) Bending circularly the electrodes around the axis perpendicular to them has a small influence in the capacitance value for typical structures (0.5 to few % for a radius down to 2.5 mm). The presence of a sensing layer on top of the electrodes in the case of gas sensors would decrease this influence. Although it has not been studied, it is expected that bending the electrodes around their axis does not have a big influence in the capacitance neither.

6.2 Fabrication of the sensors

All the devices were fabricated on commercially available polymeric foils, mainly polyethylene terephthalate (PET) and polyethylene naphthalate (PEN) for those devices requiring high process temperatures (up to 180°C). Despite its high thermal resistance, polyimide (PI) substrate was discarded due to its higher price, an specially after showing poor results in terms of printability and adhesion of the printed metal. Commercially available silver nanoparticles-based inks were used as base material to pattern the sensors by inkjet printing. For every ink/substrate pair, the optimum printing parameters were defined. Since the silver ink needed thermal sintering at only around 150°C to become conductive, its use was compatible with the use of PET and PEN. Bare-printed silver nanoparticles lines resulted typically very thin and chemically instable. Therefore, a process of electroplating Ni on bare-printed lines (to a maximum thickness of 15 μm) was explored to thicken and passivate them. Problem of delamination between lines and substrate were observed for thicker layers. Contrary to bare-printed lines, the Nickel-plated lines did not show appreciable signs of oxidation with time. The sensing layer used for the most part of the devices was R.H. sensitive cellulose acetate butyrate (CAB). The preparation of a CAB solution with the right values of viscosity and surface tension for inkjet printing was successfully achieved.

As commented above, small electrodes pitch is desirable in IDE capacitive sensors since it increases the capacitance per surface area and the sensitivity of the sensor. A reduction of the IDE pitch was achieved by depositing a thin film of parylene-C between both printed combs. In that way, the pitch of the fingers could be reduced as much as their width allowed it without risking electrode shortcircuits. Parylene-C is a very chemically stable and tight chemical compound that served at the same time as passivation layer for the PET substrate, making unnecessary the use of differential measurements.

In the case of standard PP-devices, we demonstrated fair chemical compatibility between the solvent of the ink used to print the top electrode and the CAB sensing layer. The high roughness of the printed top electrode and its porosity allowed moisture to reach the sensing layer without the need of complex patterning of gas intake windows on the top electrode. However, the unevenness of the CAB sensing layer limited the thinness of the sensing layer to few micrometers.

In order to develop PP-MEMS, I succeeded to find an inkjet-printable sacrificial layer compatible with the solvent of the silver ink, permitting me to fabricate suspended microbridges. The dissolution of the sacrificial layer was critical to avoid stiction problems. Hence freeze-drying process was used to avoid capillarity forces responsible of the microbridges collapse and stiction during the releasing step.

Inkjet-printed microhotplates were fabricated using PEN foil as substrate due to its higher thermal resistance than PET. A laminated thin film of dry photoresist was laminated onto a microheater inkjet-printed on the substrate and then, IDE was inkjet-printed and gold electroplated on top of the pre-patterned photoresist. High temperature sintering (180°C)

improved the thermal stability of the heaters and the IDE stability during the subsequent step of PANI deposition.

Finally, all the previous devices (except the PP-MEMS) were inkjet-patterned on the same substrate in one metallization step (except for the microhotplate that required two metallization steps). The utilized substrate was PEN, compatible with the microhotplates fabrication and operation temperature. The multisensing platform is to be functionalized by our *FlexSmell* partners for different analyte detection.

6.3 Performances of the different developed sensors

Table 6.1 summarizes the performances at room temperature (25 ± 5°C) of all the capacitive R.H. sensors developed along this thesis, i. e., the standard IDE devices with 5 µm-thick layer of plated Nickel and the IDE devices with reduced size described in Chapter 3, the standard and MEMS-based PP structures detailed in Chapter 4 and the IDE sensors (with RTD integrated) developed for the multisensing platform reported in Chaper 5.

Table 6.1: Comparative summary of the performances at room temperature of all the capacitive R.H. sensors developed along this thesis: capacitance per surface area C/A, sensitivity defined as change of capacitance normalized to the nominal value per 1% R.H. variation ($\Delta C/C_0$ / 1% R.H.), time response defined as the necessary time to rise from 10 to 90% of the stable signal, and linearity of the curve capacitance versus R.H. defined by the coefficient of linear determination R^2.

	C/A (pF/mm^2)	Sensitivity (/ 1% R.H.) (%)	Linearity (R^2) (-)	Response time (sec)
Standard IDE (plated)	0.12	0.040	0.997	270 ± 60 (diff. mode)
Reduced size IDE	0.44	0.073	0.992	270 ± 60 (single mode)
Standard PP	3.8	0.330	0.970 (up to 60% R.H.)	50 ± 20
PP-MEMS	1.5	0.128	0.976	> 30 min.[1]
IDE in the tag	0.17 to 0.23	0.121	0.981	360 ± 60 (single mode)

Every sensor was fabricated with CAB sensing layers of similar thickness ~ 7 µm, facilitating their comparison in terms of geometry. The table includes capacitance per surface area C/A of every device, their sensitivity defined as change of capacitance normalized to the nominal

[1] Measured in a static mode in a climatic chamber.

value per 1% R.H. variation ($\Delta C/C_0$ / 1% R.H.), time response defined as the necessary time to rise from 10 to 90% of the stable sensor signal for the step 10 to 30 ± 5 % R.H., and linearity of the curve capacitance versus R.H. (up to 70 ± 5 % R.H.) defined by the coefficient of linear determination R^2.

According to the data in Table 6.1, the best performances for a standalone device correspond to the standard PP sensor. Although its fabrication imposes some restrictions in terms of used materials, they provide the highest capacitance per surface area and sensitivity. The PP sensor also presents the lowest response time among the fabricated sensors, although compared to a commercial humidity sensor *Sensirion SHT15*, its time constant (from 0 to 63% of the total signal shift) is still relatively high, τ = 17 s against 8 s. However, the combination of several devices with different sensing layers would be facilitated by IDE, which are easier to coat and offer wider choice for sensing materials than PP devices. PP-MEMS devices exploit a new sensing principle, and even though their sensitivity towards R.H. is already comparable to that of IDE sensors, there is a lot of room for improvement specially for detection of other gases. Their novel sensing principle suggest them as the perfect complement for IDE and standard PP gas sensors. The linearity of the sensors is very high in every case.

Regarding the resistive thermodetectors (RTD), their temperature coefficient of resistance (TCR) increased from 652 ± 5 ppm/°C for non-plated devices to 1820 ± 60 ppm/°C after plating the devices with a thin layer (1 ± 0.5 µm) of Ni.

7 Conclussions

In this thesis, I worked on printed microsensors on plastic flexible foil for gas detection. The work was performed within the frame of the *FP7 Marie Curie ITN* European project, *FlexSmell*, which targeted the development of a printed chemical sensing systems on flexible plastic substrates for wireless applications, such as perishable goods monitoring during transportation. Therefore, low-power consumption, low-cost, light-weight and mechanical flexibility are key points of the system. Bearing in mind these requirements, different inkjet-printed devices were developed on foil and their functionality was demonstrated by functionalizing them with sensing layers for proof of concept. Interdigitated electrode (IDE) capacitors were developed for relative humidity (R.H.) detection utilizing a customized sensing layer of cellulose acetate butyrate (CAB). In addition to the optimization of the printing process to minimize the foot print of the devices, achieving a minimum patterned line width of ~ 40 μm, a fabrication strategy was developed to further reduce the IDE dimensions while increasing the fabrication yield and improving simultaneously the sensing performance through passivation of the substrate. Using the same technology, resistive thermodetectors for temperature measurement and calibration of the temperature influence in R.H. sensing were developed. Besides IDE, performing parallel plates (PP) R.H. capacitive sensors in which the CAB sensing layer was sandwiched between the two plates were successfully fabricated. Their fabrication led to the development of a novel kind of MEMS-based PP sensors consisting of arrays of microbridges utilizing the substrate as swelling sensing layer. Compared to their PP counterparts, IDE sensors presented the advantage of requiring only one metalization step to be patterned, and of having the sensing layer in the topmost part of the sensor, maximizing its exposure with the environment. On the other hand, the employed polymeric substrate introduced a parasitic contribution to the sensor signal which required either passivation of the substrate or differential measurements with a second device used as reference. PP devices on their side, encountered many constraints regarding material choice due to chemical incompatibility issues arising between different printed stack material layers. However, they are inherently more sensitive and were easier to miniaturized than IDE sensors. Indeed, as displayed in Table 6.1 in Chapter 6, the standard PP humidity sensor was the most performing one developed in this thesis in terms of capacitance per surface area (3.8 pF/mm^2), sensitivity (33% full range)

and response time (50 seconds). The short term operation performances of the the developed sensors are comparable to those of commercial humidity sensors fabricated on rigid substrate with standard clean room techniques. However, the long term operation, cross sensitivity behaviour and mechanical robustness of this novel kind of printed sensors on foil has not been evaluated yet.

Finally microhotplates formed of a stack of foil substrate, meander-shaped heater, thin dielectric, IDE and conductive sensing layer of polyaniline (PANI) were developed on only 1 mm^2 of surface area. Their functionality has been demonstrated for resistive sensing of ammonia at high temperature of 90°C, which demanded 35 mW. The aforementioned devices were successfully demonstrated independently and the added value of their integration on a common multisensing platform was highlighted by simultaneous detection for the first time of temperature, R.H. and ammonia. The inkjet-printed sensing platform was readily integrable on a printed flexible radio frequency identification (RFID) label developed in collaboration with our *FlexSmell* partners at Holst Centre (The Netherlands). The multisensing platform is being currently customized for different analyte detection by our *FlexSmell* partners at University of Manchester and IPC-University of Tübingen (Germany).

As future improvements for the devices presented in this thesis, alternative printing methods such as microcontact printing or electrohydrodynamic jet printing can be used to drastically increase the IDE patterning resolution to few microns or even sub-micrometer resolution. High printing resolution would favor gas sensitivity and response time of IDE sensors, but also minimize the power consumption of the microhotplate. The mentioned printing methods involves very low amounts of solvent compared to more standard printing technologies, eliminating the chemical incompatibility problem of printed stack layers that we faced during the fabrication of PP sensors. Reducing the amount of solvent involved in the printed process, thus smoothing the PP sensing layer, or cross linking it would allow us to reduce the thickness of the sensing layer of PP sensors, increasing as a result their sensitivity and decreasing their time response. Very fast and small (hundreds micrometer size) PP sensors fabricated by single drop inkjet and microcontact printing with very thin (~ 1µm) CAB sensing layer with improved homogeneity are currently being investigated in our laboratory. In order to measure sensors with sensing response time below 20 seconds, a new gas measurement set-up using a smaller measuring chamber is required.

Another improvement which could be taken into account consists of the possibility to explore more advanced moisture barriers for the substrate consisting of stacked layers combining organic (such as parylene-C) and inorganic materials (such atomic layer deposited aluminum oxide), which could be used to improve the stability of both R.H. and temperature sensors, and totally eliminate the influence of the substrate. The stability of the devices could be also improved by substituting the printed silver lines with gold lines. Silver tends to oxidize and is less chemically stable than gold. There currently exists a commercial inkjet printable gold nanoparticles ink. We ran preliminary gold printing tests in our laboratory but so far we have not been able to achieve better resolution than ~ 150 µm. Special coatings could be

applied to the substrate to increase the contact angle between gold and substrate, increasing the resolution of the patterns. Another drawback of printable gold ink is that the standard thermal annealing process recommended by the manufacturer involves temperatures as high as 250°C, difficult to make compatible with the PET and PEN polymers used in this thesis. Nonetheless, photonic sintering methods could be applied to sinter the gold, or improve the sintering of the printed silver. They would increase at the same time the fabrication throughput by significantly reducing the sintering time. Two photonic sintering methods are available at EPFL-SAMLAB, exposure to near-infrared light and flash sintering using the equipment *PulseForge*® from *Novacentrix*®.

As for sensing layers, more specific sensing materials could be also developed and adapted to the different sensors, benefiting from their sensing particularities to obtain high selectivity. For instance, the PP-MEMS have been demonstrated only for R.H. detection for the time being, but for more specific applications, the microbridges could be functionalized with specific sensing layers for diverse analytes such as volatile organic compounds by using non contact printing methods such as inkjet printing or LIFT (Laser Induced Forward Transfer). In this case, the microbridge would deflect by itself rather than by the swelling of the substrate, although the combination of both effects could occur. Else the substrate could be passivated against the analyte using a barrier like the one described above. Compared to a membrane-like gas sensor providing an equivalent capacitance value, the array developed here should be relatively insensitive to acceleration due to the small mass of every independent microbridge; however gas sensing tests while the array is subjected to acceleration should be carried out to experimentally evaluate this affirmation.

The combination of an array of PP-MEMS with sensing layers customized to maximize their sensitivity, along with standard PP sensors, IDE sensors and chemiresistors could set the ground for simultaneous sensitive and selective detection of different analytes. In any case, a theoretical model to predict the sensor response to gases is currently missing and should be elaborated for future improvements. The model developed in [153] to predict the bending of flexible substrates coated with a metallic layer due to thermal mismatch could be adapted to this scenario by treating the sensing layer swelling due to gas absorption in a similar way to thermal expansion.

The geometry of the PP-MEMS (length, width, height and thickness) could be tuned to attain a feasible pull-in voltage value, with the aim to achieve an array of MEMS microswitches that could work in combination with arrays of printed sensors in a fully-printed sensing system. The MEMS devices could also find application as electrostatic resonant sensors or actuators. Finally, there exists nowadays commercially available inkjet-printable piezoelectric materials such as polyvinylidene fluoride(PVDF) that combined with the PP-MEMS structures described in this thesis could lead to the development of inkjet-printed piezoelectrically-driven actuators or resonators. In any case, the mechanical robustness of the structures should be reviewed and improved.

Regarding the microhotplates, the minimization of their surface area by using the alternative printing methods mentioned above would yield to a minimization of their power consumption. Also, the substrate should be as thin as possible. In the cases where the substrate cannot be chosen to be very thin, as in the multisensing platform presented in Chapter 5, the substrate and dielectric on top of the heating element should be patterned around the heater (by laser milling for instance) to decrease lateral heat loss by conduction and subsequent convection. The long-term stability of the heaters should be evaluated and enhanced if necessary by electrodeposition of nickel or gold.

The multisensing platform is at an early stage of development. Different combinations of sensing layer should be tried and the platform should be tested for different gas analytes, R.H. and temperature "in operando" conditions using the RFID label for long-term (few weeks or months) data logging or direct wireless communication.

Last but not least, the polymeric foil utilized as substrate for all the presented devices renders the sensors potentially flexible. Thus static and cycling bending tests should be performed for each of the presented device to evaluate their bending reliability. In that regard the presented theoretical models should be expanded to bending along different axis for all the different utilized geometries.

In terms of general field of application, the work performed in this thesis contributes to the concept of the "Internet of Things" where multiple very low-cost and flexible sensing systems can interact with their environment an wirelessly communicate to each other, opening the door to a number of new applications in the fields of security, health or logistics. In that sense, the quest of fully printed smart systems becomes of high interest for the large-scale production by means of roll-to-roll process of ultra low-cost systems including not only printed sensors, actuators, interconnections and antennas, but also batteries and printed logics. Fully printed electronic circuitry, able to replace rigid cumbersome Si chips which are difficult to assemble on foil, is nowadays far from being a reality even for relatively simple circuits. However, recent improvements in stability and mobility of solution-based organic and inorganic semiconductors and the development of novel printing methods allowing sub-micrometer resolution such as hydroelectrodynamic jet printing, suggest the potential of medium- or large-scale integration of printed transistors in a mid-term future. In this scenario, printed copper could replace silver for interconnection due to its lower price.

Since inkjet makes possible drop-on-demand deposition of material without contact, it could be applied in scenarios requiring high customization and quick adaptation, such as customized sensors directly patterned on the surface of products or personalized sensors directly printed on the skin. The flexible and large area characteristics of polymer foils could be further exploited to create sensing foils for artificial robotic skin or even artificial skin if the materials employed are biocompatible. Biocompatibility and adaptation to curved surfaces are two of the most promising features of flexible and printed electronics that are likely to take a good deal of the research effort in the future for health care applications. On one side,

there is a number of biocompatible polymers that could be employed in electronic systems placed in close contact with the human body (or even implanted inside), adapting to its shapes and even stretching with it. Such flexible biocompatible devices could occupy large areas wrapping around organs and tissues to perform space-time mapping of medical parameter of interest and communicate them wirelessly to the exterior. The implanted systems could be "chemically programmed" to be bioresorbed in the body once their function is accomplished. On the other hand, inkjet printing could be employed to deposit a wide range of biocompatible materials on a large area and on curved surfaces.

Bibliography

[1] D. Briand, A. Oprea, J. Courbat, and N. Bârsan, "Making environmental sensors on plastic foil," *Materials Today*, vol. 14, no. 9, pp. 416 – 423, 2011.

[2] A. Huebler, U. Hahn, W. Beier, N. Lasch, and T. Fischer, "High volume printing technologies for the production of polymer electronic structures," in *2nd International IEEE Conference on Polymers and Adhesives in Microelectronics and Photonics, 2002 (POLYTRONIC 2002), Zalaegerszeg, Hungary, 26 June 2002*, pp. 172–176.

[3] V. Subramanian, J. B. Chang, A. de la Fuente Vornbrock, D. C. Huang, L. Jagannathan, F. Liao, B. Mattis, S. Molesa, D. R. Redinger, D. Soltman, S. K. Volkman, and Q. Zhang, "Printed electronics for low-cost electronic systems: Technology status and application development," in *34th European Solid-State Circuits Conference, 2008 (ESSCIRC 2008), Edinburgh, UK, 15-19 September 2008*, pp. 17–24.

[4] M. Singh, H. M. Haverinen, P. Dhagat, and G. E. Jabbour, "Inkjet printing—process and its applications," *Advanced Materials*, vol. 22, no. 6, pp. 673–685, 2010.

[5] W. Clemens, W. Fix, J. Ficker, A. Knobloch, and A. Ullmann, "From polymer transistors toward printed electronics," *Journal of Materials Research*, vol. 19, no. 7, pp. 1963–1973, 2004.

[6] T.-M. Lee, H.-S. Han, B. Kim, S.-W. Kwak, J.-H. Noh, and I. Kim, "Roll offset printing process based on interface separation for fine and smooth patterning," *Thin Solid Films*, vol. 548, no. 0, pp. 566 – 571, 2013.

[7] H. Klauk, ed., *Organic Electronics: Materials, Manufacturing, and Applications*. John Wiley and Sons, 2006.

[8] B. Derby, "Inkjet printing of functional and structural materials: Fluid property requirements, feature stability, and resolution," *Annual Review of Materials Research*, vol. 40, no. 1, pp. 395–414, 2010.

[9] D. Soltman and V. Subramanian, "Inkjet-printed line morphologies and temperature control of the coffee ring effect," *Langmuir*, vol. 24, no. 5, pp. 2224–2231, 2008. PMID: 18197714.

[10] D. Gunders, "Wasted: How america is losing up to 40 percent of its food from farm to fork to landfill," August 2012. http://www.nrdc.org/food/files/wasted-food-IP.pdf.

[11] K. D. Hall, J. Guo, M. Dore, and C. C. Chow, "The progressive increase of food waste in america and its environmental impact," November 2009. http://www.plosone.org/article/info

[12] J. Courbat, *Gas Sensors on plastic foil with reduced power consumption for wireless applications*. PhD thesis, Ecole Polytechnique Fédérale de Lausanne, Switzerland, June 2010.

[13] D. Briand, A. Krauss, B. Van Der Schoot, U. Weimar, N. Barsan, W. Göpel, and N. De Rooij, "Design and fabrication of high-temperature micro-hotplates for drop-coated gas sensors," *Sensors and Actuators, B: Chemical*, vol. 68, no. 1, pp. 223–233, 2000. cited By (since 1996)115.

[14] A. Bailey, A. M. Pisanelli, and K. Persaud, "Development of conducting polymer sensor arrays for wound monitoring," *Sensors and Actuators B: Chemical*, vol. 131, no. 1, pp. 5 – 9, 2008.

[15] R. A. Bissell, K. C. Persaud, and P. Travers, "The influence of non-specific molecular partitioning of analytes on the electrical responses of conducting organic polymer gas sensors," *Phys. Chem. Chem. Phys.*, vol. 4, pp. 3482–3490, 2002.

[16] T. Kinkeldei, C. Zysset, N. Münzenrieder, and G. Tröster, "The influence of bending on the performance of flexible carbon black/polymer composite gas sensors," *Journal of Polymer Science Part B: Polymer Physics*, vol. 51, no. 5, pp. 329–336, 2013.

[17] B. Yang, B. Aksak, Q. Lin, and M. Sitti, "Compliant and low-cost humidity nanosensors using nanoporous polymer membranes," *Sensors and Actuators B: Chemical*, vol. 114, no. 1, pp. 254 – 262, 2006.

[18] K. Parikh, K. Cattanach, R. Rao, D.-S. Suh, A. Wu, and S. K. Manohar, "Flexible vapour sensors using single walled carbon nanotubes," *Sensors and Actuators B: Chemical*, vol. 113, no. 1, pp. 55 – 63, 2006.

[19] P.-G. Su and C.-S. Wang, "Novel flexible resistive-type humidity sensor," *Sensors and Actuators B: Chemical*, vol. 123, no. 2, pp. 1071 – 1076, 2007.

[20] D. Briand, S. Colin, J. Courbat, S. Raible, J. Kappler, and N. de Rooij, "Integration of mox gas sensors on polyimide hotplates," *Sensors and Actuators B: Chemical*, vol. 130, no. 1, pp. 430 – 435, 2008.

[21] A. Pecora, L. Maiolo, E. Zampetti, S. Pantalei, A. Valletta, A. Minotti, F. Maita, D. Simeone, M. Cuscuna, A. Bearzotti, A. Macagnano, L. Mariucci, and G. Fortunato, "Chemoresistive nanofibrous sensor array and read-out electronics on flexible substrate," in *International Solid-State Sensors, Actuators and Microsystems Conference, 2009 (TRANSDUCERS 2009), Denver (Colorado), USA, 21-25 June 2009*, pp. 144–147.

[22] N.-B. Cho, T.-H. Lim, Y.-M. Jeon, and M.-S. Gong, "Humidity sensors fabricated with photo-curable electrolyte inks using an ink-jet printing technique and their properties," *Sensors and Actuators B: Chemical*, vol. 130, no. 2, pp. 594 – 598, 2008.

[23] K. Crowley, A. Morrin, A. Hernandez, E. O'Malley, P. G. Whitten, G. G. Wallace, M. R. Smyth, and A. J. Killard, "Fabrication of an ammonia gas sensor using inkjet-printed polyaniline nanoparticles," *Talanta*, vol. 77, no. 2, pp. 710 – 717, 2008. 14th International Conference on Flow Injection Analysis and Related Techniques.

[24] K. Crowley, A. Morrin, R. L. Shepherd, M. in het Panhuis, G. G. Wallace, M. R. Smyth, and A. J. Killard, "Fabrication of polyaniline-based gas sensors using piezoelectric inkjet and screen printing for the detection of hydrogen sulfide," *IEEE Sensors Journal*, vol. 10, no. 9, pp. 1419–1426, 2010.

[25] S. Claramunt, O. Monereo, M. Boix, R. Leghrib, J. D. Prades, A. Cornet, P. Merino, C. Merino, and A. Cirera, "Flexible gas sensor array with an embedded heater based on metal decorated carbon nanofibres," *Sensors and Actuators B: Chemical*, vol. 187, pp. 401 – 406, 2013.

[26] A. Humbert, B. J. Tuerlings, R. J. O. M. Hoofman, Z. Tan, D. Gravesteijn, M. A. P. Pertijs, C. W. M. Bastiaansen, and D. Soccol, "A low-power CMOS integrated sensor for CO2 detection in the percentage range," in *2013 Transducers Eurosensors XXVII: The 17th International Conference on Solid-State Sensors, Actuators and Microsystems, 2013 (TRANSDUCERS EUROSENSORS XXVII), Barcelona, Spain, 16-20 June 2013*, pp. 1649–1652.

[27] P. Kurzawski, C. Hagleitner, and A. Hierlemann, "Detection and discrimination capabilities of a multitransducer single-chip gas sensor system," *Analytical Chemistry*, vol. 78, no. 19, pp. 6910–6920, 2006.

[28] Y. Li, C. Vancura, D. Barrettino, M. Graf, C. Hagleitner, A. Kummer, M. Zimmermann, K.-U. Kirstein, and A. Hierlemann, "Monolithic cmos multi-transducer gas sensor microsystem for organic and inorganic analytes," *Sensors and Actuators B: Chemical*, vol. 126, no. 2, pp. 431 – 440, 2007.

[29] A. M. Kummer, A. Hierlemann, and H. Baltes, "Tuning sensitivity and selectivity of complementary metal oxide semiconductor-based capacitive chemical microsensors," *Analytical Chemistry*, vol. 76, no. 9, pp. 2470–2477, 2004.

[30] A. M. Kummer, T. P. Burg, and A. Hierlemann, "Transient signal analysis using complementary metal oxide semiconductor capacitive chemical microsensors," *Analytical Chemistry*, vol. 78, no. 1, pp. 279–290, 2006.

[31] A. Oprea, J. Courbat, N. Bârsan, D. Briand, N. F. de Rooij, and U. Weimar, "Temperature, humidity and gas sensors integrated on plastic foil for low power applications," *Sensors and Actuators B: Chemical*, vol. 140, no. 1, pp. 227 – 232, 2009.

[32] C.-Y. Lee, W. G.-W., and H. W.-J., "Fabrication of micro sensors on a flexible substrate," *Sensors and Actuators A: Physical*, vol. 147, no. 1, pp. 173 – 176, 2008.

[33] A. Arena, N. Donato, and G. Saitta, "Capacitive humidity sensors based on MWCNTs/polyelectrolyte interfaces deposited on flexible substrates," *Microelectronics Journal*, vol. 40, no. 6, pp. 887 – 890, 2009.

[34] S. K. Mahadeva, S. Yun, and J. Kim, "Flexible humidity and temperature sensor based on cellulose–polypyrrole nanocomposite," *Sensors and Actuators A: Physical*, vol. 165, no. 2, pp. 194 – 199, 2011.

[35] E. Starke, A. Turke, M. Krause, and W. Fischer, "Flexible polymer humidity sensor fabricated by inkjet printing," in *16th International Solid-State Sensors, Actuators and Microsystems Conference, 2011 (TRANSDUCERS 2011), Beijing, China, 5-9 June 2011*, pp. 1152–1155.

[36] E. Starke, A. Turke, M. Schneider, and W. Fischer, "Setup and properties of a fully inkjet printed humidity sensor on pet substrate," in *IEEE Sensors, 2012, Taipei, Taiwan, 28-31 October 2012*, pp. –.

[37] J. Courbat, Y. B. Kim, D. Briand, and N.-F. de Rooij, "Inkjet printing on paper for the realization of humidity and temperature sensors," in *16th International Solid-State Sensors, Actuators and Microsystems Conference, 2011 (TRANSDUCERS 2011), Beijing, China, 5-9 June 2011*, pp. 1356–1359.

[38] J. Weremczuk, G. Tarapata, and R. S. Jachowicz, "The ink-jet printing humidity sorption sensor—modelling, design, technology and characterization," *Measurement Science and Technology*, vol. 23, no. 1, p. 014003, 2012.

[39] A. S. G. Reddy, B. B. Narakathu, M. Z. Atashbar, M. Rebros, E. Rebrosova, and M. K. Joyce, "Fully printed flexible humidity sensor," *Procedia Engineering*, vol. 25, no. 0, pp. 120 – 123, 2011.

[40] A. Rivadeneyra, J. Fernández-Salmerón, M. Agudo, J. López-Villanueva, L. Capitan-Vallvey, and A. Palma, "Design and characterization of a low thermal drift capacitive humidity sensor by inkjet-printing," *Sensors and Actuators B: Chemical*, vol. 195, no. 0, pp. 123 – 131, 2014.

[41] Y. Liu, T. Cui, and K. Varahramyan, "All-polymer capacitor fabricated with inkjet printing technique," *Solid-State Electronics*, vol. 47, no. 9, pp. 1543 – 1548, 2003.

[42] B. Chen, T. Cui, Y. Liu, and K. Varahramyan, "All-polymer rc filter circuits fabricated with inkjet printing technology," *Solid-State Electronics*, vol. 47, no. 5, pp. 841 – 847, 2003.

[43] H. Al-Chami and E. Cretu, "Inkjet printing of microsensors," in *IEEE 15th International Mixed-Signals, Sensors, and Systems Test Workshop, 2009 (IMS3TW '09), Scottsdale (Arizona), USA, 10-12 June 2009*, pp. 1–6.

[44] P. V. Gerwen, W. Laureyn, W. Laureys, G. Huyberechts, M. O. D. Beeck, K. Baert, J. Suls, W. Sansen, P. Jacobs, L. Hermans, and R. Mertens, "Nanoscaled interdigitated electrode arrays for biochemical sensors," *Sensors and Actuators B: Chemical*, vol. 49, no. 1–2, pp. 73 – 80, 1998.

[45] R. Igreja and C. Dias, "Analytical evaluation of the interdigital electrodes capacitance for a multi-layered structure," *Sensors and Actuators A: Physical*, vol. 112, no. 2–3, pp. 291 – 301, 2004.

[46] R. Igreja and C. Dias, "Extension to the analytical model of the interdigital electrodes capacitance for a multi-layered structure," *Sensors and Actuators A: Physical*, vol. 172, no. 2, pp. 392 – 399, 2011.

[47] S. S. Gevorgian, T. Martinsson, P. L. J. Linner, and E. L. Kollberg, "CAD models for multilayered substrate interdigital capacitors," *IEEE Transactions on Microwave Theory and Techniques*, vol. 44, no. 6, pp. 896–904, 1996.

[48] R. Igreja and C. Dias, "Dielectric response of interdigital chemocapacitors: The role of the sensitive layer thickness," *Sensors and Actuators B: Chemical*, vol. 115, no. 1, pp. 69 – 78, 2006.

[49] E. Zampetti, S. Pantalei, A. Pecora, A. Valletta, L. Maiolo, A. Minotti, A. Macagnano, G. Fortunato, and A. Bearzotti, "Design and optimization of an ultra thin flexible capacitive humidity sensor," *Sensors and Actuators B: Chemical*, vol. 143, no. 1, pp. 302 – 307, 2009.

[50] E. Zampetti, L. Maiolo, A. Pecora, F. Maita, S. Pantalei, A. Minotti, A. Valletta, M. Cuscunà, A. Macagnano, G. Fortunato, and A. Bearzotti., "Flexible sensorial system based on capacitive chemical sensors integrated with readout circuits fully fabricated on ultra thin substrate," *Sensors and Actuators B: Chemical*, vol. 155, no. 2, pp. 768 – 774, 2011.

[51] T. Thundat, R. J. Warmack, G. Y. Chen, and D. P. Allison, "Thermal and ambient-induced deflections of scanning force microscope cantilevers," *Applied Physics Letters*, vol. 64, no. 21, pp. 2894–2896, 1994.

[52] A. Boisen, S. Dohn, S. S. Keller, S. Schmid, and M. Tenje, "Cantilever-like micromechanical sensors," *Reports on Progress in Physics*, vol. 74, no. 3, p. 036101, 2011.

[53] H. P. Lang, R. Berger, F. Battiston, J.-P. Ramseyer, E. Meyer, C. Andreoli, J. Brugger, P. Vettiger, M. Despont, T. Mezzacasa, L. Scandella, H.-J. Güntherodt, C. Gerber, and J. K. Gimzewski, "A chemical sensor based on a micromechanical cantilever array for the identification of gases and vapors," *Applied Physics A*, vol. 66, no. 1, pp. S61–S64, 1998.

[54] Z. Hu, T. Thundat, and R. J. Warmack, "Investigation of adsorption and absorption-induced stresses using microcantilever sensors," *Journal of Applied Physics*, vol. 90, no. 1, pp. 427–431, 2001.

[55] S. Singamaneni, M. E. McConney, M. C. LeMieux, H. Jiang, J. O. Enlow, T. J. Bunning, R. R. Naik, and V. V. Tsukruk, "Polymer–silicon flexible structures for fast chemical vapor detection," *Advanced Materials*, vol. 19, no. 23, pp. 4248–4255, 2007.

[56] S. Singamaneni, M. C. LeMieux, H. P. Lang, C. Gerber, Y. Lam, S. Zauscher, P. G. Datskos, N. V. Lavrik, H. Jiang, R. R. Naik, T. J. Bunning, and V. V. Tsukruk, "Bimaterial microcantilevers as a hybrid sensing platform," *Advanced Materials*, vol. 20, no. 4, pp. 653–680, 2008.

[57] R. Pechmann, J. M. Kohler, W. Fritzsche, A. Schaper, and T. M. Jovin, "The novolever: A new cantilever for scanning force microscopy microfabricated from polymeric materials," *Review of Scientific Instruments*, vol. 65, no. 12, pp. 3702–3706, 1994.

[58] G. Genolet, J. Brugger, M. Despont, U. Drechsler, P. Vettiger, N. F. de Rooij, and D. Anselmetti, "Soft, entirely photoplastic probes for scanning force microscopy," *Review of Scientific Instruments*, vol. 70, no. 5, pp. 2398–2401, 1999.

[59] M. Hopcroft, T. Kramer, G. Kim, K. Takashima, Y. Higo, D. Moore, and J. Brugger, "Micromechanical testing of su-8 cantilevers," *Fatigue & Fracture of Engineering Materials & Structures*, vol. 28, no. 8, pp. 735–742, 2005.

[60] S. Keller, D. Haefliger, and A. Boisen, "Fabrication of thin su-8 cantilevers: initial bending, release and time stability," *Journal of Micromechanics and Microengineering*, vol. 20, no. 4, p. 045024, 2010.

[61] M. Calleja, J. Tamayo, A. Johansson, P. Rasmussen, L. M. Lechuga, and A. Boisen, "Polymeric cantilever arrays for biosensing applications," *Sensor Letters*, vol. 1, no. 1, pp. 20–24, 2003.

[62] J. H. T. Ransley, M. Watari, D. Sukumaran, R. A. McKendry, and A. A. Seshia, "Su8 biochemical sensor microarrays," *Microelectronic Engineering*, vol. 83, no. 4–9, pp. 1621 – 1625, 2006. Proceedings of the 31st International Conference on Micro- and Nano-Engineering.

[63] A. W. McFarland and J. S. Colton, "Chemical sensing with micromolded plastic microcantilevers," *Journal of Microelectromechanical Systems*, vol. 14, no. 6, pp. 1375–1385, 2005.

[64] A. Gaitas and Y. B. Gianchandani, "An experimental study of the contact mode afm scanning capability of polyimide cantilever probes," *Ultramicroscopy*, vol. 106, no. 8–9, pp. 874 – 880, 2006. Proceedings of the Seventh International Conference on Scanning Probe Microscopy, Sensors and Nanostructures.

[65] G. Zhang, V. Chu, and J. P. Conde, "Electrostatically actuated bilayer polyimide-based microresonators," *Journal of Micromechanics and Microengineering*, vol. 17, no. 4, p. 797, 2007.

[66] X. R. Zhang and X. Xu, "Development of a biosensor based on laser-fabricatedpolymer microcantilevers," *Applied Physics Letters*, vol. 85, no. 12, pp. 2423–2425, 2004.

[67] T.-J. Yao, X. Yang, and Y.-C. Tai, "Brf3 dry release technology for large freestanding parylene microstructures and electrostatic actuators," *Sensors and Actuators A: Physical*, vol. 97–98, no. 0, pp. 771 – 775, 2002. Selected papers from Eurosenors.

[68] S. Satyanarayana, D. T. McCormick, and A. Majumdar, "Parylene micro membrane capacitive sensor array for chemical and biological sensing," *Sensors and Actuators B: Chemical*, vol. 115, no. 1, pp. 494 – 502, 2006.

[69] R. Katragadda, Z. Wang, W. Khalid, Y. Li, and Y. Xu, "Parylene cantilevers integrated with polycrystalline silicon piezoresistors for surface stress sensing," *Applied Physics Letters*, vol. 91, no. 8, pp. –, 2007.

[70] A. Greve, S. Keller, A. L. Vig, A. Kristensen, D. Larsson, K. Yvind, J. M. Hvam, M. Cerruti, A. Majumdar, and A. Boisen, "Thermoplastic microcantilevers fabricated by nanoimprint lithography," *Journal of Micromechanics and Microengineering*, vol. 20, no. 1, p. 015009, 2010.

[71] S. B. Patil, V. Chu, and J. P. Conde, "Performance of thin film silicon MEMS on flexible plastic substrates," *Sensors and Actuators A: Physical*, vol. 144, no. 1, pp. 201 – 206, 2008.

[72] M. Ahmed, D. Butler, and Z. Celik-Butler, "Mems absolute pressure sensor on a flexible substrate," in *IEEE 25th International Conference on Micro Electro Mechanical Systems, 2012 (MEMS 2012), Paris, France, 29 January - 2 February 2012*, pp. 575–578.

[73] M. Ataka, M. Mita, H. Toshiyoshi, and H. Fujita, "Electrostatic microactuators in a flexible sheet-smart MEMS sheet," in *2013 Transducers Eurosensors XXVII: The 17th International Conference on Solid-State Sensors, Actuators and Microsystems, 2013 (TRANSDUCERS EUROSENSORS XXVII), Barcelona, Spain, 16-20 June 2013*, pp. 2341–2344.

[74] M. Ataka and H. Fujita, "micro actuator array in a flexible sheet-smart MEMS sheet," in *IEEE Sensors, 2012, Taipei, Taiwan, 28-31 Octubre 2012*, pp. 536–539.

[75] A. Hense, C. Fromm, and D. Zielke, "Acceleration sensors based on polymer-electronic materials," *Procedia Engineering*, vol. 5, no. 0, pp. 713 – 716, 2010. Conference Eurosensor {XXIV}.

[76] N. Klejwa, R. Hennessy, J. W. P. Chen, and R. Howe, "A reel-to-reel compatible printed accelerometer," in *16th International Solid-State Sensors, Actuators and Microsystems Conference, 2011 (TRANSDUCERS 2011), Beijing, China, 5-9 June 2011*, pp. 699–702.

[77] T. Yokota, S. Nakano, T. Sekitani, and T. Someya, "Plastic complementary microelectromechanical switches," *Applied Physics Letters*, vol. 93, no. 2, p. 023305, 2008.

[78] S. Nakano, T. Sekitani, T. Yokota, and T. Someya, "Low operation voltage of inkjet-printed plastic sheet-type micromechanical switches," *Applied Physics Letters*, vol. 92, no. 5, p. 053302, 2008.

[79] Y. Kato, T. Sekitani, Y. Noguchi, M. Takamiya, T. Sakurai, and T. Someya, "A large-area, flexible, ultrasonic imaging system with a printed organic transistor active matrix," in *IEEE International Electron Devices Meeting, 2008 (IEDM 2008), San Francisco (California), USA, 15-17 December 2008*, pp. 1–4.

[80] L. Cheng-Yao, O.-H. Huttunen, J. Hiitola-Keinanen, J. Petaja, H. Fujita, and H. Toshiyoshi, "MEMS-controlled paper-like transmissive flexible display," *Journal of Microelectromechanical Systems*, vol. 19, no. 2, pp. 410–418, 2010.

[81] X. Liu, M. Mwangi, X. Li, M. O'Brien, and G. Whitesides, "Paper-based piezoresistive MEMS sensors," *Lab Chip*, vol. 11, pp. 2189–2196, 2011.

[82] R. Lakhmi, H. Debeda, I. Dufour, and C. Lucat, "Force sensors based on screen-printed cantilevers," *IEEE Sensors Journal*, vol. 10, pp. 1133–1137, June 2010.

[83] D. Zhu, S. Beeby, M. Tudor, and N. Harris, "A credit card sized self powered smart sensor node," *Sensors and Actuators A: Physical*, vol. 169, no. 2, pp. 317 – 325, 2011.

[84] E. Park, Y. Chen, T.-J. K. Liu, and V. Subramanian, "A new switching device for printed electronics: inkjet-printed microelectromechanical relay," *Nano Letters*, vol. 13, no. 11, pp. 5355–5360, 2013.

[85] S. Fuller, E. Wilhelm, and J. Jacobson, "Ink-jet printed nanoparticle microelectromechanical systems," *Journal of Microelectromechanical Systems*, vol. 11, pp. 54–60, Feb 2002.

[86] E. W. Lam, H. Li, and M. Schmidt, "Silver nanoparticle structures realized by digital surface micromachining," in *International Solid-State Sensors, Actuators and Microsystems Conference, 2009 (TRANSDUCERS 2009), Denver (Colorado), USA, 21-25 June 2009*, pp. 1698–1701.

[87] J. Rogers, R. Jackman, and G. Whitesides, "Microcontact printing and electroplating on curved substrates: Production of free-standing three-dimensional metallic microstructures," *Advanced Materials*, vol. 9, no. 6, pp. 475–477, 1997.

[88] W. V. Houston, "The temperature dependence of electrical resistance," *Phys. Rev.*, vol. 88, pp. 1321–1323, Dec 1952.

[89] S. Xiao, L. Che, X. Li, and Y. Wang, "A cost-effective flexible MEMS technique for temperature sensing," *Microelectronics Journal*, vol. 38, no. 3, pp. 360 – 364, 2007.

[90] Y. Moser and M. A. M. Gijs, "Miniaturized flexible temperature sensor," *Journal of Microelectromechanical Systems*, vol. 16, no. 6, pp. 1349–1354, 2007.

[91] D. J. Lichtenwalner and A. E. a. A. I. Hydrick, "Flexible thin film temperature and strain sensor array utilizing a novel sensing concept," *Sensors and Actuators A: Physical*, vol. 135, no. 2, pp. 593 – 597, 2007.

[92] J. Felba, K. Nitsch, T. Piasecki, P. Paluch, A. Moscicki, and A. Kinart, "The influence of thermal process on electrical conductivity of microstructures: Made by ink-jet painting with the use of ink containing nano sized silver particles," in *9th IEEE Conference on Nanotechnology, 2009 (IEEE-NANO 2009), Genoa, Italy, 26-30 July 2009*, pp. 408–411.

[93] R. Deegan, O. Bakajin, T. Dupon, G. Huber, S. Nagel, and T. Witten, "Capillary flow as the cause of ring stains from dried liquid drops," *Nature*, no. 6653, p. 827–829, 1997.

[94] R. Deegan, "Pattern formation in drying drops," *Physical Review E*, vol. 61, pp. 475–485, Jan 2000.

[95] R. Deegan, O. Bakajin, T. Dupont, G. Huber, S. Nagel, and T. Witten, "Contact line deposits in an evaporating drop," *Physical Review E*, vol. 62, pp. 756–765, Jul 2000.

[96] J. Doggart, Y. Wu, and S. Zhu, "Inkjet printing narrow electrodes with < 50 μm line width and channel length for organic thin-film transistors," *Applied Physics Letters*, vol. 94, no. 16, p. 163503, 2009.

[97] T. H. J. van Osch, J. Perelaer, A. W. M. de Laat, and U. S. Schubert, "Inkjet printing of narrow conductive tracks on untreated polymeric substrates," *Advanced Materials*, vol. 20, no. 2, pp. 343–345, 2008.

[98] J. Perelaer, P. J. Smith, D. Mager, D. Soltman, S. K. Volkman, V. Subramanian, J. Korvink, and U. S. Schubert, "Printed electronics: the challenges involved in printing devices, interconnects, and contacts based on inorganic materials," *Journal of Materials Chemistry*, vol. 20, pp. 8446–8453, 2010.

[99] M. L. Allen, M. Aronniemi, T. Mattila, A. Alastalo, K. Ojanperä, M. Suhonen, and H. Seppä, "Electrical sintering of nanoparticle structures," *Nanotechnology*, vol. 19, no. 17, p. 175201, 2008.

[100] C.-Y. Kao and K.-S. Chou, "Electroless copper plating onto printed lines of nanosized silver seeds," *Electrochemical and Solid-State Letters*, vol. 10, no. 3, pp. D32–D34, 2007.

[101] R. Cauchois, M. Saadaoui, J. Legeleux, T. Malia, B. Dubois-Bonvalot, K. Inal, and J.-C. Fidalgo, "Wire-bonding on inkjet-printed silver pads reinforced by electroless plating for chip on flexible board packages," in *3rd Electronic System-Integration Technology Conference , 2010, (ESTC 2010), Berlin, Germany, 13-16 September 2010*, pp. 1–6.

[102] P. Hidber, W. Helbig, E. Kim, and G. Whitesides, "Microcontact printing of pallaidum colloids: Micron-scale patterning by electroless desposition of copper," *Langmuir*, vol. 12, no. 5, pp. 1375–1380, 1996.

[103] U. Zschieschang, H. Klauk, M. Halik, G. Schmid, and C. Dehm, "Flexible organic circuits with printed gate electrodes," *Advanced Materials*, vol. 15, no. 14, pp. 1147–1151, 2003.

[104] C.-H. Hsu, M.-C. Yeh, K.-L. Lo, and L.-J. Chen, "Application of microcontact printing to electroless plating for the fabrication of microscale silver patterns on glass," *Langmuir*, vol. 23, no. 24, pp. 12111–12118, 2007.

[105] J. Tate, J. Rogers, C. Jones, B. Vyas, D. Murphy, W. Li, Z. Bao, R. Slusher, A. Dodabalapur, and H. Katz, "Anodization and microcontact printing on electroless silver: solution-based fabrication procedures for low-voltage electronic systems with organic active components," *Langmuir*, vol. 16, no. 14, pp. 6054–6060, 2000.

[106] U. Zschieschang, M. Halik, and H. Klauk, "Microcontact-printed self-assembled monolayers as ultrathin gate dielectrics in organic thin-film transistors and complementary circuits," *Langmuir*, vol. 24, no. 5, pp. 1665–1669, 2008. PMID: 18198917.

[107] A. Bietsch, J. Zhang, M. Hegner, H. Lang, and C. Gerber, "Rapid functionalization of cantilever array sensors by inkjet printing," *Nanotechnology*, vol. 15, no. 8, p. 873, 2004.

[108] N. Inagaki, S. Tasaka, and K. Hibi, "Surface modification of kapton film by plasma treatments," *Journal of Polymer Science Part A: Polymer Chemistry*, vol. 30, no. 7, pp. 1425–1431, 1992.

[109] D. Hegemann, H. Brunner, and C. Oehr, "Plasma treatment of polymers for surface and adhesion improvement," *Nuclear Instruments and Methods in Physics Research Section B: Beam Interactions with Materials and Atoms*, vol. 208, no. 0, pp. 281 – 286, 2003.

[110] Y.-S. Lin and H.-M. Liu, "Enhanced adhesion of plasma-sputtered copper films on polyimide substrates by oxygen glow discharge for microelectronics," *Thin Solid Films*, vol. 516, no. 8, pp. 1773 – 1780, 2008.

[111] Y.-S. Goo, Y.-I. Lee, N. Kim, K.-J. Lee, B. Yoo, S.-J. Hong, J.-D. Kim, and Y.-H. Choa, "Ink-jet printing of cu conductive ink on flexible substrate modified by oxygen plasma treatment," *Surface and Coatings Technology*, vol. 205, Supplement 1, no. 0, pp. S369 – S372, 2010. Proceedings of the 7th Asian-European Inernational Conference on Plasma Surface Engineering (AEPSE 2009).

[112] A. Oprea, N. Bârsan, U. Weimar, M.-L. Bauersfeld, E. D, and J. Wöllenstein, "Capacitive humidity sensors on flexible RFID labels," *Sensors and Actuators B: Chemical*, vol. 132, no. 2, pp. 404 – 410, 2008.

[113] S. Capone, C. De Pascali, L. Francioso, P. Siciliano, K. Persaud, and A. M. Pisanelli, "Electrical characterization of a pig odorant binding protein by impedance spectroscopy," in *IEEE Sensors, 2009, Christchurch, New Zealand, 25-28 October 2009*, pp. 1758–1762.

[114] D. James, S. M. Scott, Z. Ali, and W. T. O'Hare, "Chemical sensors for electronic nose systems," *Microchimica Acta*, vol. 149, no. 1-2, pp. 1–17, 2005.

[115] B.-J. de Gans, P. C. Duineveld, and U. S. Schubert, "Inkjet printing of polymers: state of the art and future developments," *Advanced Materials*, vol. 16, no. 3, pp. 203–213, 2004.

[116] E. Tekin, B.-J. de Gans, and U. Schubert, "Ink-jet printing of polymers - from single dots to thin film libraries," *J. Mater. Chem.*, vol. 14, pp. 2627–2632, 2004.

[117] F. Molina-Lopez, D. Briand, and N. F. de Rooij, "All additive inkjet printed humidity sensors on plastic substrate," *Sensors and Actuators B: Chemical*, vol. 166–167, no. 0, pp. 212 – 222, 2012.

[118] F. Molina-Lopez, D. Briand, and N. F. de Rooij, "Decreasing the size of printed comb electrodes by the introduction of a dielectric interlayer for capacitive gas sensors on polymeric foil: Modeling and fabrication," *Sensors and Actuators B: Chemical*, vol. 189, no. 0, pp. 89 – 96, 2013.

[119] F. Molina-Lopez, T. Kinkeldei, D. Briand, G. Tröster, and N. F. de Rooij, "Theoretical and experimental study of the bending influence on the capacitance of interdigitated micro-electrodes patterned on flexible substrates," *Journal of Applied Physics*, vol. 114, no. 17, pp. –, 2013.

[120] A. Tételin, C. Pellet, C. Laville, and G. N'Kaoua, "Fast response humidity sensors for a medical microsystem," *Sensors and Actuators B: Chemical*, vol. 91, no. 1–3, pp. 211 – 218, 2003.

[121] A. Tetelin and C. Pellet, "Modeling and optimization of a fast response capacitive humidity sensor," *IEEE Sensors Journal*, vol. 6, no. 3, pp. 714–720, 2006.

[122] N. Lazarus and G. Fedder, "Integrated vertical parallel-plate capacitive humidity sensor," *Journal of Micromechanics and Microengineering*, vol. 21, no. 6, p. 065028, 2011.

[123] A. L. Buck, "New equations for computing vapor pressure and enhancement factor," *Journal of Applied Metereology*, vol. 20, no. 12, pp. 1527–1532, 1981.

[124] D. Schönauer and R. Moos, "Detection of water droplets on exhaust gas sensors," *Sensors and Actuators B: Chemical*, vol. 148, no. 2, pp. 624 – 629, 2010.

[125] J.-Y. Wang, C.-F. Hu, C. Hong, W.-S. Su, and W. Fang, "Development of 3D CNTS interdigitated finger electrodes on flexible polymer for bending strain measurement," in *24th International Conference on Micro Electro Mechanical Systems 2011, (MEMS 2011), Cancun, Mexico, 23-27 January 2011*, pp. 408–411.

[126] T. Someya, T. Sekitani, S. Iba, Y. Kato, H. Kawaguchi, and T. Sakurai, "A large-area, flexible pressure sensor matrix with organic field-effect transistors for artificial skin applications," *Proceedings of the National Academy of Sciences of the United States of America*, vol. 101, no. 27, pp. 9966–9970, 2004.

[127] K. Fukuda, T. Sekitani, U. Zschieschang, H. Klauk, K. Kuribara, T. Yokota, T. Sugino, K. Asaka, M. Ikeda, H. Kuwabara, T. Yamamoto, K. Takimiya, T. Fukushima, T. Aida, M. Takamiya, T. Sakurai, and T. Someya, "A 4 v operation, flexible braille display using organic transistors, carbon nanotube actuators, and organic static random-access memory," *Advanced Functional Materials*, vol. 21, no. 21, pp. 4019–4027, 2011.

[128] P. Cosseddu, S. Lai, M. Barbaro, and A. Bonfiglio, "Ultra-low voltage, organic thin film transistors fabricated on plastic substrates by a highly reproducible process," *Applied Physics Letters*, vol. 100, no. 9, pp. –, 2012.

[129] H.-D. Wu, Z. Zhang, F. Barnes, C. M. Jackson, A. Kain, and J. D. Cuchiaro, "Voltage tunable capacitors using high temperature superconductors and ferroelectrics," *IEEE Transactions on Applied Superconductivity*, vol. 4, no. 3, pp. 156–160, 1994.

[130] P. I. Hsu, M. Huang, Z. Xi, S. Wagner, Z. Suo, and J. C. Sturm, "Spherical deformation of compliant substrates with semiconductor device islands," *Journal of Applied Physics*, vol. 95, no. 2, pp. 705–712, 2004.

[131] Z. Suo, E. Y. Ma, H. Gleskova, and S. Wagner, "Mechanics of rollable and foldable film-on-foil electronics," *Applied Physics Letters*, vol. 74, no. 8, pp. 1177–1179, 1999.

[132] S.-I. Park, J.-H. Ahn, X. Feng, S. Wang, Y. Huang, and J. A. Rogers, "Theoretical and experimental studies of bending of inorganic electronic materials on plastic substrates," *Advanced Functional Materials*, vol. 18, no. 18, pp. 2673–2684, 2008.

[133] K. Sidler, O. Vazquez-Mena, V. Savu, G. Villanueva, M. van den Boogaart, and J. Brugger, "Resistivity measurements of gold wires fabricated by stencil lithography on flexible polymer substrates," *Microelectronic Engineering*, vol. 85, no. 5–6, pp. 1108 – 1111, 2008. Proceedings of the Micro- and Nano-Engineering 2007 Conference {MNE} 2007.

[134] K. Alzoubi, M. M. Hamasha, S. Lu, and B. Sammakia, "Bending fatigue study of sputtered ito on flexible substrate," *Journal of Display Technology*, vol. 7, pp. 593–600, Nov 2011.

[135] K. J. Binns and P. J. Lawrenson, *Analysis and Computation of Electric and Magnetic Field Problems*, pp. 134–135. Pergamon Press, New York, 2004.

[136] Y. Kim, "Elastic modulus measurement of thin film using a dynamic method," *Journal of Electronic Materials*, vol. 26, no. 9, pp. 1002–1008, 1997.

[137] B. Harris, *Analysis and Computation of Electric and Magnetic Field Problems*, pp. 33–37. Institute of Metals, UK, 1986.

[138] C. Ataman, T. Kinkeldei, G. Mattana, A. V. Quintero, F. Molina-Lopez, J. Courbat, K. Cherenack, D. Briand, G. Tröster, and N. de Rooij, "A robust platform for textile integrated gas sensors," *Sensors and Actuators B: Chemical*, vol. 177, no. 0, pp. 1053 – 1061, 2013.

[139] U. Caglar, K. K., and P. Mansikkamaki, "Analysis of mechanical performance of silver inkjet-printed structures," in *2nd IEEE International Nanoelectronics Conference, 2008 (INEC 2008), Shanghai, China, 24-27 March 2008*, pp. 851–856.

[140] U. Altenberend, F. Molina-Lopez, A. Oprea, D. Briand, N. Bârsan, N. F. D. Rooij, and U. Weimar, "Towards fully printed capacitive gas sensors on flexible pet substrates based on ag interdigitated transducers with increased stability," *Sensors and Actuators B: Chemical*, vol. 187, no. 0, pp. 280 – 287, 2013.

[141] M. Matsuguchi, S. Umeda, Y. Sadaoka, and Y. Sakai, "Characterization of polymers for a capacitive-type humidity sensor based on water sorption behavior," *Sensors and Actuators B: Chemical*, vol. 49, no. 3, pp. 179 – 185, 1998.

[142] M. Matsuguchi, E. Hirota, T. Kuroiwa, S. Obara, T. Ogura, and Y. Sakai, "Drift phenomenon of capacitive-type relative humidity sensors in a hot and humid atmosphere," *Journal of The Electrochemical Society*, vol. 147, no. 7, pp. 2796–2799, 2000.

[143] V. Ducéré, A. Bernès, and C. Lacabanne, "A capacitive humidity sensor using cross-linked cellulose acetate butyrate," *Sensors and Actuators B: Chemical*, vol. 106, no. 1, pp. 331 – 334, 2005. {ISOEN} 2003 - Selected Papers from the 10th International Symposium on Olfaction and Electronic Noses.

[144] B. C. Johnson, "Electrical resistivity of copper and nickel thin-film interconnections," *Journal of Applied Physics*, vol. 67, pp. 3018–3024, Mar 1990.

[145] H. Jung, S.-H. Cho, J. Joung, and Y.-S. Oh, "Studies on inkjet-printed conducting lines for electronic devices," *Journal of Electronic Materials*, vol. 36, no. 9, pp. 1211–1218, 2007.

[146] F. Molina-Lopez, D. Briand, N. F. de Rooij, and M. Smolander, "Fully inkjet-printed parallel-plate capacitive gas sensors on flexible substrate," in *IEEE Sensors, 2012, Taipei, Taiwan, 28-31 October 2012*, pp. 1–4.

[147] D.-Y. Lee, Y.-S. Shin, S.-E. Park, T.-U. Yu, and J. Hwang, "Electrohydrodynamic printing of silver nanoparticles by using a focused nanocolloid jet," *Applied Physics Letters*, vol. 90, pp. 081905–081905–3, Feb 2007.

[148] F. Molina-Lopez, D. Briand, and N. F. de Rooij, "Large arrays of inkjet-printed MEMS microbridges on foil," in *26th International Conference on Micro Electro Mechanical Systems 2014, (MEMS 2014), San Francisco (California), USA, 26-30 January 2014*, pp. 506–509.

[149] K. Uksong and K. Wise, "A high-speed capacitive humidity sensor with on-chip thermal reset," *IEEE Transactions on Electron Devices*, vol. 47, pp. 702–710, Apr 2000.

[150] Y. Kato, T. Sekitani, Y. Noguchi, T. Yokota, M. Takamiya, T. Sakurai, and T. Someya, "Large-area flexible ultrasonic imaging system with an organic transistor active matrix," *IEEE Transactions on Electron Devices*, vol. 57, pp. 995–1002, May 2010.

[151] S. Schmidt and C. Grimes, "Characterization of nano-dimensional thin-film elastic moduli using magnetoelastic sensors," *Sensors and Actuators A: Physical*, vol. 94, no. 3, pp. 189 – 196, 2001.

[152] A. Kamyshny, J. Steinke, and S. Magdassi, "Metal-based inkjet inks for printed electronics," *The Open Applied Physics Journal*, vol. 4, pp. 19 – 36, 2011.

[153] W. S. Wong and A. Salleo, eds., *Flexible electronics materials and applications*, pp. 42–47. Springer, 2009.

[154] F. Molina-Lopez, A. V. Quintero, G. Mattana, D. Briand, and N. F. de Rooij, "Large-area compatible fabrication and encapsulation of inkjet-printed humidity sensors on flexible foils with integrated thermal compensation," *Journal of Micromechanics and Microengineering*, vol. 23, no. 2, p. 025012, 2013.

[155] M. Camara, F. Molina-Lopez, E. Danesh, G. Mattana, A. Bontempi, D. Teyssieux, L. Thiery, P. Breuil, C. Pijolat, K. Persaud, D. Briand, and N. F. de Rooij, "Printed micro-hotplates on flexible substrates for gas sensing," in *2013 Transducers Eurosensors XXVII: The 17th International Conference on Solid-State Sensors, Actuators and Microsystems, 2013 (TRANSDUCERS EUROSENSORS XXVII), Barcelona, Spain, 16-20 June 2013*, pp. 1059–1062.

[156] D. De Koninck, F. Lopez, D. Briand, and N.-F. de Rooij, "Foil-level fabrication of inkjet-printed pyroMEMS balloon actuators," in *IEEE 25th International Conference on Micro Electro Mechanical Systems, 2012 (MEMS 2012), Paris, France, 29 January - 2 February 2012*, pp. 64–67.

[157] E. Danesh, F. Molina-Lopez, M. Camara, A. Bontempi, A. V. Quintero, D. Teyssieux, L. Thiery, D. Briand, N. F. de Rooij, and K. C. Persaud, "Development of a new generation of ammonia sensors on printed polymeric hotplates," *Submitted*.

[158] E. Danesh and K. Persaud, "Flexible ammonia sensor based on polyaniline/carbon black composites operating at elevated temperatures," in *14th International Meeting on Chemical Sensors, 2012 (IMCS 2012), Nürenberg, Germany, 20-23 May 2012*, pp. 1134–1136.

[159] A. Bontempi, L. Thiery, D. Teyssieux, D. Briand, and P. Vairac, "Quantitative thermal microscopy using thermoelectric probe in passive mode," *Review of Scientific Instruments*, vol. 84, no. 10, pp. –, 2013.

[160] G. Arutinov, E. C. P. Smits, M. Mastrangeli, G. van Heck, J. van den Brand, H. F. M. Schoo, and A. Dietzel, "Capillary self-alignment of mesoscopic foil components for sensor-systems-in-foil," *Journal of Micromechanics and Microengineering*, vol. 22, no. 11, p. 115022, 2012.

[161] A. Gonzalez-Martin, B. Lewis, M. Raducanu, and J. Kim, "An array-based sensor for seafood freshness assessment," *Bulletin of the Korean Chemical Society*, vol. 31, no. 11, pp. 3084–3092, 2010.

[162] T. Boerjesson, U. Stoellman, and J. Schnuerer, "Off-odorous compounds produced by molds on oatmeal agar: Identification and relation to other growth characteristics," *Journal of Agricultural and Food Chemistry*, vol. 41, no. 11, pp. 2104–2111, 1993.

[163] R. Guillén-Sans and M. Guzmán-Chozas, "Aldehydes in food and its relation with the TBA test for rancidity," *Lipid / Fett*, vol. 97, no. 7-8, pp. 285–286, 1995.

[164] A.-L. Pasanen, S. Lappalainen, and P. Pasanen, "Volatile organic metabolites associated with some toxic fungi and their mycotoxins," *Analyst*, vol. 121, pp. 1949–1953, 1996.

[165] K.-H. Kim, R. Pal, J.-W. Ahn, and Y.-H. Kim, "Food decay and offensive odorants: A comparative analysis among three types of food," *Waste Management*, vol. 29, no. 4, pp. 1265 – 1273, 2009.

[166] H. Zhu, B. Zhu, D. Fu, Y. Xie, Y. Hao, and Y. Luo, "Role of ethylene in the biosynthetic pathways of aroma volatiles in ripening fruit," *Russian Journal of Plant Physiology*, vol. 52, no. 5, pp. 691–695, 2005.

[167] J. H. H. in't Veld, "Microbial and biochemical spoilage of foods: an overview," *International Journal of Food Microbiology*, vol. 33, no. 1, pp. 1 – 18, 1996. Specific Spoilage Organisms.

[168] H. Belitz, W. Grosch, and P. Schieberle, eds., *Food chemistry*. Springer-verlag, 2004.

[169] A. V. Quintero, B. van Remoortere, E. Smits, J. van den Brand, D. Briand, H. F. M. Schoo, and N. F. de Rooij, "Foil-to-foil lamination and electrical interconnection of printed components on flexible substrates," *Microelectronic Engineering*, vol. 110, pp. 52 – 58, 2013.

Francisco Molina-Lopez
Rue du Maupas 11, 1004 – Lausanne (Switzerland) ● francisco.molinalopez@epfl.ch ●
+41 762 26 20 82 / +34 606 54 80 41 ●
Nationality: Spanish ● Date of birth: 26.11.1984

Current Occupation — (Mar. 2010 – Present)

(Expected completion date: May 2014)

Ph.D. Candidate in SAMLAB-IMT at the **Ecole Polytechnique Fédérale de Lausanne (EPFL),** Switzerland**,** under the supervision of **Dr. Danick Briand** and **Prof. Nico de Rooij**.

Thesis title: **Inkjet-Printed Multisensor Platform on Flexible Substrates for Environmental Monitoring**.

Funding: FP7-***Marie-Curie*** Initial Training Network (ITN) **fellowship**;
Project: ***FlexSmell*** - Gas Sensors on Flexible Substrates for Wireless Applications - http://www.flexsmell.eu/.

Main aspects covered and acquired competences:

- Extensive theoretical and practical knowledge on **printed, large area and flexible electronics.** Familiar with **thin films** technology, **flexible** materials (polymers, paper and textiles) and **solution-based functional materials.** Proficient in **microelectronics fabrication** processes including **printing** (especially inkjet) and **cleanroom** related methods.
- Proficient in **design, fabrication and characterization** (electrical and mechanical) of **MEMS** and **sensors**.
- Collaborated in several **industrial** and **research projects** and with different **research institutions** such as CSEM (Switzerland), ETH Zürich (Switzerland), the Hebrew University of Jerusalem (Israel), Holst Centre (The Netherlands), University of Manchester (UK) , VTT (Finland), etc.
- **Teaching experience** acquired through (co-)supervision of several student projects as well as assisting a bachelor level mechanics course for two years, imparted by Prof. Herbert Shea at EPFL.

Research Exchange: **(Oct. 2011 – Jan. 2012)**
At **VTT**, Espoo (**Finland**) under the supervision of **Dr. Maria Smolander**, **(Dec. 2012 – Feb. 2013)**
within the frame of the *FlexSmell* project.

Undergraduate education and training — (2002 – 2009)

University of Granada, Spain.
Double Major: **Electrical Engineering** (**GPA: 8.091 / 10)** and **Physics** (**GPA: 8.265 / 10)**

- Solid background in physics and mathematics.
- Experience with programming, simulations and data acquisition software.
- Experience in analog/digital electronics (RF, Microwave, Instrumentation, etc.).

Education Abroad I: EPFL, Switzerland (GPA: 5.3 / 6) **(Oct. 2006 – Jun. 2007)**

- Training in analog / digital integrated electronic circuits design.
- Experience with IC design software Cadence.
- **Projects**. Successfully completed:
  A semester project on **Customized Design of an Integrated Sinusoidal Oscillator** under supervision of **Professor R. S. Popovic** (**Grade 6/6**).

A group project consisting of the **Development of a SRAM Memory** using Cadence software under supervision of **Professor Y. Leblebici** (**Grade 6/6**).

Education Abroad II: University of California San Diego, USA (GPA: 3.771 / 4) **(Sep. 2008 – Jun. 2009)**

- Acquired knowledge and training in Nanotechnology and Nanoelectronics.
- Gained experience in micro-fabrication within a clean room facility.

Academic Honors

- Awarded for having the **highest GPA** (8.091 out of 10) in Elect. Eng. at the University of Granada, 2008.
- Honors in Final Degree Project (Semester Project at the EPFL).
- Elected by the University of California for the Education Abroad Program.
- Honors in High School Degree.

Work Experience

- **Internship** in the Lab. of Microsystems and Microelect. at **EPFL**, **Switzerland** **(Jul. 2007 – Aug. 2007)**
  Under supervision of **Professor R.S. Popovic**: Measurements, characterization and simulation of a new Hall effect magnetic microsensor using a multi-step spinning current method.

- **Internship** at the High Speed Device Group at **UCSD**, **USA** **(Jul. 2009 – Aug. 2009)**
  Under supervision of **Professor Peter Asbeck**: Monte Carlo simulation of carrier transport in graphene following a semi-classical approach.

Other technical / personal skills:

- Experienced in **operating** a variety of **laboratory instruments and equipment** and preparing data acquisition **set-ups**. I can use commercial electronic components and elaborate PCBs.
- Experienced in working in **chemistry** research facilities.
- **Great capacity for communication** (both oral and written) and **teamwork,** developed throughout collaborations with different partners and presenting results at several events.
- **Disciplined**, effective **time management** skills, **self-directed**, **hands-on** spirit and **career-oriented**.
- Ability to adapt to **multicultural situations** acquired through living abroad (Switzerland, Finland and USA).
- **Languages: Spanish** (Native), **English** (Fluent), **French** (Fluent), **German** (Beginner), **Mandarin** (Beginner).
- **Extracurricular activities:** I have studied classical music for ten years, obtaining the certificate for intermediate level in piano from the Superior Conservatory of Music Victoria Eugenia of Granada.

Main Publications (Refer to http://scholar.google.es/citations?user=YaAZ2PIAAAAJ&hl=en for a complete list)

Journal Papers:

F. Molina-Lopez, T. Kinkeldei, G. Tröster, D. Briand, N.F. de Rooij, *Theoretical and experimental study of the bending influence on the capacitance of interdigitated micro-electrodes patterned on flexible substrates*, J. Appl. Phys. (2013), vol. 114, pp. 174907.

F. Molina-Lopez, D. Briand, N.F. de Rooij, *Decreasing the size of printed comb electrodes by the introduction of a dielectric interlayer for capacitive gas sensors on polymeric foil: Modeling and fabrication*, Sens. Act. B: Chem. (2013), vol. 189, pp. 89-96.

F. Molina-Lopez, A. Vásquez Quintero, G. Mattana, D. Briand, N.F. de Rooij, *Large-area compatible fabrication and encapsulation of inkjet-printed humidity sensors on flexible foils with integrated thermal compensation*, J. Micromech. Microeng. (2013), vol. 23, pp. 025012.

F. Molina-Lopez, D. Briand and N.F. de Rooij, *All additive inkjet printed humidity sensors on flexible substrate*, Sens. Act. B: Chem. (2012), vol. 166-167, pp. 212-222.

D. de Koninck, **F. Molina-Lopez**, D. Briand, N.F. de Rooij, *Foil-level, inkjet-printed pyroMEMS balloon actuators: Fabrication, modeling and validation*, J. Microelectromech. Syst., *Accepted.*

J. F. Salmerón, **F. Molina-Lopez**, D. Briand, J.J. Ruan, A. Rivadeneyra, M.A. Carvajal, L.F. Capitán-Vallvey, N.F. de Rooij, A.J. Palma, *Properties and printability of inkjet and screen printed silver patterns for RFID antennas*, J. Electron. Mater. (2013), vol. 43 (2), pp. 604-617.

U. Altenberend, **F. Molina-Lopez**, A. Oprea, D. Briand, N. Barsan, N.F. De Rooij, U. Weimar, *Towards fully printed capacitive gas sensors on flexible PET substrates based on Ag interdigitated transducers with increased stability*, Sens. Act. B: Chem. (2013), vol. 187, pp. 280-287.

G. Mattana, T. Kinkeldei, D. Leuenberger, C. Ataman, J.J. Ruan, **F. Molina-Lopez**, A. Vásquez Quintero, G. Nisato, G. Tröster, D. Briand, N.F. de Rooij. *Woven temperature and humidity sensors on flexible plastic substrates for e-textile applications*, Sensors Journal, IEEE (2013), vol. 13 (10), pp. 3901-3909.

C. Ataman, T. Kinkeldei, G. Mattana, A. Vásquez Quintero, **F. Molina-Lopez**, J. Courbat, K. Cherenack, D. Briand, G. Tröster, N.F. De Rooij, *A robust platform for textile integrated gas sensors*, Sens. Act. B: Chem. (2013), vol. 177, pp. 1053-1061.

Participation in conferences:

F. Molina-Lopez, D. Briand, N.F. de Rooij, *Large arrays of inkjet-printed MEMS microbridges on foil*, In proceedings of the 27th International Conference on Micro Electro Mechanical Systems, MEMS 2014, San Francisco, USA, 26-30 January 2014, pp. 506-509. (Poster presentation & **presenter**)

F. Molina-Lopez, M. Rupakula, N. Bongard, D. Briand, N.F. de Rooij, *Surface micromachined inkjet-printed MEMS micro-bridge on plastic foil***,** International Conference on Flexible and Printed Electronics, ICFPE 2013, Jeju, Korea, 11-13 September 2013. (Oral presentation & **speaker**)

F. Molina-Lopez, D. Briand, N.F. De Rooij, M. Smolander, *Fully inkjet-printed parallel-plate capacitive gas sensors on flexible substrate*, In proceedings of the 11th IEEE Sensors Conference, IEEE SENSORS 2012, Taipei, Taiwan, 28-31 October 2012, pp. 1-4. (**Special session** oral presentation & **speaker**)

F. Molina-Lopez, D. Briand, N. F. de Rooij, *Inkjet printing of interdigitated capacitive chemical sensors with reduced size by the introduction of a dielectric interlayer*, Procedia Engineering, 26th European Conference on Solid-State Transducers, EUROSENSORS 2012, Kraków, Poland, 9-12 September 2012, vol. 47, pp. 1173-1176. (Oral presentation & **speaker**)

D. Briand, **F. Molina-Lopez**, A. Vásquez Quintero, G. Mattana, N. Frolet, N.F. de Rooij, *Recent advances in printed smart sensing RFID labels,* Printed Electronics Asia 2013, Tokyo, Japan, 9-10 July 2013. (**Invited** oral presentation & **speaker**)

A. Vásquez Quintero, **F. Molina-Lopez**, G. Mattana, D. Briand, N.F. de Rooij, *Self-standing printed humidity sensor with thermo-calibration and integrated heater*, In proceedings of the 17th International Solid-State Sensors, Actuators and Microsystems Conference, TRANSDUCERS 2013, Barcelona, Spain, 16-20 July 2013, pp. 838-841. (Oral presentation)

M. Camara, **F. Molina-Lopez**, E. Danesh, G. Mattana, A. Bontempi, D. Teyssieux, L. Thiery, P. Breuil, C. Pijolat, K. Persaud, D. Briand, N.F. de Rooij, *Printed micro-hotplates on flexible substrates for gas sensing*, In proceedings of the 17th International Solid-State Sensors, Actuators and Microsystems Conference, TRANSDUCERS 2013, Barcelona, Spain, 16-20 July 2013, pp. 1059-1062. (Poster presentation & **presenter**)

J.F. Salmeron, L.F. Capitan-Vallvey, A.J. Palma, **F. Molina-Lopez**, D. Briand, N.F. de Rooij, *Physical and electrical properties of ink-jet and screen printed patterns for RFID HF antennas*, In proceedings of the IEEE International Conference on RFID-Technologies and Applications, RFID-TA 2012, Nice, France, 5-7 November 2012, pp. 188-192. (Oral presentation)

D. Briand, **F. Molina-Lopez**, A. Vasquez Quintero, J. Ruan, G. Mattana, N.F. de Rooij, *All additive inkjet printed capacitive chemical gas sensors on flexible foil*, ICT OPEN 2012, Rotterdam, The Netherlands, 22-23 October 2012. (Invited oral presentation)

D. Briand and **F. Molina-Lopez**, A. Vasquez Quintero, J. Ruan, G. Mattana, N.F. de Rooij, *Printing and integration of Sensors into Smart Objects*, Innovative Printed Smart Object Conference, IPSO 2012, Gardanne, France, 16-17 October 2012. (Invited oral presentation)

D. Briand, G. Mattana, **F. Molina-Lopez**, J. Courbat, N.F. de Rooij, M. Grouchko, S. Magdassi, *Printed temperature and humidity sensors on paper*, In proceeding of the Large-area, Organic and Printed Electronics Convention, LOPE-C 2012, Frankfurt, Germany, 19-21 June 2012, pp. 13-16. (Oral presentation & **speaker**)

U. Altenberend, **F. Molina-Lopez**, D. Briand, A. Oprea, N. Barsan, N. F. De Rooij, U. Weimar, *Inkjet printed capacitive transducers on flexible plastic substrates with increase stability: Ag on PET*, In proceedings of the 14th International Meeting on Chemical Sensors, IMCS 2012, Nuremberg, Germany, 20 – 23 May 2012, pp. 527-530. (Oral presentation)

D.A. de Koninck, **F. Molina-Lopez**, D. Briand, and N.F. de Rooij, *Foil-level fabrication of inkjet-printed pyroMEMS balloon actuators*, In proceedings of the 25th International Conference on Micro Electro Mechanical Systems, MEMS 2012, Paris, France, 29 January - 2 February 2012, pp. 64-67. (Oral presentation)

D. Briand, **F. Molina-Lopez**, A. Vásquez Quintero, C. Ataman, J. Courbat and N.F. de Rooij, *Why going towards plastic and flexible sensors?* Procedia Engineering, 25th European Conference on Solid-State Transducers, EUROSENSORS 2011, Athens, Greece, 4-7 September 2011, vol. 25, pp. 8-15. (Plenary session)

L. Wang, V. Lee, **F. Molina Lopez**, Y. Taur, J.S. Moon, P.M. Asbeck, *Comparison of Ballistic Performance of Graphene and Planar III-V MOSFETs for RF Low Voltage Applications*, 2010 Electronic Materials Conference, Notre Dame, IN, USA, 23-25 June 2010. (Oral presentation)

Patents:

F. Molina-Lopez, A. Vásquez Quintero, D. Briand, N.F. de Rooij, *Printed capacitive sensing* device, PCT/IB2013/056784, 21 August 2013.